NASA
CP
2020
c.1

NASA Conference Publication 2020

TECH LIBRARY KAFB, NM
0067340
LOAN COPY: RE
AFWL TECHNICA
KIRTLAND AFI

Solar Cell High Efficiency and Radiation Damage

A Conference held at
Lewis Research Center
Cleveland, Ohio
April 28-29, 1977

NASA

TECH LIBRARY KAFB, NM

0067340

NASA Conference Publication 2020

Solar Cell High Efficiency and Radiation Damage

A Conference held at
Lewis Research Center
Cleveland, Ohio
May 18-19, 1977

National Aeronautics
and Space Administration

Scientific and Technical
Information Office

1977

PREFACE

This conference is the second of its kind. In November 1974 the High Efficiency Silicon Solar Cell Review was held at the Lewis Research Center. That meeting was the vehicle for many fruitful discussions. The major conclusions reached during those discussions were as follows:

- The maximum practical efficiency of silicon solar cells is between 17 and 20 percent (AMO) and is still a reasonable goal.

- The long-range R&D approach toward this goal should continue to focus on low resistivity (0.1 ohm-cm) silicon.

- Near term R&D should continue to focus on higher resistivity silicon, back surface fields, thinner grid fingers, and surface texturing to produce efficiency improvements.

- More research should be undertaken on radiation damage to raise end-of-life efficiency.

- Development of a production cell involves tradeoffs among fabricability, cost, and performance.

Since two years have passed since the first meeting, it was timely to hold another to exchange and review opinions on high efficiency solar cells. The title of this conference, Solar Cell High Efficiency and Radiation Damage, reflected the increased emphasis on gallium arsenide cells and radiation damage, although they were touched on in the earlier meeting as well.

The purpose of this second meeting was to raise the end-of-life efficiency of solar cells in space. It was intended to be primarily a forum for discussion. In order to lay a foundation for the discussions, short, prepared papers were presented to review the present state of the art.

The group was small enough, yet contained more than a sufficiency of expertise, so that there were lively and rewarding discussions. The free and open exchange of information and opinions made the meeting highly successful.

Daniel T. Bernatowicz
NASA Lewis Research Center
Chairman

CONTENTS

Page

PREFACE iii

SUMMARY

Daniel T. Bernatowicz. 1

OVERVIEW

1. Status of NASA-Lewis Research Center Silicon Solar Cell Program
   Henry W. Brandhorst, Jr., Lewis Research Center. . . . 3

2. The Goddard Space Flight Center High Efficiency Cell Development and Evaluation
   Luther W. Slifer, Jr., Goddard Space Flight Center . . 7

3. A Review of Air Force Space Photovoltaic Development Efforts
   W. Patrick Rahilly, Air Force Aero Propulsion Laboratory 25

ANALYSIS AND FUNDAMENTAL MEASUREMENTS ON SILICON CELLS

4. Impurity Gradients and High Efficiency Solar Cells
   C. R. Fang and J. R. Hauser, North Carolina State University 33

5. Measurement of Material Parameters That Limit the Open-Circuit Voltage in P-N-Junction Silicon Solar Cells
   F. A. Lindholm and A. Neugroschel, University of Florida, and C. T. Sah, University of Illinois. . . 51

6. Surface Recombination Velocity and Diffusion Length of Minority Carriers in Heavily Doped Silicon Layers
   Harry C. Gatos, Masaharu Watanabe and Geri Actor, Massachusetts Institute of Technology 59

7. Impurity Concentrations and Surface Charge Densities on the Heavily Doped Face of a Silicon Solar Cell
   I. Weinberg, Lewis Research Center and Lon Hsu, Wayne State University. 69

8. Investigation of the Topographical Features of Surface Carrier Concentration In Silicon Cell Material Using Electrolyte Electroreflectance
   Fred H. Pollak, Cajetan E. Okeke, and Paul M. Raccah, Yeshiva University 81

SILICON CELL TECHNOLOGY

9. Advanced High Efficiency Wraparound Contact Solar Cell
   J. A. Scott-Monck, F. M. Uno and J. W. Thornhill, Spectrolab, Inc. 91

10. The Sawtooth Cover Slide
A. Meulenberg, Jr., Communications Satellite Corporation. . . 95

11. Applications of Ion Implantation for High Efficiency Silicon Solar Cells
John A. Minnucci and Allen R. Kirkpatrick, Simulation Physics, Inc. 99

12. Transmutation Doping of Silicon Solar Cells
R. F. Wood, R. D. Westbrook, R. T. Young, and J. W. Cleland, Oak Ridge National Laboratory. 109

13. Developments in Vertical-Junction Silicon Solar Cells
J. Lindmayer, C. Wrigley, and J. Wohlgemuth, Solarex Corporation. 117

14. Project STOP-Spectral Thermal Optimization Program
L. J. Goldhammer, R. W. Opjorden, G. S. Goodelle, and J. S. Powe, Hughes Aircraft Co. 127

GALLIUM ARSENIDE REVIEW

15. High Efficiency GaAs Solar Cells
Gilbert H. Walker, Edmund J. Conway, and Charles E. Byvik, NASA Langley Research Center 133

16. Theoretical Studies of A New Double Graded Band-Gap $Al_xGa_{1-x}As$-$Al_yGa_{1-y}As$ Solar Cell
James A. Hutchby, NASA Langley Research Center 139

17. GaAs Solar Cell Development
R. C. Knechtli, S. Kamath, and R. Loo, Hughes Research Laboratories 149

RADIATION EFFECTS

18. The Status of Defect Studies Pertinent to Radiation Damage in Silicon Solar Cells
J. W. Corbett, L. J. Cheng, J. C. Corelli, and Y. H. Lee, State University of New York at Albany . . . 159

19. Effects of Defect Recombination Centers on Radiation Damage in Solar Cells
L. J. Cheng, P. W. Sours, J. P. Karins, J. C. Corelli, and J. W. Corbett, State University of New York at Albany. 165

20. EPR and Transient Capacitance Studies on Electron-Irradiated Silicon Solar Cells
Y. H. Lee, L. J. Cheng, P. M. Mooney, and J. W. Corbett, State University of New York at Albany. 179

21. Radiation Tests of SEP Solar Cells
Henry Oman, Boeing Aerospace Company. 187

22. Electron Irradiation of Modern Solar Cells
Bruce E. Anspaugh, Jet Propulsion Laboratory, and Tetsuo F. Miyahira, Xerox-Electro-Optical Systems. 207

23. Ionization Induced Damage in Crystalline Silicon
A. Meulenberg, Jr., Communications Satellite Corporation 221

24. Radiation Damage Profile Studies In Ion Implanted Silicon
J. P. Sadowski and E. B. Hale, University of Missouri, Rolla 225

25. Ultraviolet Damage in Solar Cell Assemblies
A. Meulenberg, Jr., Communications Satellite Corporation 227

26. Electron, Proton and Fission Spectrum Neutron Radiation Damage in Advanced Silicon and Gallium Arsenide Solar Cells
W. Patrick Rahilly, Air Force Aero Propulsion Laboratory and Bruce Anspaugh, Jet Propulsion Laboratory. 231

ATTENDEES 243

SUMMARY OF THE MEETING

Daniel T. Bernatowicz, Meeting Chairman
NASA-Lewis Research Center
Cleveland, Ohio

The following is the Chairman's summary of the meeting, with emphasis mainly on those topics brought out during the discussion periods.

Silicon solar cells with efficiency approaching 20% (AMO, 25° C) may be achievable if the open-circuit voltage can be raised to near 0.7 V. Theory indicates such a voltage is attainable with heavily doped, low-resistivity silicon. Such voltages have not been approached in practice. It is not known whether a single loss mechanism or several are presently limiting the open-circuit voltage. The several mechanisms that were discussed are bandgap narrowing; recombination in the emitter region; areal inhomogeneity of doping, defects, and carrier lifetime; high field recombination; and surface recombination.

It is not yet clear whether higher silicon quality (purity, uniformity, perfection) is needed to reduce the limiting loss mechanism. Although the maximum voltage does not seem to respond to improvements in silicon quality or processing procedures, there was concern that the silicon might be critically damaged by the processing or that inadequate silicon quality might mask any benefits due to processing improvements. It may be necessary to develop improved materials and device processing techniques simultaneously.

Junction quality alone is not the key to high voltage and efficiency. Epitaxially grown junctions in silicon with A-factors essentially equal to unity did not display especially high voltages.

For silicon cells, technology is far advanced for fine grids, wraparound contacts, textured surfaces, antireflection coatings and for back surface fields. These are not expected to yield further large gains in silicon cell performance.

There was concern voiced that too much attention to initial efficiency might cause neglect of the more important end-of-life efficiency. If high initial efficiency is achieved by using highly doped silicon, the higher radiation damage in that material might result in a negligible gain or even a loss in end-of-life efficiency.

There was strong concurrence that there are major gains yet to be made in improving the radiation tolerance of solar cells. Reduction of radiation damage in silicon by providing more sites for the recombination of

radiation-induced defects appears possible. However, accomplishment of this improvement will require a considerable amount of theoretical and experimental work.

High efficiencies before and after irradiation have been achieved with the vertical junction silicon solar cell and more improvement is expected.

Efficiencies of 18% are being achieved with heteroface Al_xGa_{1-x} As-GaAs solar cells and the maximum achievable efficiency is estimated to be about 22%. The theoretical models for the heteroface gallium arsenide cell are somewhat inadequate; the experimental behavior has been better than theory predicts.

The heteroface gallium arsenide cells degraded more rapidly than silicon cells under 1-MeV electron irradiation, but it is premature to conclude that this type of cell is inherently more or less tolerant of radiation. The damage mechanisms are not well understood and, because of the more complicated cell and lattice structure, are likely to be harder to study than those in silicon. The Chairman noticed while reviewing the meeting transcript that the equivalence of 1-MeV electron fluence to time in orbit was not raised as an issue. It was implicitly assumed during the comparisons of silicon and gallium arsenide cells that the equivalence for the two types of cells was the same.

Overall the major views and opinions expressed were in general agreement with those in the 1974 meeting. The Conclusions reached in the earlier meeting (listed in the Preface of these proceedings) remain valid, with the addition of one supporting the continued development of gallium arsenide solar cells.

1. SUMMARY OF THE NASA SPACE PHOTOVOLTAIC RESEARCH AND TECHNOLOGY PROGRAM

Henry W. Brandhorst, Jr.

NASA Lewis Research Center
Cleveland, Ohio

Abstract

The NASA Lewis Research Center research and technology program for space photovoltaic cells has as its objective the development of low-cost solar cells and arrays with high end-of-life efficiency. The low cost comes through two approaches: one, to obtain increased device efficiency at no increase in cost and two, to reduce the manufacturing costs of space solar cells and arrays. Specific program targets are shown in figure 1. The general approach to the realization of improved cells is shown in figure 2.

Figure 3 details the R and D contract efforts in Si solar cell development. The research phase of the program is aimed at understanding the fundamental loss mechanisms that limit cell performance. Key interests at this time focus on understanding mechanisms controlling open-circuit voltage (NCSU, U. Fla., Yeshiva U. and Worcester Poly. Inst.), affecting cell surface recombination velocity (MIT) and determining and controlling radiation damage loss mechanisms (SUNY).

Technology efforts encompass development of high efficiency epitaxial cells (RCA), high efficiency wraparound contact solar cells (Spectrolab), economical diffusion sources (O-I), automated cell fabrication (Spectrolab) and development of easily applied, durable cover "glasses" (Pantek). The examination of ion-implanted profile tailored junctions and additional development of screen printed contact technology to cell development are also in process.

Key program status is shown in figure 4. In basic research, nothing has been uncovered yet which casts doubt on the 18% BOL efficiency goal. However, cell open-circuit voltage is still the key limiting factor. Unless this voltage can be raised to near 0.7 V, 18% efficiencies will be difficult to achieve. The cell surface recombination velocity does not appear to significantly limit cell short-circuit current. However, the full role of surface recombination on cell voltage has not been resolved yet.

In technology developments, recent blending of low-cost print-on technology for insulated wraparound layers and back surface fields has led to the significant development of wraparound contact cells with efficiencies above 13% BOL. This represents an increase in two efficiency points over

what was previously available. This blending of seemingly diverse technologies gives the hope that high efficiency, low-cost cells are achievable with continued development. Complete non-vacuum solar cell processing that can be fully automated has been demonstrated. Screen printed contacts and wraparound insulators, texturized surfaces and spin-on antireflection coatings were used to demonstrate cells with efficiencies of 11.5% BOL. Epitaxial base and emitter layers have led to junctions with near ideal junctions. Generation recombination currents are almost entirely eliminated in these structures. Finally, 50 μm thick, texturized surface cells with efficiencies over 12% have been produced by several programs at both the NASA-LeRC and JPL. These significant breakthroughs offer the hope of high efficiency, radiation resistant solar cells in the future.

In summary, the NASA-Lewis research and technology program in space photovoltaic cell research seeks to understand and to eliminate undesirable mechanisms that cause loss of cell efficiency and to develop and implement the technologies necessary to produce low-cost, high efficiency, radiation-tolerant solar cells. Significant advances have been made which offer the hope that high efficiency and low cost are not mutually exclusive.

NASA-LEWIS PROGRAM IN SPACE SOLAR CELL RESEARCH & TECHNOLOGY

OBJECTIVE: DEVELOP TECHNOLOGY FOR LOW-COST SOLAR CELLS AND ARRAYS WITH HIGH END-OF-LIFE EFFICIENCY

TARGETS:
- 18% BOL EFFICIENCY
- GAIN IMPROVED UNDERSTANDING OF RADIATION DAMAGE
- PRODUCE RADIATION RESISTANT SOLAR CELLS WITH HIGHER END-OF-LIFE EFFICIENCY
- DEVELOP TECHNOLOGY FOR LOW-COST FABRICATION OF SPACE QUALITY CELLS THAT CAN RESULT IN $5/W IN AUTOMATED PRODUCTION
- CONTRIBUTE TO SPACE MODULE TECHNOLOGY READINESS
- CONTRIBUTE TO AUTOMATIC MODULE FABRICATION

FIGURE 1

GENERAL APPROACH TO REALIZATION OF IMPROVED SOLAR CELLS

- RESEARCH -- UNDERSTANDING OF MECHANISMS AND LIMITS TO PERFORMANCE
- TECHNOLOGY ON INDIVIDUAL PROCESSES
- INTEGRATION OF NEW PROCESSES INTO CELL FABRICATION
- ADAPTATION TO COST-EFFECTIVE PRODUCTION

THE THREE TECHNOLOGY "PHASES" ARE STRONGLY INTERRELATED. ADAPTATION TO COST-EFFECTIVE PRODUCTION IS A VERY IMPORTANT BARRIER.

FIGURE 2

R AND D CONTRACT EFFORTS IN Si SOLAR CELL DEVELOPMENT

BASIC RESEARCH

- COMPUTER MODELLING OF SOLAR CELLS, NCSU, DR. J. R. HAUSER
- STUDY OF RECOMBINATION CENTERS IN 0.1 Ω-CM Si, U. FLA, DR. F. A. LINDHOLM
- STUDIES IN SILICON SURFACE PHENOMENA, MIT, DR. H. C. GATOS
- SOLAR CELL RADIATION DAMAGE THEORY REVIEW, SUNY, DR. J. C. CORBETT
- MEASUREMENT OF DIFFUSED LAYER PROPERTIES, YESHIVA U., DR. F. H. POLLAK
- INVESTIGATION OF THE 1.14 μM PHOTOCONDUCTIVE RESPONSE OF Si DEVICES, WORCESTER POLY., DR. H. P. D. LANYON

TECHNOLOGY DEVELOPMENT

- EPIJUNCTION SOLAR CELL FABRICATION, RCA, DR. H. KRESSEL
- HIGH EFFICIENCY WRAPAROUND CONTACT SOLAR CELLS, SPECTROLAB, J. SCOTT-MONCK
- STUDIES ON ALTERNATE DIFFUSION SOURCES, OWENS-ILLINOIS, J. E. RAPP
- AUTOMATED Si SOLAR CELL FABRICATION, SPECTROLAB, J. SCOTT-MONCK
- GLASS RESIN COATING DEVELOPMENT, PANTEK, INTERNATIONAL, DR. M. B. FIELD
- ION IMPLANTED TAILORED JUNCTIONS, ----
- THICK FILM TECHNOLOGY APPLIED TO SOLAR CELL FABRICATION, ----

FIGURE 3

PROGRAM STATUS

BASIC RESEARCH

- 18% BOL EFFICIENCY STILL A GOAL
- CELL V_{OC} KEY LIMITING FACTOR
- SURFACE RECOMBINATION VELOCITY NOT A MAJOR PROBLEM

TECHNOLOGY

- 13 + % BOL EFFICIENT WRAPAROUND CONTACT SILICON SOLAR CELLS PRODUCED
- FEASIBILITY OF AUTOMATION OF COMPLETE NON-VACUUM SOLAR CELL PROCESSING DEMONSTRATED
- EPITAXIAL PROCESSING PRODUCES NEAR-IDEAL JUNCTIONS AND ALLOWS CONTROL OF PROFILES
- HIGH EFFICIENCY, THIN, TEXTURIZED SURFACE SILICON SOLAR CELLS PRODUCED

FIGURE 4

2. THE GODDARD SPACE FLIGHT CENTER

HIGH EFFICIENCY CELL DEVELOPMENT AND EVALUATION PROGRAM

Luther W. Slifer, Jr.
Goddard Space Flight Center

SUMMARY

The Goddard Space Flight Center's high efficiency cell development and evaluation program covered a variety of laboratory tests and flight experiments as well as development work. Cells from COMSAT Laboratories, Optical Coating Laboratory, Inc., and Spectrolab, Inc. were included in the overall program. Results showed that the cells could be produced in quantity, that they were suitable for space flight applications, and that the power produced ranged from 20 to 35% more than that of conventional cells. In a benign flight environment, the cells degraded at approximately the same rate as conventional cells. In synchronous orbit, the rate exceeded that of conventional cells, but high efficiency cells still showed significant power advantage after two years. Irradiation test results showed the voltage-temperature coefficients to be comparable to conventional cells. However, current-temperature coefficients were not only higher initially, but also increased significantly with irradiation. Although thin cells with good performance characteristics were made, significant problem areas pertinent to production were disclosed, particularly for cells with thicknesses of 0.100 mm or less. The overall program led to the use of advanced high efficiency cells on the International Sun-Earth Explorer solar panels.

INTRODUCTION, OBJECTIVES, AND APPROACH

In May 1972, COMSAT announced (ref. 1) the violet solar cell. This high efficiency cell represented the first major advance in silicon solar cells in a decade, and initiated an era in which a variety of advanced cell designs have been and are being developed.

In January 1973, Goddard Space Flight Center (GSFC) initiated its high efficiency cell development and evaluation program with the following objectives:

1. To ascertain the potential of the COMSAT violet cell for space flight applications,

2. To promote the advance of the art from experimental laboratory cells to production items,

3. To establish high efficiency cells as flight power system components.

A flexible approach, modified primarily to take advantage of current opportunities but also to keep abreast of current technology developments, was used in accomplishing these objectives. The main elements of the approach were laboratory and flight evaluation of violet cells, development and evaluation of production cells, evaluation of advanced high efficiency cells, and, finally, incorporation of the advances in a flight solar array.

VIOLET CELL EVALUATION

The first opportunity for a flight evaluation of violet cells was obtained by preparing, on a non-interference basis, a qualified Violet Cell Technology Panel for flight as part of the solar array for the Interplanetary Monitoring Platform - J (IMP-J). Associated laboratory evaluations were performed in preparation for this flight. A second opportunity was obtained by modifying the Applications Technology Satellite - 6 (ATS-6) Solar Cell Radiation Damage Experiment (SCRDE). This modification consisted of the substitution of violet cells for grouted cells previously planned for the experiment. In this case laboratory evaluations were performed both in preparation for the flight and also, later, to clarify some questions which arose from the data for the first year of flight. A third flight, a Lewis Research Center solar cell experiment on the Space Plasma High Voltage Interaction Experiment (SPHINX) spacecraft, was also anticipated. This set of flights, IMP-J in a high (200,000 km) circular orbit, ATS-6 in a synchronous orbit, and SPHINX in an orbit through the Van Allen belts below synchronous altitude, would provide a relatively complete set of flight environment performance data for the cell. Unfortunately the SPHINX spacecraft was lost, so data were obtained only from IMP-J and ATS-6.

IMP-J Violet Cell Technology Panel

The first step of preparation of the IMP-J Technology Panel was the evaluation and flight qualification of subassemblies. Cells, both bare and glassed, were evaluated for electrical output from -100°C to +100°C (figs. 1, 2, 3 and 4); under low energy (0.3, 1.0, and 2.0 MeV) proton irradiation to 10^{15} p/cm^2 ; under ultraviolet exposure to 5000 equivalent sun hours; and under extreme temperature-humidity (shelf life) test of 8.5°C and 90% RH for 75 days.

In addition, two thermo-compression bonded modules of 15 cells each (3 in parallel by 5 in. series) on aluminum honeycomb substrates were thermal-vacuum cycled for 58 cycles between -130°C and +95°C and an additional 70 cycles from -110°C to +60°C with each cycle being 3 hours in duration.

These tests verified the high (13 to 14%) efficiency of the cells with the additional benefit that the power output of the violet cell continued to rise at low temperatures (below -40°C) unlike conventional cells which frequently exhibit a drop-off in power as shown in figure 4. The suitability of violet cells for flight on IMP-J was proven. The only unfavorable observation was failure of a few of the 50 micron silver ribbon

interconnects during the second thermal-vacuum cycling sequence. This could be serious for other spacecraft but not for the limited cycling of five cycles from -110°C to +30°C in the lifetime for IMP-J. The failures were in the interconnects themselves, not in the cell contact or the thermo-compression bond joints.

Having determined that the subassemblies were suitable for the IMP-J flight, GSFC prepared and flight qualified the Technology Panel itself using COMSAT assembled cell modules. The panel was flight qualified simultaneously with the conventional IMP-J solar array panels. Qualification consisted of electrical output tests, vibration tests on the spacecraft, a rapid decompression test, two thermal shock tests from +30°C to -120°C, and sequential thermal soak tests at +30°C, -50°C, +40°C, and -60°C for 40 hours each. The panel successfully passed all tests. The electrical output of the Violet Cell Technology Panel compared to a conventional cell panel (reference panel) as determined in laboratory tests is shown in figure 5. The violet cell panel produced 20% more power than the reference panel. Reference 2 gives details of the tests and results for the above assembly and panel qualification tests.

The Violet Cell Technology Panel was flown on the IMP-J spacecraft as one of the 48 panels of the solar array (fig. 6).

The ATS-6 Solar Cell Radiation Damage Experiment

The ATS-6 SCRDE incorporated a variety of experimental cell and shield assembly configurations. It is described in detail in reference 3. Some unexpected results were obtained in the first year's flight data (ref. 4) so detailed angle of incidence and radiation effects experiments were performed on laboratory correlation cells of identical configurations to refine the treatment of the flight data. This work was performed under Contracts NAS 5-11677 and NAS 5-22873 with Hughes Aircraft Co.

The angle of incidence test results for the correlation violet cells showed no deviation from the cosine law (ref. 5). However, irradiation test results (ref. 6) showed significant differences between violet and conventional cells. These are illustrated in figure 7. It can be seen that, although effects on open circuit and maximum power voltage (V_{oc} and V_{mp} respectively) were similar for the two types of cells, the effects on short circuit and maximum power current (I_{sc} and I_{mp} respectively) were quite different. Not only was the degradation due to irradiation higher for the violet cells, but also the effects of temperature were significantly more pronounced. The temperature coefficients are compared in table I.

Air Mass Zero (AMO) Results

AMO evaluations were obtained for the violet cells on the IMP-J Technology Panel and ATS-6 SCRDE flights. In addition, cells were calibrated on Jet Propulsion Laboratory balloon flights. The balloon flight and IMP-J Technology Panel results are reported in reference 7.

Table II summarizes the balloon flight results as compared to laboratory calibrations. Except for a relatively consistent deviation of 1 to 2 percent between laboratory and balloon flight calibrations (attributed primarily to solar simulator variation) performance was as expected with the short circuit current of the 2 x 2 cm violet cells running about 25 to 30 ma higher than that for conventional cells.

The IMP-J spacecraft was launched on October 25, 1973 into a nearly circular orbit at an altitude of approximately 200,000 km. The flight results are shown in table III. Since the solar array was shunt regulated at 28 volts, the maximum attainable power was not determined for either the reference panel or the violet cell panel. The superiority of the violet cell panel in table III represents the gains in current but not the voltage. Because of the high altitude of the orbit, the degradation observed is believed to be primarily untraviolet degradation. It amounted to about 4 percent for both the violet and the conventional cells in one year's time. Although a shift in calibration, which affected the absolute readings, occurred near or during launch, there is a high degree of consistency in the post-launch data and the percentage degradation values are considered reliable.

Flight results for the ATS-6 SCRDE (refs. 6, 8) are summarized in table IV. Here it appears that ultraviolet degradation, taken at 50 days after launch during which time hard particle radiation effects are considered negligible, is a little more severe for the violet cells than for conventional cells. For this flight, as opposed to IMP-J, hard particle radiation losses are important and degradation of the cell parameters is significant. Losses for the violet cells were half again as high as for conventional cells, correlating with laboratory test results. Nevertheless, even with the higher degradation rate, the violet cells still outperformed the conventional cells on an absolute power basis after two years in synchronous orbit.

PRODUCTION CELL DEVELOPMENT AND EVALUATION

As successful results with the violet cell began developing, serious attention was given to the problem of getting high efficiency cells in production quantities for flight use. To accomplish this GSFC contracted with Optical Coating Laboratory, Inc. (OCLI) to develop high efficiency cells using processes and procedures amenable to production line requirements. Within this contract (NAS 5-20652) OCLI also performed a preliminary investigation of thin cell production. As OCLI approached completion of the development phase, GSFC also procured high efficiency cells from Spectrolab, Inc. who had chosen to develop them independently.

OCLI Cell Development

The contract with OCLI consisted of three phases: development of manufacturing methods, thin cell development, and pilot production. Manufacturing methods for silicon preparation, diffusion, contact application, contact systems, anti-reflection coating

application, and heat treatments were investigated (ref. 9) and progress cells were shipped to GSFC for evaluation. GSFC evaluations of cells produced in this phase resulted in an estimate of a nominal attainable efficiency level of 12.5% which was short of the 13% minimum goal desired. In the secondary area of thin cell development, the goal was to obtain 20 cells each of nominal thickness 0.050, 0.100, 0.150 and 0.200 mm. Although good cells were produced with nominal thicknesses above 0.100 mm, it was found that warpage and breakage problems became severe at 0.100 mm and below (ref. 10). Electrical test results for thin cells are shown in figure 8.

Finally, to meet the major objective of the contract, 1000 - 2 x 4 cm solar cells were made in pilot line production (ref. 11). Of these 100 were delivered bare, 200 were delivered glassed with 0.300 mm thick Corning 7940 fused silica with an anti-reflective coating and a 350 nm cut-off filter, and 700 were delivered glassed with the same glass but with a conductive coating in place of the anti-reflective coating. The latter requirement was directed toward meeting experimenter and spacecraft requirements for the International Sun-Earth Explorer (ISEE) spacecraft.

The pilot production of 1000 cells represented a yield of 40% with losses consisting of 25% electrical, 22% visual, and 13% mechanical rejects. This yield is, of course, somewhat variable depending on the stringency of electrical, cosmetic, and mechanical requirements specified.

The electrical characteristics of the cells shipped are given in table V. The typical efficiency was 12.8% for bare cells and 13.6% for glassed cells. With conductive coated glass, the losses due to the coating essentially equalled the gains due to glassing, resulting in an efficiency of 12.9%. These achievements exceed the contract goals and were most encouraging for the ISEE project.

Spectrolab High Efficiency Cells

As the development phase of the OCLI contract neared completion, high efficiency cells were procured from Spectrolab. The cells requested in this procurement and the Spectrolab offer are shown in table VI. The offered efficiency was estimated to be equivalent to 12.6% after glassing, which was essentially equal to the OCLI capability at that time. Although it appeared at that time that this would be the limit of production capability, it was gratifying to find the appearance to be deceiving, as demonstrated in the OCLI pilot production phase, previously discussed, and in the Spectrolab production of ISEE panels, to be discussed later.

EVALUATION OF ADVANCED HIGH EFFICIENCY CELLS

In November 1975 when advanced COMSAT non-reflective (CNR) cells became available, they were added into the GSFC high efficiency cell program. Ten 2 x 2 cm cells with 0.150 mm thick fused silica coverglasses were procured and evaluated for

electrical performance over the temperature range from 10°C to 70°C. Average characteristics of the cells are shown in table VIII. The average efficiency for the ten cells at 25°C was 14.8%, a significant increase over the 10-11% efficiency of conventional cells and a moderate improvement over the OCLI and Spectrolab production high efficiency cells.

INCORPORATION INTO FLIGHT SOLAR ARRAYS

The program was terminated in October 1976 after the advances developed and/or evaluated were incorporated into the design of the ISEE-A and C solar arrays. Spectrolab fabricated the arrays using Spectrolab textured (non-reflective) cells and OCLI conductive coated coverglasses. Each spacecraft array uses 4352 - 2 x 4 cm and 1088 - 2 x 2 cm solar cells. Cell performance for the average flight panel at the anticipated flight temperature of 20°C is 17.5 mW/cm^2 for an assembled efficiency of 12.9%. By way of general comparison, output for IMP-J conventional cells was 14.7 mW/cm^2 for an assembled efficiency of 10.9%. The overall increase attained was approximately 20% in spite of conductive coating losses. The current-voltage curve for a randomly selected (slightly below average) ISEE panel is shown in figure 9.

Because of the major changes incorporated in this new design, thermal (α/ϵ) characteristics were measured for textured cells with typical fused silica coverglasses and for the ISEE panels. These data are shown in table VIII. The α/ϵ ratio for these advanced assemblies was found to be nominally 20% higher than for conventional cells, a factor of significance to both the thermal design of spacecraft and the electrical design of solar arrays.

CONCLUSIONS

The overall program led to the following general conclusions:

1. The COMSAT violet cell showed high potential for significant power gains.

2. Support of development into production hardware was warranted.

3. Quantity production of cells of better than 13% efficiency was attained.

4. Although some progress was made in producing thin high efficiency cells, more work is needed, particularly below 0.100 mm.

5. Evaluation of high efficiency cells, including non-reflecting textured cells showed suitability for flight.

6. Design data for many spaceflight applications was obtained.

7. Use of these advanced cells for the ISEE spacecraft solar array completed the effort of transforming a laboratory experimental cell into an applied flight component.

8. The cell, announced in May 1972, will be established as a power system component with the flight of ISEE-A in October 1977, an elapsed time of 5 years.

REFERENCES

1. Lindmayer, J. and Allison, J.: An Improved Silicon Solar Cell - The Violet Cell. Conference Record of the Ninth IEEE Photovoltaic Specialists Conference, May 1972, pp. 83-84.

2. Gaddy, Edward M.: Flight Qualification Test Results for Violet Cells. Conference Record of the Tenth IEEE Photovoltaic Specialists Conference, November 1973, pp. 153-162.

3. Goldhammer, L. J. and Dunkerly, W. C.: Solar Cell Radiation Damage Experiment, Final Report. NASA Contract NAS 5-11677, January 1974.

4. Goldhammer, L. J.: ATS-6 Solar Cell Flight Experiment after 325 Days in Synchronous Orbit. IEEE Transactions on Aerospace and Electronic Systems, Vol. AES-11, No. 6, November 1975.

5. Goldhammer, L. J.: Addendum to Final Report Solar Cell Radiation Damage Experiment. NASA Contract NAS 5-11677, March 1976.

6. Goldhammer, L. J.: ATS-6 Solar Cell Experiment/Improvement Final Report. NASA Contract NAS 5-22873, December 1976.

7. Gaddy, Edward M.: Results from the IMP-J Violet Solar Cell Experiment and Violet Cell Balloon Flights. NASA TN D-8393, December 1976.

8. Goldhammer, L. J. and Slifer, L. W.: ATS-6 Solar Cell Flight Experiment Through Two Years in Orbit. Conference Record of the Twelfth IEEE Photovoltaic Specialists Conference, November 1976, pp. 199-207.

9. Iles, P. A.: High Efficiency Solar Cell Development. Phase Report #1, NASA Contract NAS 5-20652.

10. Iles, P. A.: High Efficiency Solar Cell Development — Thin Violet Cells. Phase Report #2, NASA Contract NAS 5-20652.

11. Iles, P. A.: High Efficiency Solar Cell Development — Pilot Production Phase. Phase Report #3, NASA Contract NAS 5-20652.

TABLE I. - TEMPERATURE COEFFICIENTS (25°C TO 100°C) AS A FUNCTION OF IRRADIATION (1 MeV ELECTRONS)

Fluence (e/cm^2)	I_{sc} Coeff. ($\mu a/cm^2/°C$)		V_{oc} Coeff. (mV/°C)		I_{mp} Coeff. ($\mu a/cm^2/°C$)		V_{mp} Coeff. (mV/°C)	
	Conv.	Violet	Conv.	Violet	Conv.	Violet	Conv.	Violet
0	19.2	25.0	-2.17	-2.15	-2.7	-0.9	-2.14	-2.18
5×10^{13}	27.3	43.1	-2.12	-2.09	0.0	+14.3	-2.18	-2.12
1×10^{14}	29.6	49.3	-2.16	-2.10	3.7	+22.4	-2.14	-2.11

TABLE II. - 1974 BALLOON FLIGHT CALIBRATIONS

Date	Cell Type	Pulsed Xenon Calibration		Flight Calibration		Percent Deviation of Laboratory from Flight Calibration
		Current (ma)	Temp.* (°C)	Current (ma)	Temp. (°C)	
February 2	Violet	156.6	51	158.44	45	-1.16
April 23	Violet	158.0	51	161.04	50	-1.89
April 23	Violet	164.0	52	166.20	54	-1.32
May 8	N/P Commercial	131.2	53	133.74	54	-1.90
May 8	N/P Commercial	134.2	51	136.20	50	-1.47

*A +5°C difference from the flight temperature would result in a reading approximately 0.4 ma high.

TABLE III. - FLIGHT PERFORMANCE OF IMP-J PANELS

Days After Launch	Reference (Conventional) Panel		Violet Cell Panel		Ratio
	Current (ma)	Degradation (%)	Current (ma)	Degradation (%)	Violet to Conventional
Pre-Launch Measurement	392	+1.6	459	+4.1	1.171
4*	386	0.0	441	0.0	1.143
128	373	-3.4	428	-2.9	1.148
280	371	-3.9	426	-3.4	1.148
392	370	-4.1	424	-3.9	1.146

*Fourth day measurement taken as zero.

TABLE IV. - ATS-6 SCRDE FLIGHT RESULTS

Ultraviolet Degradation (50 Days) - I_{sc} Losses (%)

Conventional Cell	1.6 ± 0.7
Violet Cell	2.3 ± 0.9

Hard Particle Radiation Effects (2 Years) - Losses (%)

	I_{sc}	V_{oc}	Max. Power
Conventional Cell	16.1 ± 1.0	2.6 ± 0.8	18.0 ± 1.4
Violet Cell	19.4 ± 2.0	4.2 ± 0.1	24.4 ± 2.2

TABLE V. - MEAN VALUES FOR OCLI PILOT PRODUCTION 2 x 4 cm CELLS

No. of Cells	Type	V_{oc} (mV)	I_{sc} (ma)	I_{485} (ma)	Typ. Eff. (%)
100	Bare	601	304	285	12.8
200	Glassed	599	324	304	13.6
700	Glassed, Conductive Coated	599	308	289	12.9

TABLE VI. - SPECTROLAB CELL PROCUREMENT (UNGLASSED - MARCH 1975)

No.	Size	Requested	Offered
300	2 x 2 cm	150 ma at 470 mV 13% Eff.	140 ma (Min. Avg.) at 470 mV 12.2% Eff.
200	2 x 4 cm	300 ma at 470 mV 13% Eff.	280 ma (Min. Avg.) at 470 mV 12.2% Eff.
Estimate with Glass (Assume 3.5% Increase)		13.5% Eff.	12.6% Eff.

TABLE VII. - AVERAGE CNR CELL PARAMETERS

	I_{sc}	V_{oc}	I_{mp}	V_{mp}	P_{mp}
At 25°C	43.9 ma/cm^2	594 mV	40.4 ma/cm^2	496 mV	19.99 mW/cm^2
Temp. Coeff.	15.1 μa/cm^2/°C	-2.06 mV/°C	-2.36 μa/cm^2/°C	-2.16 mV/°C	-0.087 mW/cm^2/°C
Eff. at 25°C = 14.8%					

TABLE VIII. - α_S/ϵ_H MEASUREMENTS

	α_S	ϵ_H	α_S/ϵ_H
Textured Cells with Fused Silica Coverglasses No Backsurface Reflector	0.93	0.77	1.21
ISEE Array as Above with Conductive Coated Coverglasses	0.905	0.75	1.21
Conventional Cells	—	—	0.95 - 1.05

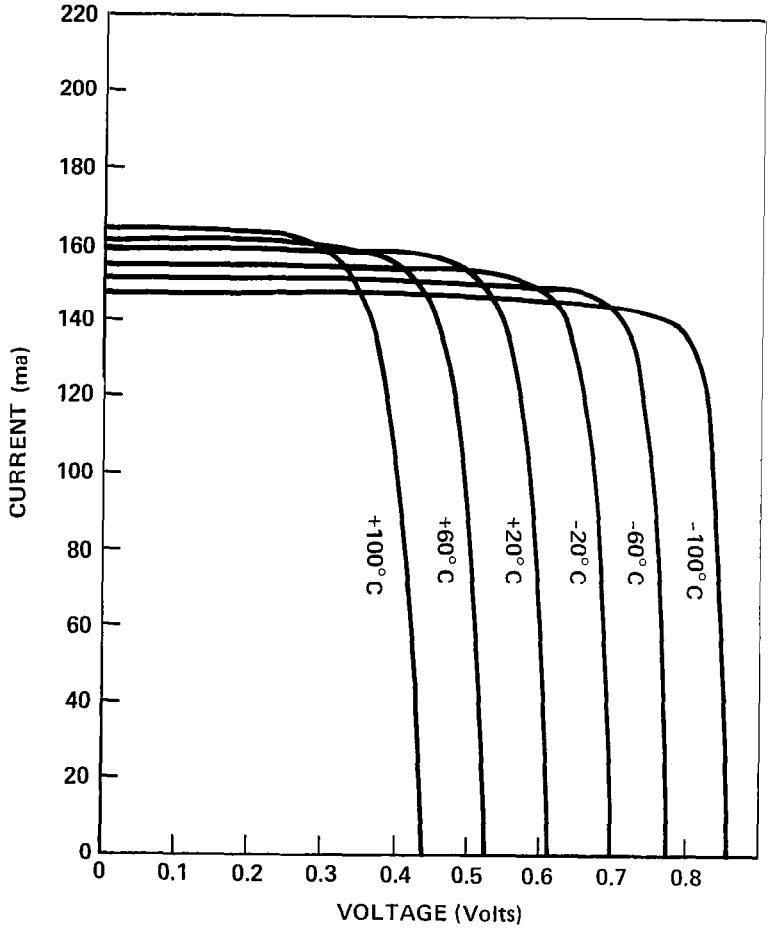

Figure 1. Current-Voltage Curves for a Typical Violet Solar Cell

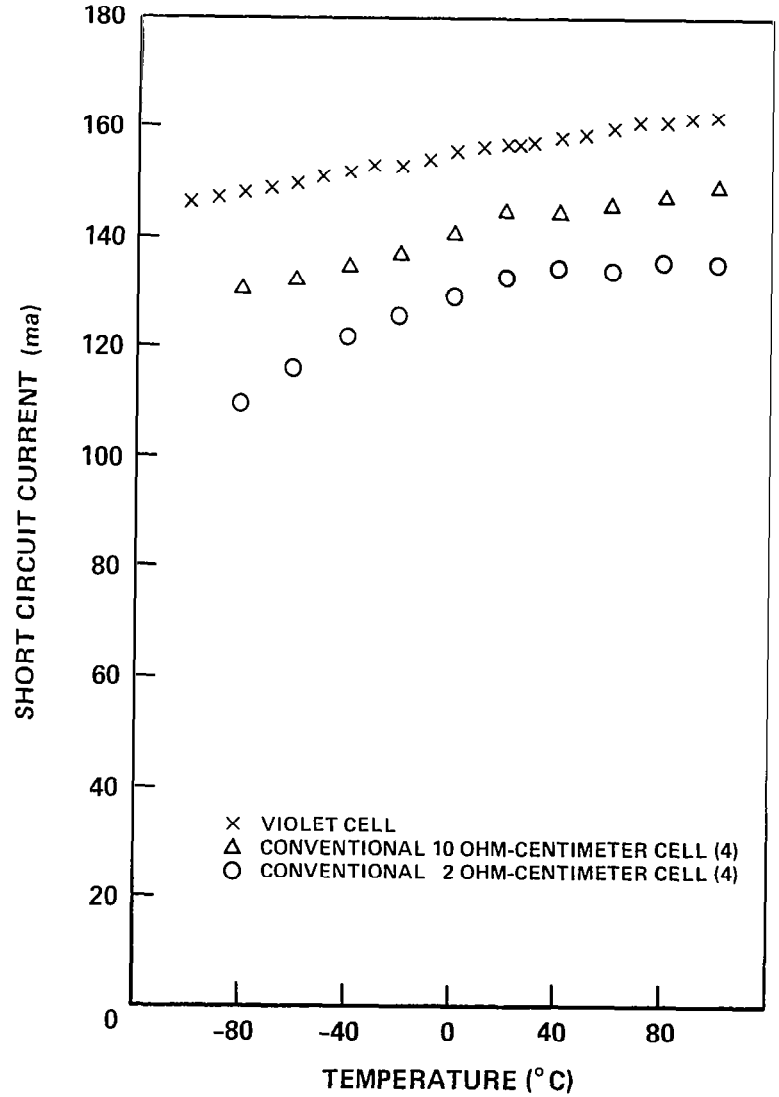

Figure 2. Effect of Temperature on Short Circuit Current

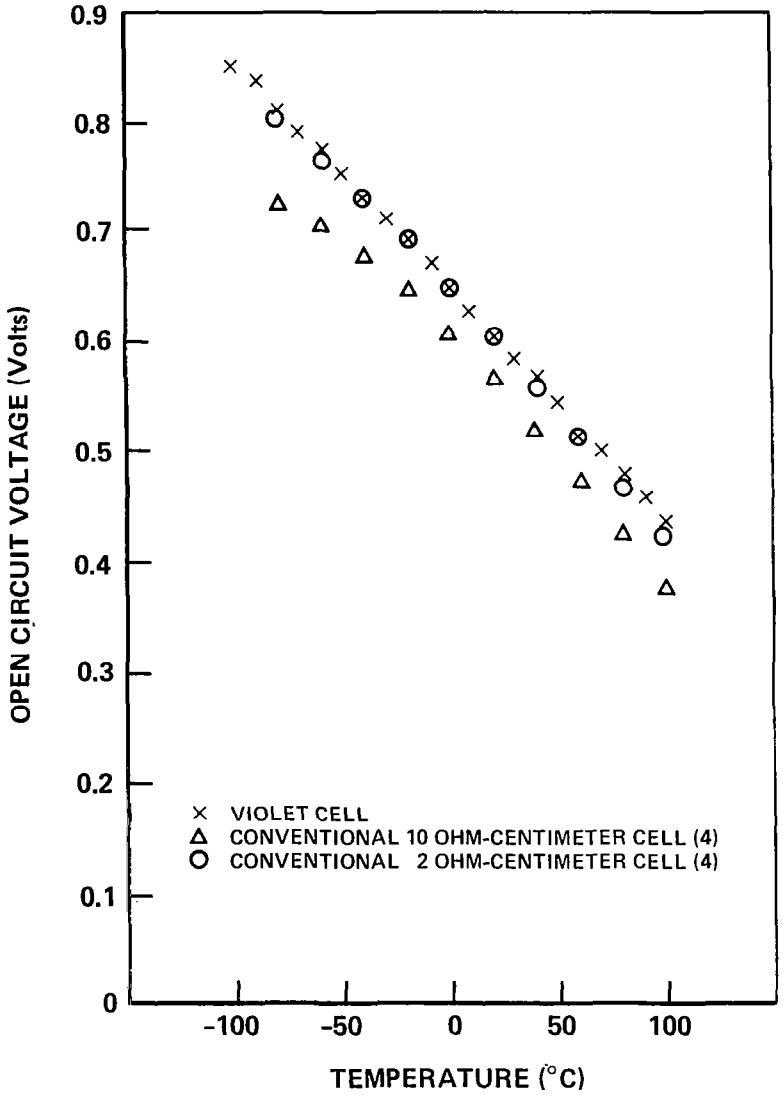

Figure 3. Effect of Temperature on Open Circuit Voltage

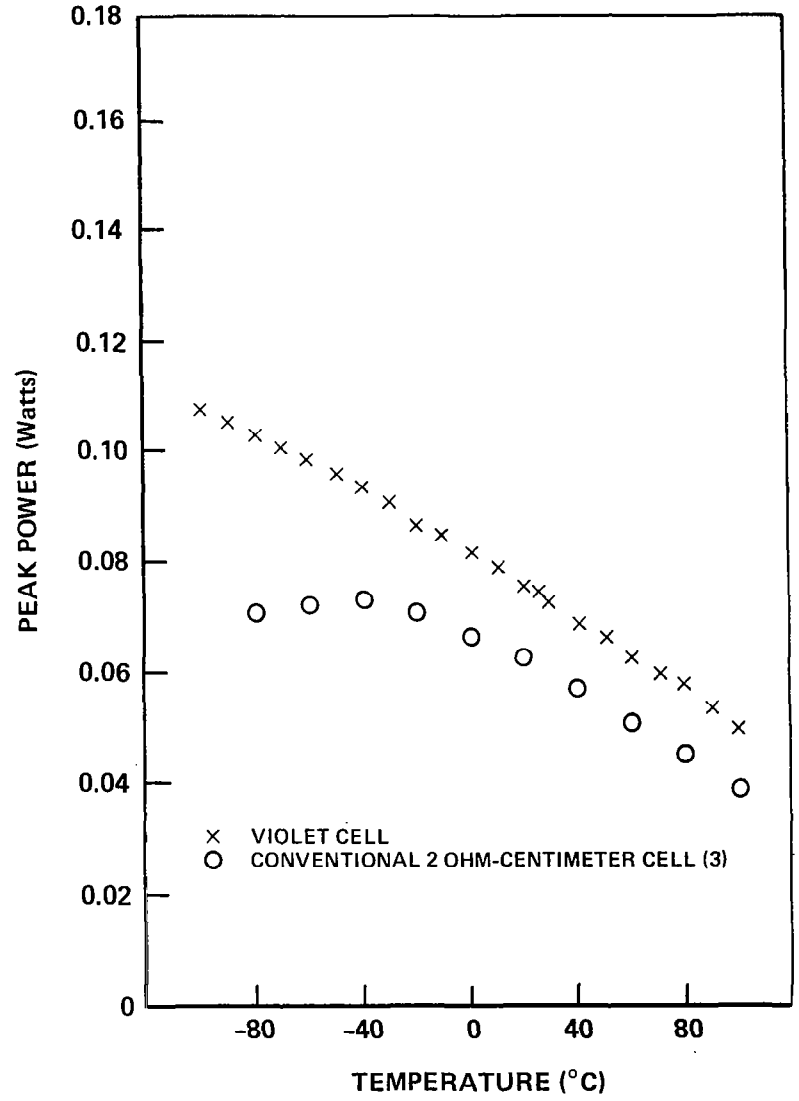

Figure 4. Effect of Temperature on Peak Power

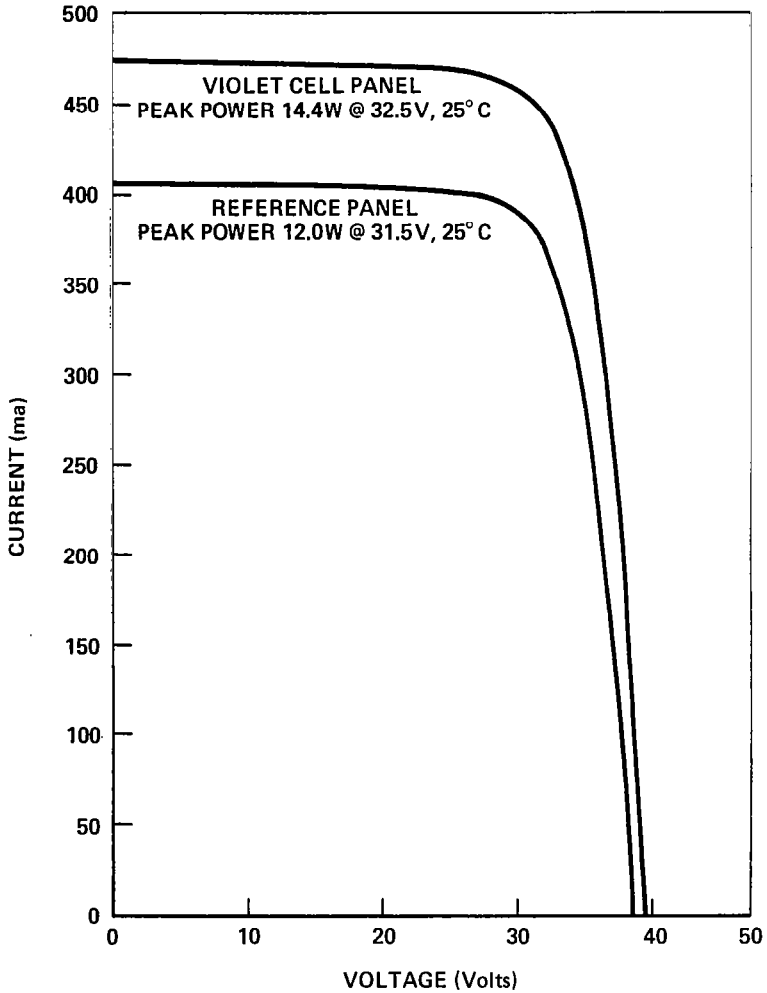

Figure 5. Current-Voltage Curves for IMP-J Panels

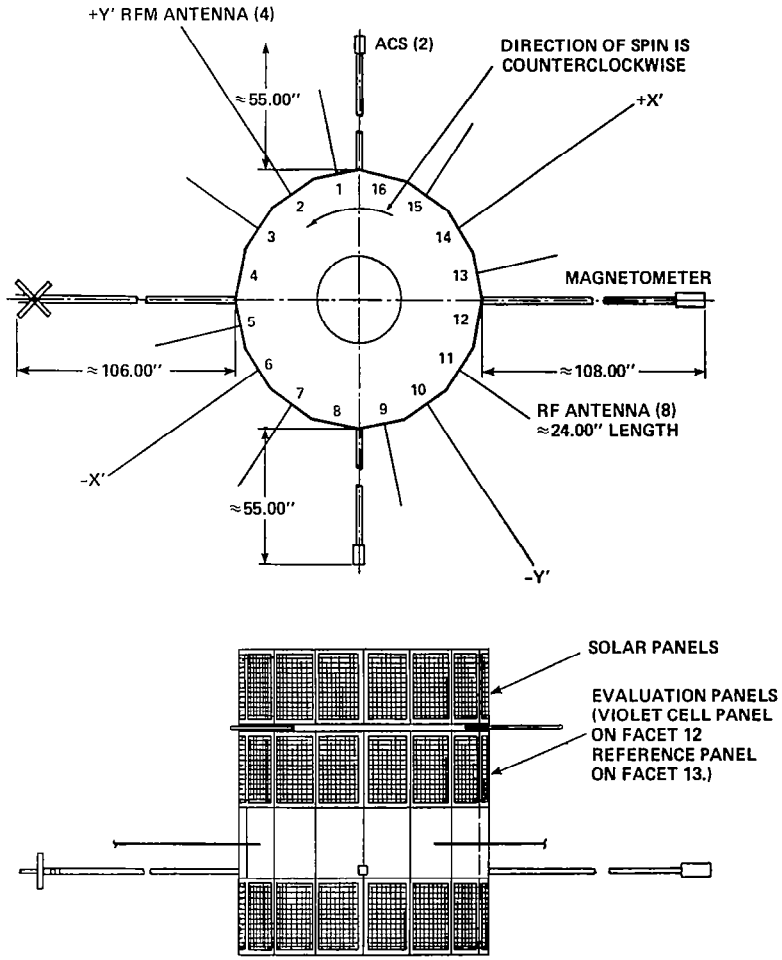

Figure 6. IMP-J Spacecraft

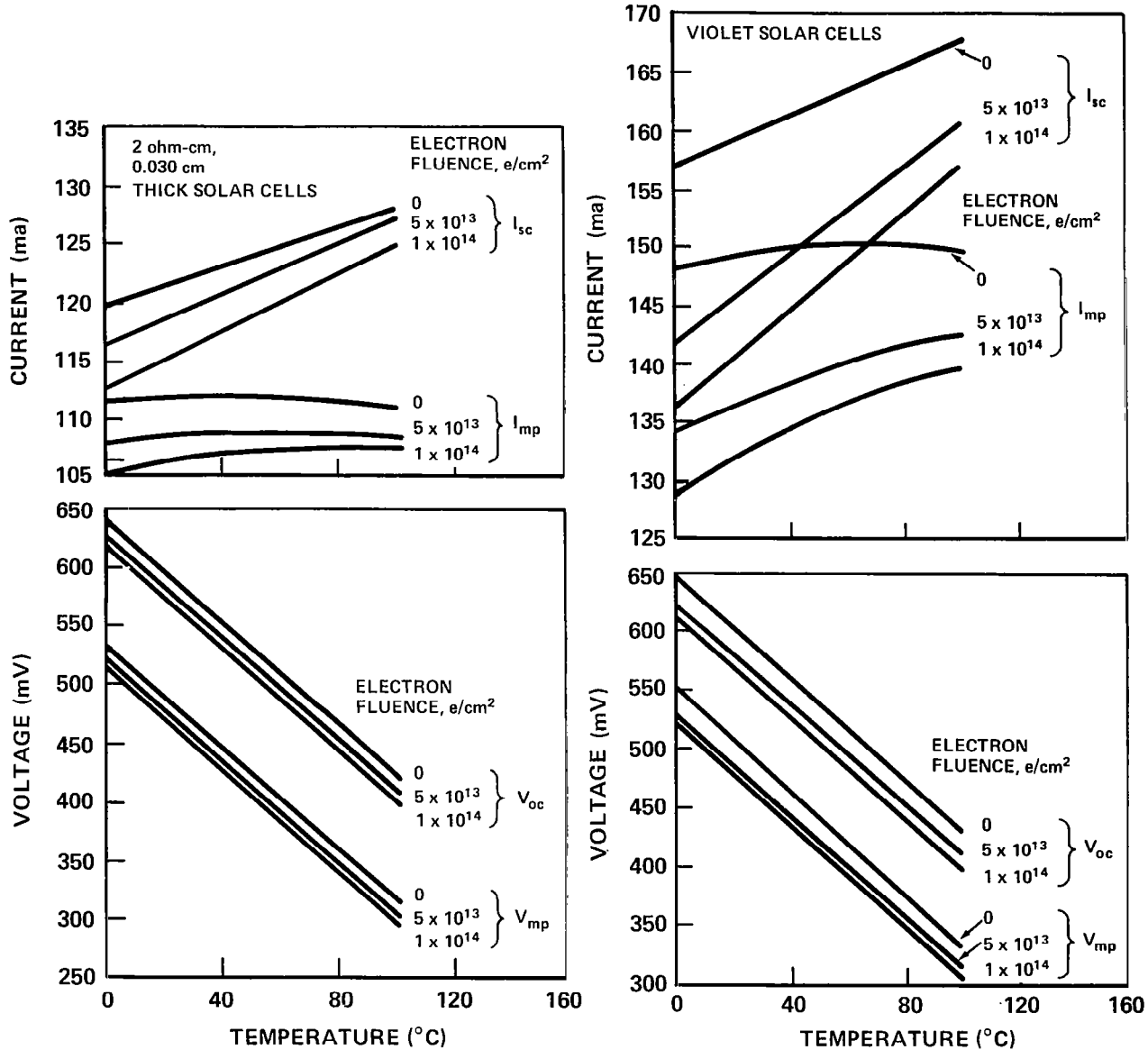

Figure 7. Irradiation Effects on SCRDE Correlation Cells

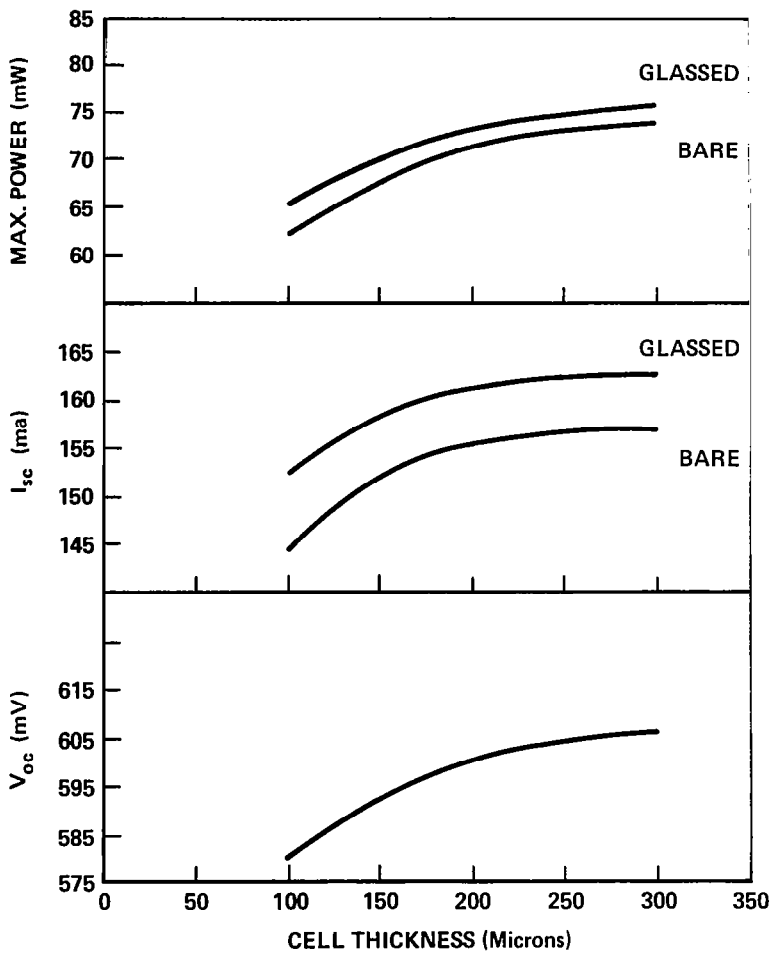

Figure 8. Effects of Cell Thickness (OCLI)

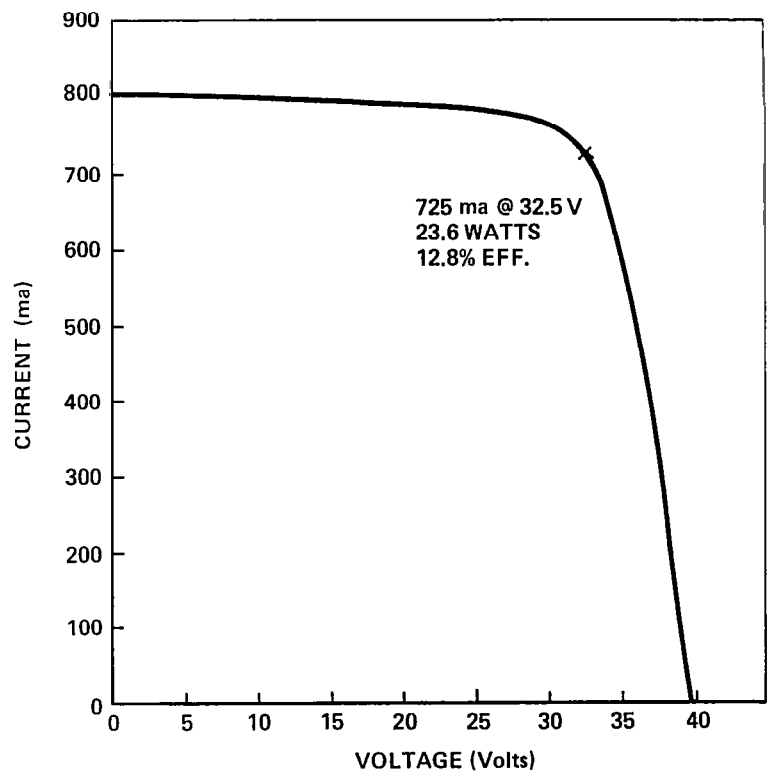

Figure 9. Current-Voltage Curve for ISEE Solar Panel - Type II

3. A REVIEW OF AIR FORCE SPACE PHOTOVOLTAIC DEVELOPMENT EFFORTS

W. Patrick Rahilly
Air Force Aero Propulsion Laboratory
Wright-Patterson Air Force Base, Ohio

SUMMARY

Current Air Force silicon and gallium arsenide solar cell developments are reviewed. The rationale for these efforts are cited showing the reasons for placing emphasis on survivability as well as high conversion efficiency.

INTRODUCTION

The Air Force has a continuing need to develop space power systems that meet a multitude of mission requirements. Too, continual improvement of these power systems provides broader flexibility in the formulation of space mission objectives.

The most cost effective means of generating electrical power aboard today's Air Force spacecraft is the use of solar photovoltaic array-battery power systems. One of the most important collection of components found in these power supplies are the solar cells. These devices must survive many deleterious environmental effects that occur normally in space as well as potential, artificially generated hostile environments. These latter environments impose a considerably different set of constraints on Air Force photovoltaic developments over and above those emphasized by other government agencies.

This paper summarizes Air Force silicon and gallium arsenide cell efforts in the context of high efficiency and survivability. These developments are discussed separately with silicon considered first.

SILICON SOLAR CELL RESEARCH AND DEVELOPMENT

The Air Force Aero Propulsion Laboratory (AFAPL) has ongoing silicon solar cell programs directed at high conversion efficiency and survivability to normal space, nuclear and laser environments. Because of the generally repetitive nature of Air Force missions in space (satellite replacement), it is desirable to develop one solar cell type that will meet all requirements. However, this goal is quite difficult to achieve since the environmental

constraints vary as a function of mission altitude and orbit inclination. It is anticipated, however, that this goal can be reached by the early to mid 1980's time period.

Figure 1 represents a general overview of the AFAPL silicon cell program objectives and approaches. The following paragraphs provide more detail in terms of meeting the efficiency and survivability objectives. The discussions refer to Figure 1.

High Efficiency

Early mathematical predictions placed an upper limit of 22% on silicon cell conversion efficiency in space application. Recent mathematical modeling has lowered the maximum conversion efficiency to lie somewhere in the 18% to 20% range. Recent advances in cell technology have led to laboratory demonstration of conversion efficiencies greater than 15% and greater than 14% in pre-production (2,3). The most significant contributions to these efficiencies (prior state of the art was at 11%) are shallow photovoltaic junctions, top surface texturing along with Ta_2O_5 anti reflective coatings and the development of a viable back surface field (BSF) (4,2,5). All of these improvements caused gains in the light generated current with some gain in voltage for high resistivity material using the BSF. The primary limitation in silicon all efficiency is the voltage performance. As the resistivity of the silicon is reduced, the voltage is expected to increase. However, this increase is not observed experimentally for resistivities below .5 ohm centimeter and is attributed to higher than expected reverse saturation currents. The specific components of the reverse saturation current that adversely affect the voltage are thought to be either the hole injection current or the space charge region recombination current or (most likely) a combination of both.

Possibly the singly most important factor contributing to these high current components is the presence of undesirable impurities such as Fe,C,O,V, etc. In an attempt to resolve the limited voltage problem, AFAPL has initiated a silicon materials improvement effort. This program will investigate the effects fo these impurities on cell performance by removing them from the single crystal silicon (to less than $1X10^{12}$ atoms/cm^3). Also included in this work will be alternate electrical dopant studies (Al and Ga as well as B for the P dopant) and an investigation to improve the quality of both the N^+P and PP^+ junction (the PP^+ junctions will be for one ohm centimeter or higher resistivity material). Other items of importance in this program are silicon processing and cell fabrication steps. It is important to keep in mind that processing/fabrication play a strong role in the performance of the final device.

AFAPL's approach to high efficiency includes optimized vertical junction cell development (exploratory) and an advanced development program (HESP) directed at 16% lot median production line efficiencies (6,3).

The vertical junction cell effort includes high particle radiation resistance goals as well as high efficiency. This type of cell has enhanced red response initially, because of the close spacing of the vertical junctions

(∿ 10 micrometers), and a preserved red response in a particle radiation environment for the same reason. The specific goals for this program are 15% initial efficiency with greater than 12% efficiency after $5X10^{15}$ electrons/ cm^2 (1Mev). The recent redesign of this cell has led to decreased series resistance and increased mechanical strength (7). The cell is not optimized and yet has already demonstrated 13.5% efficiency with an electron damage power degradation rate of half-slope compared to that of conventional or other advanced silicon cells (8,9).

The High Efficiency Solar Panel program (HESP) is now in Phase II procurement for the 16% efficiency goals. The Phase I effort was to achieve 14.5% lot median initial efficiency with specific radiation resistance requirements. As mentioned previously, the achievement of one cell type that satisfies all environmental requirements is difficult. This program resulted in a "shopping list" of cells that permits a selection of cell type to meet a specific requirement. Included in this shopping list were variations of silicon resistivity and cell thickness. Further details concerning this program can be found in the final report which is now in distribution.

AFAPL has just completed an exploratory development program to investigate/develop the method of using a pulsed electron beam to anneal ion implant damage (10). The ion implantation was employed to introduce the N dopant into the wafer top surface thus forming an N^+P photovoltaic junction after the pulse anneal has occurred. The major reasons for this unique approach to N^+P junction formation was to (a) obtain a tailored profile N dopant distribution to achieve high blue response, (b) provide a method of N^+P junction formation that does not cycle the wafer through high temperature and (c) provide a cell fabrication method that is quick and of high yield. This program was plagued with electron beam control problems. However, toward the end of the work, good junctions were demonstrated (open circuit voltage was used as the merit parameter). Efficiencies of 12% AMO were demonstrated. Although the objectives of this program were not met, this approach to N^+P (and PP^+) junction formation deserves further support because of its high rate high yield potential.

Survivability

High efficiency and the ability to resist earth orbit environmental effects are of considerable importance. However, of equal importance is the survivability of Air Force satellites in potential hostile environments. As mentioned previously, this latter situation imposes a myriad of problems to high efficiency cell development. The approaches shown in Figure 1 by no means constitute a complete listing. It is sufficient to state that the nuclear environment consists of X rays, prompt gammas and neutrons (fission and fusion) steps have been taken in earlier development efforts to reduce or eliminate their effects. In the case of system level, the effects of electromagnetic pulse have been eliminated. For potential laser environments, it is sufficient to state that high temperature cycling can cause complete cell/array failure and steps are being taken to eliminate this failure mode.

AFAPL is supporting electrostatic bonded (ESB) cover development for two

major reasons (11). These reasons are (a) to reduce cell covering costs by more than 50% and (b) to eliminate the cover-to-cell adhesive for high temperature survivability. The high temperature contacting work ensures compatibility with the ESB cover technology and is consistent with the reduction of laser effects. AFAPL is sponsoring work to develop a cell-to-array substrate adhesive. This effort involves investigation and test of carborane siloxane elastomers (12).

All AFAPL effort in developing high temperature survivable power systems is within the context of compatibility with hardening to nuclear and normal space environments. The cost penalties for normal space, nuclear and laser hardening are not expected to be severe. Essentially all of the costs are being absorbed in the exploratory development phase.

GALLIUM ARSENIDE SOLAR CELL RESEARCH AND DEVELOPMENT

Calculations show that if series resistance is neglected, gallium arsenide solar cells have a theoretical maximum obtainable conversion efficiency of 26%. Recent developments in this technology have demonstrated efficiencies as high as 17% for large area cells and 18.5% for somewhat smaller sized cells (13,14). These gallium arsenide solar cell developments offer a potential 22% efficiency. If this type cell is to be used aboard Air Force satellites, many problems must be overcome. Figure 2 represents an overview of the AFAPL gallium arsenide solar cell development work.

High Efficiency

The approaches indicated in Figure 2 are all tied to the high efficiency objective (22%). The most important approaches in this effort is associated with the optical coupling of light into the cells. Location of the junction (thickness of the GaAs P type layer) plays a major role in the behavior of the blue response. Making the junction shallow provides the best blue response along with enhanced resistance to electron damage effects (13,15). The anti-reflective coating and electrical contacting are important in that adherance of the materials to the cell is critical. In particular, the contact metalization must withstand thermal cycling, humidity and tape peel testing. These tests are severe. Large cell area (greater than 2cmX2cm) is important in that achievement of high conversion efficiencies for such areal dimensions lends considerable credibility to this type of cell having potential for space application.

Survivability

Data for particle irradiation effects to gallium arsenide cells is available elsewhere in this proceedings (16). The results of these tests suggests considerable sensitivity of gallium arsenide cells to low energy protons. The electron damage data suggests that the thickness of GaAs P type layer is critical to cell hardness. The fission spectrum neutron data shows excellent resistance of these type cells to such environments. The effects of X rays

on these cells is unknown but testing will be accomplished to identify problems/failure modes. The high temperature environment poses a serious problem to the cell electrical contacting. High temperature contacts must be developed and thouroughly evaluated.

REFERENCES

1. P.M. Dunbar and J.R. Hauser, "A Theoretical Analysis of the Current-Voltage Characteristics of Solar Cells", Annual Report, NASA Grant NGR 34-002-195, August 1975.

2. J. Haynos et al.,"The COMSAT Non-Reflective Silicon Solar Cell: A Second Generation Improved Cell", International Conference on Photovoltaic Power Generation, Hamburg, Germany, September 25-27, 1974.

3. AF Contract F33615-75-C-2028, "High Efficiency Solar Panel", Spectrolab.

4. J. Lindmayer and J. Allison, "An Improved Silicon Solar Cell - The Violet Cell", Late News, 9th IEEE Photovoltaic Specialists Conference, Cat. Nr. 72CHO 613-0-ED, May 1972.

5. J. Mandelkorn, et al.,"Studies of the BSF Cell", NASA TM X-3326, 199, December 1975.

6. AF Contract F33615-75-C-2058, "Non Reflecting Vertical Junction Silicon Solar Cell Optimization", Solarex Corp.

7. W.P. Rahilly, U.S. Patent 3,985579, "Rib and Channel Vertical Junction Solar Cell", October 1976.

8 J. Lindmayer and C. Wrigley, "New Developments in Vertical Junction Solar Cells", Late News Item, 12th IEEE Photovoltaic Specialists Converence, November 1976.

9. J. Lindmayer et al.,"Developments in Vertical Junctions Silicon Solar Cells", This proceedings.

10. AF Contract F33615-75-C-2006, "Low Temperature Fabrication of High Efficiency Silicon Solar Cells" Simulation Physics Inc.

11. AF Contract F33615-74-C-2001, "Stress Free Application of Glass Covers Hardened Solar Cells and Arrays", Simulation Physic Inc.

12. AF Contract F33615-76-C-2023, "High Temperature Bonding Techniques for Solar Cell Arrays", Hughes Aircraft Company.

13. AF Contract F33615-76-C-2121, "High Efficiency Gallium Arsenide Solar Cell Development", Hughes Aircraft Company.

14. G. Walker et al., "High Efficiency GaAs Solar Cells", This proceedings.

15. R. Knechtli and S. Kamath, "Gallium Arsenide Solar Cell Effort", This proceedings.

16. P. Rahilly and B. Anspaugh, "Electron Proton and Fission Spectrum Neutron Damage in Advanced Silicon and Gallium Arsenide Solar Cells" This proceedings.

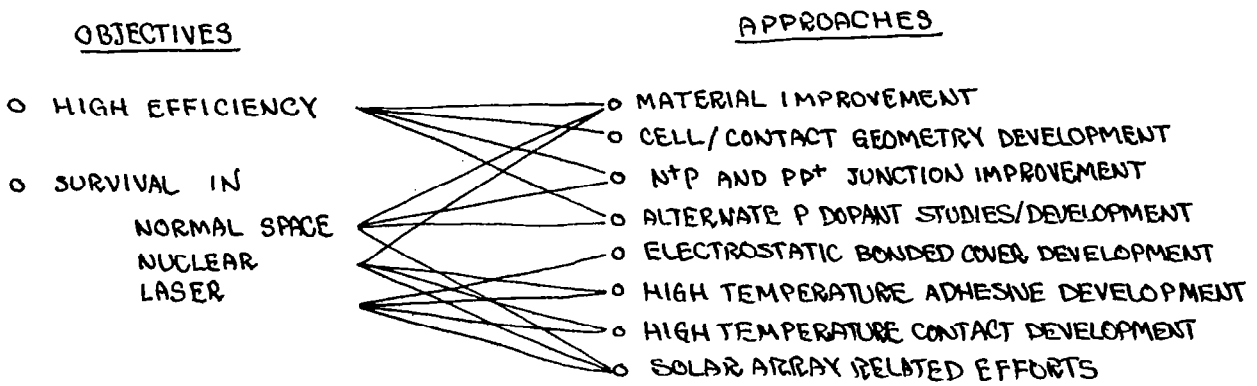

FIGURE 1 AFAPL SILICON SOLAR CELL PROGRAM

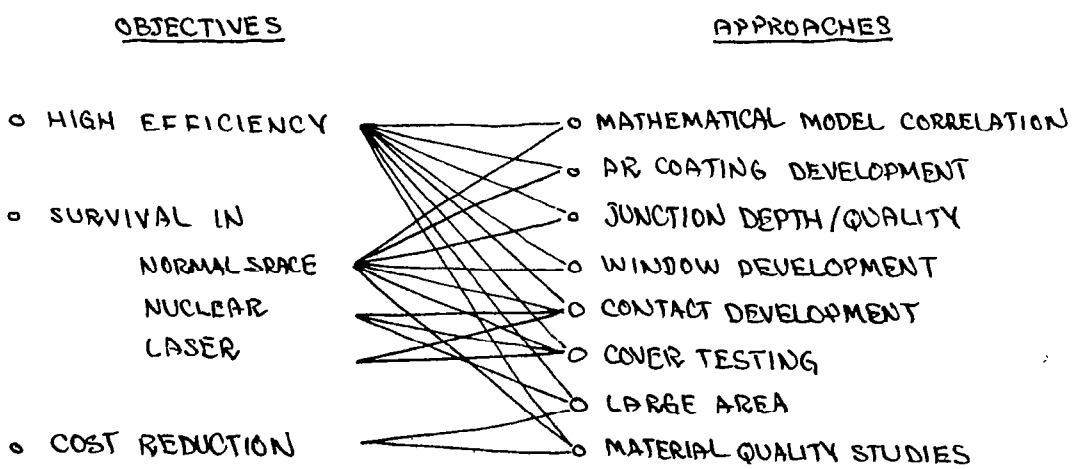

FIGURE 2 AFAPL GALLIUM ARSENIDE SOLAR CELL DEVELOPMENT

4. IMPURITY GRADIENTS AND HIGH EFFICIENCY SOLAR CELLS*

C. R. Fang and J. R. Hauser
North Carolina State University

ABSTRACT

One potential means of improving the efficiency of solar cells especially after space irradiation is to incorporate built-in fields into the device through the use of impurity doping gradients. Previously published papers have indicated an improved minority carrier collection efficiency and improved efficiency when doping gradients are present. In this work a detailed numerical calculation of solar cell performance has been used to study various types of doping gradients. In general the predicted improvements in performance have been less than previously reported due to various device effects such as high injection and the dependence of lifetime on doping density.

I. INTRODUCTION

There have been a number of theoretical investigations into the efficiency of drift field solar cells in recent years [1-4]. In these earlier investigations the emphasis has been on the calculation of collection efficiency as a result of including drift fields, with somehow different approximations in lifetime, mobility and other important parameters. Wolf [1] was the first to demonstrate that a surface drift field helps the short wavelength response and to show that a base field can considerably reduce the radiation damage and increase the useful life of solar cells. In 1967 Bullis and Runyan [3] found that there exists an optimum field width which is approximately twice the diffusion length or about 25 μ whichever is shorter in n^+-p cells for maximum collection efficiency. Overstraeten, et al. [4] have shown that the advantage of the drift field is mainly determined by the layer close to the collection junction. To obtain higher collection efficiency, the magnitude of the drift field should be high, at its optimum width and the doping density should be as low as possible.

In considering impurity doping gradients, it is useful to distinguish two somewhat different types of doping gradients. First, if the doping change is very rapid, space charge regions form. On the other hand if the change in doping density is very gradual, a state of quasi-neutrality exists at every point and a built-in electric field is produced throughout the bulk of a solar cell. A gradient sufficient to give rise to a space charge region will be referred to here as a high-low junction while a gradual change in doping will be referred to as a drift field region.

*This work was supported by a NASA Lewis research grant.

Despite the theoretical predictions of the drift field enhancing the collection efficiency, the advantages of drift fields are still unconfirmed experimentally, especially with regard to total conversion efficiency [5]. The purpose of this paper is to explain the physical mechanism governing the operation of drift field cell and the discrepancies of those earlier results. The emphasis is on maximizing the total conversion efficiency as a result of including the base field. In this paper the major mechanisms which tend to limit the conversion efficiency due to the incorporation of drift field in Si solar cells are discussed.

The use of a high-low junction in solar cells is a more recent innovation than the drift field concept. However, the advantages of such abrupt doping gradients have been experimentally demonstrated and incorporated into the design of high efficiency solar cells. Basically the high-low junction near the back surface prevents minority carriers from reaching the back ohmic contact and thus acts as a minority carrier reflecting boundary.

II. FIRST ORDER THEORY

The structure of the basic solar cell to be considered here is shown in Figure 1. The n^+ surface layer is a thin (0.1-0.5 μm typically) heavily doped layer which may have a doping gradient. The p-type base layer is shown with a high-low junction near the back ohmic contact and a wide, drift field region. Because of the dominance of the base layer properties in determining solar cell performance, the discussion here concentrates on the base layer.

Within the drift field region of the base, excess minority carrier electrons ($\bar{n}$) are controlled by the basic drift-diffusion and continuity equations which when combined into a single equation for steady state gives

$$D_n \frac{d^2\bar{n}}{dx^2} + [\frac{dD_n}{dx} + \mu_n E] \frac{d\bar{n}}{dx} + [\frac{d}{dx} (\mu_n E) - \frac{1}{\tau_n}]\bar{n} + G = 0 \qquad (1)$$

where G is the optical pair generation rate. For a general doping profile Equation (1) must be solved by numerical techniques. Also the dependence of mobility μ_n and lifetime τ_n on doping density complicates the solution.

The special case of a constant electric field (exponential doping profile) with constant τ_n and μ_n has been frequently used for drift cells and provides certain insight into drift cell operation. If the simpler equation

$$D_n \frac{d^2\bar{n}}{dx^2} + \mu_n E \frac{d\bar{n}}{dx} - \frac{\bar{n}}{\tau_n} + G = 0, \qquad (2)$$

is considered, an exact solution can be obtained of

$$\bar{n} = A_1 \exp(x/L^+) + A_2 \exp(-x/L^-) + \tau_n G, \tag{3}$$

where

$$1/L^{\pm} = \sqrt{(1/L_n)^2 + (qE/2kT)^2} \mp (qE/2kT). \tag{4}$$

The basic theory behind the drift field solar cell is that the electric field increases the collection depth for optically generated minority carriers within the base layer since $L^+ > L_n$.

The value of a constant drift field can be written as

$$E = \frac{kT}{q} \frac{1}{N_A} \frac{dN_A}{dx} = \frac{kT}{qW} \ell n \left(\frac{N_2}{N_1}\right), \tag{5}$$

where W is the width of the drift field region and N_2, N_1 are the doping densities at the ends of the drift field region. The ratio N_2/N_1 is limited in value to around 10^5 in practical cases and this sets an upper limit to the field which can exist. From Equation (5) it is seen that the largest field occurs when W is as small as possible. However, if W becomes less than L^+, Equation (4) begins to lose meaning since the field doesn't exist over the assumed dimensions. Thus by setting W equal to L^+ and combining Equations (4) and (5) a limit on L^+ can be established as

$$L^+ < L_n \sqrt{1 + \ell n(N_2/N_1)}. \tag{6}$$

With a ratio of 10^5 for N_2/N_1 this gives $L^+ < 3.54\ L_n$. Thus an enhancement in collection depth by a factor of about 3 is the most that can be realized due to doping density limitations.

Previous studies of drift field cells have concentrated on the improved collection efficiency. Equally important in determining solar cell efficiency is dark forward current and open circuit voltage which, according to first order device models, are related as

$$J_{dark} = J_o \exp(qV/kT) \tag{7}$$

$$V_{oc} = \frac{kT}{q} \ell n(J_{sc}/J_o), \tag{8}$$

where J_{sc} is short circuit current density and J_o is a function of device geometry, and material parameters. For a drift field cell with constant mobility

$$J_o = \frac{qD_n}{L^+} \frac{n_i^2}{N_1} > \frac{qD_n}{L_n\sqrt{1+\ell n(N_2/N_1)}} \frac{n_i^2}{N_1} . \tag{9}$$

For a large open circuit voltage, J_o should be minimized. A large drift field requires that N_2 be large and N_1 be small, while Equation (9) shows that this is far from the condition for minimum dark current where N_1 should be as large as possible. Thus large drift fields and minimum dark current are incompatible objectives. For many potential drift field designs, it appears that increases in dark current almost completely eliminate any increased collection efficiency due to the drift field.

The previous considerations have been for cells with a base layer thickness large compared with a diffusion length. These considerations must be modified considerably if the cell thickness is comparable or less than the diffusion length. For such thin cells, the diffusion length is not the major factor determinining collection efficiency and a back surface high-low junction has been found to be effective in increasing the efficiency of such cells.

The purpose of a high-low junction such as shown in Figure 1 is to prevent minority carriers created either by light or forward injection from recombining at the back surface. The high-low junction interface can be characterized as a low surface recombination boundary to the base layer. The high-low junction is most effective for solar cells in which the base width is less than a diffusion length. As discussed elsewhere [6,7], the high-low junction can be very effective in reducing back surface losses, giving a collection depth approximately equal to the total cell thickness. An ideal high-low junction minimizes dark current and maximizes short circuit current simultaneously.

III. NUMERICAL CALCULATIONS

In order to investigate in detail the ideas discussed above, a series of calculations have been made of solar cell performance with various types of drift fields and high-low junctions. The analysis consists of a detailed numerical solution of the semiconductor device equations. Details of the modeling and solution techniques have been discussed elsewhere [8]. The solutions include all types of nonlinear device effects such as high level injection as well as doping and field dependences of device parameters.

In any comparison of solar cell performance with and without drift fields, the type of cell and the parameters which are held constant in the analysis are very important. In this work the approach has been as follows. Since a uniformly doped base layer solar cell with a back surface high-low junction has so far demonstrated the highest experimental efficiencies, the approach has been to take this cell as a reference cell and to see if other types of doping gradients improve the efficiency. The analysis has been performed for a cell with the device parameters listed in Table I. The density of $2\times10^{19}/cm^3$

is chosen as a constant surface density, since this is approximately the highest doping density obtainable after considering heavy doping effect which doesn't produce any retrograde surface field [8,9].

SiO is used as the antireflection layer in its optimum thickness of 800 Å where it allows 45.4 mA/cm^2 current density to be available for collection. Despite the short wavelength absorption in SiO, it makes little difference in the collection efficiency of the base layer since most of the short wavelength photons are absorbed in the surface layers. To avoid problems in interpreting the results, heavy doping effects were not considered throughout this work. However, such effects as bandgap reduction would not significantly change the results because of the low doping density used for the surface layer in the calculations. The irradiance condition used is AMO and total optical reflection at the back ohmic contact was assumed.

Another very important factor in any solar cell study is the assumed relationship between diffusion length, or lifetime, and doping density. Three different relationships as shown in Figure 2 have been used in this work. These curves are based upon experimental data by Iles, et al. [10] with the top and bottom curves representing limits near the top and bottom of measured diffusion length data, while the middle curve represents values near the center of the measured range. These curves are convenient for the 150 μm cell thickness since the three curves represent, at light doping densities, cases where the diffusion length is much larger, approximately equal and much less than the total cell thickness. The behavior of the cell and the importance of drift fields depends on which of these three cases is considered.

For a given cell thickness and given diffusion length curve, there is an optimum uniform base layer doping density which results in maximum efficiency, and this condition was first determined. Table II (E_B= 0 case) lists the optimum uniform doping density for maximum efficiency and the corresponding device parameters for the three diffusion length cases. Also shown in Table II are performance parameters for cells with drift fields (E_B) of 10 and 20 V/cm. For each different L_D case the average doping density remains constant as the field increases.

N_1 and N_2 are the doping density near the high-low junction and p-n junction respectively. It is clear that the collection efficiency as measured by I_{sc} indeed increases after building in the drift field with the larger increase for the lower base layer diffusion length. For the minimum L_D case I_{sc} increases from 22.6 mA to 31.3 mA as the drift field increases.

Figure 3 shows the minority carrier current density as a function of position in the base region for the calculations of Table II. It can be seen in the table that the increase in collection efficiency is very limited for the maximum diffusion length used here which is already larger than the base width. Figure 3 shows that the collection distance can be effectively expanded all across the base layer with the appropriate drift field for the case of the medium diffusion length. The curves for the minimum diffusion length indicate a much smaller increase in collection depth. Since collection occurs only over part of the base, this suggests that an improved cell can be obtained

by grading only over part of the base layer near the p-n junction. This has been verified and is discussed later.

With the inclusion of the base field, the doping density near the p-n junction (N_2 of Table 3) is inevitably reduced assuming that the average doping density remains constant. This reduction in doping density has profound effects on the cell operations. In analyzing the calculated results the dark current was approximated by an equation of the form

$$J = J_o \exp(qV/kT) + J_R \exp(qV/2kT). \tag{10}$$

The J_o and J_R values which give the best fit to the calculated dark current curves are listed in Table II. The forward injection current density as evidenced by the J_o term increases as a result of lowering the injecting barrier, and this typically results in a reduced open circuit voltage as also seen in Table II. The depletion layer expands which leads to a larger space charge recombination current density as evidenced by the increased J_R term. Third, and perhaps most importantly is the fact that high injection may easily occur at a voltage well below the operating voltage of the maximum power point.

In Table III the transition voltage V_H^* between the low and high injection regions is calculated from the equation

$$V_H^* = 2 \frac{kT}{q} \ell n(N_2/n_i). \tag{11}$$

The table also shows the transition voltage V_R^* where the depletion region current equals the ideal injection current density. It's clear that the cell is operating at a voltage well above the high injection limit for the case of 20 V/cm for both the maximum and medium diffusion length cases. The high injection effect is the major reason for the reduction of the curve factor CF in Table II and the overall drop in conversion efficiency.

Although there is a small reduction in CF due to the increased depletion region recombination current density, the major reduction is due to the deterioration of the open circuit voltage as a result of a much higher forward injection current density. The increased dark current which is predicted by the approximate model of Equation (8) due to a decreased N_1 is definitely verified by the computer calculations.

From the results of Table II several conclusions can be drawn with regard to solar cells with the same average base doping levels. First, a drift field enhances the collection efficiency with the largest changes occurring when the diffusion length is much less than the base layer thickness. Second, almost all of the increased collection efficiency is offset by increases in dark current and a reduced open circuit voltage. Third, for large drift fields, operation near the p-n junction tends to be in the high injection region which further tends to reduce efficiency due to a reduced curve factor.

Table IV shows calculations for cells with the same electric field but with different average base layer doping densities. In comparing this data with that of Table III, it is seen that the highest efficiency results from a compromise between retaining a large open circuit voltage and achieving an enhanced collection efficiency due to the drift field. The calculations have shown that for highest efficiency the doping density near the p-n junction should be kept near the value which gives highest efficiency for a uniformly doped base layer.

A series of calculations have been made to determine the optimum drift field conditions for highest efficiency for the three different lifetime cases. The general impurity profile considered is shown in Figure 4. The n^+ surface layer is taken as uniformly doped at $2x10^{19}/cm^3$. The back surface p^+ layer is also uniformly doped at $10^{19}/cm^3$. The base region was assumed to have a constantly doped region near the back p^+ region of varying doping density N_W. The graded doping region was varied in width and type of doping profile to study the effects on overall efficiency. The types of doping profiles studied were 1) constant, 2) exponential and 3) erfc. The erfc profile gives the largest electric field at the p-n junction while the exponential profile gives a uniform electric field.

Table V shows calculated results for cells with the maximum L_D values for different doping profiles. For these large values of L_D the diffusion length is larger than the cell thickness and therefore the drift field width was taken as equal to the cell thickness. The field is seen to have little effect on cell efficiency giving an increase from 18.19% to only 18.29%. Larger fields than those shown in the table were found to give lower efficiencies because of reductions in open circuit voltage.

Calculated results using the medium diffusion length case are shown in Figure 5. In this series of calculations the doping density was varied exponentially between $9x10^{16}/cm^3$ at the p-n junction to $10^{18}/cm^3$ at the edge of the drift region (W). The width of the drift region was varied from 20 μm to 100 μm with the results shown in Figure 5. The peak efficiency is seen to occur when the drift field exists over about 40 μm. This peak value of 14.64% is slightly better than the 13.70% obtained without the drift field.

Similar calculations to those shown in Figure 5 have been made with the graded region doping varying between $9x10^{16}/cm^3$ and $10^{19}/cm^3$. The results as a function of width of graded region are similar to those of Figure 5. The major differences are a peak efficiency of 14.70% for a graded region width of about 80 μm.

Calculations for the medium diffusion length case using an erfc doping profile between the same doping limits as used for the exponential doping have also been made. The results are very similar to those shown in Figure 5. For an erfc doping profile between $9x10^{16}/cm^3$ and $10^{18}/cm^3$ the peak efficiency was calculated as 14.62% which is slightly less than the 14.64% value obtained with the exponential doping. For the erfc doping profile between $9x10^{16}/cm^3$ and $10^{19}/cm^3$ the peak efficiency was found to be 14.76% at a graded region width of about 100 μm. This efficiency is slightly larger than the correspond-value for the exponential profile.

Calculations made with the minimum diffusion length curve of Figure 2 have given results similar to those discussed above. The largest calculated efficiencies were found to occur when the doping density was graded between $5 \times 10^{17}/cm^3$ at the p-n junction to $10^{19}/cm^3$ at some distance W from the junction. Optimum values of W were found to be about 10 μm for the exponential grading and about 5 μm for the erfc grading with peak calculated efficiencies of 9.50% and 9.45% respectively.

In all of the calculations, the maximum efficiency has been observed to ocur when the width of the drift region is approximately twice the diffusion length. This appears to be the best compromise between enhanced collection efficiency and increased dark current.

The maximum efficiencies in various drift field type cells calculated in the present study are shown in Table VI. Shown for comparison purposes (in parenthesis) are the maximum efficiencies for cells with uniformly doped base layers. These values may not represent absolute maximum values since optimization studies were not done on all possible parameters. However they should be close to the efficiency enhancement to be expected in drift field cells. The largest improvements are observed in cells with low diffusion lengths which is to be expected. However the improvement which can be achieved is fairly limited. This is consistent with the first order models of Section II which show that the collection depth can only be improved by about a factor of three. The major limitation, however, is the increased dark current and lowered open circuit voltage which tends to accompany any attempt to build in a large drift field through the use of doping gradients.

IV. RADIATION RESISTANCE

One of the major reasons for considering cells with built-in fields is the potential for improved radiation resistance. This is consistent with the results of the previous section where it was shown that the drift field had the largest improvement in cells with low diffusion lengths.

The degradation in lifetime with radiation fluence ϕ is normally modeled by an equation of the form

$$\frac{1}{\tau} = \frac{1}{\tau_o} + K\phi \qquad (12)$$

where τ_o is the initial lifetime and K is a damage coefficient, which may change with doping density and radiation dose. In the present calculations for electron irradiation, K has been taken as a constant and of value 3.2×10^{-9} cm^2/sec.

To investigate the expected degradation in efficiency, calculations have been made on three different cells with the basic device parameters of Table I. In the first cell the base region was uniformly doped at $5.6 \times 10^{16}/cm^3$. In the

second cell an exponentially graded region from $5.6 \times 10^{16}/cm^3$ to $10^{19}/cm$ was taken over a distance of 54 μm, while in the third cell the graded region width was taken over a distance of 18 μm. The calculated changes in maximum efficiency with electron fluence are shown in Figure 6. It is seen that the drift fields do improve the efficiency for large radiation doses. The graded width of 54 μm and 18 μm were selected as approximately twice the diffusion length after total doses of 10^{15} and $10^{16}/cm^2$ respectively. The cell with a 54 μm graded region is seen to be best at $10^{15}/cm^2$ and the 18 μm cell is best at $10^{16}/cm^2$ as expected from the selection of graded region widths. Other potential devices have also been studied and in all cases an enhanced radiation resistance could only be achieved at the expense of the initial cell efficiency.

V. CONCLUSIONS AND SUMMARY

In this work a detailed numerical computer analysis program has been used to study the efficiency of silicon solar cells with various internal drift fields achieved by use of doping gradients. In agreement with earlier works, it has been found that a drift field can be used to significantly enhance the short circuit current of solar cells with short diffusion lengths. However, these improvements are to a large extent offset in terms of peak efficiency by increases in dark current and by reductions in curve factor when a drift field is present.

For a given ratio of doping density across the drift field region, there is an optimum width for the drift field region. The optimum width was found to be on the order of twice the diffusion length when the diffusion length is less than the cell thickness. When the diffusion length is larger than the cell thickness, very little improvement was found in efficiency due to the drift field. This conclusion holds only for cells with a high-low junction at the back surface and larger improvements are observed for n^+-p cells with a back surface ohmic contact.

The calculations indicate that drift field cells can have somewhat higher efficiencies after electron irradiation than similar cells without the drift field. However, this is obtained only at the expense of lower initial efficiencies.

REFERENCES

1. M. Wolf, "Drift fields in photovoltaic solar energy converter cells," Proc. IEEE, vol. 51, May 1963, pp. 674-693.

2. S. Kaye and G. P. Polik, "Optimum bulk drift-field thicknesses in solar cells," IEEE Trans. on ED, vol. ED-13, July 1966, pp. 563-570.

3. W. Murray Bullis and W. R. Runyan, "Influence of mobility and lifetime variations on drift field effects in silicon junction devices," IEEE Trans. on ED, ED-14, Feb. 1967, pp. 75-81.

4. R. V. Overstraeten and W. Nuyts," Theoretical Investigation of the efficiency of drift-field solar cells," IEEE Trans. on ED, vol. ED-16, July 1969, pp. 632-641.

5. W. R. Runyan and E. G. Alexander, "An experimental study of drift-field silicon solar cells," IEEE Trans. on ED, vol. ED-14, Jan. 1967, pp. 3-9.

6. M. P. Godlewski and C. R. Baraona, "Low-high junction theory applied to solar cells,", Tenth Photovoltaic Specialists Conference, Palo Alto, CA, Nov. 13-15, 1973.

7. J. R. Hauser and P. M. Dunbar, "Minority carrier reflecting properties of semiconductor high-low junctions," Solid-State Elec., vol. 18, pp. 715-716.

8. P. M. Dunbar and J. R. Hauser, "A study of efficiency in low resistivity silicon solar cells," Solid-State Elec., vol. 19, 1976, pp. 95-102.

9. M. P. Godlewski, H. W. Brandhorst, Jr. and C. R. Baraona, "Effects of high doping levels on silicon solar cell performance," Eleventh IEEE Photovoltaic Specialists Conference, Scottsdale, AZ, May 1975.

10. P. A. Iles and S. I. Soclof "Effect of impurity doping concentration on solar cell output," Proceedings of Eleventh Photovoltaic Specialists Conference, Scottsdale, AZ, May 1975.

TABLE I. DEVICE STRUCTURE PARAMETERS

Overall cell thickness	150 μm
n^+ surface thickness	0.2 μm
p base thickness	144.8 μm
p^+ thickness	5 μm
n^+ surface doping	$2 \times 10^{19}/cm^3$
p base doping	Optimized
p^+ doping	$10^{19}/cm^3$
Lifetime model	Iles [10]
Surface recombination velocity	10^3 cm/sec
Antireflection layer	SiO, 800 Å
Irradiance	AMO

TABLE II. RESULTS OF SOLAR CELL CALCULATIONS FOR DIFFERENT DIFFUSION LENGTHS AND DIFFERENT DRIFT FIELDS

E_B (V/cm)	L_D	N_1 (cm^{-3})	N_2 (cm^{-3})	J_{sc} (mA/cm^2)	V_{oc} (Volts)	η (%)	CF	J_o (mA/cm^2)	J_R (A/cm^2)
0	Max	5.6×10^{16}	5.6×10^{16}	42.40	0.690	18.19	0.841	4.44×10^{-13}	2.87×10^{-10}
10	Max	3.24×10^{17}	9.9×10^{14}	42.79	0.693	17.79	0.812	1.45×10^{-12}	3.73×10^{-10}
20	Max	6.49×10^{17}	6.04×10^{12}	42.82	0.698	17.60	0.798	6.24×10^{-11}	1.11×10^{-9}
0	Med	9×10^{16}	9×10^{16}	35.82	0.623	13.70	0.830	7.43×10^{-13}	2.96×10^{-9}
10	Med	3.6×10^{17}	1.1×10^{15}	40.83	0.561	13.71	0.810	7.19×10^{-11}	1.92×10^{-8}
20	Med	7.2×10^{17}	6.7×10^{12}	42.09	0.524	11.79	0.724	4.29×10^{-9}	7.7×10^{-8}
0	Min	5×10^{17}	5×10^{17}	22.63	0.613	8.39	0.818	4.69×10^{-12}	2.77×10^{-8}
10	Min	2.9×10^{18}	8.8×10^{15}	27.13	0.501	7.91	0.787	4.12×10^{-10}	3.39×10^{-7}
20	Min	5.8×10^{18}	5.4×10^{13}	31.29	0.385	6.35	0.713	7.53×10^{-8}	1.83×10^{-6}

TABLE III. COMPARISON OF TRANSITION VOLTAGES V_R^* AND V_H^* WITH THE OPEN CIRCUIT VOLTAGE V_{oc} AND THE MAXIMUM POWER VOLTAGE V_m

E_B (V/cm)	L_D	V_R^* (volts)	V_H^* (volts)	V_M (volts)	V_{oc} (volts)
0	Max	0.334	0.780	0.600	0.690
10	Max	0.286	0.572	0.597	0.693
20	Max	0.148	0.309	0.594	0.698
0	Med	0.428	0.805	0.450	0.623
10	Med	0.288	0.577	0.444	0.561
20	Med	0.149	0.315	0.413	0.524
0	Min	0.448	0.893	0.309	0.613
10	Min	0.346	0.685	0.427	0.501
20	Min	0.165	0.422	0.301	0.385

TABLE IV. CALCULATED PARAMETERS FOR CELLS WITH DIFFERENT AVERAGE DOPING DENSITIES

	N_1 (cm^{-3})	N_2 (cm^{-3})	J_{sc} (mA/cm^2)	V_{oc} (volts)	CF	η (%)
Max L_D						
E_B=3	3.14×10^{17}	1.15×10^{15}	42.63	0.689	0.839	18.21
E_B=3	3.02×10^{17}	5.6×10^{16}	42.28	0.694	0.844	18.29
Min L_D						
E_B=10	1.37×10^{20}	5×10^{17}	23.28	0.617	0.818	8.69
E_B=10	6.87×10^{18}	2.5×10^{16}	26.61	0.530	0.790	8.23
E_B=10	1.37×10^{21}	5×10^{18}	18.53	0.674	0.824	7.60

TABLE V. COMPARISON OF CELLS WITH DIFFERENT DOPING PROFILES (W=144.8 μm, MAX L_D)

Doping Profile	N_1 (cm^{-3})	N_2 (cm^{-3})	J_{sc} (mA/cm^2)	V_{oc} (volts)	CF	η (%)
Constant	$5.6x10^{16}$	$5.6x10^{16}$	42.40	0.690	0.841	18.19
Exponential	$3.02x10^{17}$	$5.6x10^{16}$	42.28	0.694	0.844	18.29
Exponential	$1.15x10^{18}$	$5.6x10^{16}$	42.20	0.695	0.844	18.29
Erfc	10^{17}	$5.6x10^{16}$	42.73	0.692	0.835	18.24
Erfc	10^{18}	$5.6x10^{16}$	41.72	0.699	0.845	18.20

TABLE VI. MAXIMUM CALCULATED EFFICIENCIES

L_D	W (μm)	E (V/cm)	J_{sc} (mA/cm^2)	V_{oc} (volts)	CF	η (%)
Max	144.8	3	42.28	0.694	0.844	18.29
		(0)	(42.40)	(0.690)	(0.841)	(18.19)
Med	80	15.3	36.61	0.650	0.836	14.70
		(0)	(35.82)	(0.623)	(0.830)	(13.70)
Min	10	77.9	24.70	0.635	0.820	9.50
		(0)	(22.63)	(0.613)	(0.818)	(8.39)

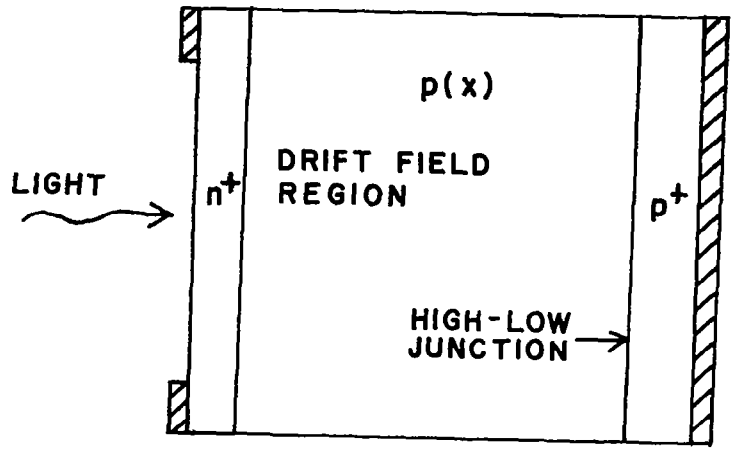

Figure 1. Solar Cell Model.

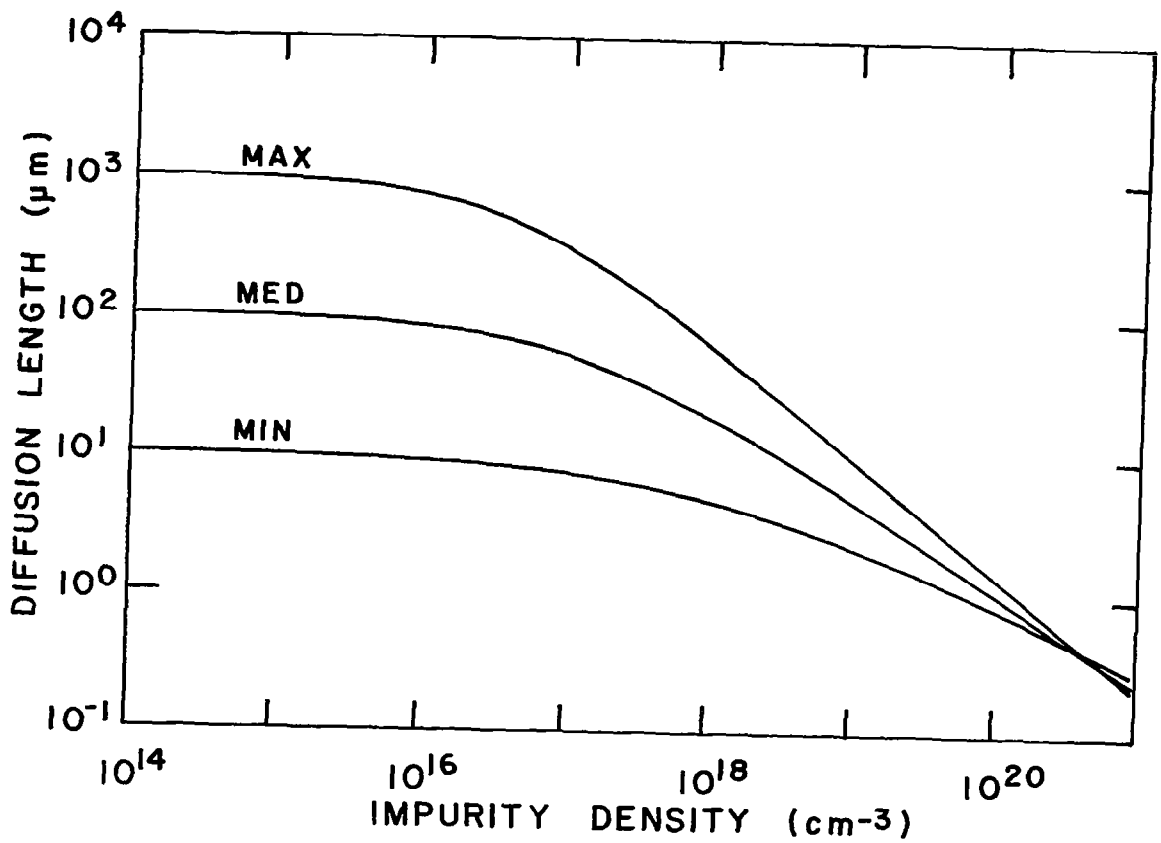

Figure 2. Diffusion Length Variations with Impurity Density used in Calculations.

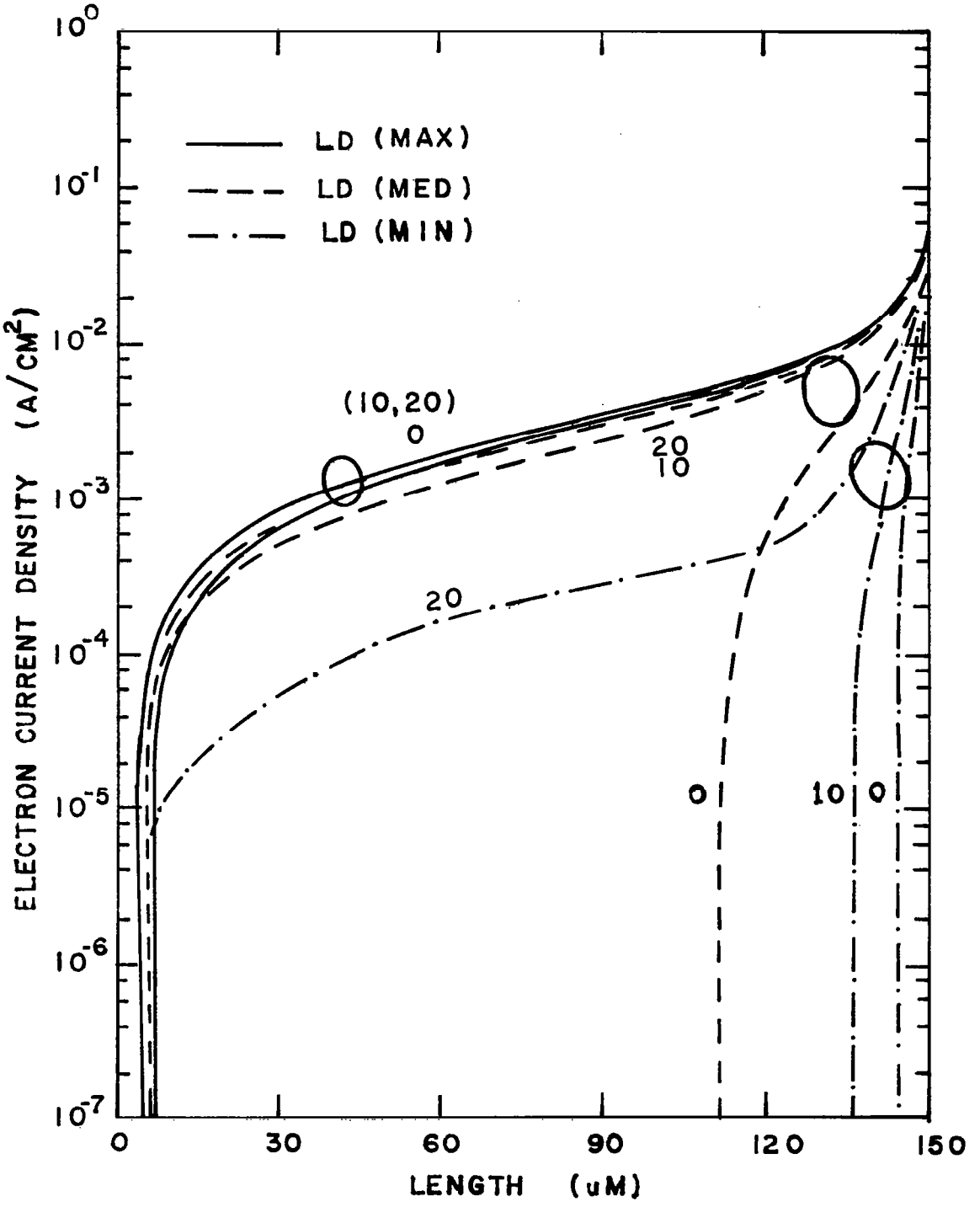

Figure 3. Illustration of Minority Carrier Current in the Base Layer for Three Diffusion Length Cases.

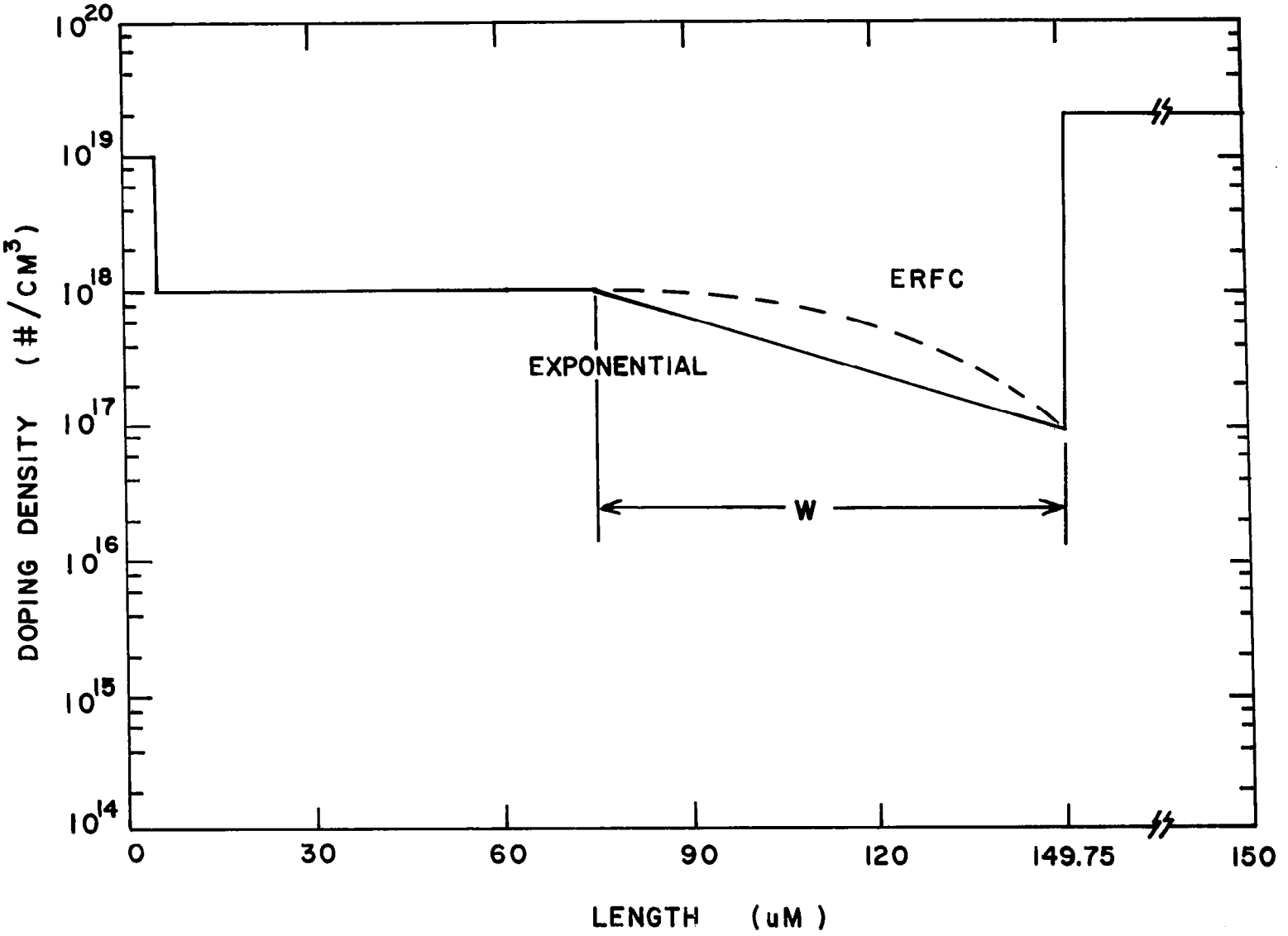

Figure 4. Types of Impurity Profiles Used in Studying the Optimum Drift Field Width.

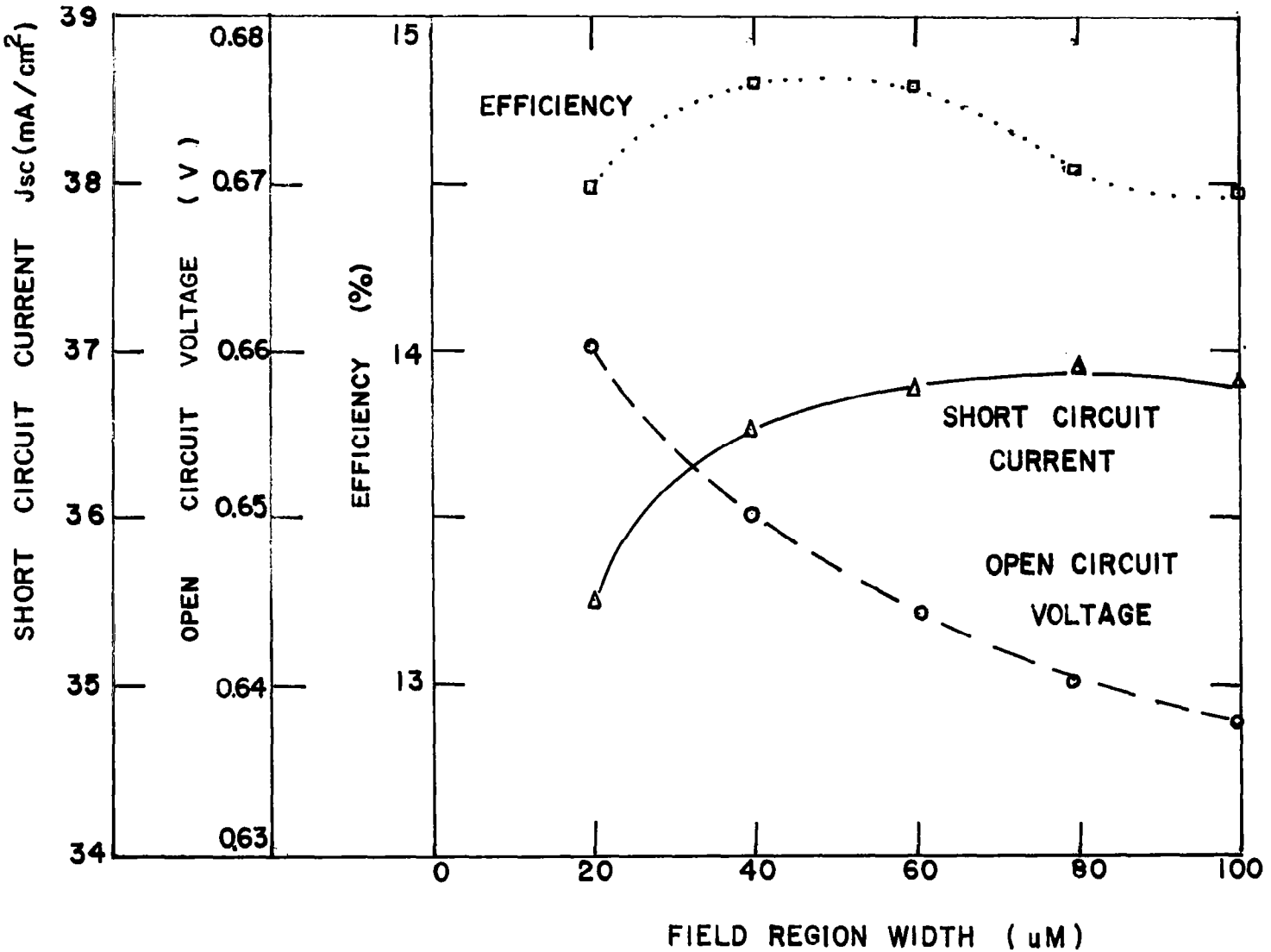

Figure 5. Efficiency as a Function of Field Region Width for the Medium Diffusion Length Case.

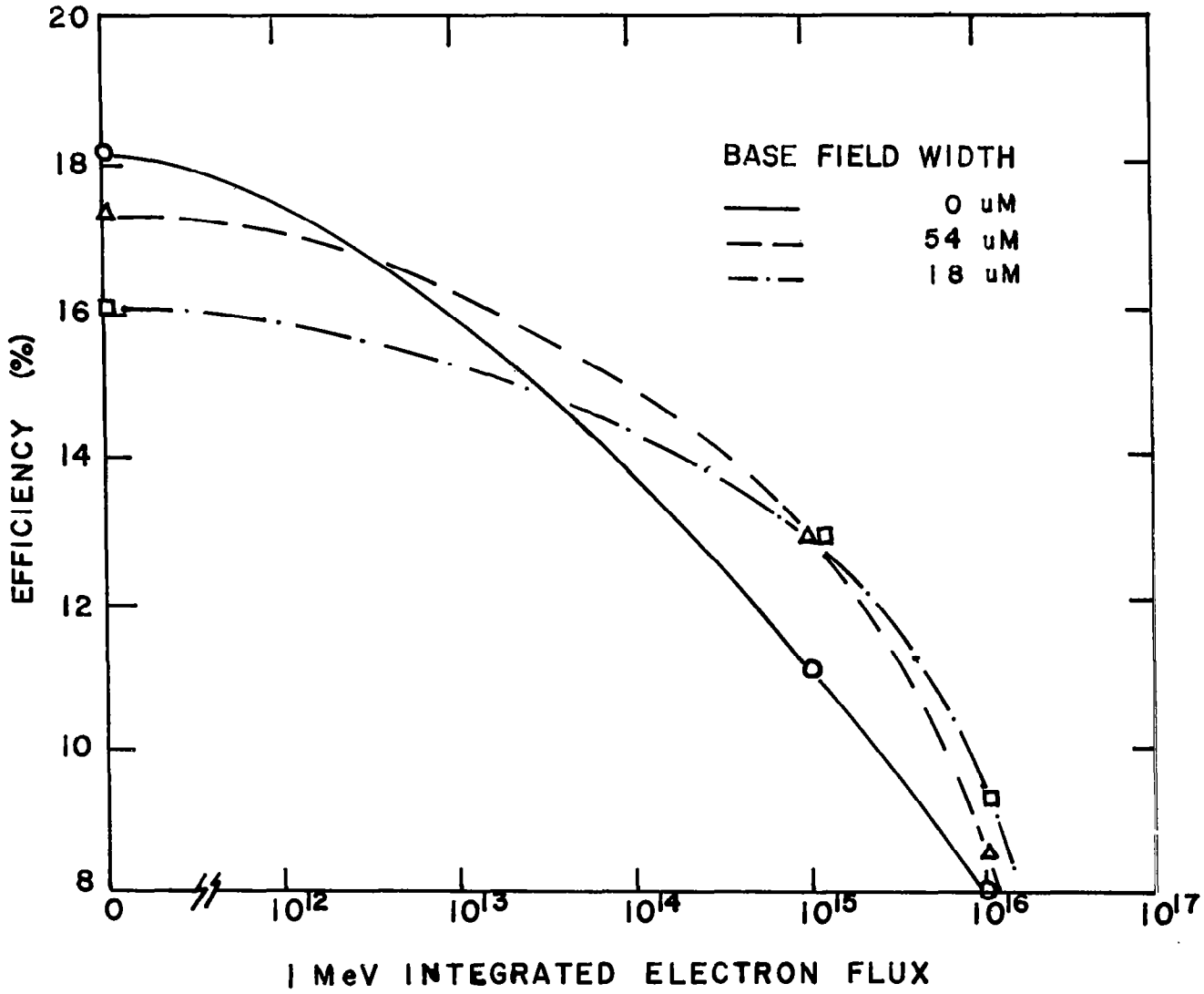

Figure 6. Comparison of Radiation Degradation of Cells With and Without Drift Fields.

5. MEASUREMENT OF MATERIAL PARAMETERS THAT LIMIT THE OPEN-CIRCUIT VOLTAGE IN P-N-JUNCTION SILICON SOLAR CELLS*

F. A. Lindholm and A. Neugroschel
Electrical Engineering Dept.
University of Florida

C. T. Sah
Electrical Engineering Dept.
University of Illinois

ABSTRACT

Because the greatest gains in solar energy conversion efficiency of p-n-junction silicon solar cells will come from increasing the open-circuit voltage V_{OC}, it is important to understand and characterize the material parameters that limit the V_{OC}. Strong experimental evidence exists to support the assertion that either an anomalously large minority-carrier charge storage or an anomalously small minority-carrier lifetime in the quasi-neutral emitter region limits the open-circuit voltage. In this paper, a method is presented for measuring this charge storage and this effective lifetime. In the method, static and transient measurements are analyzed using physical models of the solar-cell characteristics. This analysis yields the emitter charge storage and lifetime, which then can be related to the various physical mechanisms, such as energy band gap shrinkage, that have been proposed earlier as responsible for limiting V_{OC}. The method is illustrated by applying it to several different device structures.

I. INTRODUCTION

This paper describes methods for determining material parameters needed in a mathematical analysis of the electrical characteristics of p-n-junction solar cells. The methods thus furnish information useful to solar-cell design. They provide quantitative procedures to remove certain discrepancies between theory and experiment that were previously unexplained.

As one example of such a discrepancy, the maximum solar energy conversion efficiency seen in fabricated silicon cells is about 25% less than the maximum value predicted by traditional theory [1]. Many speculations have been made on the origin of this discrepancy. In these speculations, attention has focused on the highly-doped emitter region of the solar cell. Energy-band distortion (energy-gap shrinkage) and high recombination rates (low lifetime) in the emitter have been suggested as probable reasons for the discrepancy [2].

---

*Work supported by the NASA Lewis Research Center [NASA Grant NSG-3018] and the Energy Research and Development Administration [ERDA contract E(40-1)-5134].

Various theoretical models have been proposed to describe the gap shrinkage and the carrier lifetime in the emitter. Solar cell performance based on these models has been calculated in various ways, including the use of detailed computer solutions [3] of the Shockley differential equations [4] for a p-n junction. But no explanation of the discrepancy has yet been generally accepted because no experimental justifications have existed to support one speculation over another.

The methods to be described in this paper are aimed to provide such experimental justifications. In the methods, the material parameters of a solar-cell structure are determined after the p-n junction is formed. Special case is taken to separate the contributions to the solar-cell characteristics from the three regions of the device: the quasi-neutral emitter, the quasi-neutral base, and the bulk and surface space-charge regions. This separation enables us to determine the effective recombination lifetimes in the quasi-neutral emitter and base regions and the effective energy-gap shrinkage in the emitter.

The novelty of the methods presented here lies not in the various measurements that are taken. Rather, it lies in the careful and critical application of the underlying device physics to the quantitative analysis of the experimental data.

II. THEORY

To provide a basis for determining material parameters of the emitter and base, the model used to describe the p-n-junction diode must be general enough

(a) to apply to any impurity doping profile of a p-n junction, and

(b) to apply in the presence of position-dependent lifetimes and gap shrinkage in the emitter.

In addition, as will be seen, the model must describe both the static and the transient electrical characteristics.

Recently such a model was proposed [5,6], based on a charge-control analysis of a p-n diode. The model gives two relations for a dark diode that are useful in material-parameter determination:

$$\Delta = Q_{EO}/Q_{BO} = (\tau_{QN} I_{QNO}/Q_{BO}) - 1 \tag{1}$$

and

$$\tau_B/\tau_E = (1/\Delta)[(\tau_B/\tau_{QN})(\Delta+1) - 1] \ . \tag{2}$$

Here Δ is a measure of the gap shrinkage in the emitter and τ_B/τ_E is the ratio of the base to the emitter lifetime. If measurements of the open-circuit current of the illuminated diode are taken, two more relations, independent from equations (1) and (2), can be obtained:

$$\Delta = \frac{\exp[q\delta V_{OC}/kT)}{\tau_B/\tau_{QN}} - 1 \tag{3}$$

and

$$\tau_B/\tau_E = 1/\Delta[\exp(q\delta V_{OC}/kT) - 1] \ . \tag{4}$$

Because equations (3) and (4) are independent of equations (1) and (2), Δ and τ_B/τ_E can be determined in two different ways to check for consistency.

The model that yields equations (1) through (4) describes the contribution to the electrical characteristics that comes from the quasi-neutral emitter and base regions. Thus, I_{QNO} is the saturation current of the dark current-voltage characteristics,

$$I = I_{QNO}[\exp(qV/kT) - 1] \ , \tag{5}$$

due to recombination in the quasi-neutral regions. Similarly, τ_{QN} is the relaxation time of the quasi-neutral regions [5]. This relaxation time determines the natural (force-free) behavior when the device is perturbed by an applied force, such as an impulse current or a voltage step. If the dark current-voltage characteristics are given by equation (5), then the illuminated diode would show an open-circuint voltage V_{OCqn}. If only the quasi-neutral base region contributed to the dark current, then an open-circuit voltage V^B_{OCqn} would result. The difference,

$$\delta V_{OC} = V^B_{OCqn} - V_{OCqn} \tag{6}$$

appears in equations (3) and (4). The coefficients Q_{EO} and Q_{BO} describe the excess minority carrier charges, Q_E and Q_B, stored in the quasi-neutral emitter and base regions:

$$Q_E = Q_{EO}[\exp(qV/kT) - 1] \ , \tag{7}$$

$$Q_B = Q_{BO}[\exp(qV/kT) - 1] \ . \tag{8}$$

If the base doping concentration N_{BB} and the base lifetime τ_B are both independent of position, then

$$Q_{BO} = qn_i^2 L_B/N_{BB} \tag{9}$$

where L_B is the minority-carrier diffusion length of the base.

To indicate a first-order estimate of the effect of gap shrinkage in equations (1)-(4), consider a solar cell in which no gap shrinkage occurs in the emitter. Then, Q_{EO} can be calculated from conventional theory as [7]

$$Q^o_{EO} \simeq qn_i^2 W_E\{N(W_E)\ln[N_{MAX}/N(W_E)]\}^{-1} \tag{10}$$

where N_{MAX} is the maximum majority carrier concentration in the emitter and $N(W_E)$ is the majority carrier concentration at the emitter edge of the junction

space-charge region. An effective energy gap shrinkage ΔE_G in the emitter is thus [2,6]

$$\Delta E_G = kT\ln(Q_{EO}/Q_{EO}^{o}) = kT\ln(\Delta/\Delta^{o}) \tag{11}$$

where $\Delta^{o} = Q_{EO}^{o}/Q_{BO}$. Equation (11) applies only for a cell in which a substantial impurity concentration gradient in the emitter [6].

There are seven parameters in equations (1)-(4): τ_E, τ_B, τ_{QN}, I_{QNO}, δV_{OC}, Q_{BO}, and Q_{EO} (or Δ or ΔE_G). Many of these parameters can be determined experimentally, thereby enabling the determination of Q_{EO}, τ_E, and τ_B.

III. MEASUREMENT TECHNIQUES

The use of equations (1)-(4) for device material-parameter determination requires that certain conditions be met in the design of the experiments. As was noted earlier, the recombination and charging current from the quasi-neutral regions must be made to greatly exceed that from the bulk and surface space-charge regions. The concentrations of excess holes and electrons must be limited to a low injection level throughout the quasi-neutral regions. The effects of series resistance must be made negligible.

In the experimental design, two choices are possible. Either the design must assure that all of the above conditions are met, or procedures must be developed to remove unwanted components from the data. For example, consider the requirement of the quasi-neutral-region currents dominating over the space-charge-region current. To satisfy this requirement, the temperature of the device can be raised, which increases the hole and electron charge stored in the quasi-neutral regions more than that in the space-charge regions. To diminish the contribution of the surface recombination current, a voltage of appropriate polarity and magnitude can be applied to an MOS guard-ring to pinch-off the surface channel. As an alternative to these procedures, the space-charge-region current can be removed from the data using a numerical or graphical procedure. In this procedure, the measured current-voltage characteristic is decomposed into components. One first identifies the bulk and surface space-charge-region component [8] and then subtracts it from the measured characteristic to bare the quasi-neutral-region component, which obeys the dependence given in equation (5).

The details of measuring the parameters in equations (1)-(4) are treated elsewhere [6,7]. Here we outline some possible methods.

3.1 Base τ_B and Q_{BO}

For high-quality silicon solar cells, the X-ray generated [9] short-circuit photocurrent originates mainly within the base region. By combining this with several other measurements [6], one can determine the base lifetime τ_B and the related charge Q_{BO}. Alternatively, transient-capacitance methods [10] provide a technique for determining the lifetime that applies to cells made with solar-grade semiconductors as well as to high-quality silicon cells. The transient-capacitance methods also establish the positional dependence of the lifetime [11].

3.2 Quasi-Neutral-Region Saturation Current I_{QNO}

The parameter I_{QNO} can be obtained either from the static I-V characteristic of a dark diode or from the static I_{SC}-V_{OC} (photo-current versus photo-voltage) characteristic of an illuminated diode. As was discussed earlier, the quasi-neutral-region component of the measured current is enhanced by heating the device, or by applying a voltage to an MOS guard ring; or it is revealed by decomposing the data.

3.3 Quasi-Neutral-Region Relaxation Time τ_{QN}

The response of a p-n diode to any time-varying excitation will contain information about the relaxation time τ_{QN}. Three methods used here to determine τ_{QN} are: junction current recovery [12], open-circuit voltage decay [13], and admittance versus voltage and frequency [14,3(c)]. To assure dominance of the quasi-neutral regions, the temperature of the device may need to be raised. The admittance dependence on voltage discloses the various components of the current, enabling an identification of those coming from the quasi-neutral regions.

3.4 Other Measurement Techniques

The above measurements involve electrical and optical excitations. Other excitation methods [10] could be used with possible advantages. The list given here is meant to be suggestive, not exhaustive.

3.5 Measurement Sensitivity

The measurement sensitivity of the effective gap shrinkage and emitter lifetime depends on the accuracy with which each of the measured quantities--I_{QNO}, τ_{QN}, τ_B, Q_{BO}, V_{OC}, and I_{SC}--are determined. Let Δ_{min} be the minimum value of Δ obtainable for a given accuracy of the measurements. Then, from equations (10) and (11), the minimum determinable value of the gap shrinkage ΔE_{Gmin} is

$$\Delta E_{Gmin} = kT\ell n(\Delta_{min}/\Delta^{\circ})$$

$$= kT\ell n\{[\Delta_{min}L_B/W_E]\ell n[N_{MAX}/N(W_E)]\} \qquad (12)$$

This defines the measurement sensitivity for the emitter gap shrinkage. Combining equations (12) with equations (2) or (4) then yields the measurement sensitivity for the emitter lifetime.

3.6 Increasing the Measurement Sensitivity

Equation (12) implies that the measurement sensitivity depends strongly on $\Delta_{min}(L_B/W_E)$. Increasing the accuracy of the measurements will increase Δ_{min}, and thikening the emitter will increase W_E. The diffusion length L_B can be decreased by using a high doping concentration in the base, above about 10^{18} cm^{-3} for silicon solar cells. Alternatively, the diffusion length can be effectively shortened by adding a collector region, making a transistor-like structure. In such structures, an electrical contact can be made to the base [15].

IV. EXAMPLES

The methods have been applied to various types of p-n structures [6,7] and efforts recently have been focussed on increasing the accuracy with which Q_{EO} and τ_E are determined. In the oral presentation, results will be given for both diffused and ion implanted emitters on a substrate of resistivity of about 0.1 ohm-cm.

V. SUMMARY

Equations (1)-(4) determine the minority-carrier charge storage in the emitter and the emitter lifetime in terms of measurable parameters. To use these relations for device material-parameter determination, the experimental design and the interpretation of data must be based on the device physics of p-n solar cells. Some specific procedures for accomplishing this are indicated in this paper; details are described elsewhere [6,7].

This paper deals with p-n solar cells whose conversion efficiency depends strongly on recombination and transport processes occurring in the emitter. Examples include cells made on low-resistivity substrates of high-quality, single-crystal silicon. For cells made from amorphous or polycrystalline semiconductors, the recombination processes in the junction space-charge region can play a central role in determining the solar energy conversion efficiency. For such cells, the transient-capacitance methods [10] mentioned earlier can determine the recombination parameters describing the space-charge region.

The methods of this paper are relevant to the engineering design of p-n solar cells. They help to discover and describe the fundamental electronic mechanisms influencing solar-cell efficiency [2], and to provide physics-based mathematical models that incorporate these mechanisms into solar-cell design. The methods yield the minority-carrier charge storage in the emitter and the lifetimes in the emitter and base. If a physical model for the gap shrinkage and the recombination rates is correct, it must predict solar-cell electrical characteristics which are consistent with the experimentally determined values of the emitter minority-carrier charge storage and lifetimes. Computer solution of the Shockley differential equations (3) permits a study of physical models of any degree of complexity, containing various combinations of the fundamental electronic mechanisms [2] that could influence the solar-cell efficiency. Comparison of the results of experiments with those of computer simulation [3] may then disclose the dominant fundamental mechanisms. The ability to determine these mechanisms enables study of their relation to the fabrication processes used in solar-cell manufacturing, which would lead toward a systematic improvement of cell efficiency.

The recombination and transport processes occurring in the emitter of a bipolar junction transistor can limit the achievable maximum current gain and can influence also the frequency and transient response. The methods treated in this paper thus apply not only to p-n solar cells, but also to p-n diodes [7] and to junction transistors [15].

REFERENCES

1. Brandhorst, H.W., Jr., "Current Status of Silicon Solar Cell Technology," TECHNICAL DIGEST, 1975 INT. ELECTRON DEVICES MEETING (75CH1023-1 ED), Dec. 1975, pp. 331-338.

2. Lindholm, F.A. and Sah, C.T.,"Fundamental Electronic Mechanisms Limiting the Performance of Solar Cells," IEEE TRANS. ELECTRON DEVICES, April 1977.

3. (a) Fossum, J.G., "Computer-aided Numerical Analysis of Silicon Solar Cells," SOLID-STATE ELECTRONICS, Vol. 19, 1976, pp. 269-277; Fossum, J.G., "Numerical Analysis of Back-Surface-Field Silicon Solar Cells," TECH. DIGEST 1975 IEDM (75CH1023-1 ED), 1975, pp. 339-342.

   (b) Dunbar, P.M. and Hauser, J.R., "Efficiency of Silicon Solar Cells as a Function of Base Layer Resistivity," RECORD ELEVENTH PHOTOVOLTAIC SPECIALISTS CONF. (75CH0948-OED), 1975, pp. 13-18; Dunbar, P.M. and Hauser, J.R., "A Study of Efficiency in Low Resistivity Silicon Solar Cells," SOLID-STATE ELECTRONICS, Vol. 19, 1976, pp. 25-102.

   (c) For another method of numerical analysis, which is based on the equivalent-circuit model, see Maes, H. and Sah, C.T., "Application of the Equivalent-Circuit Model for Semiconductors to the Study of Au-doped p-n Junctions under Forward Bias," IEEE TRANS. ELECTRON DEVICES, Vol. ED-23, Oct. 1976.

4. Shockley, W., "The Theory of p-n Junctions in Semiconductors and p-n Junction Transistors," BELL SYS. TECH. J., Vol. 28, July 1949, pp. 435-489.

5. Lindholm, F.A. and Sah, C.T., "Normal Modes of Semiconductor pn Junction Devices for Material-Parameter Determination," J. APPL. PHYS., Vol. 47, Sept. 1976, pp. 4203-4205.

6. Lindholm, F.A.; Neugroschel, A.; Sah, C.T.; Godlewski, M.P. and Branhorst, H.W., Jr., "Methodology for the Experimental Determination of Gap Shrinkage and Lifetimes in the Emitter and Base of p-n-Junction Solar Cells and Other p-n Junction Devices," IEEE TRANS. ELECTRON DEVICES, April 1977; also RECORD OF TWELFTH PHOTOVOLTAIC SPECIALISTS CONF., Nov. 1976.

7. Neugroschel, A.; Lindholm, F.A. and Sah, C.T., "A Method for Determining the Emitter and Base Lifetimes in pn-Junction Diodes," IEEE TRANS. ELECTRON DEVICES, June 1977.

8. Sah, C.T., "Effect of Surface Recombination and Channel on p-n Junction and Transistor Characteristics," IRE TRANS. ON ELECTRON DEVICES, Vol. ED-9, Jan. 1962, pp. 94-108.

9. Lamneck, J.H., Jr., "Diffusion Lengths in Silicon Obtained by an X-ray Method," NASA TM X-1894, Oct. 1969.

10. (a) Sah, C.T.; Forbes, L.; Rosier, L.L. and Tasch, A.F., Jr., SOLID-STATE ELECTRONICS, Vol. 13, June 1970, pp. 759-788.

(b) Sah, C.T., "Bulk and Interface Imperfections in Semiconductors," SOLID-STATE ELECTRONICS, 1976.

(c) Sah, C.T., "Detection of Recombination Centers in Solar Cells from Capacitance Transients," IEEE TRANS. ELECTRON DEVICES, Feb. 1977.

11. Sah, C.T. and Neugroschel, A., "Concentration Profiles of Recombination Centers in Semiconductor Junctions Evaluated from Capacitance Transients," IEEE TRANS. ON ELECTRON DEVICES, Vol. ED-23, Sept. 1976.

12. Kingston, R.H., "Switching Time in Junction Diodes and Junction Transistors," PROC. IRE, Vol. 42, May 1954, pp. 829-834.

13. Lederhandler, S.R. and Giacoletto, L.J., "Measurement of Minority Carrier Lifetime and Surface Effects in Junction Devices," PROC. IRE, Vol. 43, April 1955, pp. 477-483.

14. Shockley, W., ELECTRONS AND HOLES IN SEMICONDUCTORS, Van Nostrand, Co., New York, 1950, pp. 313-318.

15. Neugroschel, A.; Lindholm, F.A. and Sah, C.T., "Experimental Determination of Emitter Lifetime and Band-edge Distortion in Transistors," IEEE TRANS. ELECTRON DEVICES, accepted for publication.

6. SURFACE RECOMBINATION VELOCITY AND DIFFUSION LENGTH OF MINORITY CARRIERS IN HEAVILY DOPED SILICON LAYERS

Harry C. Gatos, Masaharu Watanabe and Geri Actor
Massachusetts Institute of Technology
Cambridge, Massachusetts

ABSTRACT

Quantitative analysis of the electron beam-induced current and the dependence of the effective diffusion length of the minority carriers on the penetration depth of the electron beam were employed for the analysis of the carrier recombination characteristics in heavily doped silicon layers. The analysis is based on the concept of the effective excitation strength of the carriers which takes into consideration all possible recombination sources. Two-dimensional mapping of the surface recombination velocity of P-diffused Si layers will be presented together with a three-dimensional mapping of minority carrier lifetime in ion-implanted Si. Layers heavily doped with As exhibit improved recombination characteristics as compared to those of the layers doped with P.

INTRODUCTION

The recombination of photo-generated excess carriers in the bulk and the surface prior to their collection is an important factor in photovoltaic solar energy conversion. In the bulk, lattice defects (point, line and plane defects) enhance significantly the recombination process. The surface, being essentially a giant lattice defect, exhibits an inherently high recombination velocity. An aspect of the combination process which has not been pursued in the past, primarily because of the lack of experimental approaches, is the variation of the lifetime of the minority carriers on a microscale. In view of the pronounced compositional inhomogeneities encountered in silicon single crystals (ref. 1) mean lifetime values are not necessarily meaningful in assessing the recombination processes in solar cells and other devices.

In the present investigation theoretical models and experimental approaches employing scanning electron microscopy were developed for the determination of surface recombination velocity and its variation on a microscale and for three-dimensional mapping of the lifetime of minority carriers in heavily doped silicon layers.

MODEL FOR THE DETERMINATION OF SURFACE RECOMBINATION VELOCITY

The electron-hole excitation by an electron beam can be approximated by a steady-state point source with an excitation strength, G, located at a distance, ξ, beneath the surface. Using Hackett's results (ref. 2) based on this

assumption, it was shown (ref. 3) that for an n-type semiconductor the total steady-state concentration of excess holes can be expressed as:

$$\Delta p(\xi) = (GL_b^2/D)\{1-[S/(S+1)]\exp(-\xi/L_b)\} \qquad (1)$$

where L_b is the bulk diffusion length of the minority carriers, $S = s\tau_b/L_b$; s is the surface recombination velocity, and τ_b is the bulk lifetime of the minority carriers.

Under steady-state conditions, $\Delta p(\xi)$ can be related to the measured L_{eff}:

$$\Delta p(\xi) = G\tau_{eff} \quad \text{and} \quad L_{eff} = (D\tau_{eff})^{1/2} \qquad (2)$$

where τ_{eff} is the effective steady-state minority-carrier lifetime; from eqs. (1) and (2) one obtains:

$$L_{eff}^{\ 2} = L_b^2\{1-[S/(S+1)\exp(-\xi/L_b)\} \qquad (3)$$

Thus, by plotting $\ln[1-(L_{eff}/L_b)^2]$ vs. ξ ($\xi \simeq V^{1.7}$, where V is the accelerating voltage of the electron beam) $S/(S+1)$ is obtained from the intercept of the straight line with the ordinate. L_{eff} for each penetration depth (i.e., accelerating voltage) is determined from the dependence of the electron beam-induced current, I, as a function of distance, x, from the current collecting potential barrier according to

$$I \simeq \exp(-x/L_{eff}) \qquad (4)$$

L_b is taken as an adjustable parameter.

This approach was applied to GaAs and the surface recombination velocity values were found to be in excellent agreement with those obtained by other techniques. Typical results are shown in Fig. 1.

In the case of Si the above approach was developed further on a more quantitative basis.

It is reasonable to assume that for excitation depths $\xi \lesssim L_b$ most of the recombination on the surface takes place near the excitation point and, thus, the total number of excess carriers is determined by the recombination on the surface near the excitation point. Actually eq. (1) means that the total number of excess carriers is reduced by an amount of $\{G\tau S/(1+S)\}\exp(-\xi/L_b)$ due to the increased recombination at the surface ($\tau = L_b^2/D$ is substituted in eq. 1).

The reduction of the excess carriers due to surface recombination can be taken as an apparent reduction of the generation rate (ref. 4). Thus, we can introduce the concept of an effective generation strength, G_{eff}, which is expressed as (ref. 5):

$$G_{eff} = G\{1 - \frac{S}{1+S}\exp(-\xi/L_b)\} \qquad (5)$$

For shallow excitation:

$$\frac{\partial}{\partial \xi} G_{eff} = \frac{G}{L_b} \frac{S}{1+S} \exp\left(-\frac{\xi}{L_b}\right) \tag{6}$$

and for surface excitation, $\xi = o$:

$$\frac{\partial}{\partial \xi} G_{eff}\Big|_{\xi=o} = \frac{G}{L_b} \frac{S}{1+S} \tag{7}$$

Since:

$$G_{eff}\Big|_{\xi=o} = \frac{G}{1+S} \tag{8}$$

and $S=s\,\tau/L_b$, $L_b = \sqrt{D\tau}$ eq. (7) becomes

$$\frac{\partial}{\partial \xi} \ln G_{eff}\Big|_{\xi=o} = \frac{s}{D} \tag{9}$$

Since the excitation strength is proportional to electron beam-induced current ($G_{eff}=kI$, where k is a geometric proportionality factor) we have:

$$\frac{\partial}{\partial \xi} \ln I\Big|_{\xi=o} = s/D \quad \text{or} \quad s = D \frac{\partial}{\partial \xi} \ln I\Big|_{\xi=o} \tag{10}$$

It is apparent that eq. (10) provides a new approach to the determination of the surface recombination velocity. The validity of eq. (10) was proven through exact current equations and for defined geometrics of the p-n junction (ref. 5).

EXPERIMENTAL

To determine the effective diffusion length and surface recombination velocity silicon diodes were designed and constructed (ref. 6) with heavily diffused layers adjacent to the p-n junctions as shown schematically in Fig. 2. The heavily diffused layers were doped with P and also with As at a level of 10^{19} to $10^{20}/cm^3$. Phosphorus was diffused for a phosphosilicate glass and by conventional transport from a $POCl_3$ source; diffusion took place at 1050° for 30 minutes. Arsenic was diffused from an arsenosilicate glass at 1000°C for 15 minutes.

The EBIC and the electron beam current were measured using an electrometer the output of which was recorded. In order to analyze the results under constant excitation the measured EBIC was normalized by dividing it be keV.I_B, where keV and I_B are the electron beam energy and the electron beam current, respectively. The effective diffusion length was determined from eq. (4) and the surface

recombination velocity from eq. (10) using a computer program.

RESULTS AND DISCUSSION

Two-Dimensional Mapping of the Surface Recombination Velocity

The EBIC in a phosphorus diffused diode was measured for energies of 5, 6, 7, 8.1, 9, and 10.4 keV, at the locations shown in Fig. 3. The EBIC intensity readings were reduced to surface recombination velocities as pointed out above. Figure 4 shows the normalized EBIC for an electron beam energy of 5 keV. Figure 5 shows the surface recombination velocity at positions corresponding to those of Fig. 4. Along a scratch shown in Fig. 3, an EBIC minimum or valley results, as seen in Fig. 4. This region corresponds to the surface recombination velocity maximum or ridge in Fig. 5. The short effective lifetime corresponding to the EBIC valley is caused by defects introduced by the scratch; these defects apparently lead also to the high surface recombination velocity. A complex distribution of the defects (EBIC valley is much wider than the scratch) is reflected in the complex distribution of the surface recombination velocity; low surface recombination velocity is observed adjacent to the high surface recombination velocity ridge even though the corresponding EBIC values are in a valley. This result can be explained as follows: if a lifetime gradient exists in the region of low surface recombination valley, it reduces the measured value of the surface recombination velocity although the EBIC is still at low level. Negative surface recombination velocity, occasionally observed in Fig. 5, is due to the same phenomena.

The spacial resolution of the surface recombination velocity in Fig. 5 is about 1 μm, whereas that of EBIC in Fig. 4 is about 0.5 μ. Actually, it is possible to obtain a spacial resolution in surface recombination velocity as small as the excitation volume (0.3 μm diameter at 5 keV). On the other hand, an 0.8 μm difference in the depth of the damage could be distinguished. Even better resolution in depth profiling of lifetime is possible.

Effective Diffusion Length and Surface Recombination Velocity in Heavily P-Doped and As-Doped Layers

The normalized EBIC 25 and 75 μm away from the p-n junction and the effective diffusion length are plotted as a function of the electron beam energy for the P-doped layer ($POCl_3$ source) in Fig. 6. In determining L_{eff}, EBIC measurements taken at distances other than those shown in Fig. 6 were also used. It is seen that L_{eff} decreases for electron beam energies below about 15 keV and remains essentially constant for energies above 15 keV. The normalized EBIC also decreases for electron beam energies below 15 keV. For higher electron beam energies the normalized EBIC goes through a maximum and then decreases. This behavior cannot be analyzed at present. The surface recombination velocity was determined from the EBIC slope in the electron beam energy region below 15 keV and was found to be 1×10^3 cm/sec.

The normalized EBIC 25 and 35 μm away from the p-n junction and the effective diffusion length for the As-doped layer are plotted in Fig. 7 as a function of the electron beam energy. It is seen that L_{eff} decreases for electron beam energies 5 to 7 keV and then increases; similarly, the EBIC decreases for electron beam energies 5 to 6 keV and then increases. The normalized EBIC exhibits

three distinct maxima at electron beam energies of about 9, 20, and 30 keV. The effective diffusion length exhibits only on occasions maxima corresponding to the maxima of the EBIC; this discrepancy is probably due to the presence of localized high or low recombination regions. The effective diffusion length depends on the recombination characteristics of relatively large regions whereas the EBIC depends to a large extent on the recombination characteristics in the vicinity of the excitation point.

The decrease of L_{eff} and EBIC with increasing penetration depth is most interesting; it shows that the minority carrier lifetime is shorter in the region below the surface than on the surface and that the apparent surface recombination velocity is negative. Similar behavior was observed in Si layers in which 55 keV He ions were implanted (ref. 5). In that case this behavior was attributed to the fact that the maximum damage due to implantation was very near the surface (but not at the surface); the effective diffusion length in the damaged region became shorter than in the surface.

In the present case it is believed that a similar situation prevails: In the P-doped layers from a $POCl_3$ source, a high concentration of diffusion-induced surface defects is present which extends below the surface causing a pronounced decrease in L_{eff} at the surface (high surface recombination velocity). In the As-doped layers the concentration of diffusion-induced surface defects is relatively low; furthermore, the defect concentration appears to be higher below the surface than in the surface; thus, the carrier recombination rate is much greater below the surface than in the surface, leading to a negative apparent recombination velocity. The pronounced difference in the concentration of diffusion-induced defects in the two cases is shown in Fig. 8. In this respect it is of interest to point out that in the P-doped layers prepared with the spun-on technique the concentration of the diffusion-induced defects was found to be much smaller than in the P-doped layers prepared by using a $POCl_3$ source; consistent with the above, the surface recombination velocity in the former was found to be 15 cm/sec as compared to a value of 10^3 cm/sec determined in the latter.

Another factor which affects the surface recombination velocity is the internal electric field associated with the distribution profile of the donors (ref. 6); in the P-doped layers from a $POCl_3$ source the electric field is approximately 10^3 V/cm. This field pulls the minority carriers from the surface leading to an apparent decrease in surface recombination velocity. Thus, the measured surface recombination velocity is modified by two opposite effects: an increase due to diffusion-induced defects and a decrease due to the internal electric fields.

SUMMARY

Excitation of electron-hole pairs by a finely focused electron beam makes it possible to investigate the recombination characteristics of the minority carriers with high spacial resolution. The effective excitation strength (effective lifetime) is a concept permitting the determination of surface recombination velocities and of lifetime profiles. Two-dimensional mapping of the surface recombination velocity was demonstrated for heavily diffused silicon

surfaces. Also a three-dimensional mapping of the recombination characteristics in the crystal is possible. Significant recombination inhomogeneities were observed. Although they can be related in part to defect inhomogeneities, a further study of the origin of such inhomogeneities is considered essential for a quantitative understanding of recombination processes in silicon solar cells.

REFERENCES

1. A. Murgai, H.C. Gatos and A.F. Witt, J. Electrochem. Soc. 123, 224 (1976).

2. W.H. Hackett, J. Appl. Phys. 43, 1649 (1972).

3. L. Jastrzebski, J. Lagowski and H.C. Gatos, Appl. Phys. Letters 27, 537 (1975).

4. D.B. Wittry and D.F. Kyser, J. Appl. Phys. 38, 375 (1967).

5. M. Watanabe, G. Actor and H.C. Gatos, submitted to Trans. I.E.E.E.; also in "Technical Digest, International Electron Device Meeting", Electron Devices Society of I.E.E.E., 1976, p. 51.

6. M. Watanabe, G. Actor and H.C. Gatos in "Proceedings of the International Symposium on Solar Energy", edited by J.B. Berkowitz and I.A. Lesk, Electrochemical Society, Princeton, N.J., 1976, p. 283.

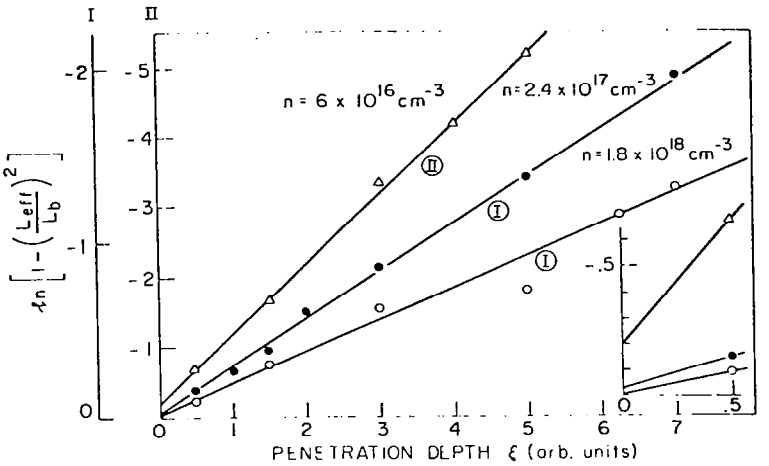

Fig. 1. $\ln[1-(L_{eff}/L_b)^2]$ as a function of the penetration depth of the electron beam, in arbitrary units. Curve I corresponds to the expanded scale, (I), curve II corresponds to the scale (II).

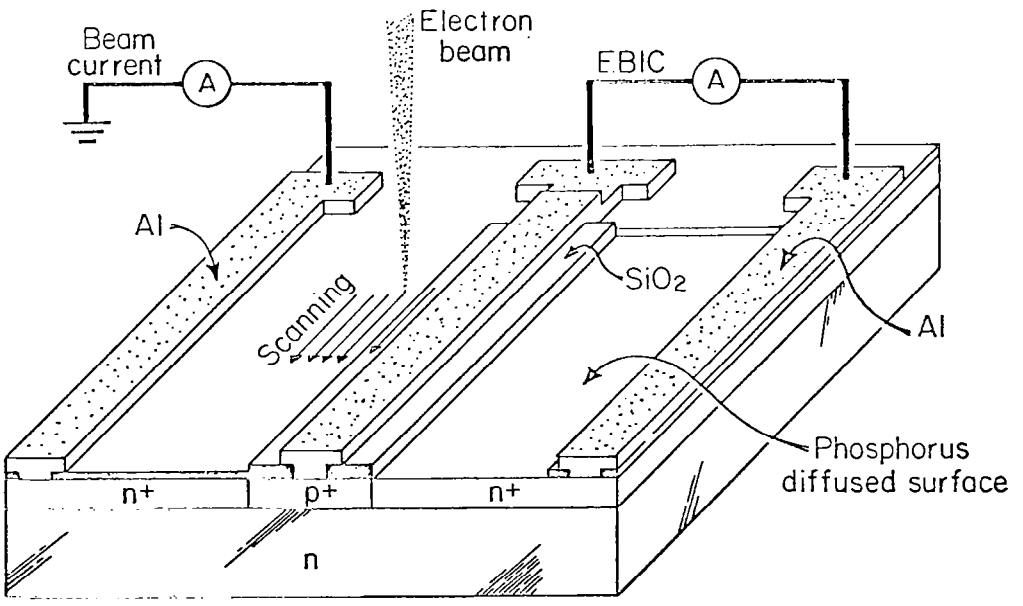

Fig. 2. Schematic representation of the silicon diode structure with heavily P-diffused surfaces

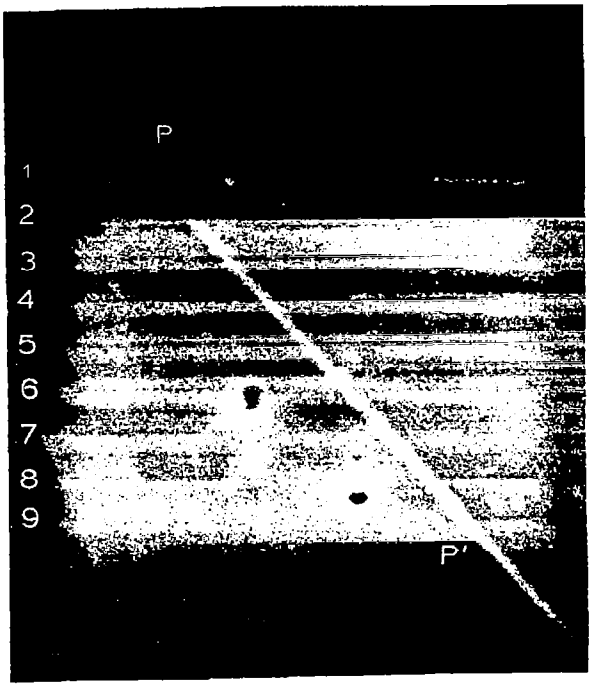

Fig. 3. Secondary electron image of scanning paths of electron beam. Numbers indicate individual scans (carried out from left to right). Distance from scan 1 to 9 is 30 μm; PP' indicates position of scratch.

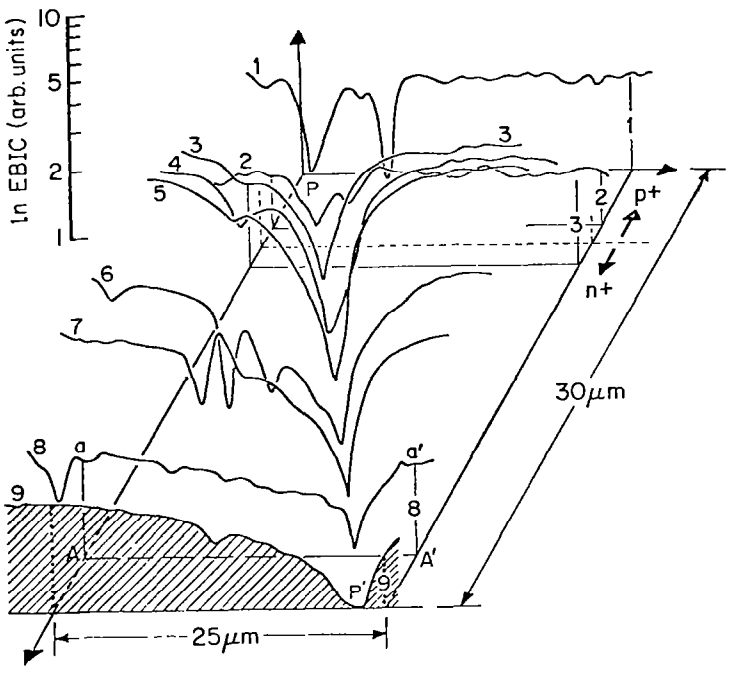

Fig. 4. Mapping of normalized EBIC (z-axis) of p-diffused surface vs. scanning position (on x-y plane). For example, scan AA' (or 3) corresponds to scan No. 3 in Fig. 3 and leads to EBIC variations represented by curve aa'. Relative values of EBIC for each curve can be obtained using scale in figure. P and P' on the figure correspond to the P and P' positions on Fig. 3.

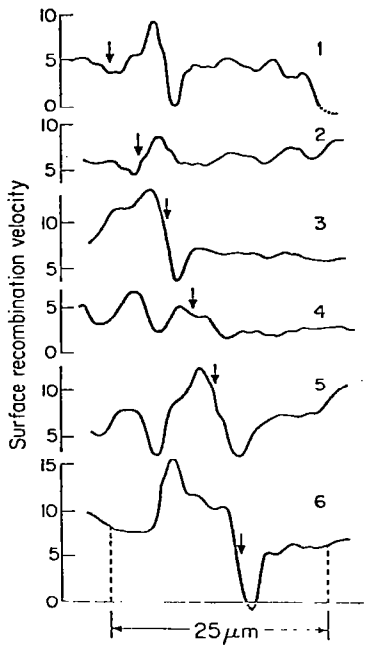

Fig. 5. Surface recombination velocity profile of p-diffused silicon surfaces. The six curves correspond to scans 1 to 6 in Fig. 3 (and also to curves 1 to 6 in Fig. 4). Vertical scale x 10^2 cm/sec is displaced for each curve. The relative changes in surface recombination velocity for each scan can be obtained using scale of curve 6. Arrows indicate the position of EBIC minima in Fig. 4.

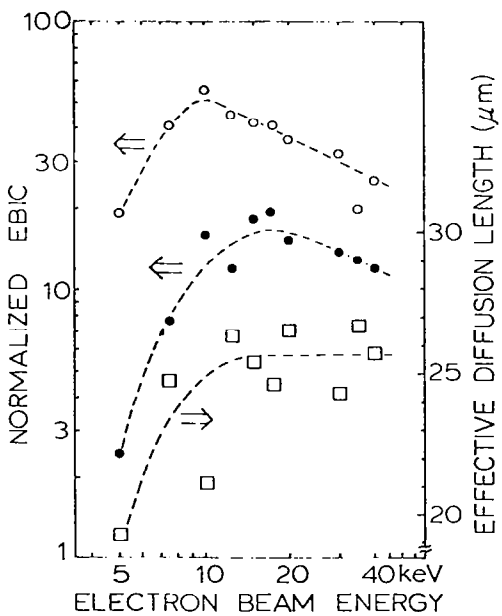

Fig. 6. Normalized EBIC and effective diffusion length of minority carriers as a function of the electron beam energy for a heavily P-doped Si layer; ○ ● 25 and 75 μm away from the p-n junction, respectively.

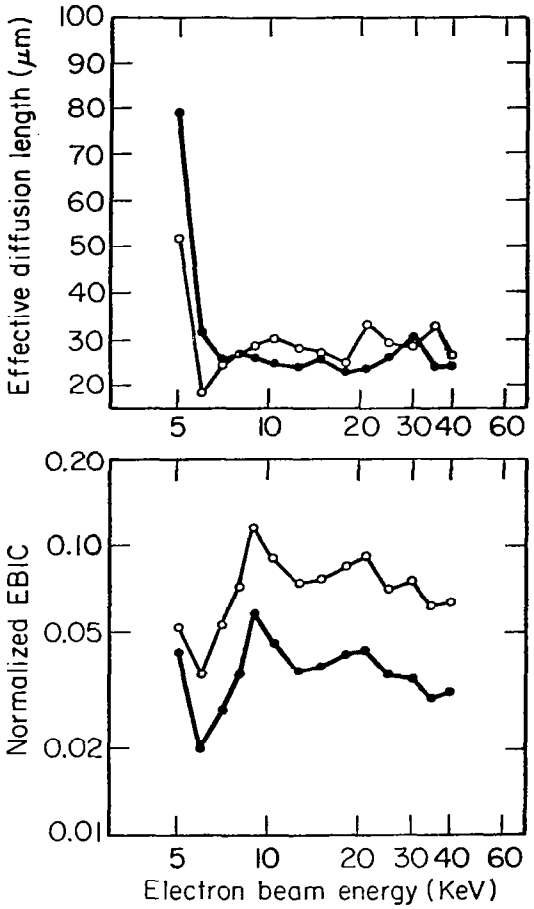

Fig. 7. Normalized EBIC and effective diffusion length of minority carriers as a function of the electron beam energy for a heavily As-doped layer; ○ ● 25 and 35 μm away from the p-n junction, respectively.

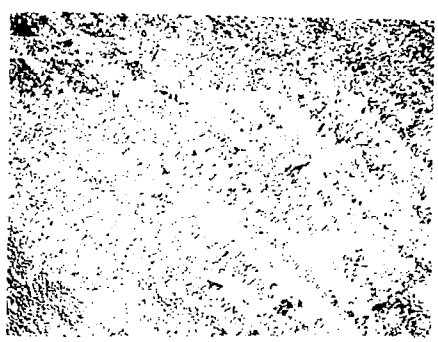

(a)

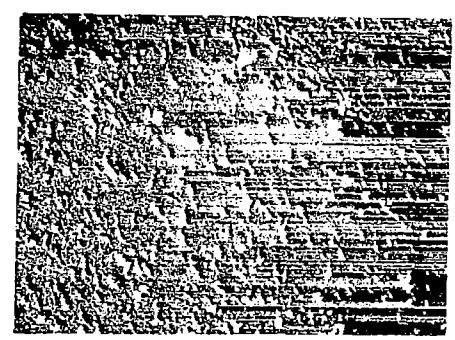

(b)

Fig. 8. Etched (with modified CP-4) silicon layer heavily doped with (a) P and (b) As. Note pronounced difference in concentration of diffusion-induced defects. Magnification 60X.

7. IMPURITY CONCENTRATIONS AND SURFACE CHARGE DENSITIES ON THE HEAVILY DOPED FACE OF A SILICON SOLAR CELL

I.Weinberg
NASA Lewis Research Center

Lon Hsu
Wayne State University

Increased solar cell efficiencies can be attained by reduction of surface recombination and variation of impurity concentration profiles at the n^+ surface of silicon solar cells. To achieve these goals it is necessary to employ diagnostic techniques which can directly evaluate the effects of specific materials preparation methodologies on surface and near surface concentrations. In this respect, it has previously been shown (ref.1) that the MOS C-V technique yields quantitative results for near surface ionized impurity concentrations (within 10 Å of the n^+ surface) and the charge in oxide and surface states at the silicon-oxide interface. In the present case, our purpose lies in demonstrating that the MOS C-V method, when combined with a bulk measurement technique, yields more complete concentration data than is obtainable be either method alone. Specifically new solar cell MOS C-V measurements are combined with bulk concentrations obtained by a successive layer removal technique (SLRT) utilizing measurements of sheet resistivity and Hall coefficient (ref. 2). At the high dopant concentrations encountered near the n^+ surface ($N \approx 10^{20} cm^{-3}$) the MOS C-V technique determines concentrations much closer to the surface than does the SLRT method (references 1 & 2). Hence combination of the two methods should result in data extending from within the bulk n^+ region up to and including the solar cell surface.

The methods used in sample preparation are outlined in

figure 1. The starting material was a 2x2 cm, 250 micrometers thick wafer of 10 ohm-cm p-type silicon. The n^+p junction was formed by heating at 848 °C for 30 minutes in $POCl_3$. The wafer was then scribed and cleaved into two 1x2 cm wafers for use in the two types of measurement. Additional sample preparation details are shown in the figure.

The MOS-solar cell configuration is shown in figure 2. The anti-reflection coating was 640 Å thick while the MOS gate consisted of a circular gold dot 2.54×10^{-2}cm in diameter. DC voltage was applied between the gate and n^+ surface contact, capacitance being measured across the gate and contact. Also shown in figure 2 are the equivalent circuit for the solar cell MOS capacitance and the relations used in obtaining N, the ionized dopant concentrations from the C-V measurements. In the figure, E_s is the dielectric permittivity of silicon, A is area of the metal gate, R_o and R_s represent losses in the oxide and semiconductor respectively and C_m, C_o and C_{sc} are the measured, oxide and space charge capacitances respectively. C_{HF} is the capacitance formed by series connection of C_o and C_{sc}. The methods used in determining the parameters of figure 2 are given in reference 1. The solar cell C-V data is shown in figure 3 together with the voltage ranges which encompass the semiconductor space charge accumulation, depletion and inversion regions.

To obtain N, it is necessary to plot $1/C_{HF}^2$ against gate voltage as shown in figure 4. However, concentrations are obtainable from the data of figure 4 only if the space charge region is in depletion,(ref.3) and if the depletion width W is at least two extrinsic Debye lengths from the surface (references 4, 5 & 6). In the present case, the extrinsic Debye length is 4.94 Å. The extent of the depletion region and the limiting distances from the surface are shown in figure 4. From the slope between data points,of the figure, a plot of concentrations close to the surface is obtained and shown in figure

5. The limiting distance (≈ 10 Å) is close enough to the surface so that the concentration obtained (1.4×10^{20} cm^{-3}) is assumed to be a surface parameter.

In addition to ionized impurity concentrations, the MOS C-V method was used to obtain N_s , the density of charge in oxide and surface states at the silicon-oxide interface. This is obtained from the flat band voltage shift (V_{fb}) and the relations shown in figure 6 (references 1 & 7).

The SLRT measurements were carried out on the second diffused wafer using the configuration shown in figure 7. The circular pattern shown was deposited on the n^+ surface by a photoresist technique and then etched to a depth of approximately 10 micrometers. The shaded portions are regions where the silicon has been etched away. The resultant mesa is in the form of a circular disc with electrical contacts made at its periphery by the remaining silicon in the areas marked 1 through 4. Successive layers are removed in 200 Å steps by anodic oxidation and etching (ref. 8). Sheet resistivities ρ_s and sheet Hall coefficients R_s are measured before and after removal of each layer. As shown in the figure, the change in the quantities R_s/ρ_s^2 and $1/\rho_s$ resulting from a single layer removal are used to determine charge concentrations N(Z) and mobilities $\mu(Z)$ for the specific layer removed (ref. 2). The SLRT method results in average values for N(Z) and μ (Z) in each layer. Hence there is some uncertainty in the determination of Z. In any event, Z is arbitrarily taken at the center of each layer. The combined results for the two measurement techniques are shown in Table 1. It is seen from the table that N(Z) obtained by the MOS C-V method agrees with the value obtained at 100 Å by the SLRT method. In addition the mobilities obtained behave in a manner which is consistent with the observed variation in active charge concentration.

In conclusion, it is noted that the MOS C-V method yields

bulk concentration data which approaches closer to the surface as the concentration increases. In particular, at the very high dopant concentrations, encountered at the surface of the n^+ region the technique yields data at distances which are only a few Angstroms removed from the surface. Hence, in addition to yielding surface parameters for the silicon solar cell, the C-V method extends, up to the cell surface, concentration data obtained by bulk profiling techniques such as the SLRT method used, as an example, in the present case.

REFERENCES

1. Weinberg, I.,"Application of the MOS C-V Technique to Determine Impurity Concentrations and Surface Parameters on the Diffused Face of Silicon Solar Cells." Proceedings of the 11th IEEE Photovoltaic Specialists Conference, 1975, pp. 78-81.

2. Buehler, M.G.," A Method for Determining the Charge Density and Mobility in Thin Semiconducting Layers, " Ph.D. Thesis, Stanford University, 1966, University Microfilms Inc, Ann Arbor, Mich.

3. Brews, J.R.," Correcting Interface State Error in MOS Doping Profile Determinations," Journal of Applied Physics, vol. 44 1973, pp.3223-3231.

4. Johnson, W.C & Panousis, P.T., "The Influence of Debye Length on the C-V Measurement of Doping Profiles, " IEEE Transactions on Electron Devices, vol. ED-18, 1971, pp. 965-973.

5. Leblanc, A.R., Kleppinger, D.E. and Walsh, J.P., "A Limitation of the Pulsed Capacitance Technique of Measuring Profiles," Journal of the Electrochemical Society vol. 119, 1972, pp. 1068-1071.

6. Zeigler, K., Klausman,E. and Kar,S., "Determination of the Semiconductor Doping Profile Right up to its Surface Using the MIS Capacitor," Solid State Electronics, vol. 18, pp. 189-198.

7. Goetzberger, A., and Sze, S.M., "Metal-Insulator Semiconductor Physics," Applied Solid State Science, vol. 1, 1969, pp. 153-238.

8. Tannenbaum, E., "Detailed Analysis of Thin Phosphorous Diffused Layers in p-Type Silicon," Solid State Electronics, vol. 2, 1961, pp. 123-132.

TABLE I: SUMMARY OF RESULTS

TECHNIQUE	PARAMETER	NUMERICAL VALUES				
	Z(Å)	0	$10 < Z < 20$	100	300	500
MOS C-V	$N_s(cm^{-2})$	$(1.3\pm0.1)x10^{13}$	-------	--------	--------	--------
	N(Z) $cm^{-3}x10^{-20}$	1.4 (EXTRAP.)	1.4 ± 0.1	--------	--------	--------
SUCCESSIVE LAYER REMOVAL		----------	-------	1.3 ± 0.2	1.8 ± 0.3	0.85 ± 0.1
	μ cm^2/V-sec	----------	-------	50.1 ± 3	50.1 ± 2	60 ± 3

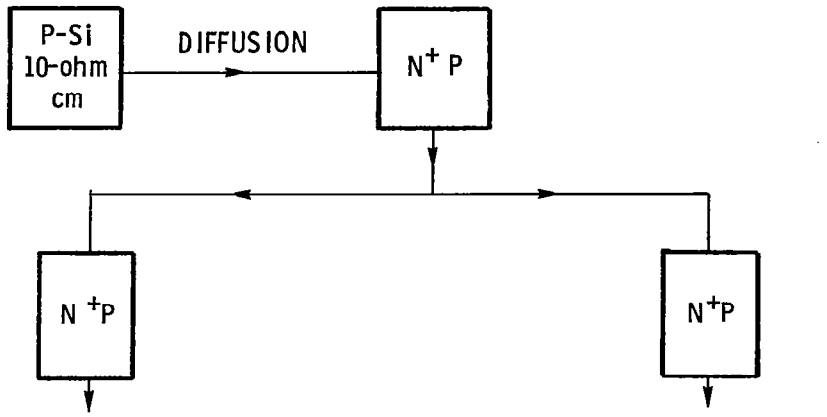

MOS C-V

SOLAR CELL CONTACTS
A-R COATING & MOS GATE
C-V MEASUREMENTS
SURFACE CONCENTRATIONS

LAYER REMOVAL

BACK CONTACT ONLY
SUCCESSIVE LAYER REMOVAL
HALL & RESISTIVITY MEAS.
NEAR SURFACE CONCENTRATIONS

Figure 1. - Sample preparation and measurement techniques.

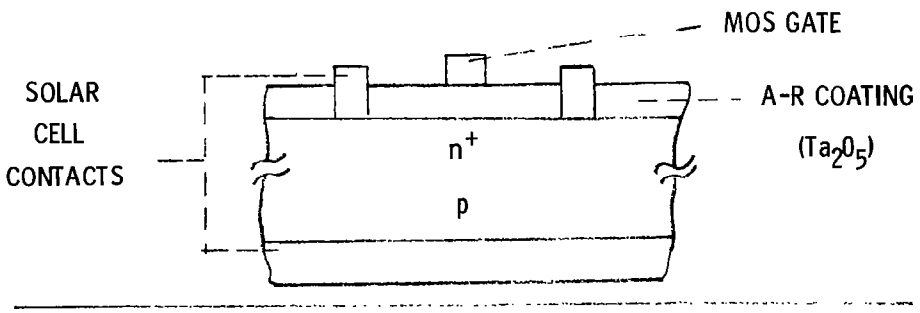

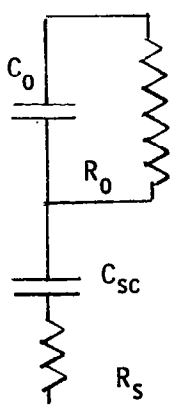

$$C_M = \frac{C_{sc}\left[1+(\omega R_0)^2 C_0(C_{sc}+C_0)\right]}{(1-\omega^2 C_{sc}C_0R_0R_s)^2 + \left[\omega C_{sc}(R_0+R_s) + \omega C_0R_0\right]^2}$$

$$C_{HF} = (C_0C_{sc})/(C_0 + C_{sc})$$

$$N = (2/q\,E_sA^2)\,(d^1/C_{HF}^2)^{-1}$$

Figure 2: Solar Cell-MOS Device Configuration and High Frequency Equivalent Circuit.

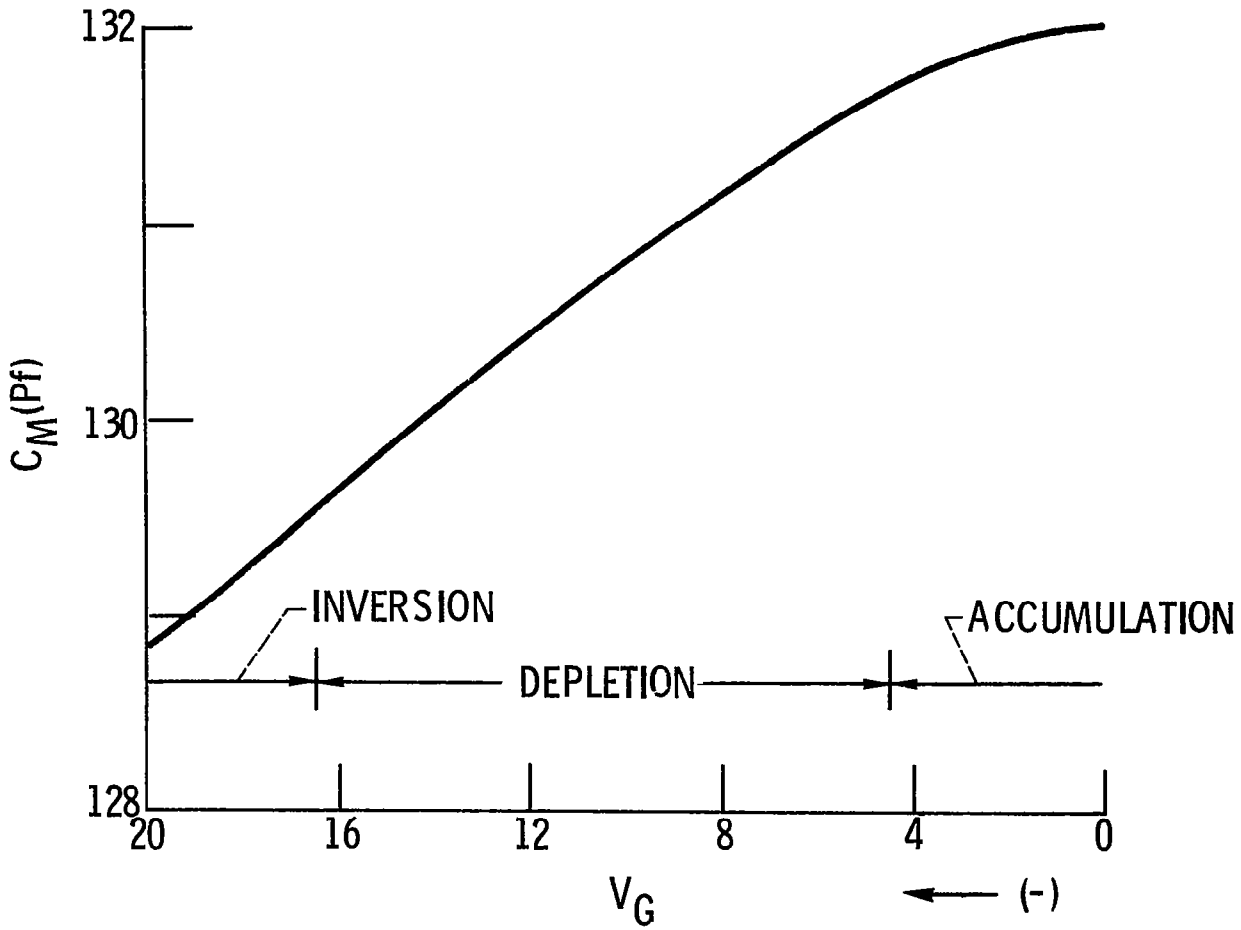

Figure 3. - Solar cell MoS C-V curve C_M is measured capacitance, V_G is DC gate voltage.

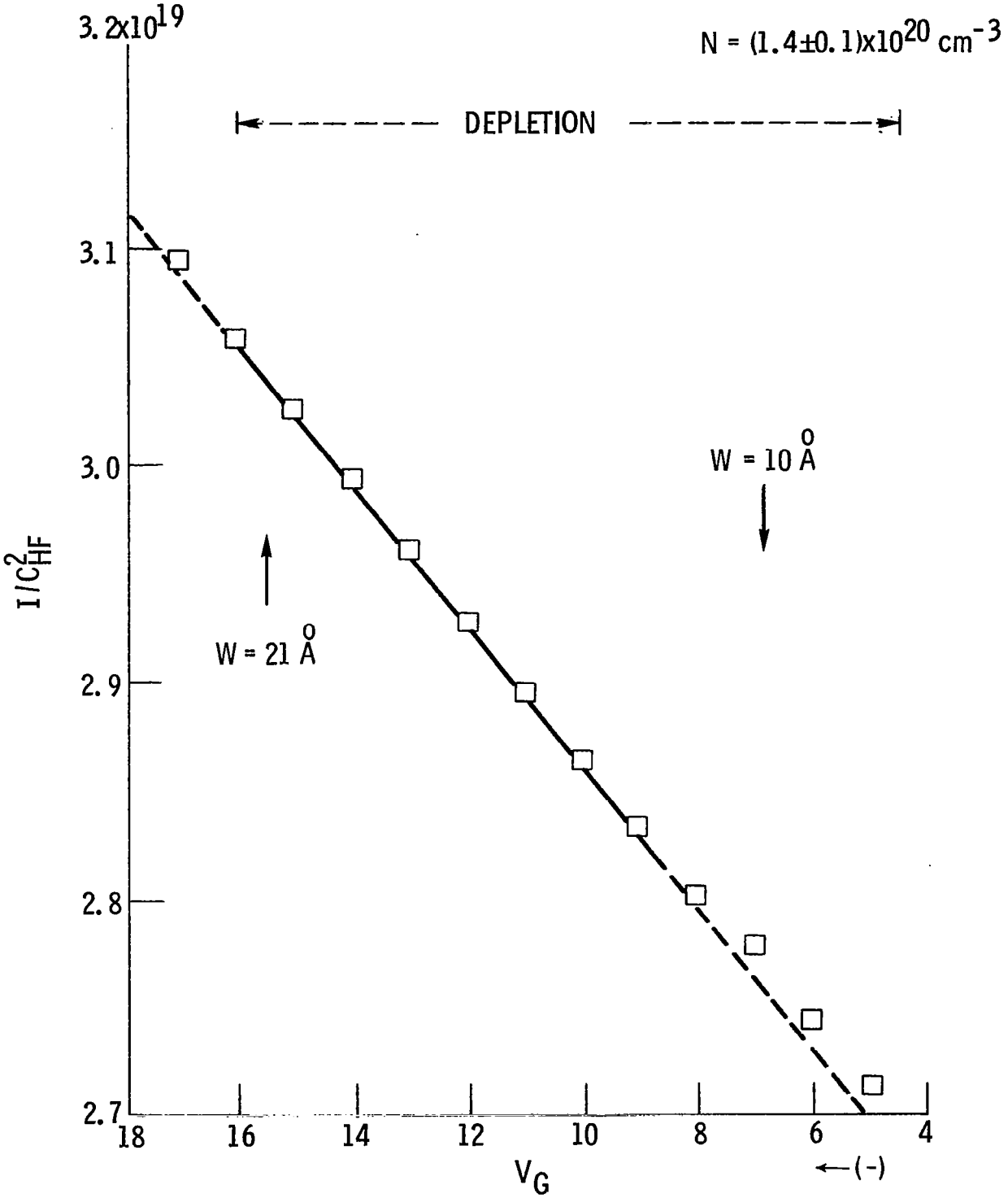

Figure 4. $-I/C_{HF}^2$ versus gate voltage.

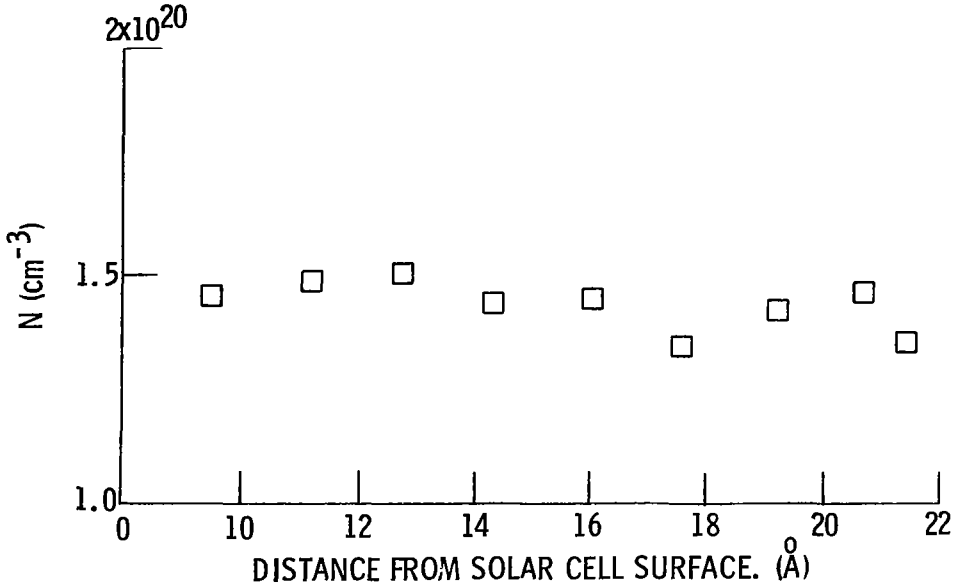

Figure 5. - Ionized impurity concentrations near the N^+ surface.

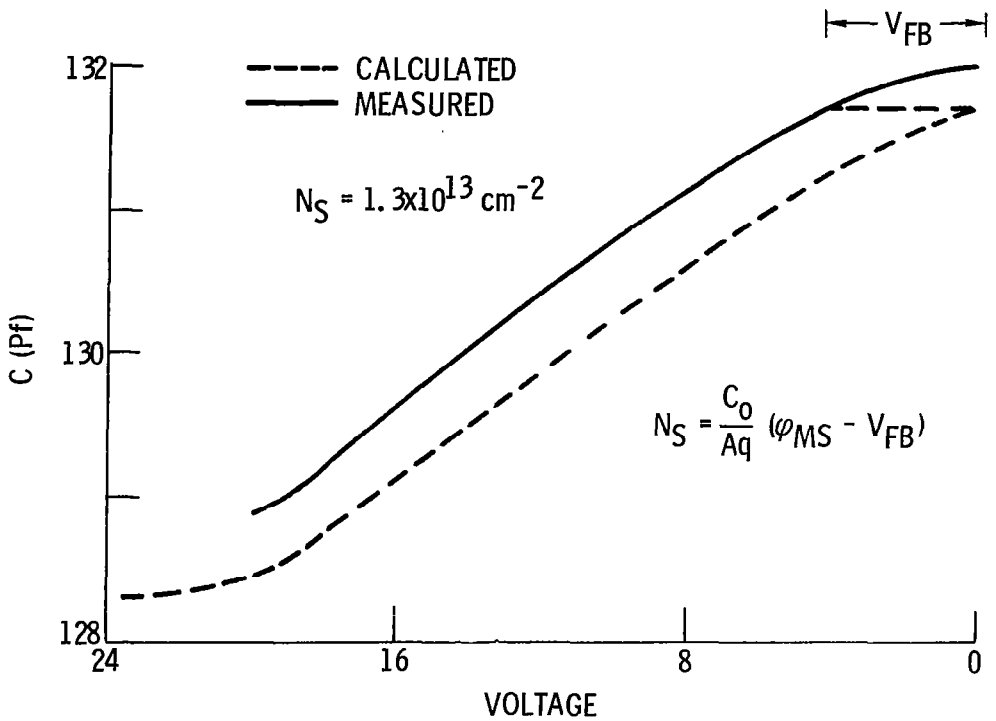

Figure 6. - Measured and calculated C-V curves. V_{FB} is the flat band voltage shift, N_S is density of charge in surface and oxide states, C_0/A is oxide cap. Per unit area and φ_{MS} is work function difference between metal and semiconductor.

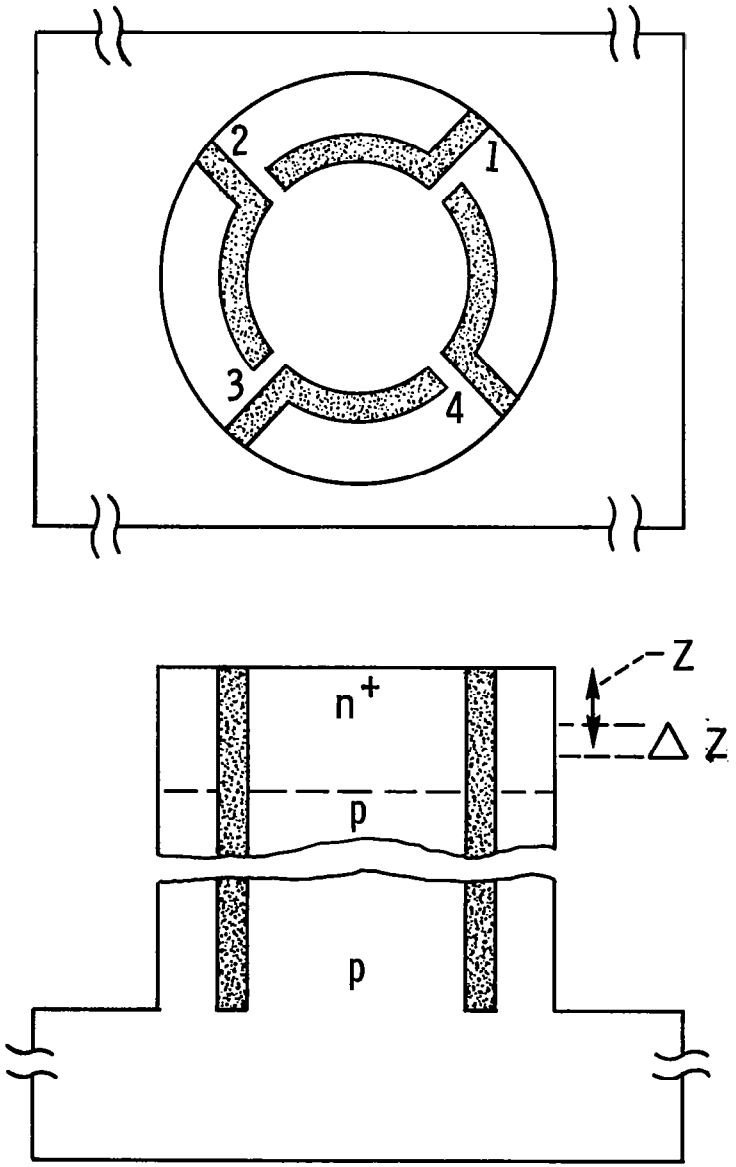

$$\rho_s = (\pi/\ell n 2)\ (V_{34}/I_{12})$$

$$R_s = (10^8\ \Delta V_{24})/(I_{13}B)$$

$$\Delta(R_s/\rho_s^2) = q\,N(Z)\mu^2(Z)\,\Delta Z$$

$$\Delta(1/\rho_s) = q\,N(Z)\mu(Z)\,\Delta Z$$

Figure 7. - Etched mesa and working relations for bulk measurements. ρ_s and R_s are sheet resistivities and Hall coefficient and μ is mobility.

8. INVESTIGATION OF THE TOPOGRAPHICAL FEATURES OF SURFACE CARRIER CONCENTRATIONS IN SILICON SOLAR CELL MATERIAL USING ELECTROLYTE ELECTROREFLECTANCE*

Fred H. Pollak, Cajetan E. Okeke† and Paul M. Raccah††
Yeshiva University

SUMMARY

One of the most important parameters for the application of epitaxial or diffused silicon for low cost solar cells is the doping of material, particularly its spatial variation. Optical techniques can be employed for this determination in a convenient, non-destructive manner at room temperature. In particular it has been found that electroreflectance (electric-field modulated reflectivity) can be utilized as just such a probe. We have investigated the topographical variations in carrier concentration $\Delta N/N$ across the surface of n^+ on p diffused silicon solar cell material utilizing electrolyte electroreflectance with a spatial resolution of 100μ within ≈ 500 Å of the surface. The topographical variations of $\Delta N/N \approx 10 - 20\%$ are found to be comparable to Czochralski grown material. Our approach has a number of advantages over the spreading resistance technique. The electroreflectance method can also be utilized to investigate other semiconductors such as GaAs.

INTRODUCTION

One of the most important parameters for the application of epitaxial or diffused silicon for low cost solar cells is the doping of the material, particularly its spatial variation. Optical techniques can be employed for the determination of spatial variations in doping level in a convenient, non-destructive manner at room temperature. In particular it has been found that electroreflectance (electric-field modulated reflectivity) can be utilized as just such a probe with a spatial resolution $\approx 100\mu$ ($1\mu = 10^{-4}$ cm). This approach has a number of advantages over the spreading resistance technique.

In modulation spectroscopy the application of a periodic external perturbation modifies the unperturbed dielectric function of the solid (refs.1 and 2). In electroreflectance the external perturbation is an electric field which is applied at a frequency Ω and hence produces a small ac modulation of the reflectivity ΔR (Ω). The experimentally observed electroreflectance signal is generally $\Delta R/R$, where R is the dc reflectivity.

It can be shown that under certain conditions the electroreflectance signal $\Delta R/R$ is given by (ref. 3):

$$\frac{\Delta R}{R} = - \frac{2e}{\epsilon_o} \text{ VNL } (\lambda) \qquad (1)$$

* Work supported by NASA Grant NSG-3123.

† On study leave from Physics Dept., University of Nigeria, Nsukka-Nigeria.

†† Present address: Physics Department, University of Illinois Chicago Circle, Chicago, Illinois 60680.

where e is the electronic charge, ϵ_0 is the static dielectric constant, V is the magnitude of the applied modulating voltage at frequency Ω, N is the carrier concentration and $L(\lambda)$ is a spectral line shape function characteristic of a particular material. Therefore, under these conditions, $\Delta R/R$ is proportional to N when the signal is measured at a fixed wavelength λ. The main criteria for equation (1) to be applicable are (a) the measurements must be made in the fully depleted space charge layer and (b) the intensity of the light must be low enough to prevent appreciable photoexcitation of carriers. The first condition can be checked by determining the region in which $\Delta R/R$ varies linearly with V while the second condition is met if $\Delta R/R$ is independent of the intensity of the incident radiation. Electroreflectance spectra can be conveniently obtained by the electrolyte technique (refs. 1, 2 and 4) as well as other methods such as Schottky barrier, metal-oxide-semiconductor, etc. (refs. 1 and 2). Electrolyte electroreflectance (EER) is particularly well suited to such an investigation since it can be performed on a free surface (i.e., nothing need be deposited on the sample surface to apply the electric field) and hence is non-destructive. In addition, it can be utilized over a wide range of carrier concentrations. Measurements of $\Delta N/N$ utilizing Schottky barrier electroreflectance have been reported (ref. 5 and 6).

EXPERIMENTAL DETAILS

The experimental arrangement for the topographical determination of the carrier concentration N is shown in figure 1. Light from a Xenon arc lamp passes through a monochromator and is focused onto one portion of the sample with a spot size $\approx 100\mu$ by means of a high quality f/1.2 camera lens. The spot size was verified by passing the beam through a 100μ slit without any loss of intensity. The sample, which is mounted on an X-Y stage, is immersed in an optical cell containing an electrolyte and a platinum electrode. The electrolyte used was a 1 normal solution of potassium chloride in water. The reflected light is collected by a large lens and focused onto a photomultiplier. The modulating voltage V ($\Omega \approx 1$ kHz) is applied by means of the audio oscillator, which also provides the reference signal to a lock-in amplifier. The sample is brought into the fully depleted space charge region by means of the dc bias.

The light detected by the photomultiplier contains two signals: a dc signal proportional to the average reflectivity R and an ac signal at Ω which is proportional to the modulated reflectivity ΔR. The dc output from the photomultiplier is applied to a servo power supply which varies the high voltage on the photomultiplier so as to keep the dc output constant. Under these conditions the output from the lock-in amplifier, which goes to a recorder, is proportional to $\Delta R/R$. This procedure automatically corrects for any fluctuations in the intensity of the reflected light due to variations in the surface of the silicon or changes in incident light intensity.

The most convenient optical structure for EER is silicon is the E_0' peak in the region of 3600Å (1Å = 10^{-8} cm) since this is the first optical reflectivity feature seen in this material and is quite large (refs. 1, 2 and 4). Shown in figure 2 is the EER signal in the region of the E_0' optical structure of silicon.

The penetration depth of the light in this wavelength region is $\approx 500\text{Å}$ and hence $\Delta N/N$ is sampled to this depth.

The signal $\Delta R/R$, at a given wavelength (corresponding to a maxima in $\Delta R/R$) and spot position, is determined and the sample is then moved by means of the X-Y stage. Step sizes were 0.2 mm in both the X and Y directions. In this manner the entire surface of the sample was scanned. The experimentally determined topographical variations in $\Delta R/R$ (and hence N) are processed by a 4051 Tektronix Graphic Display system which produces contour mapx of $\Delta N/N$, the variations in N.

The samples, which were provided by NASA - Lewis, consist of n^+ diffused layers on p silicon with a layer thickness of about 0.5μ and carrier concentration $\approx 2\text{-}4 \times 10^{20}\ cm^{-3}$.

EXPERIMENTAL RESULTS

We have verified the applicability of equation (1) by measuring $\Delta R/R$ as a function of the magnitude of V (peak-to-peak) to determine the region of linearity. Plotted in figure 3 are those results which shows $\Delta R/R$ is linear in V over a wide range. We have also found $\Delta R/R$ to be independent of the intensity of the incident beam.

Plotted in figure 4 is a contour map of the variations in N across the face of sample Y-1. The numbers on the contours indicate percentage variations where we have arbitrarily taken the smallest measured value of $\Delta R/R$ (and hence N) to correspond to zero variation. Figure 4 shows a region of relatively large $\Delta N/N$ ($\approx 24\%$) along the right hand region.

Shown in figure 5 is the topographical variations in carrier concentration, $\Delta N/N$ for sample Y-2. The largest value of $\Delta N/N \approx 11\%$, a factor of two smaller than sample Y-1.

The topographical variations in carrier concentration, $\Delta N/N$, for sample Y-3 are plotted in figure 6.

CONCLUSIONS

We have determined the topographical variations in carrier concentrations, $\Delta N/N$, across the surface of n^+ on p diffused silicon layers utilizing EER. Three samples have been examined and found to have $\Delta N/N \approx 10\text{-}20\%$. The value compares favorably with Czochralski grown material which was examined in a similar manner using Schottky barrier electroreflectance (ref. 5).

The EER technique has a distinct advantage over the spreading resistance technique since the latter method damages the surface by scratches. Since in the EER procedure only the electrolyte comes into contact with the sample surface this disadvantage is overcome. In addition our method probes the material to within only 500Å of the surface.

The EER method can also be used to evaluate $\Delta N/N$ in other semiconductors such as GaAs (ref. 7).

REFERENCES

1. Cardona, M. in Solid State Physics, Suppl. 11, Modulation Spectroscopy (Academic Press, New York, 1969) and references therein.

2. Hamakawa, Y., and Nishino, T., in Optical Properties of Solids - New Developments, ed. by B. O. Seraphin (North-Holland Publishing Co., Amsterdam, 1976) p. 256 and references therein.

3. Aspnes, D.E., Phys. Rev. Letters 28, 913 (1972).

4. Cardona, M., Shaklee, K.L., and Pollak, F.H., Phys. Rev. 154, 696 (1967).

5. Sittig, R., Surface Science 37, 987 (1973).

6. Kressel, H., D'Aiello, R.V., Robinson, P.H., Raccah, P.M., and Pollak, F.H. in Proceedings of the First ERDA Semiannual Photovoltoic Conversion Program Conference, Los Angeles, California, 1975.(JPL Document 5040-13) p. 368.

7. Pollak, F.H., Okeke, C.E., Vanier, P.E., and Raccah, P.M., to be presented at the 1977 Device Research Conference ,Cornell University, June 1977.

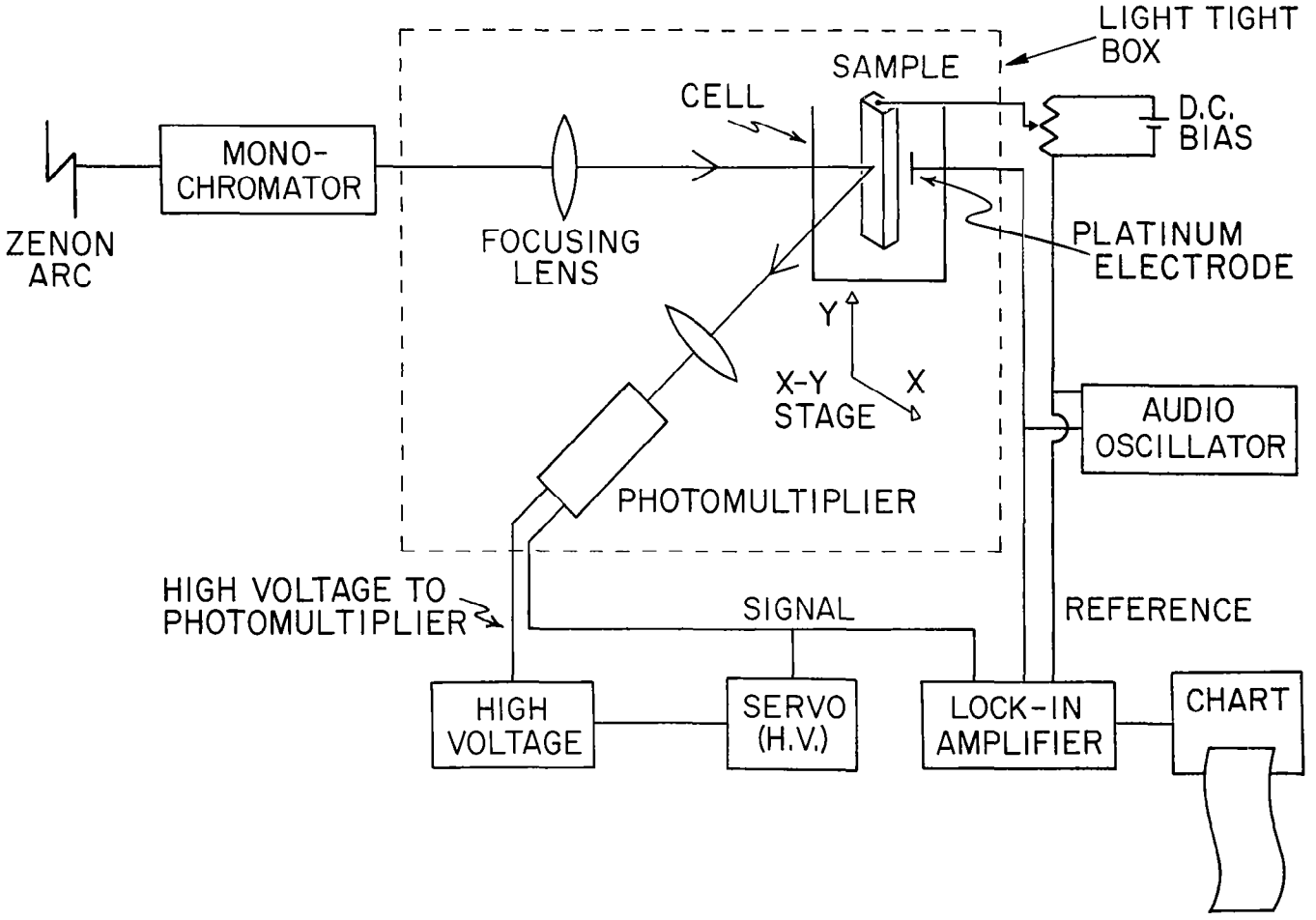

Fig. 1. Experimental arrangement for the determination of the topographical variations in carrier concentration, $\Delta N/N$, using electrolyte electroreflectance (EER).

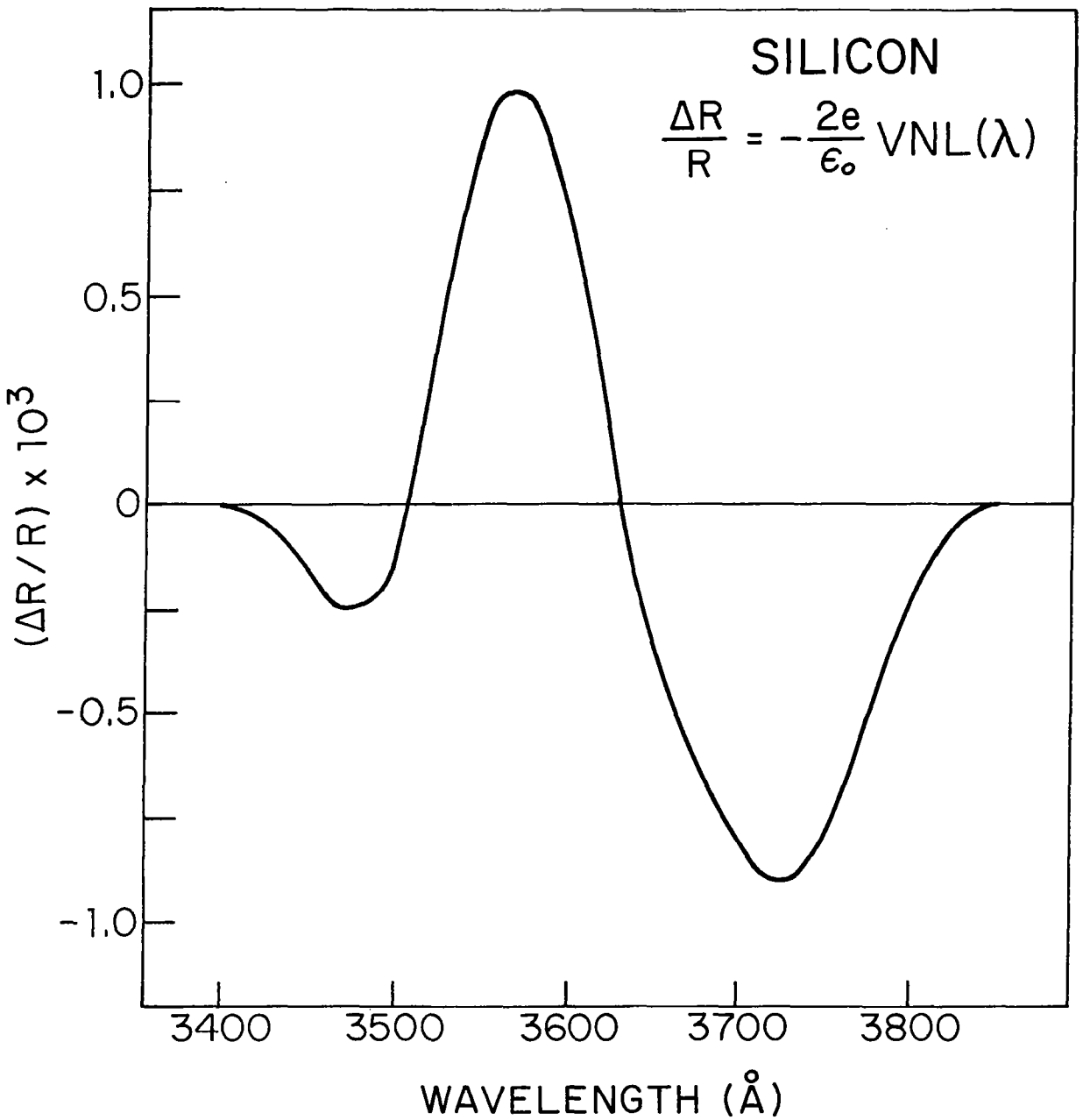

Fig. 2. Electroreflectance spectrum of the E_o' optical structure of Silicon.

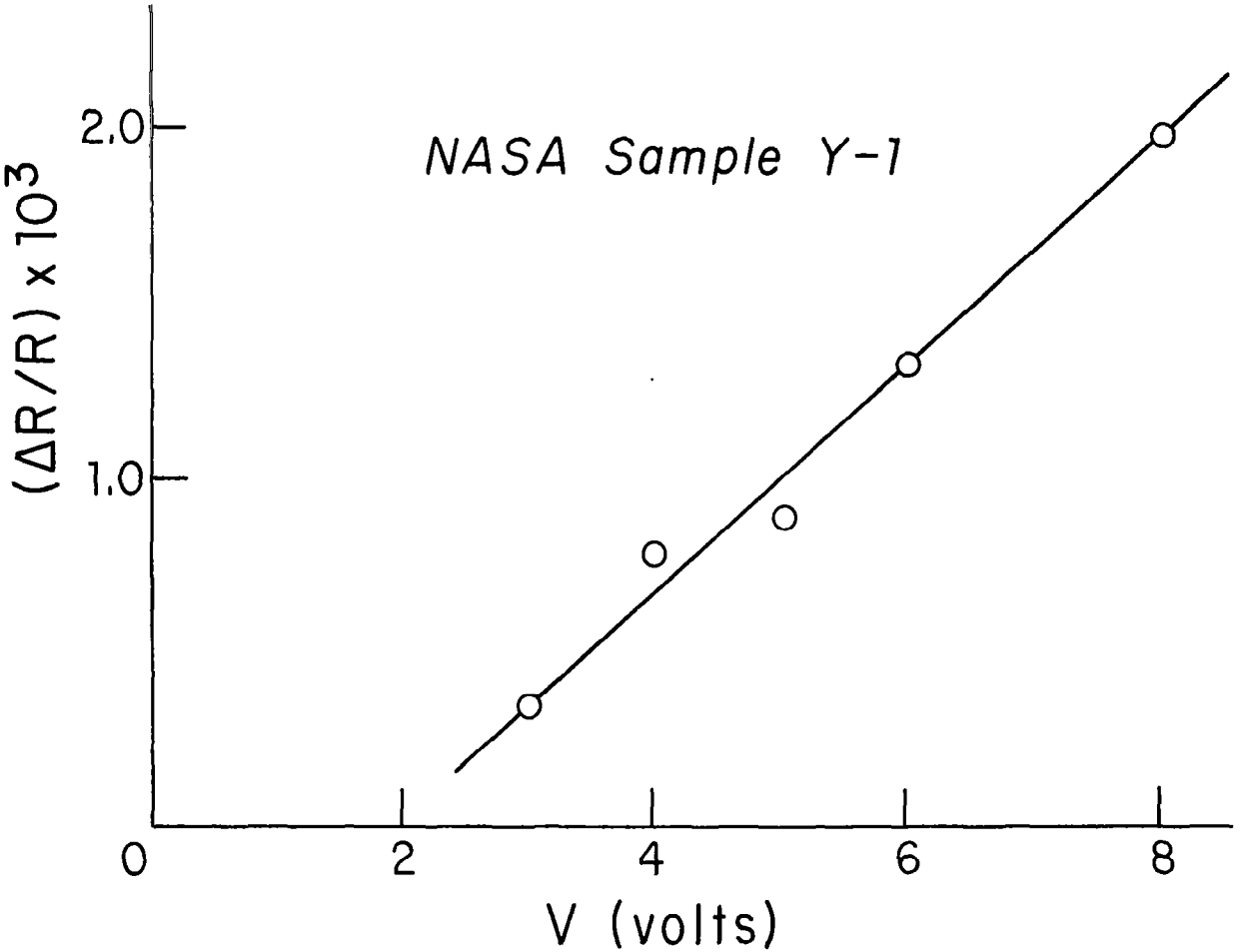

Fig. 3. Electroreflectance signal ΔR/R as a function of the applied modulating voltage V (peak-to-peak) for NASA sample Y-1 in order to verify the validity of Eq. (1).

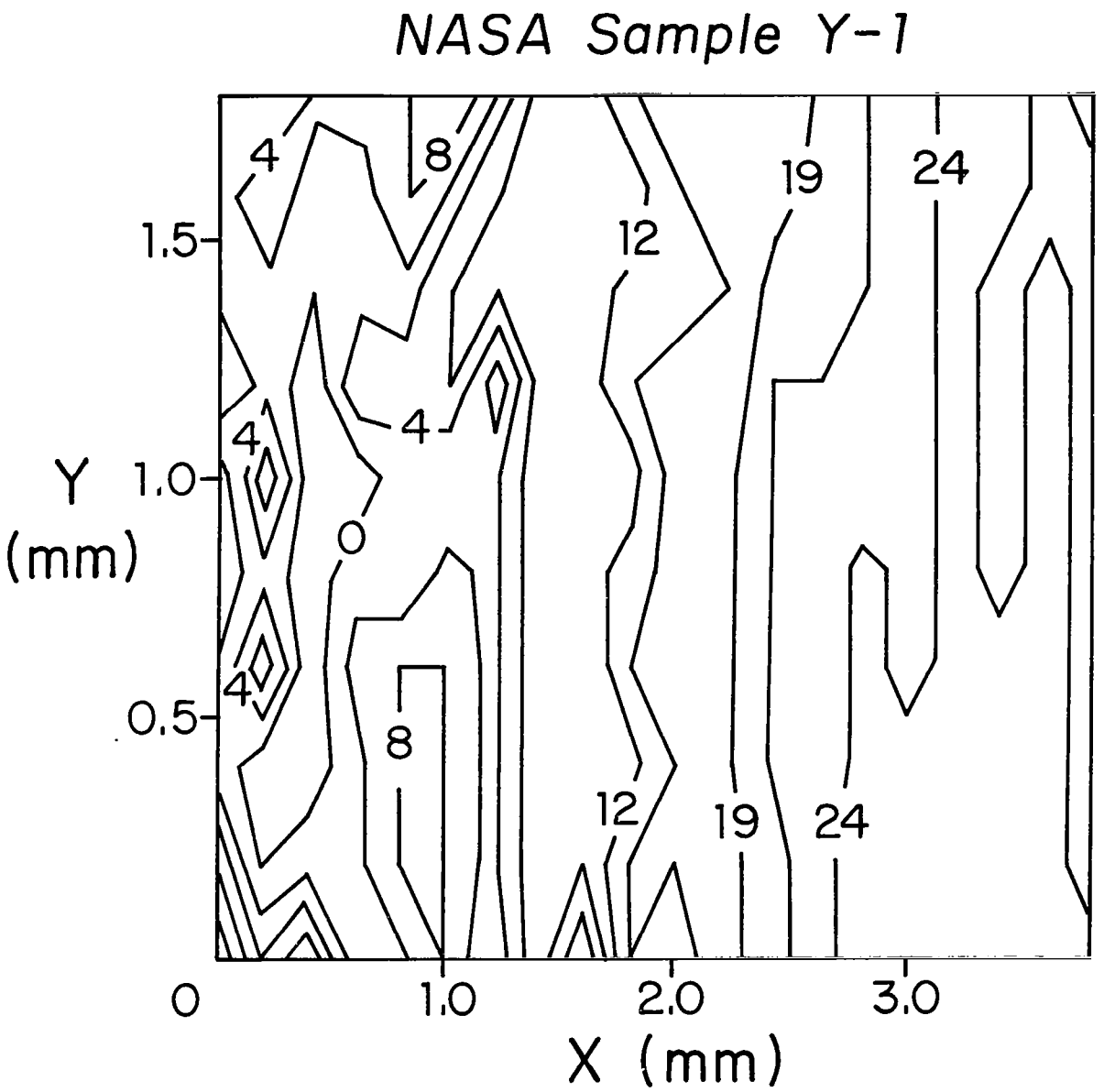

Fig. 4. Contour map of the topographical variations in carrier concentration, $\Delta N/N$, for NASA sample Y-1. The numbers in the contours indicate percentage variation where the lowest measured value of N has arbitrarily been taken to be $\Delta N/N = 0$.

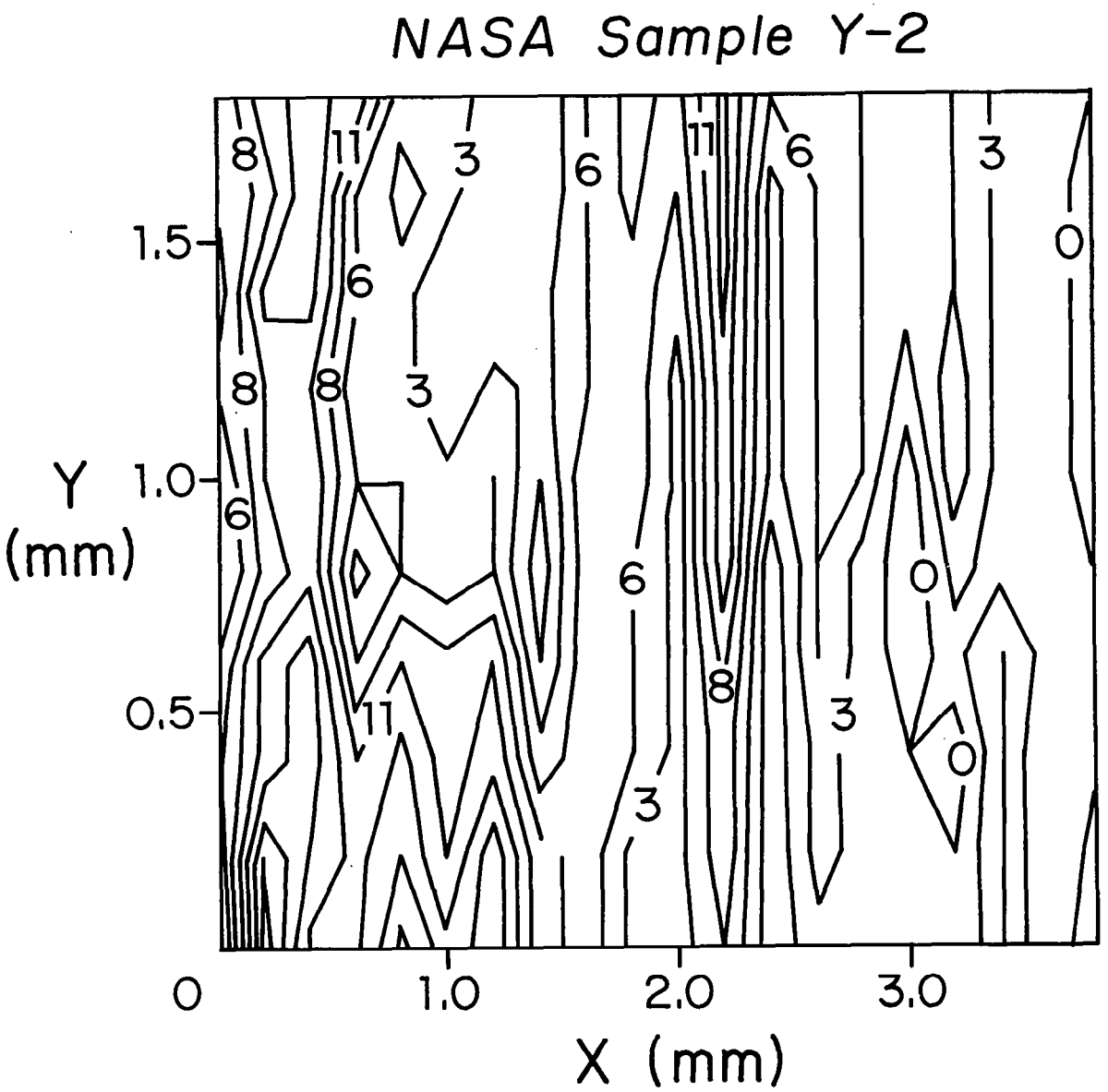

Fig. 5. Contour map of the topographical variations in carrier concentration, $\Delta N/N$, for NASA sample Y-2. The numbers in the contours indicate percentage variation where the lowest measured value of N has arbitrarily been taken to be $\Delta N/N = 0$.

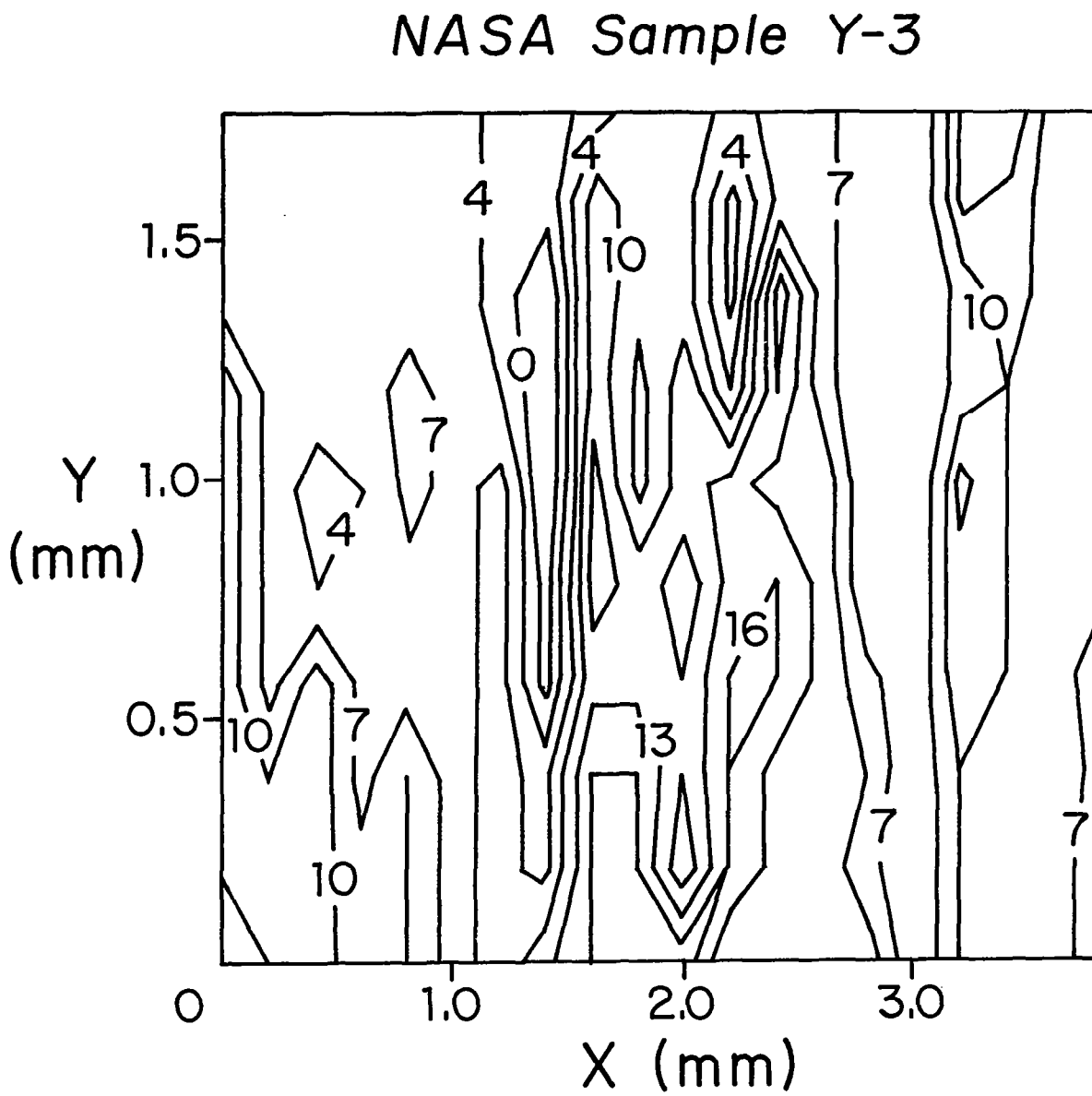

Fig. 6. Contour map of the topographical variations in carrier concentration, $\Delta N/N$, for NASA sample Y-3. The numbers in the contours indicate percentage variation where the lowest measured value of N has arbitrarily been taken to be $\Delta N/N = 0$.

9. ADVANCED HIGH EFFICIENCY WRAPAROUND CONTACT SOLAR CELL* †

J. A. Scott-Monck, F. M. Uno and J. W. Thornhill
Spectrolab, Inc.
Sylmar, California 91342

Abstract

A significant advancement in the development of thin high efficiency wraparound contact silicon solar cells has been made by coupling space and terrestrial processing procedures. Although this new method for fabricating cells has not been completely reduced to practice, some of the initial cells have delivered over 20 mW/cm^2 when tested at 25°C under AMO intensity. This approach not only yields high efficiency devices, but shows promise of allowing complete freedom of choice in both the location and size of the wraparound contact pad area.

I. Introduction

A wraparound contact cell is one where both the junction and base contacts are located on the back (base) surface. This can be accomplished in two ways, either by allowing the diffused junction to go around the edge to the back side of the cell, or by providing an insulated region at the cell edge and over the back area that will carry the wraparound contact. A variation of the latter concept using a wraparound contact was demonstrated in 1970.[1]

The first silicon solar cells ever built employed the wraparound contact configuration.[2] However, to avoid the high series resistance inherent to this relatively unsophisticated design, separate front (junction) and rear (base) contacts were soon devised. The wraparound contact cell received little attention for the next ten years as technical progress was made using planar silicon solar cell configurations. In the mid 1960's a re-evaluation of the wraparound contact cell was made by Spectrolab. This showed that loss of contact area on the back of the wraparound cell was responsible for the originally observed high series resistance value, and that it was possible to conserve enough back area to fabricate a cell that exhibited electrical performance comparable to planar silicon cells.

The emphasis on low cost arrays developing power outputs in the multikilowatt range has made the wraparound contact cell extremely attractive to array designers for a variety of reasons. For planar cells the laydown cost may be nearly equivalent to the cost of the cell. Wraparound cells, by confining all contacting to one surface of the cell, could reduce laydown cost substantially, as well as provide greater interconnection reliability due to simplified interconnector patterns. The fact that the front surface would be free of interconnects will allow better array cell packing and also result in improved cell radiation protection because the cell's active surface can more easily be completely shielded by the glass or quartz cover. The final advantage, which up until now had not been fully realized, was that additional power could be obtained from increased active area (no collector bar on the front surface).

II. Wraparound Contact Production Methods

In 1971 a serious effort, aimed at developing the wraparound contact silicon solar cell, was initiated by the NASA-Lewis Research Center. The two major producers of space flight solar cells were each funded to examine the technical problems associated with wraparound contact cells and to deliver one thousand 2 x 2 cm cells representing their best efforts, for evaluation by NASA-Lewis.[3,4] This initial effort yielded cells ranging from 14 to 15 mW/cm^2 for 0.30mm thick nominal ten ohm-cm silicon. Two main approaches were examined during this phase. The main effort concentrated on developing tooling for depositing contact metals around the cell edge, while some attention was given to producing a wraparound contact metallization that was separated from the wraparound junction by means of a thin dielectric material such as silicon dioxide or aluminum oxide. The dielectric isolation work was unsuccessful, but both companies developed tooling concepts that made it possible for them to produce small quantities of prototype wraparound contact cells for evaluation by organizations considering them for future missions.

These cells displayed a higher than average series resistance which reduced the curve fill factor of the cell, thus cancelling the gain in active area obtained by eliminating the front collector bar. In addition the mechanical integrity of the wraparound contact at the cell edge was suspect and seemed to be quite dependent on the contact metals' angle of incidence during evaporation.[3]

Work on new wraparound configurations was initiated by panel manufacturers and 2 x 4 cm cells were made using various schemes for obtaining reliable high efficiency wraparound cells.[5] Two basic configurations emerged, the full edge wrap and the front spine wrap. The former approach kept the junction collector area on the back surface of the cell, thus providing more current but a lower curve factor. The latter approach used a narrow (0.8-1.0mm) front spine collector bar that wrapped around the 2 cm edges of the cell and terminated at contact pads. Although this approach sacrificed active area, the curve factor improved because the base contact area was more completely utilized and there was a statistically higher probability of the wraparound contact avoiding any

*Previously presented at the AIAA Conference on the Future of Aerospace Power Systems, St. Louis, Missouri, March 1-3, 1977. (AIAA Paper 77-521.)

†Much of this work was supported by the NASA Lewis Research Center.

cell edge chips which are shorting sources if created after the diffusion. Two ohm-cm cells, 0.35mm thick, delivering 16 mW/cm^2 when measured at 28°C under air-mass-zero (AMO) conditions (135 mW/cm^2) were produced in limited quantities for evaluation during 1973.

The Comsat "violet" cell achievement[6] created additional activity in this area. Programs were started to develop shallow junction wraparound cells incorporating all the technology of the violet cell such as an optimized grid collector pattern and the more transparent, higher refractive index antireflection coating. The desire of the panel manufacturer to have a weldable version of the "violet" or "hybrid" cell prevented full utilization of the shallow junction technology, but improvements in power were obtained and by mid 1974 cells averaging 16.5 mW/cm^2 at 28°C could be produced.

The reduction to practice of the back surface field (BSF) effect by the NASA Lewis Research Center[7] stimulated some limited prototype work in producing BSF wraparound contact cells because of the attractive power to weight ratios this technology offered. Although the two ohm-cm silicon used was not an optimum choice for the BSF effect, 2 x 4 cm, wraparound contact, BSF cells 0.20mm thick were produced which gave 16 mW/cm^2 at 28°C when tested under AMO conditions. However the coarse surface finish caused by the BSF incorporation method created serious concern that reliable welds could be made to the cell and further work along these lines was not pursued.

This entire phase of wraparound contact cell development resulted in a significant optimization of cell size, thickness and configuration. It also helped, in a minor way, to encourage the cell manufacturer to install new production equipment that would lend itself more readily to mass production of wraparound contact silicon solar cells. Figures 1 and 2 show advanced 2 x 2 cm wraparound cells

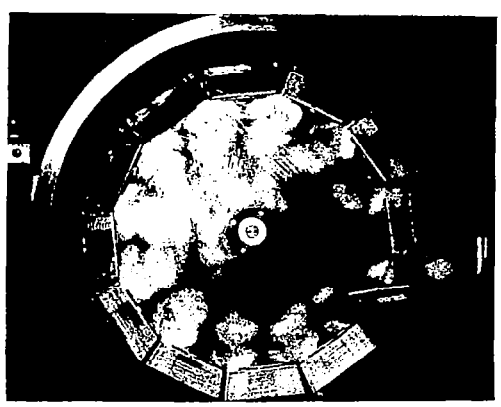

Figure 1. Rotating Substrate Evaporator

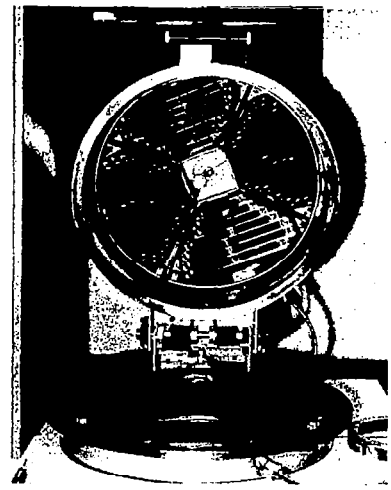

Figure 2. Electron Beam AR Coater

being produced in the most modern equipment now available within the solar cell manufacturing industry.

III. Laboratory Development of Wraparound Contact Cells

As mentioned previously NASA-Lewis initiated a serious effort committed to the wraparound cell concept. Once the original baseline program was completed[3], a series of continuing contracts was let to Spectrolab[8,9,10], each oriented towards incorporating the latest silicon solar cell technology into the wraparound contact cell. These contracts were mainly responsible for the continued progress in prototype production cells, an excellent example of mission oriented research and development.

The second program[8] was aimed at initially developing the technology for shallow junction and BSF cells using planar type silicon solar cells as a vehicle. Once this was secured, these advancements were applied to the wraparound contact configuration. Approximately one hundred 2 x 2 cm, front spine, single pad wraparound cells were built and subjected to those tests mandated for typical space flight cells. During the pilot phase, rotisserie tooling was developed which allowed the front and wraparound contacts to be deposited during a single pumpdown. Cells, 0.20mm thick, of ten ohm-cm silicon were produced which had an average power at 28°C under AMO intensity of between 14.5 and 15.5 mW/cm^2.

When compared to planar cells using the same technology, the wraparound devices appeared rather inferior with respect to power. The planar cell was averaging about 17 mW/cm^2 with some cells approaching 18 mW/cm^2. This difference was due to

the relatively poor fill factor of the wraparounds, 0.69 vs. 0.77 for a planar cell, and to a slightly lower value of short circuit current. The lower current was due to the fact that a trade-off between junction depth and fill factor for the wraparound cell forced the use of a deeper junction.

Although this device was not equivalent to a planar cell in output, significant progress had been demonstrated. Figure 3 shows typical wraparound cells from the first two contracts. It was still felt that edge chips were responsible for the poor fill factors, especially considering the difference in thickness between the 1972 and 1974 cells. The latter cells, being only 0.20mm thick, are more prone to chipping during processing, thus increasing the chance for potential shorting on the wraparound edges. Another problem that had not been satisfactorily resolved was edge contact adherence. Although rotisserie tooling could provide edge adherence using the titanium-palladium-silver contact system, it was not a true rotary process because it was necessary to stop the fixture during rotation so that the cell edge was normal to the evaporation source.

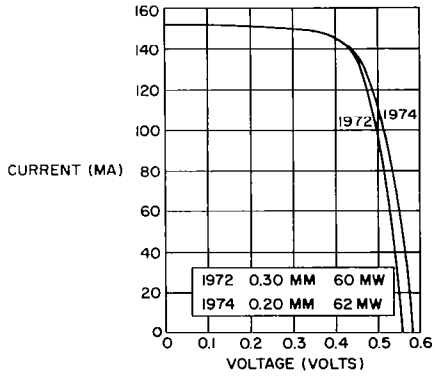

FIGURE 3. WRAPAROUND CELL PROGRESS (2 x 2 cm)

A continuation contract was then let to Spectrolab aimed at pilot line production of a matured wraparound contact silicon solar cell under formal documentation and control[9]. The cell was to be 0.20 mm thick, 2 x 4 cm, end-tab front spine configuration (see Figure 4), using all the latest technology developed on the previous contracts. In essence this device was almost identical to the cell that had evolved for use on the "Solar Electric Propulsion Stage" (SEPS) program supported by the Marshall Space Flight Center.

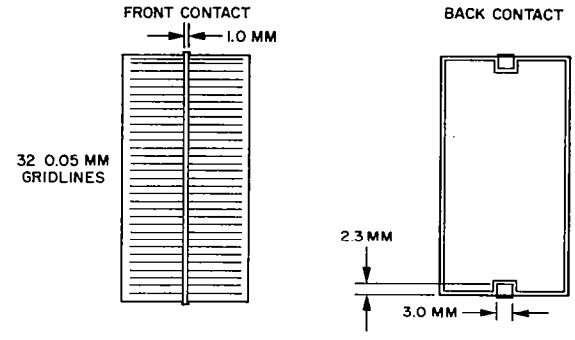

FIGURE 4. END TAB WRAPAROUND CONTACT CONFIGURATION

During this contract a new metallization system consisting of chromium-palladium-silver was developed which solved the edge adherence problem. This system allowed pilot line cells to be fabricated on the Spectrolab solar cell production line using a new rotating substrate evaporator. One thousand cells were delivered to NASA for evaluation. The minimum output was 15.5 mW/cm^2 at 25°C based on total cell area. By using more sophisticated tooling it was possible to produce cells with a minimum fill factor of 0.72 in the case of nominal ten ohm-cm silicon, and 0.71 in the case of nominal twenty ohm-cm silicon. Both cell types employed the BSF effect which allows higher than normal silicon resistivity to be considered for solar cell use.

IV. Future Wraparound Contact Cell

Anticipating that wraparound cells for multi-kilowatt missions would have to be relatively inexpensive, NASA-Lewis began a series of contracts with Spectrolab aimed at developing an automated production line for the manufacturing of low cost silicon solar cells[11,12]. Since vacuum processing steps are relatively costly and can be the rate limiting steps in high volume production, it was the goal of these contracts to eliminate, wherever possible, vacuum processing operations.

As a result of these efforts a wraparound contact solar cell was developed which employed a number of new non-vacuum processing steps for producing the BSF effect, the cell contacts and AR coating. Of even greater significance, a dielectric was successfully employed to protect the cell wraparound edge from shorting effects.

Over one thousand 2 x 4 cm wraparound cells were produced during this program. A sampling from each cell batch was subjected to various environmental screening tests such as temperature and humidity, contact adherence, thermal shock, AR durability and the like. The results were extremely encouraging, and this coupled with the tremendous improvement observed in the wraparound cell curve fill factor (average values of ~0.75) led us to conclude that the ideal wraparound contact cell was within reach.

Therefore a preliminary attempt at combining the best technical features from vacuum and non-vacuum wraparound contact technology was made. Improvised evaporation tooling was used to produce approximately twenty cells incorporating the textured surface first introduced by the Comsat Corporation[13], a back surface field using a non-vacuum deposition process, narrow vacuum deposited grid-lines, a tantalum pentoxide AR coating and a non-vacuum deposited dielectric to insulate the wraparound contact from the silicon edge. Figure 5 is an I-V characteristic of the best wraparound contact silicon solar cell produced from these preliminary fabrication runs.

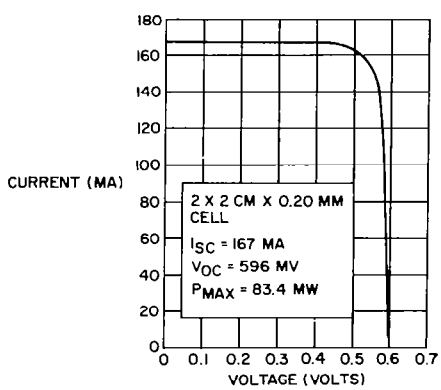

FIGURE 5. PROTOTYPE WRAPAROUND CONTACT SOLAR CELL

This cell is 2 x 2 cm, 0.20 mm thick, made from ten ohm-cm silicon, and at 25°C under AMO intensity delivers approximately 84 mW, equivalent to an AMO conversion efficiency of 15.5 percent. The curve fill factor is greater than 0.83, which is surprisingly high. This cell has no front collector bar thus increasing its active area, and it employs dielectric isolation so that no back contact area is lost. Any interconnect configuration can be used in assembly with relative ease. It should be stated that the other cells made by this technique have power outputs ranging from 75 to 80 mW in the best cases.

V. Conclusions

Although preliminary, the results of this work give strong indications that the solar cell industry may be on the verge of developing a high efficiency wraparound contact silicon solar cell with technology that lends itself to high production rates in a cost effect manner. A great deal of work remains to be done before we can be assured of this hope. During the following months strong efforts will be made to understand, control and then optimize the radical new technology that has been incorporated into this cell. Once this has been accomplished, the cell will then have to demonstrate the ability to conform to the various environmental and mechanical requirements expected of a space flight solar cell.

If this does come to pass, as we feel it ultimately will, then those space missions faced with the requirement of multikilowatt power outputs will stand a much better chance of becoming reality. The new type of wraparound cell is in a very primitive state. However in view of the rapidity with which the solar cell industry has developed the major advancements in cell technology made during the last five years, we are confident that this device will follow the same pattern, provided that there is a stimulus for its utilization from mission planners.

References

1. E. L. Ralph and R. K. Yasui, Proceedings of the Eighth IEEE Photovoltaic Specialists Conference, p. 276, August (1970).
2. D. M. Chapin, C. S. Fuller and G. L. Pearson, Journal of Applied Physics, 25, p. 676 (1954).
3. J. A. Scott-Monck, P. M. Stella & J. E. Avery, NASA CR-121021 (1972).
4. G. Goodelle, NASA CR-121003 (1973).
5. D. R. Lott, et al., NAS8-28432, Phase III Progress Report, (1973).
6. J. Lindmayer and J. Allison, Conference Record of the Ninth IEEE Photovoltaic Specialists Conference, p. 83, May (1972).
7. J. Mandelkorn and J. Lamneck, Jr., Conference Record of the Ninth IEEE Photovoltaic Specialists Conference, p. 66, May (1972).
8. J. A. Scott-Monck, P. M. Stella & J. E. Avery, NASA CR-134740 (1975).
9. J. E. Avery and J. A. Scott-Monck, NASA CR-135114 (1976).
10. "Development of Improved Wraparound Contacts for Silicon Solar Cells", NAS3-20065 (In progress).
11. J. W. Thornhill and W. E. Taylor, NASA CR-135095 (1976).
12. "Automated Fabrication of BSF Silicon Solar Cells with Screen Printed Wraparound Contacts" NAS3-20029 (To be published).
13. J. Haynos, J. Allison, R. Arndt and A. Meulenberg, Proceedings of the International Conference on Photovoltaic Power Generation, p. 487, September (1974).

10. THE SAWTOOTH COVER SLIDE*

A. Meulenberg, Jr.
Communications Satellite Corporation

SUMMARY

A novel cover slide has been proposed (refs. 1 and 2) which increases solar cell output by reducing the reflection of light from the cover slide surface and by redirecting incident light so that none falls on the collection grids of the cell. The new cover slide is fabricated with a sawtooth surface having a periodicity equal to that of the solar cell grids. This configuration refracts the light so that it is directed onto the semiconductor surface between the grid lines. Conventional grid patterns obstruct 7-10 percent of the light incident on the cell; at least half of this loss has been recovered by using the sawtooth cover slide. In addition, surface reflection from the conventional coated cover slide (normally 2-4 percent) is suppressed by presenting a second surface to any light reflected at the first plane of contact. This double reflection results in a greater reduction of the reflection loss from the cover slide than does an antireflection coating on a flat surface.

An examination of the light paths within the cover slide (fig. 1a) shows a series of shadow patches at various depths under each valley and peak. The size, shape, and position of these patches can be calculated given the peak-to-peak spacing, G (equal to the grid spacing), the cover slide index of refraction, n_c, and the included half angle, θ_1, of the sawtooth (fig. 2):

$$\theta_2 = 90° - \theta_1 , \qquad \theta_3 = \sin^{-1}\left(\frac{n_a}{n_c}\cos\theta_1\right) , \qquad \theta_4 = \theta_2 - \theta_3$$

$$h = \frac{G}{2}\cot\theta_1 , \qquad h' = \frac{G}{2}\cot\theta_4$$

$$S = (h' - h)\tan\theta_4 , \qquad T = \frac{h' + h}{2}$$

where

h = height of the teeth

h' = distance between the top of the teeth and the bottom of the first layer of shadows

S = maximum shadow width

T = distance between the top of the teeth and the plane containing S.

*This paper is based upon work performed in COMSAT Laboratories under the sponsorship of the Communications Satellite Corporation.

Specifically, for $\theta_1 = 45°$, $n_c = 1.5$, and $G = 760$ μm, the maximum width of the shadow is $S = 265$ μm at a depth of $T = 810$ μm below the level of the sawtooth peaks.

Table 1 gives further dimensions for various sawtooth cover slide parameters, including the extremes likely to be used, $30° < \theta_1 < 45°$. The quantity T_{eff}, which represents the effective thickness of the cover slide for mass and radiation protection calculations, is the thickness that would result if the sawtooth cover slide were to be reduced to a planar slab. The quantity ΔT represents the variation in cover slide thickness within which the shadow width exceeds a convenient grid width of 50 μm.

It can be seen in table 1 and fig. 1 that a wide range of cover slide thicknesses is possible. Figures 1b and 1c show the difference in light patterns in the cell as the cover slide thickness is varied. The greater light concentration in the silicon of fig. 1c is evident. To provide approximately the same amount of radiation protection and the same cover slide mass/cm^2 used presently, T_{eff} would be equal to 300 μm. The corresponding grid density would exceed 13 grids/cm, which is highly suitable for minimizing series resistance of the n-layer in shallow junction cells. Since nearly 30 percent of the cell surface can be shadowed by a sawtooth cover slide of the proper thickness, broad grid lines (50-100 μm wide) can be used without penalty, thereby eliminating the only objection to closely spaced grid geometries. The ability to use wide grids under a sawtooth cover slide also enhances the desirability of large (4- x 2- or 6- x 2-cm) solar cells.

It is anticipated that the use of wrap-around grids and sawtooth cover slides will make it possible to reduce losses from contact and grid obstruction to zero and losses from surface reflection to less than 1 percent. This novel cover slide can thereby provide a potential improvement of >10 percent in solar cell efficiency.

REFERENCES

1. Meulenberg, A.: A Novel Cover Slide for Solar Cells. Proceedings of the International Conference on Solar Electricity, Toulouse, France, March 1976, pp. 199-208.

2. Meulenberg, A.: The Sawtooth Cover Slide: A New Means of Coupling Light into Solar Cells. Journal of Energy, May/June 1977.

Table 1. Typical Sawtooth Cover Slide Dimensions as Defined in Figure 2

G (μm)	Grids/ cm	θ_1	S (μm)	T (μm)	T_{eff} (μm)	$T \pm \Delta T$ (μm)	$T_{eff} + \Delta T$ (μm)
760	12.5	45°	265	810	670	460-1160	320-1020
380	25	45°	132	405	335	270-540	200-470
254	37.5	45°	88	270	223	240-300	193-253
760	12.5	30°	75	825	495	765-885	435-555
510	19	30°	50	550	330		

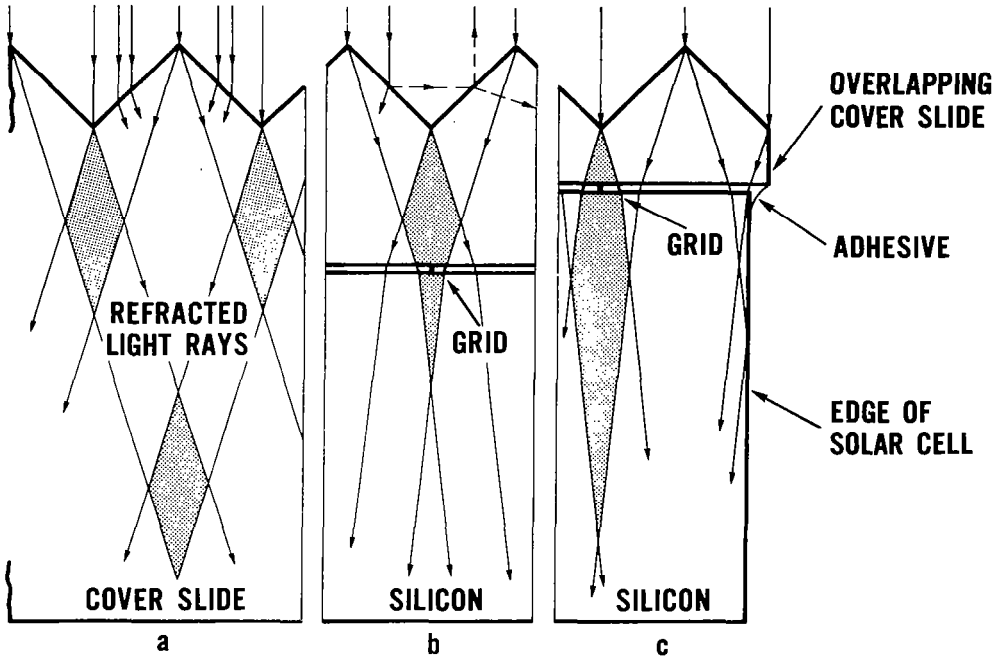

Figure 1. Structure and Effect of the Sawtooth Cover Slide

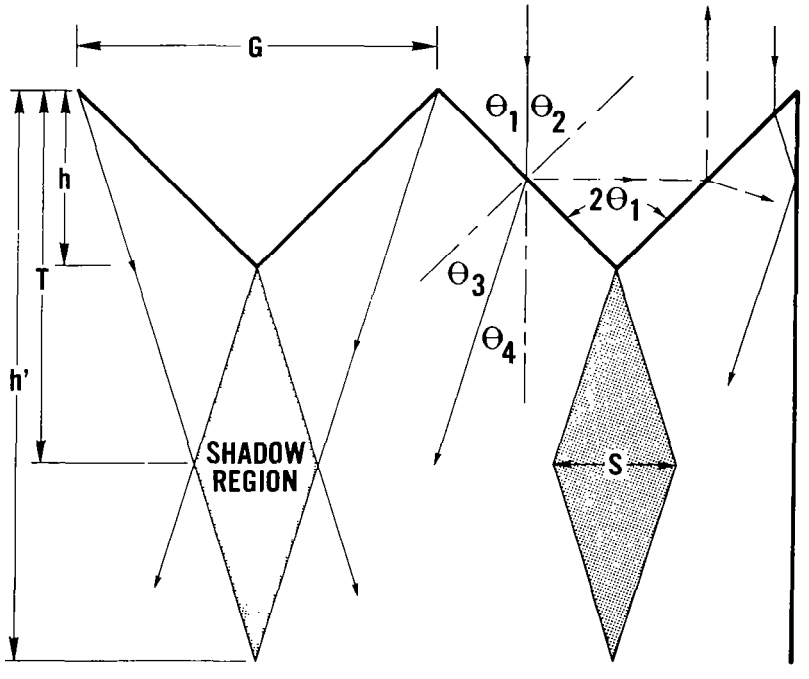

Figure 2. Geometry of Light Paths in the Sawtooth Cover Slide

11. APPLICATIONS OF ION IMPLANTATION FOR HIGH EFFICIENCY SILICON SOLAR CELLS*

John A. Minnucci and Allen R. Kirkpatrick
Simulation Physics, Inc.

ABSTRACT

Ion implantation can be utliized for the dopant introduction processes necessary to fabricate a silicon solar cell. Implantation has several advantages and some disadvantages relative to diffusion methods, but correctly utilized, provides a versatile powerful tool for development of high efficiency cells. This paper discusses advantages and problems of implantation and present status of developmental use of the technique for solar cells.

INTRODUCTION

Ion implantation has been utilized for solar cell applications for more than the past decade. During the 1960's, implantation was used to produce developmental N/P and P/N cells (ref. 1,2,3) with efficiencies of 10-11% AMO which were competitive with diffused cell technology of the time. Ion implantation machines with sufficiently large throughput to allow practical production of ion implanted cells did not exist.

Simulation Physics has been actively developing ion implanted solar cells since 1974. Until late 1976, this work emphasized combination of ion implantation with a new concept for cell fabrication (ref. 4,5) using pulsed electron beam effects in place of thermal processing. Combined implantation/electron beam processing resulted in achieved efficiency of approximately 10.5% AMO limited by the structure of the cell itself.

Since late 1976, Simulation Physics has been working to improve the basic implanted cell by incorporating advanced structural characteristics now responsible for improved performance of diffused junction cells. These include shallow lightly doped junctions, better contacts, back surface fields and improved antireflective coatings. This paper describes present status of ion implanted solar cell development.

* This work has been supported by the Air Force Aero Propulsion Laboratory under Contract F33615-75-C-2006.

ADVANTAGES OF ION IMPLANTATION

Ion implantation machine technology has evolved rapidly during recent years. There is no longer any question regarding practical potential of implantation for solar cell production purposes. The advantages of implantation for general production of solar cells include:

1. Implantation is simple and reproducible.

2. Implantation involves only the surface under process and leaves no residue.

3. Automation and scale up to large volumes can be relatively easy.

For the purpose of high efficiency cells, implantation represents a powerful technique with several additional advantages:

4. Dopant profiles can be controlled and tailored even at very low concentration levels.

5. Ion implantation can be an absolutely pure process which introduces no contaminant impurities.

6. Implantation can be utilized in processing schemes which allow cell fabrication without subjecting the cell structure to elevated temperatures.

7. Implantation allows flexibility in cell structure design.

PROBLEMS OF ION IMPLANTATION

The use of ion implantation for silicon solar cells with efficiencies up to approximately 11% AMO is relatively straightforward. However, for higher efficiency cells, solutions must be developed for two major problems.

1. Effective techniques are required for annealing of damage to the silicon lattice in the implanted region.

2. Junction layer dopant distributions by direct ion implantation are not correctly profiled, particularly near the surface, and must be modified.

Annealing Requirements

Ion implantation is a high energy particle impact process which causes severe damage to the silicon lattice. An annealing step is generally

necessary in order to restore the crystal structure. Requirements of good annealing are complex and, among other things, depend upon:

1. Orientation of the silicon

2. Ion species

3. Ion fluence

4. Ion energy

5. Substrate temperature during implant

The implants used for solar cell purposes, when performed at room temperature, are particularly hard to correctly anneal. This is because during annealing competition occurs between polycrystallite formation around nucleation sites within the implanted region and epitaxial regrowth on the implanted base material. Furnace anneal parameters must be carefully selected in order to suppress polycrystallite formation and achieve good annealed layers. For the junction of the N^+/P cell, the furnace anneal generally utilizes maximum temperature conditions comparable to those for junction diffusion, i.e. temperatures to between 700 and 850°C.

Simulation Physics has been investigating a new method for annealing of implantation damage. The method utilizes a short duration pulsed beam of relatively low energy electrons to create a transient thermal spike in the implant damaged region. Calculated temperature profiles given in Figure 1 for immediately after the electron pulse and for a few instants later show that the implanted material is apparently momentarily raised to or close to incipient melt, melting temperature in the absence of heat of fusion. This spike collapses from interior toward the surface with a time constant of the order of a microsecond. Favorable single crystal growth conditions result due to strong thermal gradient at the rapidly advancing recrystallization interface.

Helium ion backscattering provides an effective means to evaluate residual damage in implanted layers (ref. 6). Using this technique the spatial distribution of crystalline imperfection can be correlated with intensity of a backscattered ion signal. Figure 2 shows ion backscattering data from three silicon samples with phosphorus ion implants. The first sample which was not annealed after implant exhibits a backscattering characteristic of a nearly amorphous implanted layer. A second sample subjected to good thermal anneal conditions exhibits much reduced but still significant crystalline imperfection. The third sample which was annealed with the pulsed electron beam shows excellent lattice structure essentially identical to that of unimplanted silicon.

Use of electron beam annealing is still being developed. Cells fabricated using this technique exhibit performance characteristics similar to those achieved with good thermal annealing except that, because the method does not subject the cell base region to elavated temperatures, the possibility exists for employing base region lifetime enhancement processes. It has been observed

elsewhere (ref. 7,8) that minority carrier lifetime can be substantially increased in silicon never processed above 600°C if it is properly treated at temperature of approximately 450°C. This effect has been observed on ion implanted cells fabricated at room temperature and then subjected to 450°C thermal treatment.

Implant Profiles

Ion implantation produces approximately Gaussian dopant distribution profiles. Representative profiles for direct implants are shown in Figure 3. The profile peak always lies below the implant surface. As a result, there is a region from the surface to the peak in which a drift field exists to block motion of minority carriers toward the junction. The region is equivalent to a dead layer and has detrimental effect upon cell performance, particularly at shorter wavelengths.

Several possibilities exist for elimination of the dead layer including:

1. Implanting through a surface oxide.

2. Use of a stripping technique after implant to move the silicon surface to the profile peak.

3. Use of shallow implants at near grazing angle to "fill" the surface deficiency.

All of these techniques give improved response characteristics but none has yet been optimized.

Another problem related to profile of implanted ions is associated with "channeling" of ions into and along crystal axes. As a result, junctions are actually deeper than predicted on the basis of stopping theory. In the case of phosphorus, junctions shallower than approximately 0.2 μm do not result even at implant energies as low as 5 keV. Very shallow junctions can be obtained using the techniques as listed above to correct the dead layer profile near the surface, but development is required.

PRESENT STATUS

Adequate solutions for the profile related problems are still under development. However, implant damage annealing which until recently was considered the most serious problem of ion implantation for solar cells, now seems well under control. Figure 4 shows the AMO I-V characteristic of an implanted 1 ohm-cm cell without optimized junction or front contact grid. Cell efficiency exceeds 12% AMO. Present best parameters of ion implanted 1 ohm-cm cells are

I_{sc} 148 mA

V_{oc} 602 mV

CF 0.75-0.80

η > 12% AMO

The use of ion implantation is now being extended to textured surface cells. Figure 5 shows the AMO I-V characteristic of a 10 ohm-cm ion implanted textured surface cell without AR coating.

SUMMARY

Ion implantation can be used for the doping operations in the fabrication of silicon solar cells. Implantation offers certain advantages not available with diffusion and these features of implantation should be exploited to achieve higher efficiency cells.

Some problems must first be solved. The ability to accomplish nearly perfect annealing of the implant damaged silicon lattice is now available. The most serious remaining problems relate to reduction of junction depth and optimization of implanted dopant profiles.

At present ion implanted cells are better than 12% efficient. Continued improvements are expected and best ion implanted cells should be comparable to the best diffused junction cells. Implantation has unique characteristics which may allow higher performance than can be achieved by diffusion methods.

REFERENCES

1. Burrill, J., King, W., Harrison, S. and McNally, P., IEEE Trans. Elec. Dev., ED-14, No. 1, 10 (1967).

2. Sudbury, R., Stirrup, K. and Smith, D., Record of the Seventh Photovoltaic Specialists Conference, Pasadena, pp. 66 (1968).

3. Kirkpatrick, A., Bartels, F., Carnes, C., Ho, J. and Smith, D., Conference on the Effects of Lithium Doping on Silicon Solar Cells, Pasadena, NASA TM33-491, pp. 31 (1971).

4. Kirkpatrick, A., Minnucci, J. and Shaughnessy, T., "Silicon Solar Cells by Ion Implantation and Pulsed Energy Processing", Record of the Twelfth Photovoltaic Specialists Conference, Baton Rouge (1976).

5. Kirkpatrick, A., Minnucci, J. and Greenwald, A., IEEE Trans. Elec. Dev., ED-24, No. 4, 429 (1977).

6. Sigmon, T., Chu, W., Muller, H. and Mayer, J., Appl. Phys., 5, 347 (1975).

7. Graff, K., Pieper, H. and Goldbach, G., "Semiconductor Silicon 1973", pp 170, Electrochem. Soc., Princeton (1973).

8. Fischer, H. and Pschunder, W., Record of the Tenth Photovoltaic Specialists Conference, Palo Alto, pp. 404 (1973).

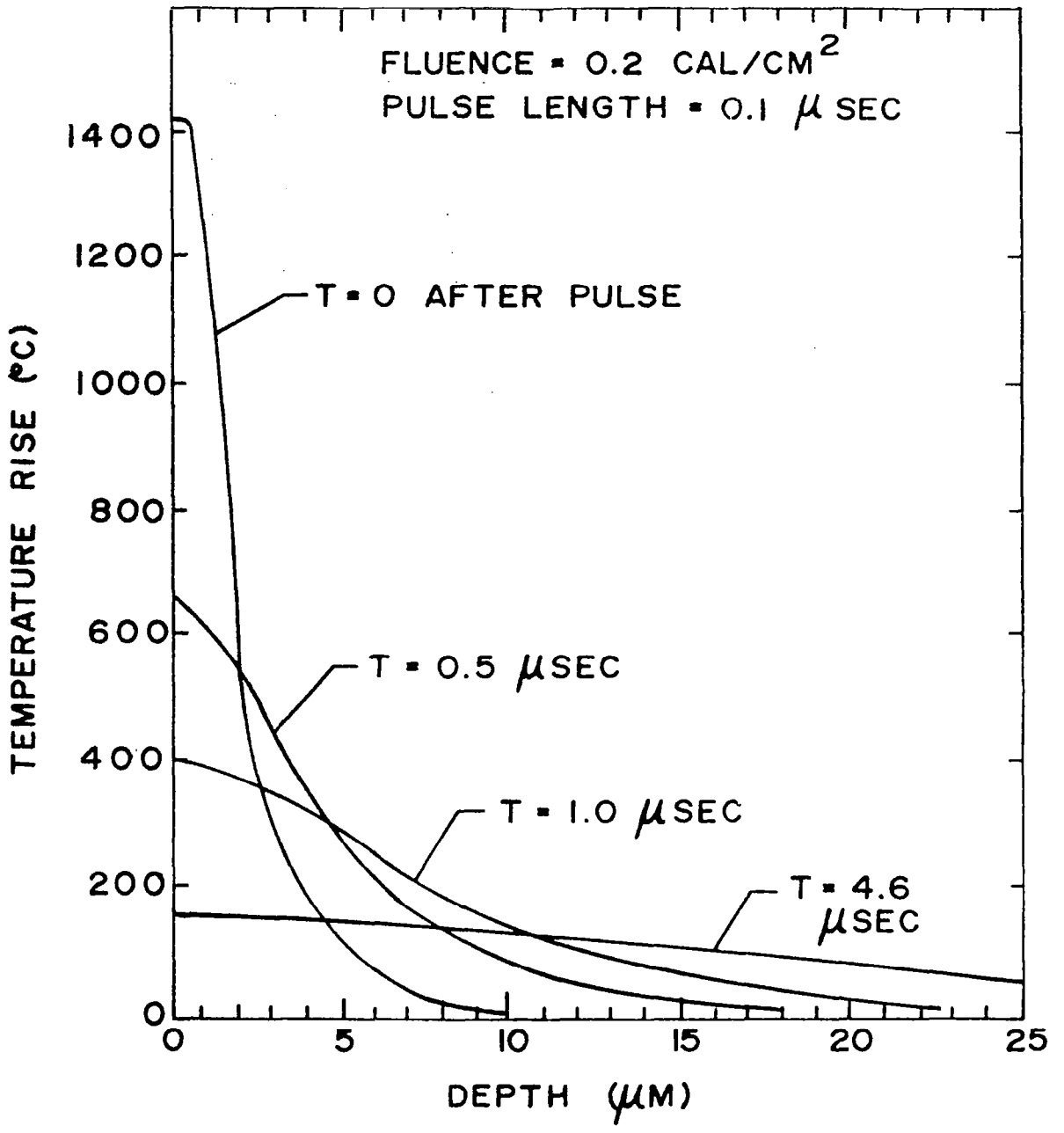

Figure 1. Temperature Profiles In Silicon Following Electron Beam Anneal Pulse

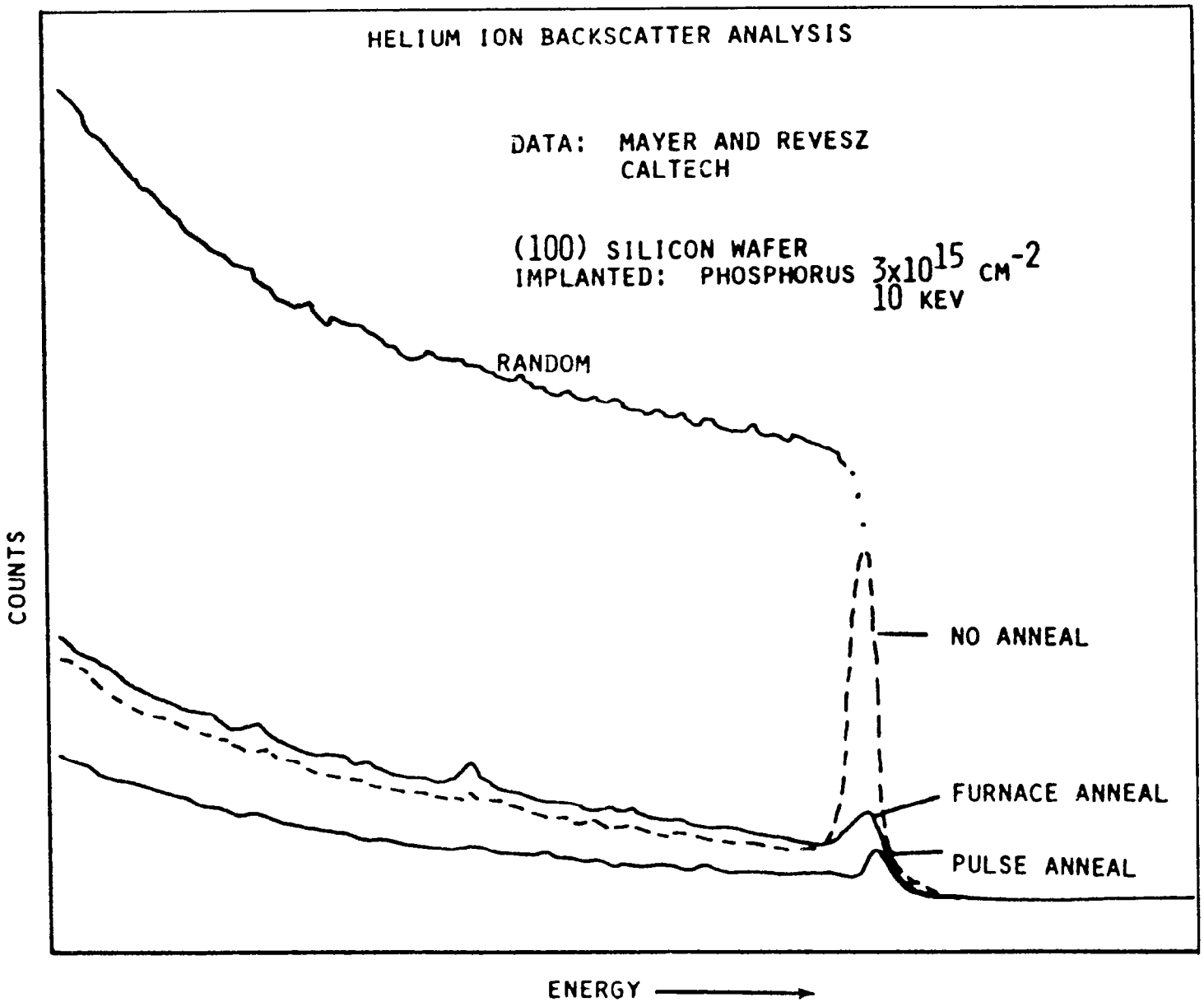

Figure 2. Helium Ion Backscattering From Furnace and Electron Beam Pulse Annealed Implanted Wafers

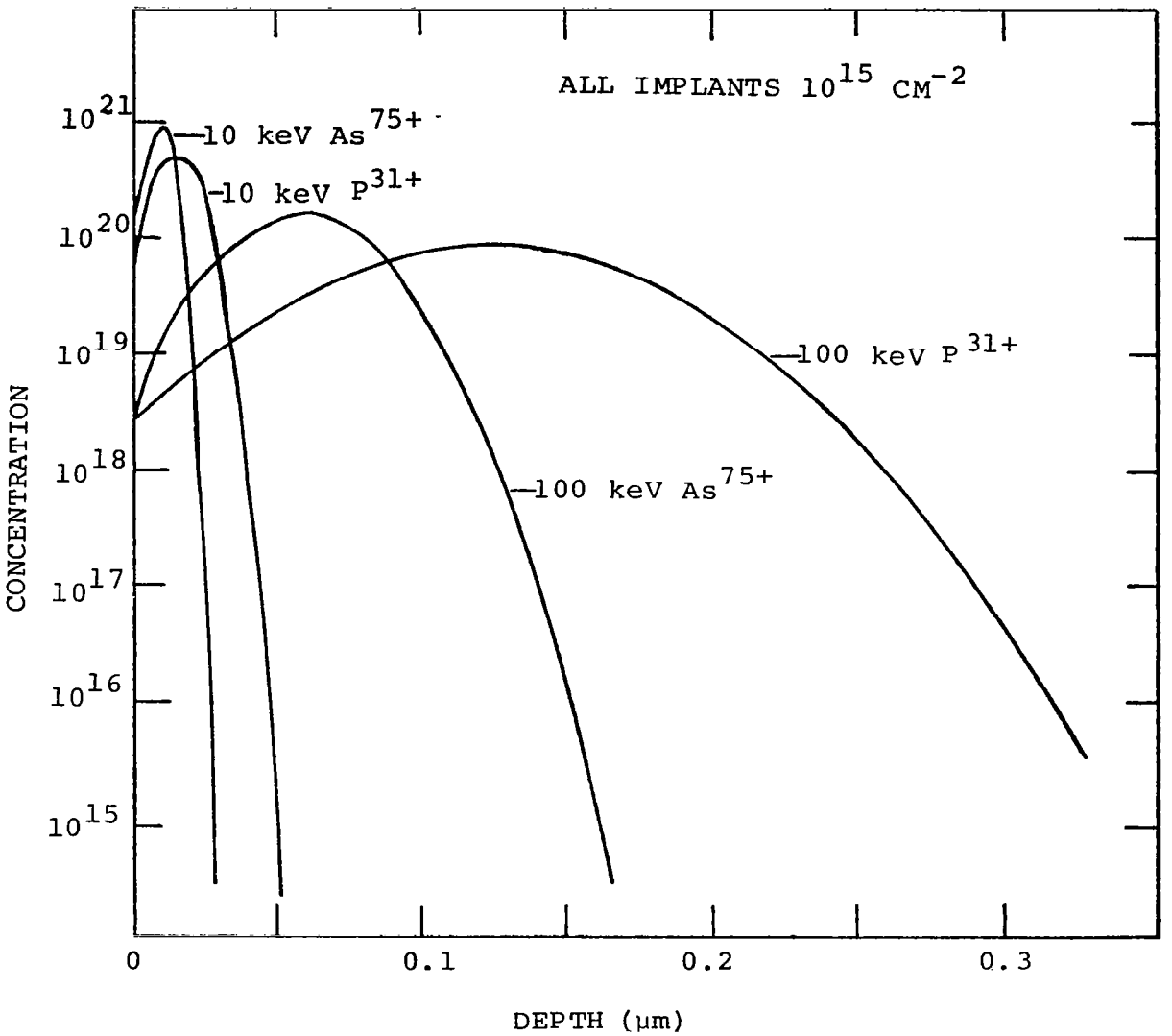

Figure 3. Representative Implanted Dopant Versus Depth Profiles

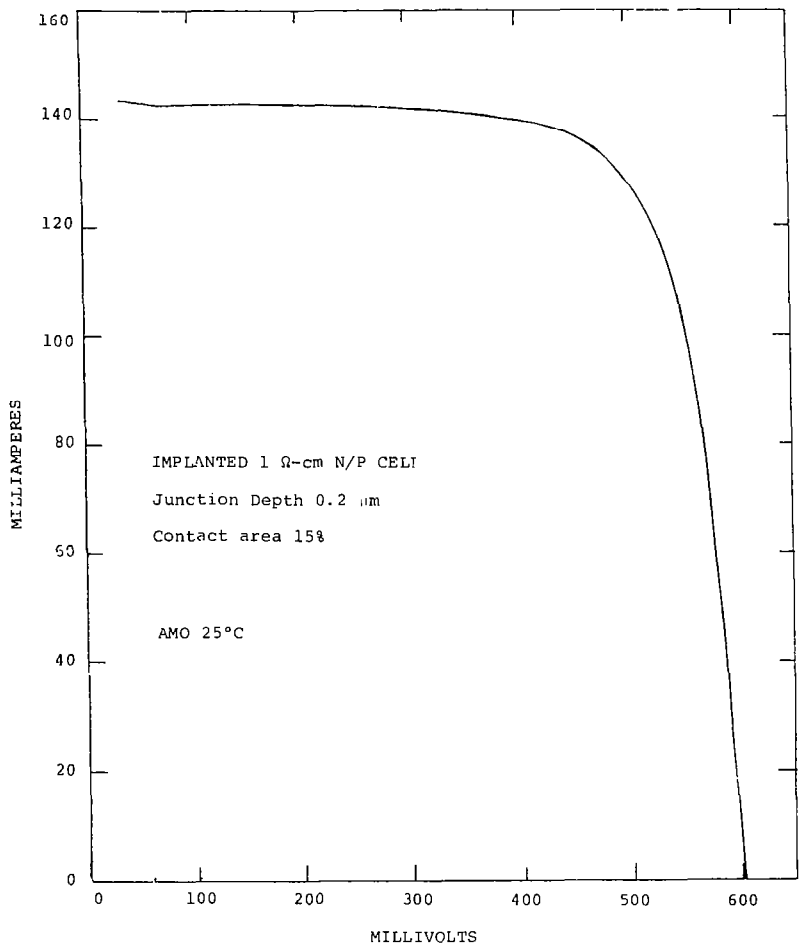

Figure 4. AMO I-V Characteristic of Ion Implanted 1 ohm-cm Cell

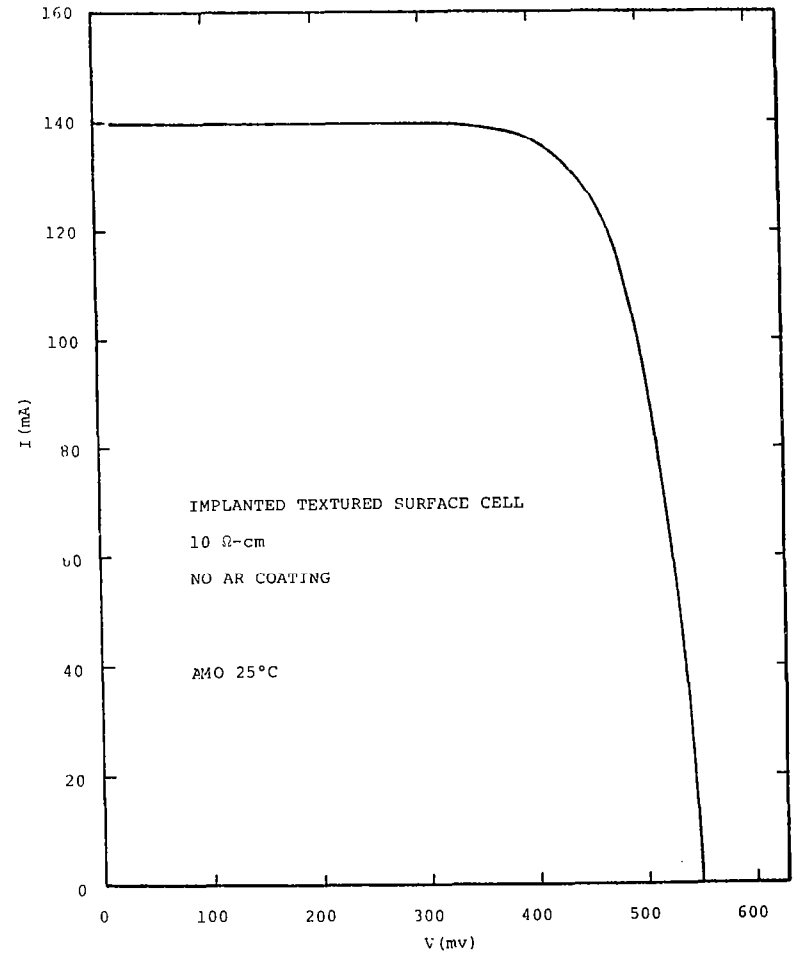

Figure 5. AMO I-V Characteristic of Implanted Textured Cell

12. TRANSMUTATION DOPING OF SILICON SOLAR CELLS*

R. F. Wood, R. D. Westbrook, R. T. Young, and J. W. Cleland
Oak Ridge National Laboratory

SUMMARY

Normal isotopic silicon contains 3.05% of ^{30}Si which transmutes to ^{31}P after thermal neutron absorption, with a half-life of 2.6 hours. This reaction can be used to introduce extremely uniform concentrations of phosphorus into silicon, thus eliminating the areal and spatial inhomogeneities characteristic of chemical doping. Annealing of the lattice damage in the irradiated silicon does not alter the uniformity of dopant distribution. Transmutation doping also makes it possible to introduce phosphorus into polycrystalline silicon without segregation of the dopant at the grain boundaries. The use of neutron transmutation doped (NTD) silicon in solar cell research and development is discussed.

INTRODUCTION

Certain impurity atoms can be introduced into a number of semiconducting materials by nuclear transmutation processes initiated by thermal neutron capture in a nuclear reactor (ref. 1). Silicon is a particularly attractive candidate for transmutation doping because it has only one isotope which transmutes to a new element and this is phosphorus, a standard n-type dopant in silicon. Normal isotopic Si contains 3.05% of ^{30}Si which transmutes to ^{31}P after thermal neutron absorption, with a half-life of 2.6 hours. The ^{28}Si and ^{29}Si isotopes transmute to ^{29}Si and ^{30}Si respectively but these processes do not directly alter the electrical properties of the material. There are no significant problems associated with induced radioactivity for phosphorus concentrations up to about 10^{16} cm^{-3}. Above this concentration, second thermal neutron absorptions by the ^{31}P atoms induce a radioactivity from ^{31}S which has a half-life of 14.3 days and requires extended cooling periods. The rate of introduction of phosphorus into silicon by the transmutation process is such that doping concentrations of interest to the semiconductor industry are readily attainable in many reactors.

Neutron transmutation doped (NTD) silicon provides four clearly identifiable advantages over silicon doped by more traditional chemical techniques. These are

---

*Research sponsored by the Energy Research and Development Administration under contract with Union Carbide Corporation.

1.) areal and spatial uniformity of dopant distribution;

2.) precise control of doping level;

3.) elimination of dopant segregation at grain boundaries in polycrystalline silicon; and

4.) superior control of heavy-atom contaminants.

Uniformity of doping has proved to be of importance in a number of device applications, particularly to high-power rectifiers and thyristors (ref. 2). The precise control of doping levels provides a method for very accurately compensating material to be used in radiation detectors (ref. 3).

NTD silicon has the disadvantage that the lattice damage introduced by the neutron irradiation must be annealed before the desired electrical properties can be recovered. However, it appears that in most applications the diffusion schedules used in device fabrication will be adequate to anneal the lattice damage.

In this paper, we shall discuss some possible advantages, related to items 1-4 listed above, of NTD silicon in solar cell applications. In this connection, we view transmutation doping as a research tool of potential importance in the investigation of the problems of areal and spatial inhomogeneities in high-efficiency single crystal silicon solar cells and of grain boundary effects and compensation in polysil cells. We assume a discrepancy of approximately five percentage points between the theoretically predicted and the experimentally obtained efficiencies of single crystal silicon solar cells still exists and that at least part of this discrepancy may be related to inhomogeneities in the dopant distribution. Our work in this area is still of a preliminary nature and therefore the primary goal of this paper is to acquaint the reader with the potentialities of transmutation doping and not to provide a body of well-developed results on photovoltaic applications.

CHARACTERISTICS OF NTD SILICON

It has been established that chemical doping methods introduce non-uniform distributions of the dopant in the form of swirls or striations (ref. 4) which may intersect the p-n junction in a silicon-based device and degrade its performance. These striations are eliminated in NTD silicon because the nuclear doping technique gives completely random distributions of the P atoms characteristic of nuclear transmutation processes. Figure 1 illustrates the type of fluctuations to be expected in conventionally doped silicon with an average resistivity of 50 Ω cm. This figure is schematic only but is based on data appearing in the literature; the maximum fluctuations are of the order of 15-20%. The dashed line for NTD silicon indicates that the resistivity fluctuations in the transmutation doped material are within the experimental error of the measurements. These fluctuations in conventionally doped material

occur on both a macroscopic scale as revealed by four-point probe measurements and on a microscopic scale as revealed by microscopic spreading resistance measurements. On both scales the fluctuations are virtually nonexistent in NTD silicon. There are two sources of concentration gradients in NTD silicon but these are of minor importance in practice. If the thermal neutron flux coming from the reactor has gradients associated with it, these will show up as slow variations in the transmutation-induced phosphorus concentration. These variations are easily eliminated by selected rotations and displacements of the silicon ingots in the reactor during irradiation. The other type of gradients is caused by self-shielding of the inner part of a cylindrical ingot by the outer part. In a cylindrical ingot with a four inch diameter it is estimated that self-shielding will give a variation of about 3% in the concentration from the outside to the center of the ingot.

Figure 2 shows a different characteristic of NTD silicon which may be of interest in solar cell research (ref. 5). From the known thermal neutron flux at a given site near the core of a reactor and from the irradiation time of the silicon sample it is possible to very accurately predict the total doping concentration achieved. The solid line on figure 2 shows that the free carrier concentration in NTD single crystal silicon, measured after the annealing of lattice damage, corresponds exactly to the predicted doping concentration. Of more interest are the results for polycrystalline silicon shown by the triangles. These data were obtained with samples prepared from chemical vapor deposited polysil with an average grain size as estimated from electron microscopy of $\sim$ 25 μm. They show that for this particular grain size the expected carrier concentration is obtained for doping levels above 10^{15} cm^{-3}. Similar measurements on polysil of much larger grain size show that the expected free carrier concentration is obtained at even lower doping levels. This data can be explained on the basis of a model for grain boundary effects developed by Seto (ref. 6) for polycrystalline silicon doped by ion implantation. According to this model, a minimum in the carrier mobility is evidence for free carrier trapping at the grain boundaries and against grain boundary aggregation of the dopant. In fact, the position of the minimum may be taken as a measure of the carrier concentration that is required to saturate the grain boundary effects in this type of material. One of the curves on figure 3 shows the behavior of the carrier mobility as a function of carrier concentration for a sample of the same material used in obtaining the data of figure 2. From Seto's model the average grain size is estimated to be $\sim$ 33 μm which is in very satisfactory agreement with the average grain size of $\sim$ 25 μm obtained from electron microscopy.

The data in figure 2 can now be interpreted as showing that below a certain doping concentration ($\sim 10^{15}$ cm^{-3}) a significant fraction of the carriers are trapped at grain boundaries (ref. 7). Above this concentration the fraction of carriers trapped becomes a relatively insignificant part of the total number of carriers. This interpretation shows clearly that there is no aggregation of dopant at the grain boundaries in NTD polycrystalline silicon. In contrast to this, measurements by Fripp (ref. 8) on conventionally doped small-grained polysil show that the resistivity does not begin to decrease from 10^5 ohm-cm until a dopant concentration of 10^{16} cm^{-3} is reached. Fripp has been able to interpret his results in terms of a model in which grain boundary segregation of the phosphorus is of major importance.

LATTICE DAMAGE

Transmutation doping introduces lattice damage which must be annealed out before the desired electrical properties can be obtained. At Oak Ridge we have carried out extensive studies of this lattice damage and its annealing characteristics. Generally speaking, the lattice damage can be roughly classified into two categories. The damage introduced by thermal neutrons by way of the so-called (n,γ) recoil process is thought to consist of relatively simple point defects such as divacancies, di-interstitials and vacancy-impurity clusters. It appears to resemble in many ways the type of damage introduced by electron and γ-ray irradiation which has been studied extensively in the past. Figure 4 shows the isochronal (20 min) annealing behavior of two 30 Ω cm samples of NTD silicon irradiated in a predominantly thermal neutron flux. It can be seen that virtually full recovery of the expected free carrier concentration is obtained at 400°C. The approximately 10% defect concentration remaining at 400°C may be due to the unavoidable presence of some fast neutron effects.

The lattice damage introduced by fast neutrons is much more complex than the thermal neutron damage. It consists of extended defect clusters which may contain as many as 1000 defects although the average cluster probably contains many fewer. This type of damage anneals at a substantially higher temperature than does the thermal neutron damage. Figure 5 shows the isochronal (20 min) annealing behavior of three samples of NTD silicon irradiated in a predominantly fast neutron flux. Full recovery of the carrier concentration occurs at about 750°C. With the possible exception of the minority carrier lifetime, all other electrical properties of the material are also recovered at this temperature.

EXPERIMENTAL SOLAR CELLS

We have tested experimental solar cells fabricated from both single crystal and polycrystalline NTD silicon as well as from conventionally doped material. These studies have primarily emphasized the characteristics of polysil cells and no concerted effort has been made to construct and test high efficiency single crystal cells. One problem we have encountered is a premature fall-off in the short circuit current as a function of dopant concentration. This may be due to incomplete annealing of lattice damage but it also may be related to our fabrication procedures. Both the open circuit voltage and the fill factor behave satisfactorily.

At best, our fabrication and testing facilities must be considered rather primitive compared to the most advanced industry standards. For example, we have not yet incorporated back surface fields nor applied antireflection coatings or etches. It is perhaps not surprising then that in our comparative studies to date we have found no clear-cut differences between single crystal cells made from NTD and conventional silicon. It should be kept in mind that we are looking for efficiency improvements of, at most, only a few percentage

points on an absolute scale. We believe that it will be necessary to utilize the most advanced cell technology and testing currently available to meaningfully test for such small improvements. Our research effort at Oak Ridge is almost entirely materials oriented and ultimately we will have to rely on outside assistance for the fabrication and testing of the highest efficiency NTD solar cells.

REFERENCES

1. Cleland, J. W.; Lark-Horovitz, K.; and Pigg, J. C.: Transmutation-Produced Germanium Semiconductors. Phys. Rev., vol. 78, no. 6, 1950, p. 814.

2. Haas, W. E.; and Schnoller, M. S.: Silicon Doping by Nuclear Transmutation. J. Electron. Mater., vol. 5, 1976, p. 57.

3. Gelezunas, V. L.; Seibt, W.; and Huth, G.: Uniform Large-Area High-Grain Silicon Avalanche Radiation Detectors from Transmutation Doped Silicon. Appl. Phys. Letters, vol. 30, no. 2, 1977, p. 118.

4. Kolbesen, B. O.; and Meyer, K. R.: Striations als Ursache von Knickstellen in pn-Übergängen von Leistungsbauelementen. Solid State Electron., vol. 17, 1974, p. 1087.

5. Cleland, J. W.; Westbrook, R. D.; Wood, R. F.; and Young, R. T.: Neutron Transmutation Doping of Polycrystalline Silicon. Proceedings NSF-ERDA National Workshop on Low Cost Polycrystalline Silicon Solar Cells. Published by Photovoltaics Branch, Division of Solar Energy, ERDA, 1976, p. 113.

6. Seto, J. Y. W.: The Electrical Properties of Polycrystalline Silicon Films. J. Appl. Phys., vol. 46, 1975, p. 5247.

7. Young, R. T.; Cleland, J. W.; and Wood, R. F.: Electrical Properties of Neutron Transmutation Doped Polycrystalline Silicon. Proceedings of the 12th IEEE Photovoltaic Specialists Conference, IEEE Conf. Record No. 76CH 1142 9ED (in press).

8. Fripp, A. L.; and Culotta, P. C.: Parameters Effecting the Resistivity of Polycrystalline Silicon. Proceedings NSF-ERDA National Workshop on Low Cost Polycrystalline Silicon Solar Cells. Published by Photovoltaics Branch, Division of Solar Energy, ERDA, 1976, p. 59.

9. Westbrook, R. D.; and Polgreen, T. L.: Neutron Transmutation Doped Silicon Solar Cells. Proceedings of the 12th IEEE Photovoltaic Specialists Conference, IEEE Conf. Record. No. 76CH 1142 9ED (in press).

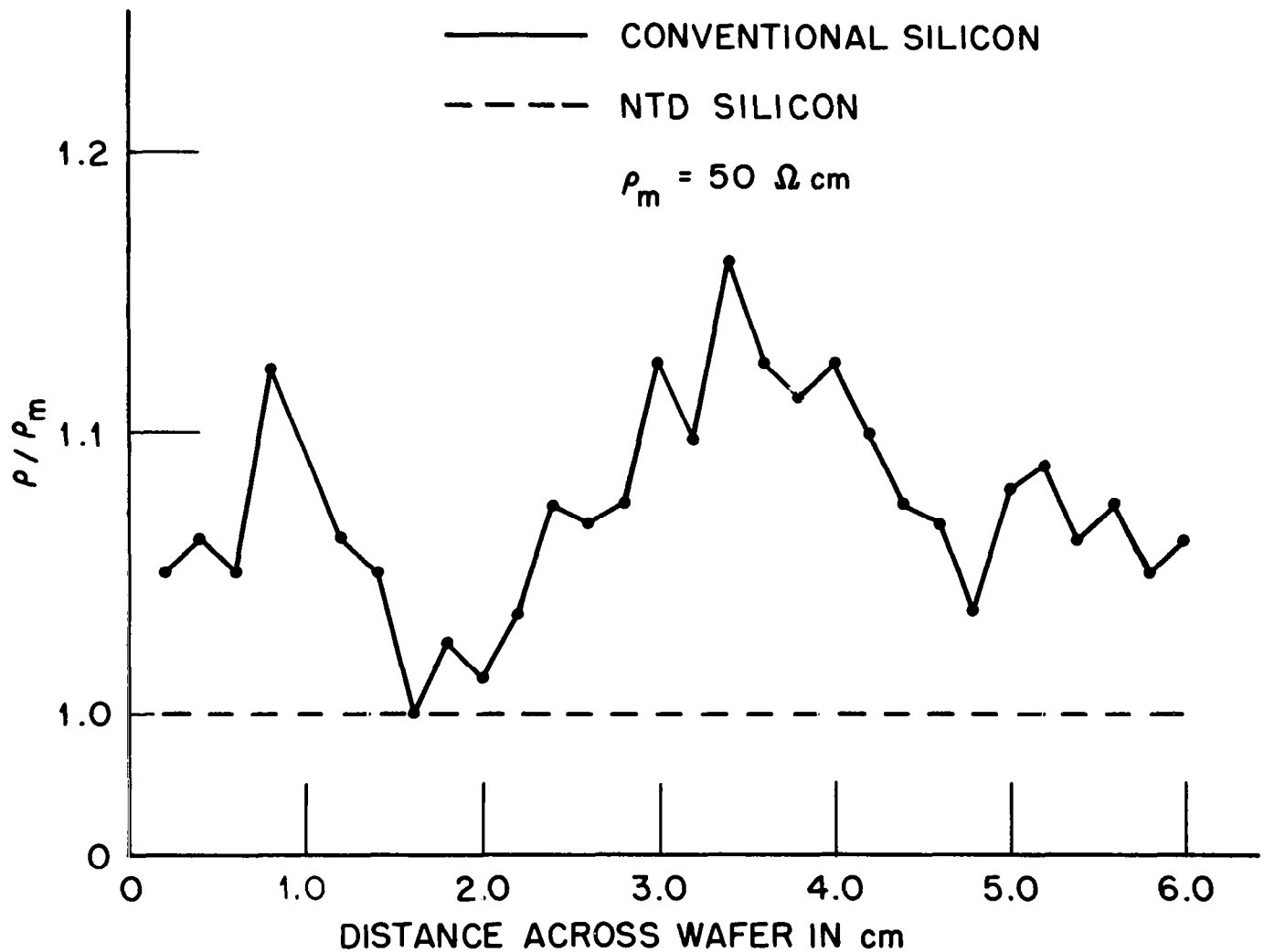

FIGURE 1. ILLUSTRATION OF RESISTIVITY FLUCTUATIONS IN SILICON

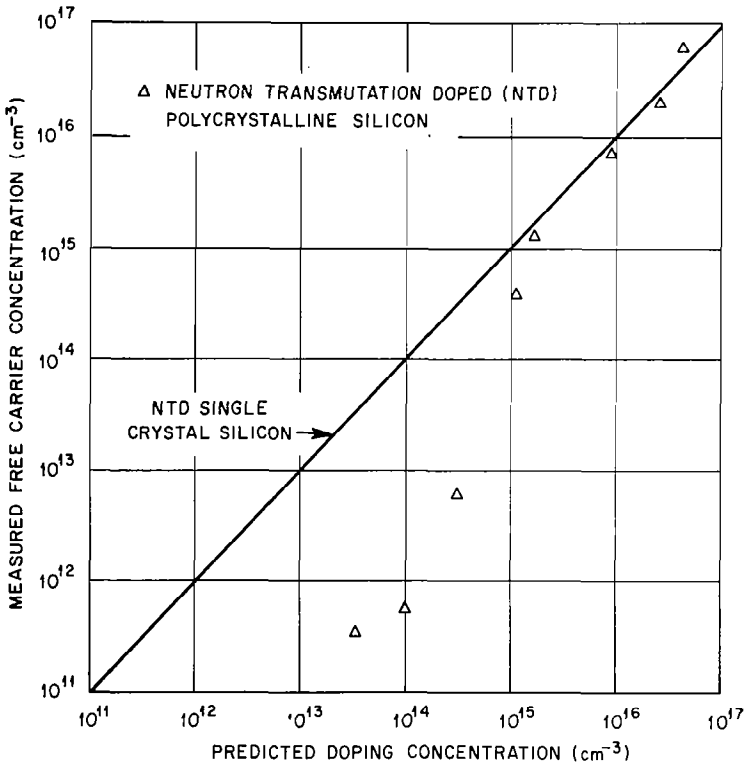

FIGURE 2. CARRIER CONCENTRATION VERSUS PREDICTED DOPING CONCENTRATION

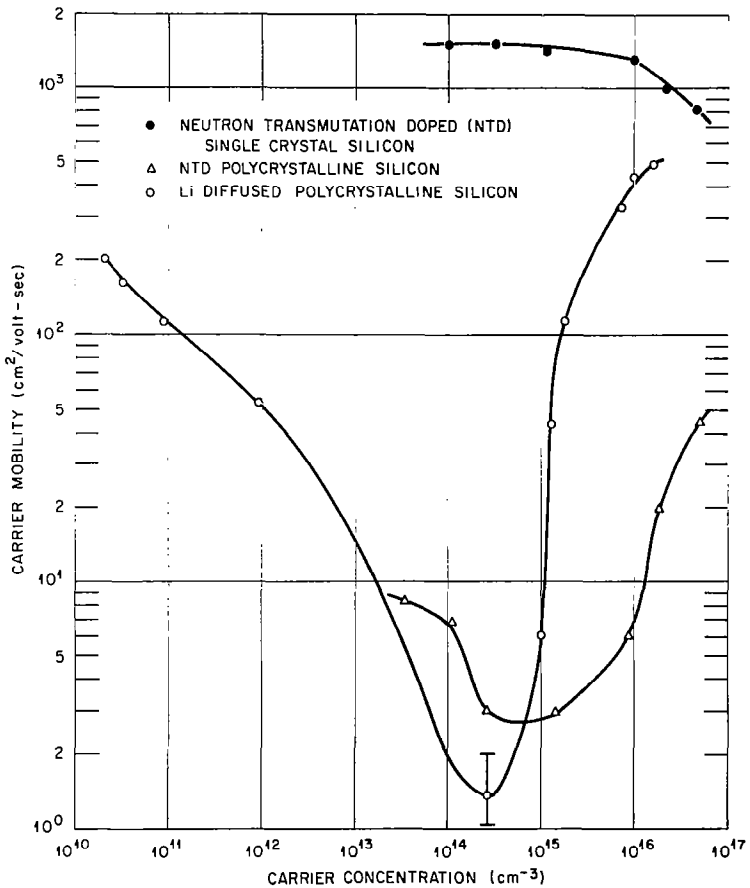

FIGURE 3. CARRIER MOBILITY VERSUS CARRIER CONCENTRATION

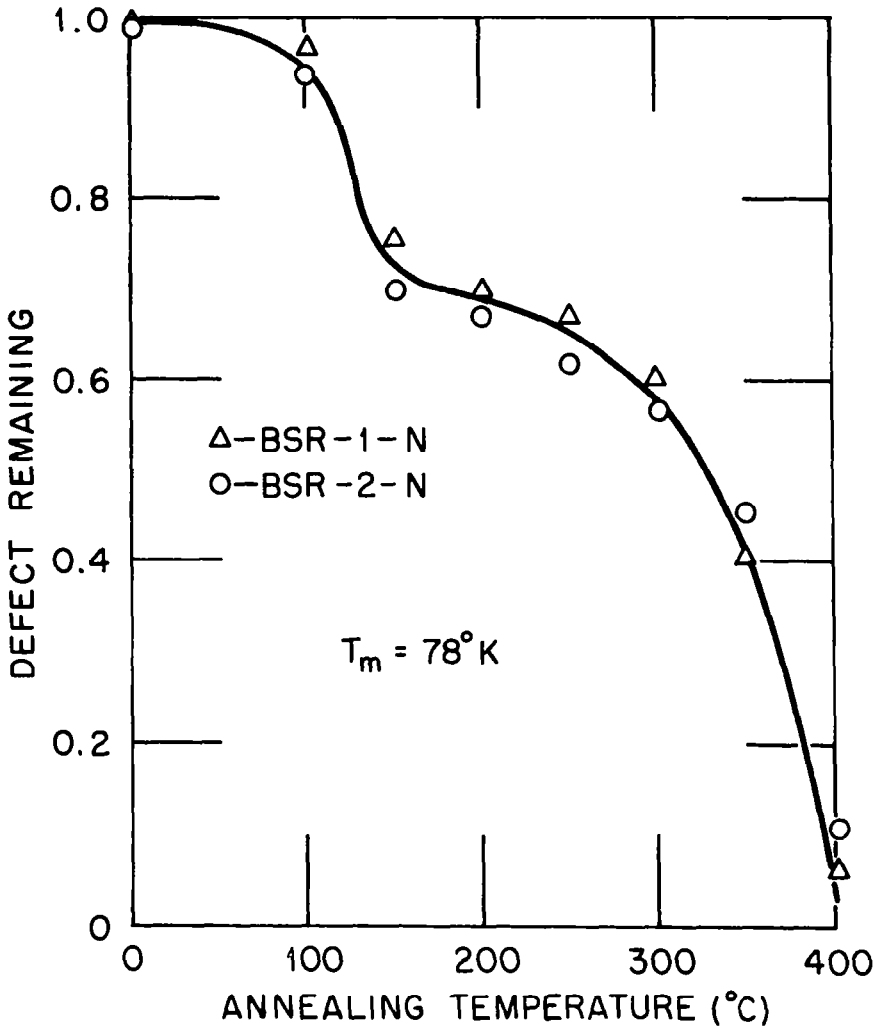

FIGURE 4. ANNEALING OF THERMAL NEUTRON DAMAGE

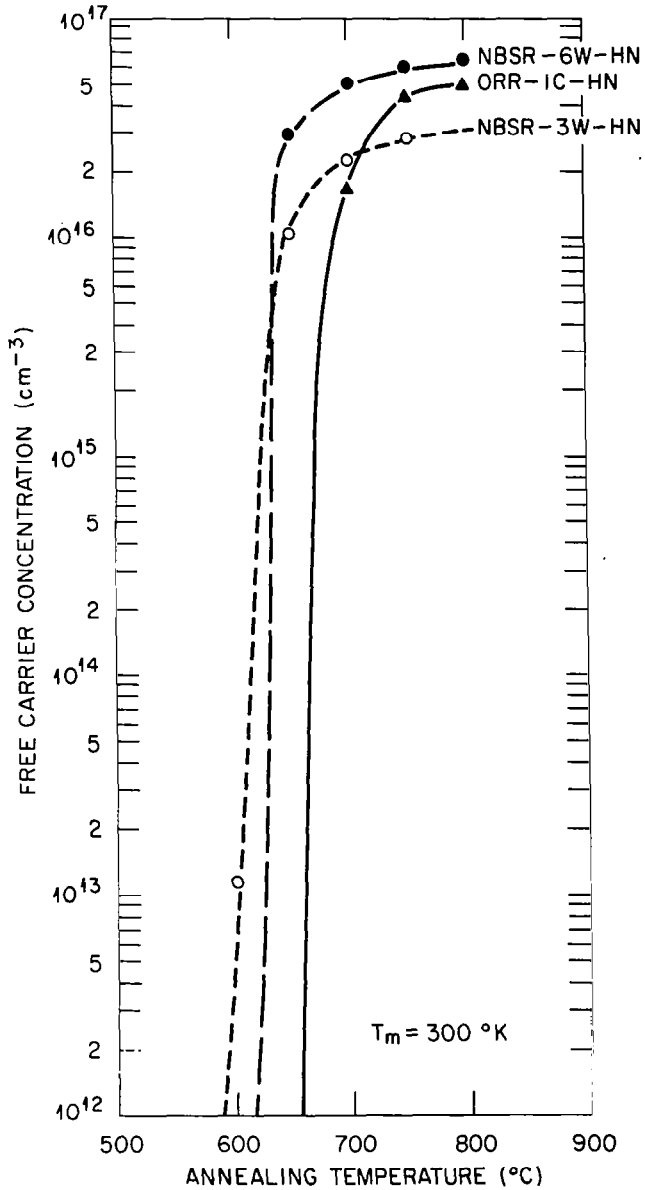

FIGURE 5. ANNEALING OF FAST NEUTRON DAMAGE

13. DEVELOPMENTS IN VERTICAL-JUNCTION SILICON SOLAR CELLS*

J. Lindmayer, C. Wrigley and J. Wohlgemuth

Solarex Corporation
Rockville, Maryland

ABSTRACT

Recent work on non-reflective vertical-junction silicon solar cells has resulted in high conversion efficiency radiation-resistant solar cells. New techniques of oxidation growth and the use of photolithography enable the use of an orientation dependent etch producing grooves 5-10 microns wide and over 100 microns deep. These silicon wafers are then processed into solar cells with all of the processes performed at temperatures compatible with producing high efficiency solar cells. Most of the photogenerated carriers are created in the walls where they are within a few microns of the collecting junction. Consequently, degradation of carrier diffusion length due to radiation has a considerably reduced effect on collection efficiency. These 2 cm x 2 cm vertical junction silicon solar cells have exceeded 13% AMO efficiency and have shown superior radiation resistance.

INTRODUCTION

Vertical junction solar cells were initially proposed by J.F. Wise (Ref.1) and W.P. Rahilly (Ref. 2) to alleviate the degradation of solar cells in space due to radiation damage. The vertical junction cells have been under development for the past few years, initially at Texas Instruments (Ref.3) and for the past year at Solarex Corporation (Ref. 4 and Ref. 5).

* Supported by Wright-Patterson Air Force Base, Aero Propulsion Laboratory Contract F33615-76C-2058, (W.P. Rahilly).

The vertical junction cell consists of deep grooves etched into the surface separated by thin walls. The solar cell junction follows the surface up and down the walls so that any carriers generated in the walls are very close to the collecting junction. This means that the carriers do not have to travel far to be collected. Therefore, they are less influenced by degredation of the lifetime during irradiation. Early attempts in realizing this device resulted in low cell efficiencies. Recent work at Solarex abruptly improved the efficiencies of the vertical junction silicon solar cells. The vertical junction cells today are high efficiency radiation resistant solar cells.

EXPERIMENTAL PROCEDURES

Under certain conditions alkaline solutions anisotropically etch silicon. Etch rate differences of 400 to 1 have been obtained (Ref. 6). Since it is the 111 plane that etches slowly, the etching is performed in aligned 110 silicon wafers. The difference in etching rates between lateral and vertical silicon removal enables grooves 5 to 10 microns wide and 100 microns deep to be etched into the surface. Figure 1 is a diagram of the geometry.

To etch 100 micron deep grooves into silicon an effective alkaline etchant mask is required. Thermally grown silicon dioxide can be used as such a mask, but it is slowly dissolved by the etchant. Therefore, it is necessary to use a layer of oxide several thousand Angstroms thick in order to etch the deep grooves. Normal thermal oxidation will not produce such thick layers of oxide at temperatures low enough to be compatible with the fabrication of high efficiency solar cells.

As is known, phosphosilicate glasses form readily during solar cell diffusions. This oxide alone is insufficient, but to improve the situation the following procedure has been performed. Silicon slices were diffused with phosphorous at temperatures between 800°C and 860°C for several minutes to grow a thin layer of phosphosilicate glass. Then the slices were exposed to steam while at the same temperature, resulting in the growth of an oxide of the required thickness. This glass was then employed as the mask for the alkaline etchant.

The required pattern was placed on the surface by photoresist techniques. Initial samples were aligned to pre-etched alignment marks to optimize the anisotiopic etching rate. However, later samples were optically aligned to an X-ray

oriented flat with no appreciable change in the resultant cells. The oxide was etched away to open 5 micron wide 122 mil long channels spaced 15 microns between centers. Then the orientation dependent etch produced 100 micron deep grooves. The remainder of the oxide is then removed. An isotropic etch is performed to remove the thin diffused layer and round the edges of the walls.

Figure 2 is a scanning electron microscope picture of a vertical junction cell broken perpendicular to the grooves. Figure 3 is an edge-on view of the same sample taken from a different angle and at a different magnification. Figures 4 and 5 are top views of the grooves and walls showing the buss bar end. Each exposed plane in the grooves is a 111 plane. The final thickness of the wall depends upon how well the initial mask was aligned to the 111 plane, usually varying from 5 to 10 microns wide.

These orientationally dependent etched silicon wafers are fabricated into solar cells by refined processes that are similar to those employed in the fabrication of planar cells. While extra care must be taken to protect the walls themselves, the basic structure of the cell is sufficiently sturdy to process without excess breakage.

RESULTS

Vertical junction solar cells have been fabricated with AMO efficiencies of greater than 13%. Figure 6 shows the I-V characteristics of a 2 cm x 2 cm cell at AMO. Fill factors of over 0.78 have been obtained for these cells. These cells exhibit excellent short circuit currents and open circuit voltages that are compatible with high efficiency cells.

Two major misconceptions about vertical junction cells have been erased by this research program. The first misconception was that deep in the narrow grooves the walls could not be uniformly diffused. Capacitance measurements have shown that the actual junction area is 10 to 20 times the area of planar cells which corresponds to the actual change in surface area. The second misconception was that the vertical junction solar cells would exhibit low photovoltages due to the large reverse saturation current. This has also turned out not to be true since the walls are depleted. The reverse saturation current in the vertical junction cells is nearly equal to that in planar cells. Therefore, the vertical junction cells have photovoltages almost as high as planar cells.

Almost all of the light entering the grooves is eventually absorbed into the silicon. Even without any tapering etches the vertical junction solar cells are nearly non-reflecting and with the proper tapering etch they can be made even more so. Under these conditions anti-reflective coatings have a modest effect, usually only raising the efficiency around 1%. Because of the large surface area of the vertical junction solar cell the AMO current density in the surface layer is much lower than for planar cells. Therefore, series resistance problems in the surface layer are reduced and the current collecting buss bars can be spaced farther apart allowing a greater portion of the surface to be available for absorbing energy. Therefore, vertical junction solar cells have produced excellent short circuit currents and have good fill factors.

Vertical-junction silicon solar cells have been subjected to electron, proton and neutron irradiation to stimulate their expected performance in space. All tests so far indicate that the radiation resistance of the vertical-junction cell is far superior to the degredation rates for other high efficiency silicon cells. Irradiation with 1 MeV electrons to accululated doses up to 5×10^{15} per square centimeter produced only one-half the degredation in vertical-junction cells that it did in similarly processed planar cells. On the power versus fluence plot the degredation slope for vertical-junction cells is one-half that for planar cells, indicating that the radiation resistants is fundamentally different from planar cells.

CONCLUSIONS

The work with vertical-junction silicon solar cells indicates that high efficiency cells are obtainable. As more cells are being made in the laboratory the learning experience indicates that fabrication of these cells is practical. With their significant increase in radiation resistance these cells should play an extremely important role in future space applications.

REFERENCES

1. Wise, J.F.: Silicon Solar Cell. Patent Application Serial Number 579,801.

2. Rahilly, W.P.: Vertical Multijunction Solar Cells. Conference Record of the Ninth IEEE Photovoltaic Specialists Conference. May, 1972, pp. 44-52.

3. Lloyd, W.W.: Fabrication of an Improved Multijunction Solar Cell. Conference Record of the Eleventh IEEE Photovoltaic Specialists Conference, 1975, pp. 349.

4. Lindmayer, J. and Wrigley, C.: New Developments in Vertical-Junction Solar Cells. Conference Record of the Twelfth IEEE Photovoltaic Specialists Conference, Nov. 1976.

5. Lindmayer, J. and Wrigley, C.: Advanced Vertical-Junction Silicon Solar Cells. Conference Record of the AIAA Conference on the Future of Aerospace Power Systems, March, 1977.

6. Kendall, D.L.: On Etching Very Narrow Grooves in Silicon. Applied Physics Letters, Vol.26, Feb. 1975, pp. 195.

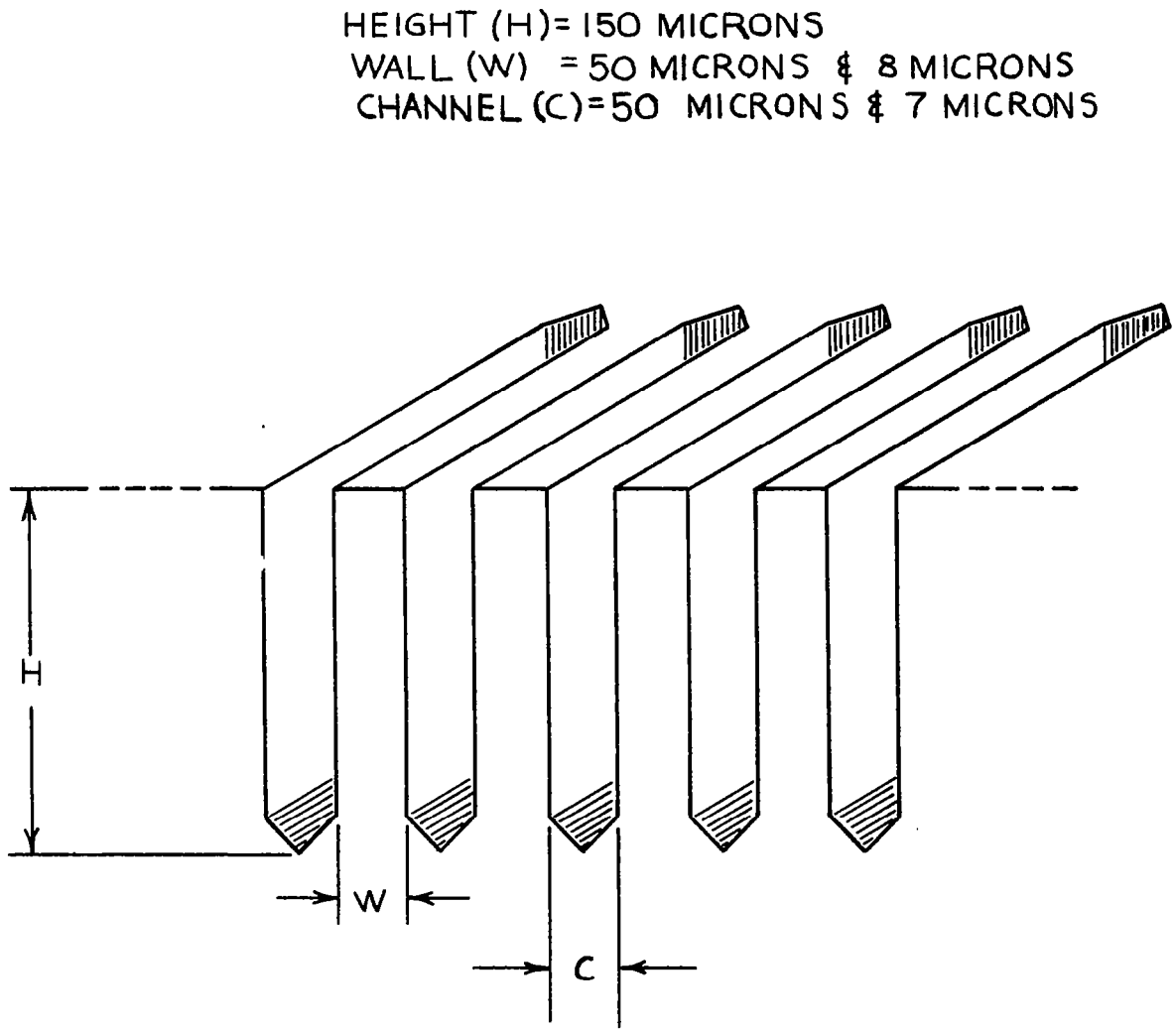

Figure 1. Structure of Vertical Junction Solar Cell

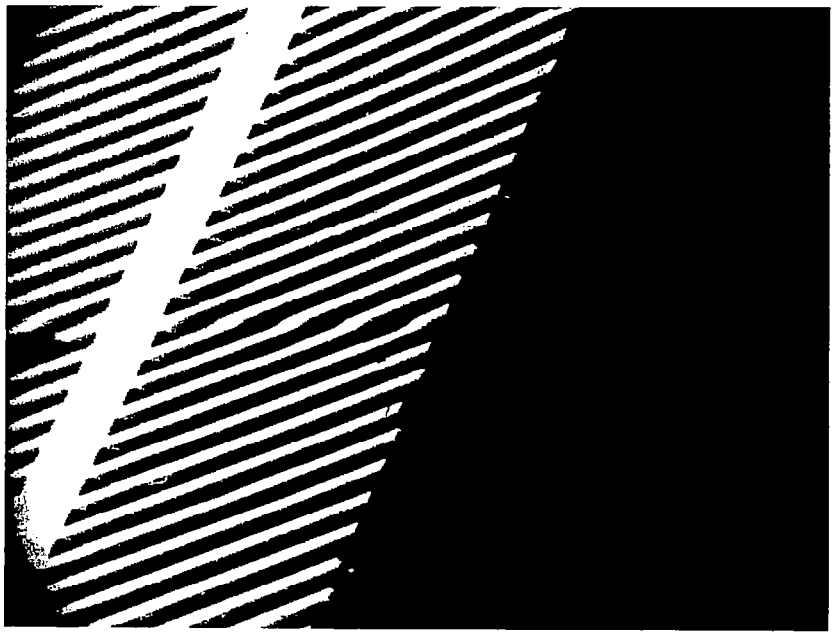

Figure 2.
Scanning electron microscope picture at a magnification of 250 X of a vertical junction cell broken perpendicular to the grooves.

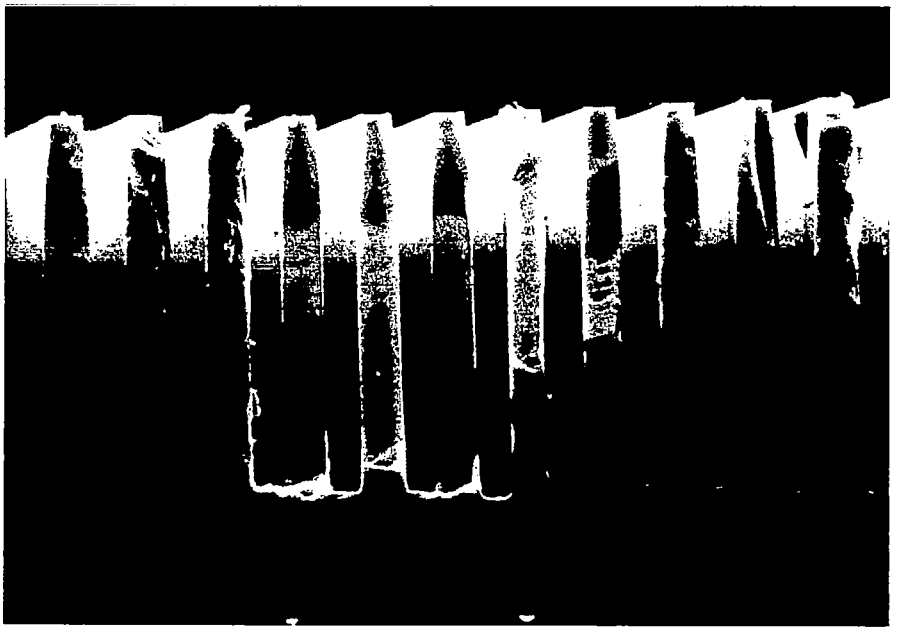

Figure 3.
SEM at 500 X of the same sample as Figure 2, but at a different angle.

Figure 4.
SEM picture at 1500 X of the buss bar end of the grooves.

Figure 5.
SEM picture at 3000 x of the buss bar end of the grooves.

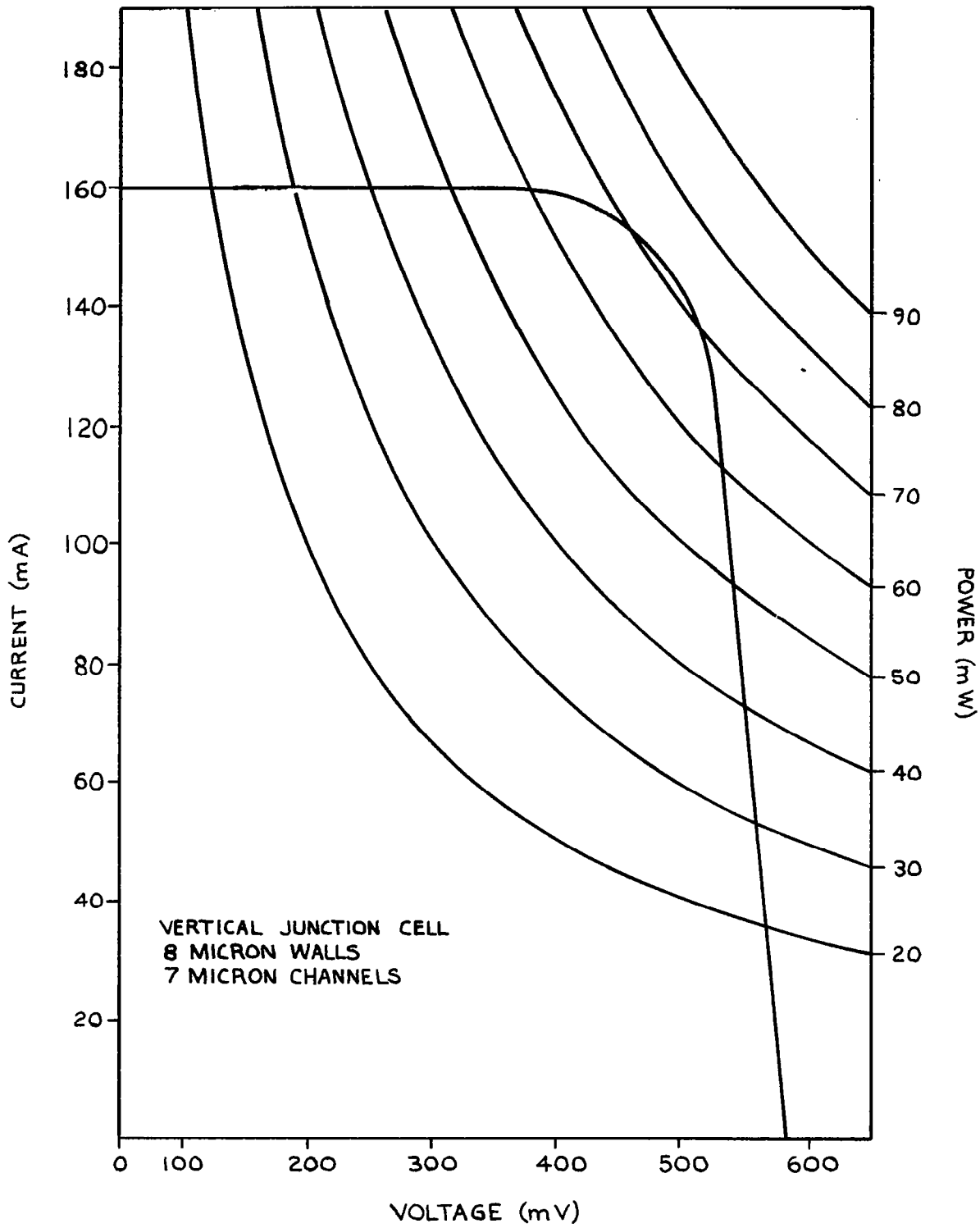

Figure 6. I-V characteristics at AMO for a thin-wall 2 cm x 2 cm Vertical Junction silicon solar cell.

14. Project STØP (Spectral Thermal Optimization Program)

L. J. Goldhammer, R. W. Opjorden, G. S. Goodelle, and J. S. Powe
Space and Communications Group
Hughes Aircraft Company

Abstract

The purpose of Project STØP is the Spectral Thermal Optimization of solar cell configurations for various solar panel applications. The method of optimization depends upon varying the solar cell configuration optical characteristics to minimize panel temperatures, maximize power output and decrease the power delta from beginning of life to end of life. Four areas of primary investigation are as follows:

1) Testing and evaluation of ultraviolet resistant coverslide adhesives, primarily FEP as an adhesive;
2) Examination of solar cell absolute spectral response and corresponding cell manufacturing processes that affect it;
3) Experimental work with solar cell manufacturing processes that vary cell reflectance (solar absorptance); and
4) Experimental and theoretical studies with various coverslide filter designs, mainly a red rejection filter.

The Hughes' solar array prediction program has been modified to aid in evaluating the effect of each of the above four areas on the output of a solar panel in orbit. The computer program can accept the characteristics of any type of solar cell, coverslide filter design, and solar panel design. The resulting output of the solar array is calculated for both beginning of life and end of life mission conditions with the aid of this computer program. The effect from each area of interest can then be evaluated for the effect on the output of a solar panel in space.

PROJECT STOP (SPECTRAL THERMAL OPTIMIZATION PROGRAM) APPROACH

HUGHES

VARY SOLAR CELL CONFIGURATION OPTICAL PROPERTIES TO

- MINIMIZE PANEL TEMPERATURES
- MAXIMIZE POWER OUTPUT
- DECREASE POWER Δ FROM BOL TO EOL
- EVALUATE SOLAR PANEL AS PART OF SPACECRAFT SYSTEM

AREAS OF PRIMARY INVESTIGATION

- CONTINUED TEST OF UV RESISTANT COVERSLIDE ADHESIVE(S) – FEP
- EXAMINATION OF SOLAR CELL ABSOLUTE SPECTRAL RESPONSE AND CORRESPONDING CELL MFG PROCESSES THAT AFFECT IT
- EXPERIMENTAL WORK WITH CELL MFG PROCESSES THAT VARY SOLAR CELL REFLECTANCE (α_S)
- EXPERIMENTAL AND THEORETICAL STUDIES WITH VARIOUS COVERSLIDE FILTER DESIGNS

PROJECT STOP (SPECTRAL THERMAL OPTIMIZATION PROGRAM) METHOD

HUGHES

- MODEL CELL PERFORMANCE WITH INPUTS FROM AREAS OF INVESTIGATION AND TEST
- VARY CELL PROCESSES AND COVERS TO CONFIRM VALIDITY OF APPROACH

TESTING OF FEP/RED FILTER

HUGHES

FEP

- 2 3/4 YEARS IN SPACE ON ATS-6 EXPERIMENT
- 2025 SUN HR UV EXPOSURE
- ELECTRON IRRADIATION
- SHEAR TESTING
- THERMAL CYCLING

RED FILTER

- HUMIDITY EXPOSURE
- ABRASION
- PEEL TEST
- TRANSMISSIVITY
- ELECTRON IRRADIATION
- UV EXPOSURE

FEP UV IRRADIATION RESULTS

HUGHES

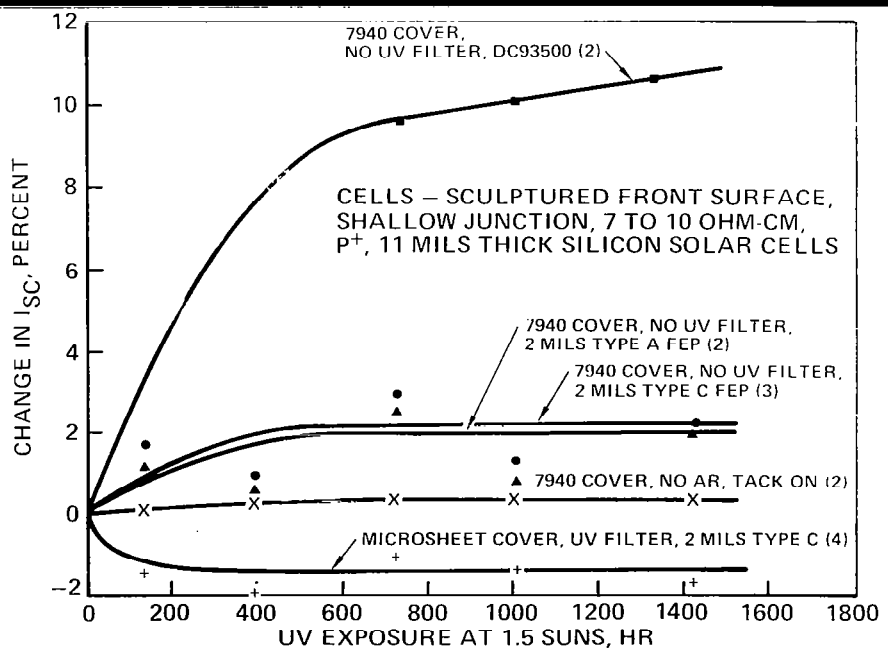

FEP ELECTRON IRRADIATION RESULTS

HUGHES

COVER ASSEMBLY	FLUENCE LEVEL, E/CM^2		
	4×10^{13}	4×10^{14}	1×10^{15}
7940 QUARTZ/UV FILTER DC 93500	0.95	0.80	0.74
7940 QUARTZ*/TYPE A	0.94	0.79	0.73
7940 QUARTZ*/TYPE C	0.94	0.78	0.74

*NO UV FILTER

SOLAR CELL/ FILTER REFLECTANCE PROPERTIES

HUGHES

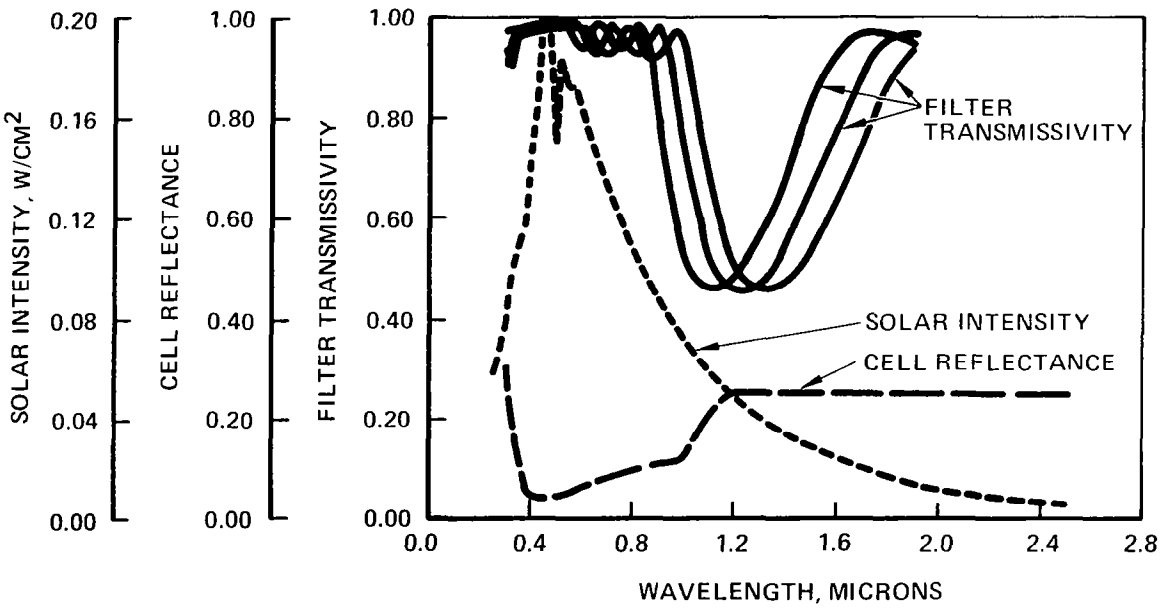

CELL ABSOLUTE SPECTRAL RESPONSE

HUGHES

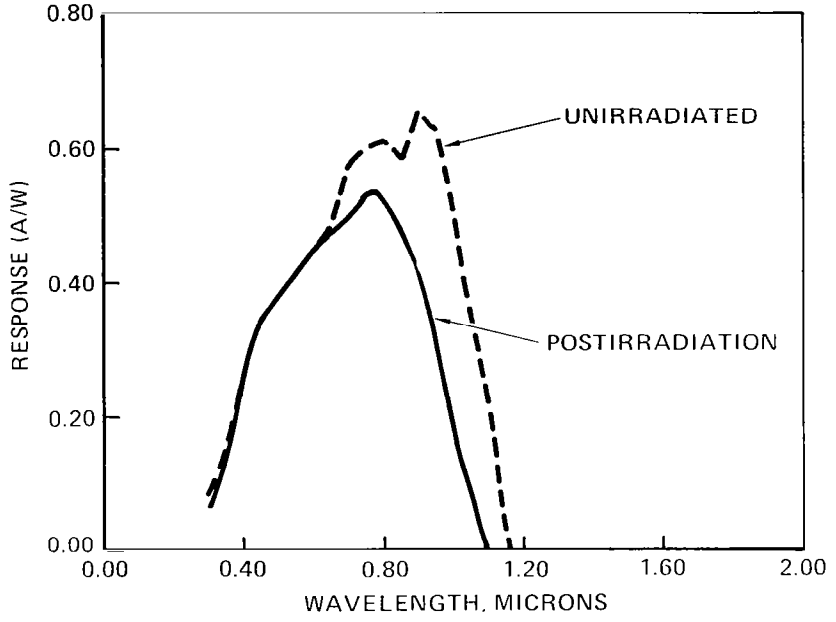

76229-10

HUGHES

COMPUTER PROGRAM FLOW

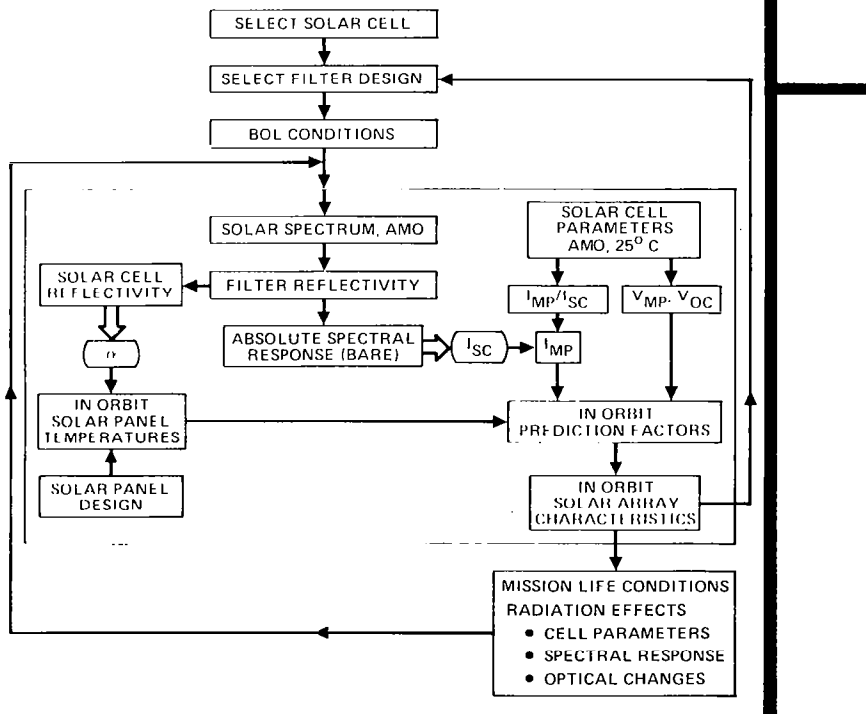

76229-8

RED FILTER – EXPECTED RESULTS

HUGHES

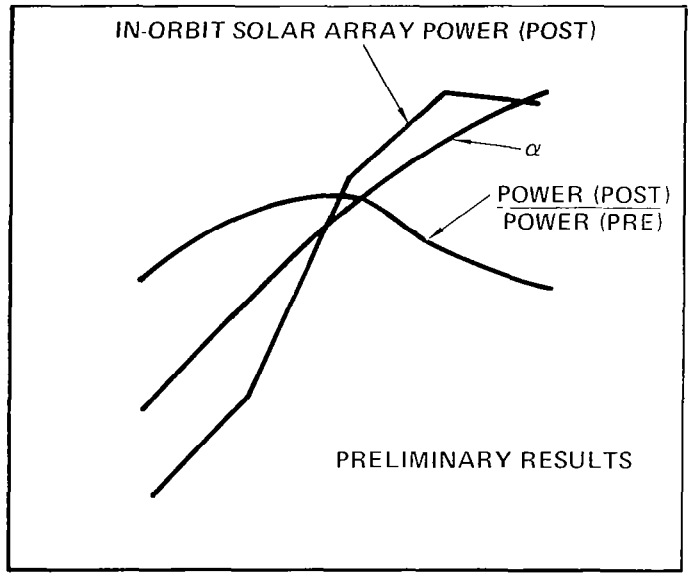

λ_C 50% CUTOFF (RED FILTER)

PROJECT STOP (SPECTRAL THERMAL OPTIMIZATION PROGRAM) PRESENT STATUS

HUGHES

UV RESISTANT COVERSLIDE ADHESIVE(S)

- COMPLETE SHEAR TESTS OF FEP SAMPLES
- COMPLETE THERMAL CYCLE TESTS OF FEP SAMPLES
- INVESTIGATING OTHER POSSIBLE APPROACHES

CELL MFG PROCESSES AFFECTING CELL SPECTRAL RESPONSE

- BACKSIDE REFLECTANCE
- MULTILAYER AR COATINGS

EXPERIMENTAL WORK ON CELL PROCESSES THAT VARY SOLAR CELL REFLECTANCE

RED FILTER

- VARYING 50% POINT
- CROSS CONFIRM WITH MODEL PREDICTIONS

EVALUATING SOLAR PANEL/SPACECRAFT DESIGN

15. High Efficiency GaAs Solar Cells

Gilbert H. Walker, Edmund J. Conway, and Charles E. Byvik
NASA Langley Research Center

Introduction

This paper describes the present status of the GaAlAs/GaAs heteroface solar cell program. Research has been conducted on contract, on grant, and in-house. Studies have been concentrated on GaAlAs/GaAs heteroface solar cells; however, some research has been conducted on thin junction, diffused GaAs solar cells. Emphasis has been on obtaining high efficiency (18% to 20%) GaAs solar cells. Two problems that have limited the efficiency of GaAs solar cells are the high recombination velocity of carriers near the surface and the low minority carrier diffusion length in n-GaAs.

Diffused GaAs Solar Cells

One method to reduce the effect of surface recombination velocity is place the p-n junction very near the front surface. This effect has been investigated on contract with IBM-Thomas J. Watson Research Center.

Diffused GaAs solar cells were prepared. Using anodizing-removal techniques, successive layers were removed from the surface of the solar cells. Alternately the solar cell properties were measured, thereby producing solar cell property data as a function of junction depth. Figure 1 is a plot of spectral response at junction depths of 500 Å, 1000 Å, and 2000 Å. The spectral response even for a junction depth of 500 Å does not reach the dotted theoretical spectral response curve. The reason for this is not fully understood, but could be caused by the lack of an electrical field in the surface layer. Figure 2 shows the short-circuit current density and the efficiency as a function of junction depth. The maximum efficiency of 10.5% was obtained at a junction depth of 500 Å.

GaAlAs/GaAs Heteroface Solar Cells

The most effective method found to date for reducing the effect of surface recombination on GaAs solar cells is to epitaxially grow a window layer of GaAlAs on the surface of the GaAs solar cell. Another consideration is the low minority carrier diffusion length of the base GaAs. Under contract to NASA Langley Research Center, IBM-Thomas J. Watson Research Center has developed a technique for improving the diffusion length of the base material as part of an epitaxial growth process. A conventional Ga-Al-As-Zn melt which is undersaturated with As is placed over the GaAs substrate. The melt, since it is undersaturated with As, etches back the surface of the substrate and at the same time getters impurities from the substrate, hence, improving the diffusion length. GaAlAs/GaAs solar cells were grown using this etch-back epitaxy technique. The spectral response of one of these cells is shown in figure 3.

The lower curve is for the cell without an antireflection coating while the upper curve is for the cell with an antireflection coating. Table 1 shows the efficiency of three such small area cells. The maximum efficiency is 18.51% air mass zero.

Electrical Contacts

The use of GaAs solar cells at high temperatures will be dependent on the stability of the electrical contacts. As part of the NASA Langley Research Center in-house research program, fundamental studies of electrical contacts are being conducted.

Since the palladium-silver system forms low resistance contacts to GaAs, a study is being conducted to determine the high-temperature stability of palladium on GaAs. As part of this study palladium films 500 Å thick were sputtered on GaAs and heated in vacuum for 1 hour. The samples were then placed in an Auger spectrometer. By alternately sputtering and measuring the Ga and As Auger intensities, the distribution of Ga and As in the palladium films can be determined. Figures 4 and 5 show the relative Auger intensities of Ga and As in palladium films heated for 1 hour. At 300°C both Ga and As have migrated to the surface of the palladium films, while at 250°C the Ga and As are still below the palladium surface. This study indicates that for high-temperature operation of GaAs solar cells with palladium contacts, a diffusion barrier will be needed.

Continuing Program

With the attainment of the 18.51% efficiency, the NASA Langley GaAs solar cell research program will begin optimizing the cells for high temperature and radiation stability. The approach will be fundamental with the objective of optimizing the cells by obtaining a fundamental understanding of the degradation processes.

Table 1 GaAlAs / GaAs SOLAR CELLS

Voc (VOLTS)	Jsc (mA/cm^2)	FF	N (%)
1.015	33.10	0.745	18.51
0.990	33.00	0.757	18.35
0.998	32.07	0.771	18.31

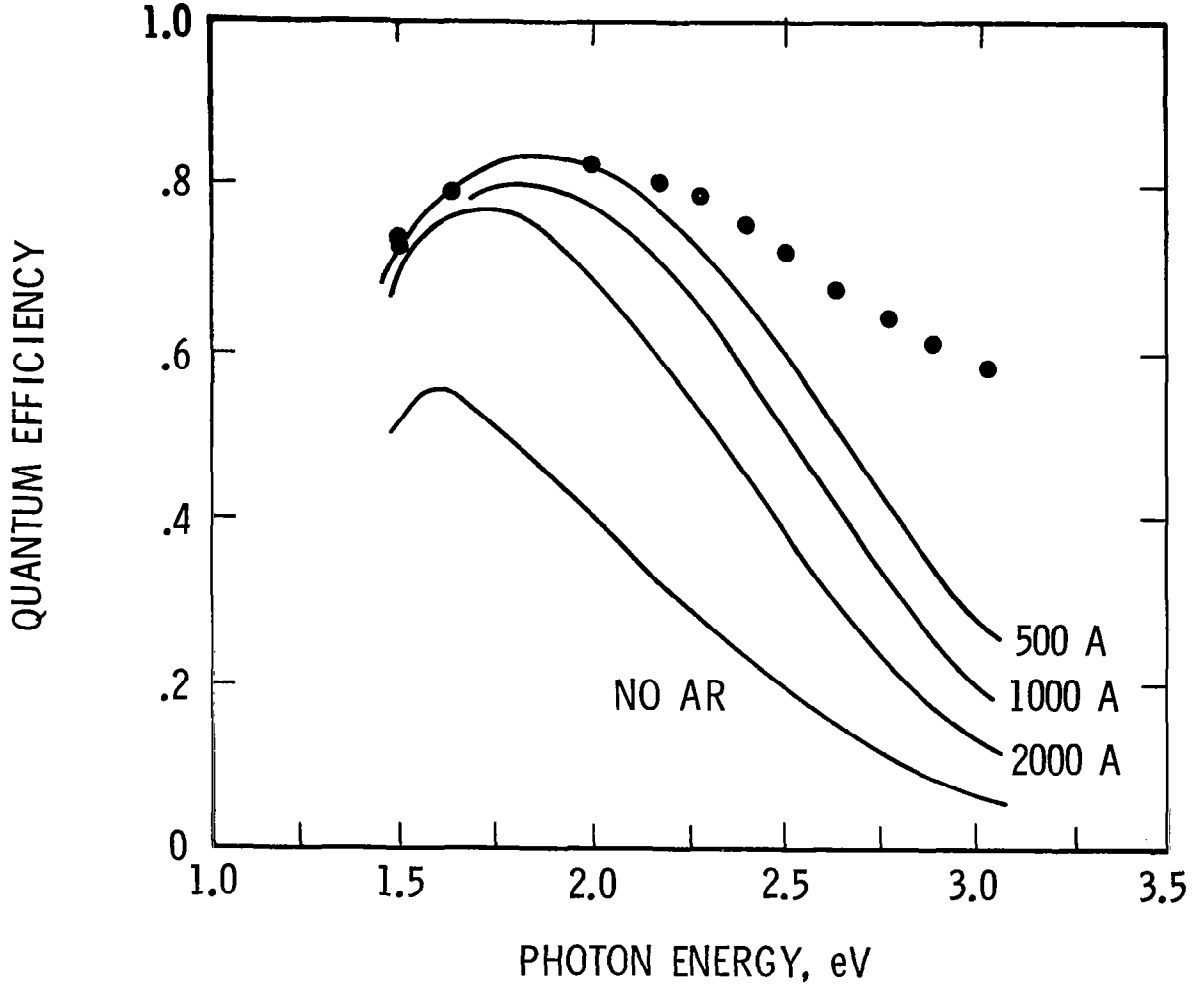

Figure 1 QUANTUM EFFICIENCY OF GaAs SOLAR CELLS WITH VARYING JUNCTION DEPTHS

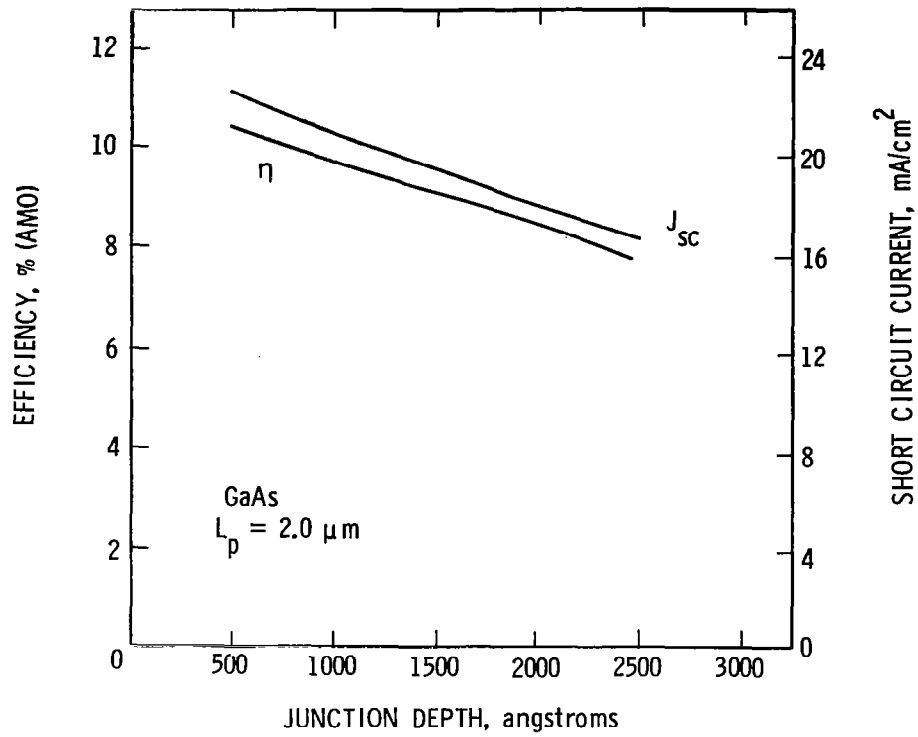

Figure 2 AMO EFFICIENCY OF GaAs SOLAR CELL AS A FUNCTION OF JUNCTION DEPTH

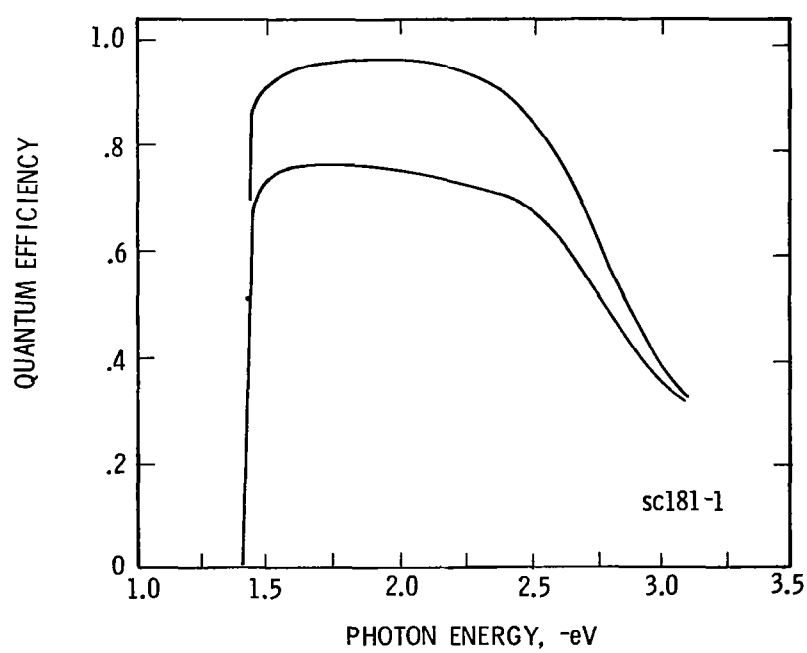

Figure 3 QUANTUM EFFICIENCY OF GaAlAs/GaAs SOLAR CELL

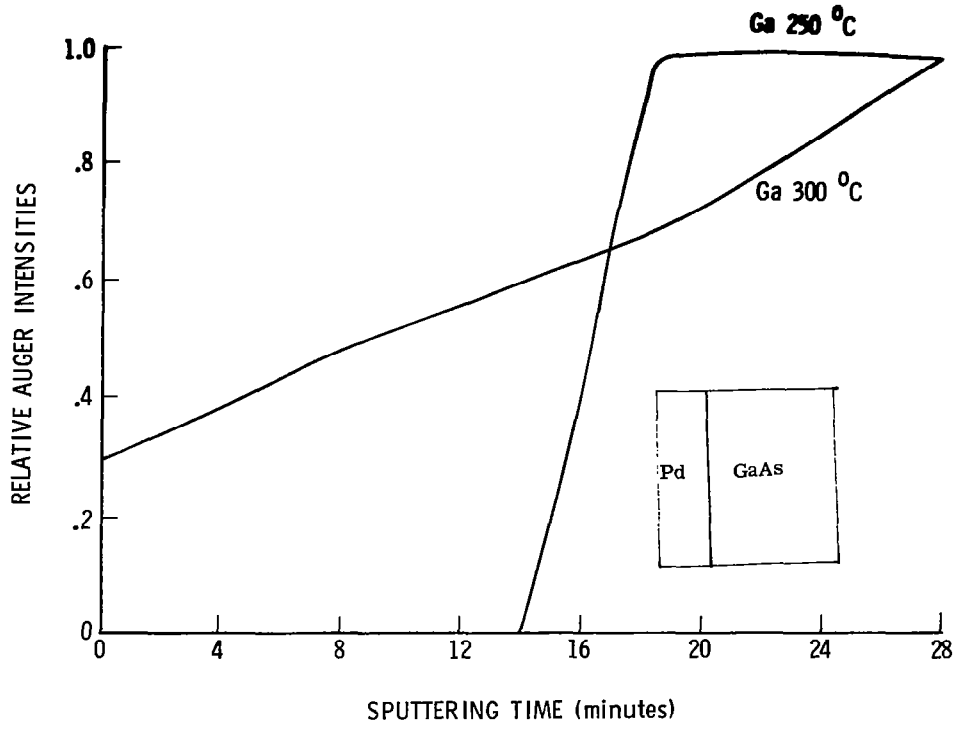

Figure 4 Ga DISTRIBUTION FOR 500 Å Pd ON GaAs HEATED FOR ONE HOUR

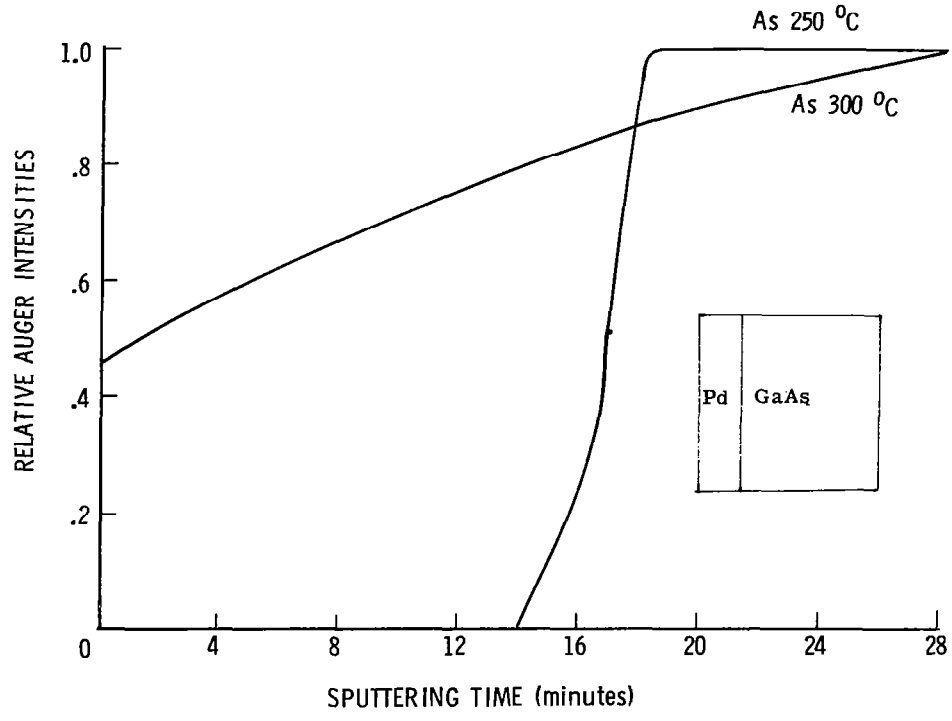

Figure 5 As DISTRIBUTION FOR 500 Å Pd ON GaAs HEATED FOR ONE HOUR

16. THEORETICAL STUDIES OF A NEW DOUBLE GRADED BAND-GAP $Al_xGa_{1-x}As$-$Al_yGa_{1-y}As$ SOLAR CELL

James A. Hutchby
NASA Langley Research Center
Hampton, Virginia 23665

SUMMARY

A new double graded band-gap (DGBG) $Al_xGa_{1-x}As$-$Al_zGa_{1-z}As$ solar cell has potential for providing high efficiency performance throughout the entire life of a solar cell in a space environment. A preliminary theoretical analysis indicates that short-circuit current available from an optimized DGBG cell is slightly larger than that of a previously reported single graded band-gap cell. However, the DGBG cell potentially offers a substantial improvement in radiation resistance of the base region.

INTRODUCTION

Current work in several laboratories is now demonstrating the realizability of high power conversion efficiencies long predicted for GaAs solar cells (refs. 1, 2, and 3). The major advance making this possible was the discovery that the large recombination velocity ($S \sim 10^6 - 10^7$ cm/sec) limiting cell performance of an exposed GaAs surface could be dramatically reduced ($S \sim 10^3 - 10^4$ cm/sec) by passivating it with a nearly transparent conductive layer of $Al_{.8}Ga_{.2}As$ (ref. 4). The $Al_{.8}Ga_{.2}As$ window layers in these early heteroface cells, typically 4-6 μm thick, were nearly opaque to photons having energies greater than 2.57 eV. Photogenerated minority charge carriers in the $Al_{.8}Ga_{.2}As$ layer did not contribute to cell current, presumably due to their annihilation through surface recombination.

One idea proposed and partially developed to circumvent this problem is the single graded band-gap (SGBG) cell in which the surface $Al_xGa_{1-x}As$ window layer has a graded composition decreasing linearly from $x = 0.35$ at the surface to $x = 0$ at the p-n junction 1.0 μm beneath the surface (refs. 5, 6, 7, 8, 9, and 10). The composition gradient provides a substantial quasi-electric field ($\sim$ 3700 V/cm) within the surface n-type layer (for an n-on-p cell) which accelerates the photogenerated holes away from the lossy surface, thus enhancing their collection at the p-n junction. Experimental efforts demonstrated that use of a composition gradient enhanced the blue-uv response of a GaAs cell; however, difficulty in growing uniform layers of graded composition material 0.5-1.0 μm thick combined with persistent growth of a constant composition layer on top of the graded layer during growth termination limited the maximum AMO efficiencies to 13.6 percent (corrected for contact area) (ref. 11).

Most recently, use of thin, constant-composition $Al_xGa_{1-x}As$ window layers (0.05-0.3 μm thick) in heteroface cells has resulted in AMO efficiencies up to 17.5 percent (ref. 2) in 4 cm^2 cells and 18.5 percent in 0.2 cm^2 cells (ref. 1). Since these thin layers absorb so few photons, the need to collect their resulting minority charge carriers no longer exists; i.e., it is no longer advantageous to grade the composition of the window layer to increase the initial short-circuit current and efficiency. However, recent experimental evidence suggests the thin window layers are graded within 0.02 μm of the metallurgical junction (to be published in Final Report on NASA Contract NAS1-13548 by R. Sahai and J. S. Harris, Rockwell International Science Center).

The high performance of these new cells has stimulated efforts to develop and demonstrate increased resistance to a space radiation environment expected for GaAs structures. In this regard, graded composition structures providing built-in, quasi-electric fields throughout the entire charge-collection region have their greatest potential for application. The double graded band-gap (DGBG) $Al_xGa_{1-x}As$-$Al_zGa_{1-z}As$ cell discussed in this paper provides direction to increasing the radiation resistance particularly of the base, p-type region. In this vein, therefore, a preliminary analysis of the DGBG cell operation and performance is presented with emphasis placed on comparison with a quite similar single graded band-gap cell previously reported (ref. 8). Concluding remarks will be made regarding the potential of the DGBG cell for providing improved radiation resistance.

THEORETICAL ANALYSIS

An energy band diagram of the cell structure, as shown in figure 1, depicts two graded-composition, direct band-gap (AlGa)As layers forming the active cell on top of a p-type, GaAs substrate. The composition gradients in the two (AlGa)As regions are established by Al concentrations decreasing linearly from maximum values at $y = 0$, $y_J + y_L$ ($x, z = 0.35$) to minimum values ($x, z = 0$) at the p/n junction ($y = y_J$). These composition gradients provide built-in quasi-electric fields which accelerate photogenerated minority charge carriers in each (AlGa)As region toward the p/n junction, thus enhancing their collection. The fields are proportional to the band-gap gradients, which, according to figure 1, means that the quasi-field for holes in the surface n-type layer is substantially larger than the field for electrons in the base, p-type region. The relatively large field (∿ 7400 V/cm) in the surface layer is required to minimize surface minority - carrier recombination, whereas in the base region the quasi-field/composition gradient is balanced between conflicting needs to maximize both carrier collection and photon absorption. Therefore, a base region 10-μm thick providing a quasi-field of approximately 370 V/cm is a near optimum choice.

The analysis was performed using the standard continuity and current density expressions (ref. 12) for the bulk material assuming a minority-carrier recombination velocity $S = 1 \times 10^5 - 1 \times 10^6$ cm/sec at $y = 0$ and $S = 1 \times 10^4$ cm/sec at the (AlGa)As-GaAs intermetallic junction at $y = y_J + y_L$. Photons absorbed in the GaAs substrate do not contribute to cell current. Excess carrier concentrations injected across the p-n junction were assumed to

be given by the standard Boltzmann boundary condition modified to include a field dependence at each depletion-layer edge. In the graded (AlGa)As layers the minority carrier transport properties were assumed to be constant, but the position dependence of the absorption coefficient required a numerical solution in each undepleted region. The minority carrier diffusion length for electrons (ℓ_{no}) and for holes (ℓ_{po}) were each assumed to have an empirical dependence on impurity concentration as compiled and given by Ellis and Moss (see ref. 7 for a discussion of ℓ_{no} and ℓ_{po}). Furthermore, junction recombination current density, series resistance, and surface reflection losses were considered. Computational techniques used in this analysis are similar in nature to those previously employed for the SGBG cell (ref. 7). The analysis was performed for air mass zero (AMO) insolation given by Johnson (ref. 13), and reported efficiencies include light incident upon the surface contact metallization covering 13 percent of the cell area.

RESULTS AND DISCUSSION

As mentioned above, introduction of a composition gradient in the base, p-type region increases the electron collection efficiency at the expense of reduced photon absorption. The quasi-electric field for electrons in the base region is proportional to the change in mole fraction AlAs per unit length. Therefore, this field is directly proportional to the mole fraction AlAs (X_{ALOD}) at the back of the base region and inversely proportional to its thickness Y_L.

The impact of X_{ALOD} and Y_L on short-circuit electron current density (J_{NS}) collected from the base region is illustrated in figures 2 and 3. As shown in figure 2, increasing X_{ALOD} from 0 to 0.35 (for Y_L = 20 μm) produces equal opposing effects of increased electron collection efficiency (Q_N) offset by reduced density of absorbed photons (N_{AD}) such that J_{NS} remains constant. Figure 3 indicates that for X_{ALOD} = 0.35, the electron collection efficiency decreases only slightly from Q_{NO} = 0.996 over the entire range of values for Y_L. This indicates that Q_N is dominated by the quasi-field and that essentially all extra photons absorbed in a thicker base region contribute to cell current. These preliminary results suggest that the simultaneous conditions of maximum J_{NS} and maximum electron quasi-electric field can be satisfied by X_{ALOD} = 0.35 and Y_L = 18 μm. Larger values of X_{ALOD} result in indirect-band-gap (AlGa)As in the deepest portion of the base region, which yields unwanted reductions in the quasi-field and photon absorption in the indirect region.

Since the electron currents collected are the same for base regions composed of either GaAs or graded composition (AlGa)As, the main difference between the two is the presence of a quasi-electric field for electrons in the graded-composition case. Consequently, major benefit provided by the DGBG cell will be through improved radiation hardness of the base region.

Degradation of J_{NS} resulting from energetic electron and proton bombardment of the base can be examined simply through comparison of the total time (τ_t) required to extract an electron from the base region to an effective minority-carrier recombination time. This effective minority-carrier lifetime

(τ_{noe}) is defined as that time interval required to recombine 5 percent of the photogenerated minority carriers, and is approximately equal to 5 percent of the standard minority-carrier lifetime τ_{no}. The total electron extraction time is given by

$$\frac{1}{\tau_t} = \frac{1}{\tau_{no}} + \frac{1}{\tau_{di}} + \frac{1}{\tau_{dr}} \tag{1}$$

where τ_{di} and τ_{dr} are the extraction times due solely to electron diffusion and electron drift, respectively. For an average distance $\bar{y}$ that photogenerated electrons must travel from their point of creation to the p/n junction,

$$\tau_{di} = \bar{y}\ \ell_{no}/D_n \tag{2a}$$

and

$$\tau_{dr} = \bar{y}/\mu_n\ E, \tag{2b}$$

where D_n, μ_n, and ℓ_{no} are the electron diffusion coefficient, mobility, and diffusion length, and E is the quasi-electric field for electrons in the base region. Assuming the dominant effect of energetic particle flux ϕ on solar cell performance is through lifetime degradation, then the influence of ϕ on τ_t is through both τ_{no} (proportional to ϕ) and τ_{di} (proportional to $\phi^{1/2}$). For a constant-composition base region having no drift field, the net dependence of τ_t on ϕ depends upon the relative magnitude of τ_{no} and τ_{di}. However, use of a sufficiently large built-in drift field can render τ_t essentially independent of ϕ, assuming μ_n and E are independent of ϕ. These cases are examined below for both a Si and a GaAs cell having no drift fields, and for an $Al_xGa_{1-x}As$-$Al_zGa_{1-z}As$ DGBG cell with a base-region drift field. In these examples τ_{noe} will be used to characterize electron recombination, so that fullfillment of either condition $\tau_{di} < \tau_{noe}$ or $\tau_{dr} < \tau_{noe}$ sets the bulk recombination loss of photogenerated electrons at less than 5 percent.

In the first example a n/p Si cell with a 2 Ω-cm, p-type base region is assumed characterized by modest electron lifetime and diffusion length of 10×10^{-6} sec and 160 μm, respectively. For a junction depth of 0.2 μm the average base region collection depth $\bar{y}$ is 7.8 μm which leads to a diffusion extraction time τ_{di} of 0.48×10^{-6} sec. This being essentially equal to an effective electron lifetime τ_{noe} of 0.5×10^{-6} sec means that approximately 95 percent of the photogenerated electrons are collected from the base region.

The second example is that of an n/p GaAs cell having a base resistivity of 0.04 Ω - cm (equilibrium hole concentration $p_o = 4 \times 10^{16}\ cm^{-3}$),

ℓ_{no} = 12 μm, τ_{no} = 1.9 x 10^{-8} sec, and $\bar{y}$ = 0.84 μm for a junction depth of 0.5 μm. In this case, τ_{di} = 1.3 x 10^{-9} sec and τ_{noe} = 9.5 x 10^{-10} sec which indicates that approximately 93 percent of the photogenerated electrons are collected from the base region.

The minority-carrier collection efficiencies for both the Si and GaAs cells examined above are quite good. However, these efficiencies will degrade substantially as τ_{noe} is reduced by radiation damage.

The last case examined is that of a DGBG cell having the same base-region parameters as the GaAs cell except for addition of a base-region quasi-electric field of 370 V/cm accelerating the electrons toward the junction. The electron-drift extraction time τ_{dr} is 7.6 x 10^{-11} sec which totally dominates τ_t, as seen from equation 1. In this case, over 99 percent of the minority carriers are collected from the base region. More importantly, τ_t for the DGBG cell is much less sensitive to degradation of τ_{no} than it is for the GaAs case. To illustrate this, a decrease of τ_{no} by a factor of 10 will decrease τ_t for the DGBG cell from 7.2 x 10^{-11} sec to 6.9 x 10^{-11} sec, only a 4 percent change. In comparison, the same decrease of τ_{no} will reduce τ_t for the GaAs cell from 1.2 x 10^{-9} sec to 7.8 x 10^{-10} sec, a 36 percent change. A factor of 100 decrease of τ_{no} for the DGBG cell reduces τ_t to 5.2 x 10^{-11} sec, a 28 percent change. These examples thus illustrate the potential of a graded-composition base region for improving the radiation resistance of a GaAs cell.

The most practical application of the graded-composition base region appears to be in conjunction with a thin, constant-composition $Al_{.9}Ga_{.1}As$ window layer in an otherwise conventional heteroface, p/n cell. In this structure a relatively thick (10-20 μm), lightly-doped n-type, graded-composition $Al_zGa_{1-z}As$ region would be grown on a heavily-doped n-type GaAs substrate. Growth of this layer gradually graded from z = 0.30 - 0.35 at the layer/substrate interface to z = 0 at the layer surface might be accomplished using Al depletion of a thin melt, particularly for a layer thickness greater than 20 μm. Cell growth would then be completed by simultaneous epitaxial deposition of a thin, p-type (Zn doped) $Al_{.9}Ga_{.1}As$ window layer and diffusion of a thin p/n junction into the n-type graded-composition buffer layer.

CONCLUSION

In conclusion, it is shown that use of graded-composition $Al_zGa_{1-z}As$ in the base region of an n/p double graded band-gap solar cell may improve the resistance of the device to energetic particle radiation, although it does not substantially increase the cell current. Also, the most practical application of the graded-composition $Al_zGa_{1-z}As$ base region may be to improve the radiation resistance of the new, thin-window, p/n heteroface cells.

REFERENCES

1. Hovel, H. J. and Woodall, J. M.: Enhanced GaAs Solar Cells With Very Thin Junctions. In Conference Record of the Twelfth IEEE Photovoltaic Specialists Conference, IEEE Press, 1977.

2. Kamath, G. S.; Ewan, J.; and Knectli, R. C.: High Efficiency and Large Area (AlGa)As-GaAs Solar Cells. In Conference Record of the Twelfth IEEE Photovoltaic Specialists Conference, IEEE Press, 1977.

3. Sahai, R.; Edwall, D. D.; Cory, E.; and Harris, J. S.: High Efficiency Thin-Window $Ga_{1-x}Al$ As/GaAs Solar Cell. In Conference Record of the Twelfth IEEE Photovoltaic Specialist Conference, IEEE Press, 1977.

4. Hovel, H. J. and Woodall, J. M.: High Efficiency $Ga_{1-x}Al_xAs$ - GaAs Solar Cells. Appl. Phys. Letters, vol. 21, no. 8, October 15, 1972, pp. 379-381.

5. Hutchby, J. A.: High Efficiency Graded Band-Gap $Al_xGa_{1-x}As$ - GaAs Solar Cell. Appl. Phys. Letter, vol. 26, no. 8, April 1975, pp. 457-459.

6. Hutchby, J. A.: High Efficiency Graded Band-Gap $Al_xGa_{1-x}As$ - GaAs p-on-n Solar Cell. In Conference Record of the Eleventh IEEE Photovoltaic Specialists Conference, IEEE Press, 1975, pp. 414-423.

7. Hutchby, J. A. and Fudurich, R. L.: Theoretical Analysis of $Al_xGa_{1-x}As$ - GaAs Graded Band-Gap Solar Cell, J. Appl. Phys., vol. 47, no. 7, July 1976, pp. 3140-3151.

8. Hutchby, J. A. and Fudurich, R. L.: Theoretical Optimization and Parametric Study of n-on-p $Al_xGa_{1-x}As$ - GaAs Graded Band-Gap Solar Cell. J. Appl. Phys., vol. 47, no. 7, July 1976, pp. 3152-3158.

9. Konagai, M. and Takahashi, K.: Graded-Band-Gap $pGa_{1-x}Al_xAs$ - nGaAs Heterojunction Solar Cells. J. Appl. Phys., vol. 46, no. 8, Aug. 1975, pp. 3542-3546.

10. Konagai, M. and Takahashi, K.: Theoretical Analysis of Graded Band-Gap Gallium-Aluminum Arsenide/Gallium Arsenide p-$Ga_{1-x}Al_xAs$/p-GaAs/n-GaAs Solar Cells. Solid-State Electron, vol. 19, 1976, pp. 259-264.

11. Hutchby, J. A.; Sahai, R.; and Harris, J. S.: Theoretical and Experimental Evaluation of a High Efficiency Graded Band-Gap AlGaAs - GaAs Solar Cell. In Technical Digest of the 1975 International Electron Devices Meeting, IEEE Press, 1976, pp. 91-94. Also in NASA TM X-72819, 1975, pp. 113-121.

12. Sze, S. M.: Physics of Semiconductor Devices, Wiley, 1969, pp. 66-67.

13. Johnson, F. S.: The Solar Constant. J. Meteorol., vol. 11, no. 6, 1954, p. 431.

ENERGY BAND DIAGRAM FOR DOUBLE GRADED BAND-GAP SOLAR CELL

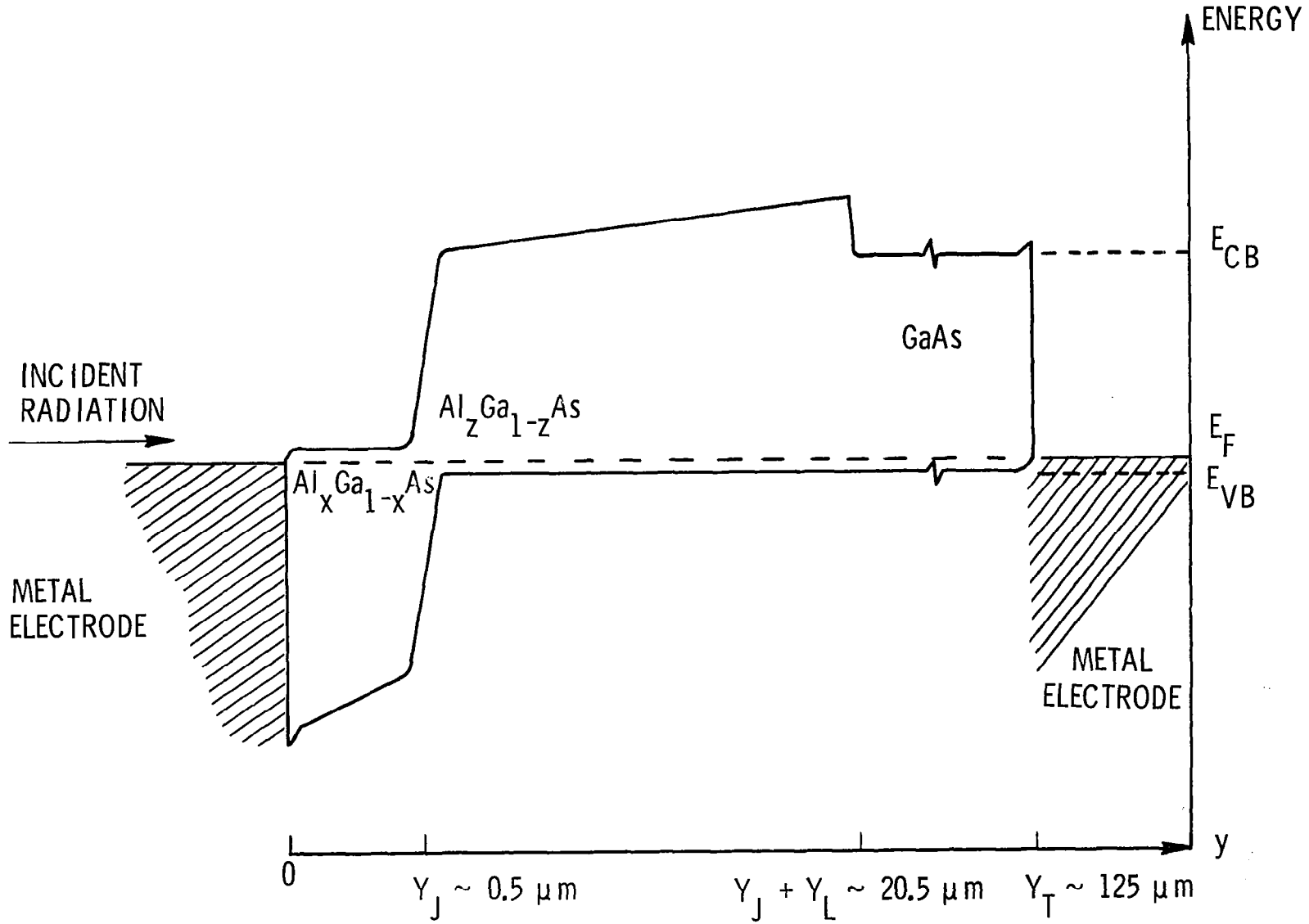

Fig. 1. Energy band diagram for n/p $Al_xGa_{1-x}As$ - $Al_zGa_{1-z}As$ double graded band-gap solar cell.

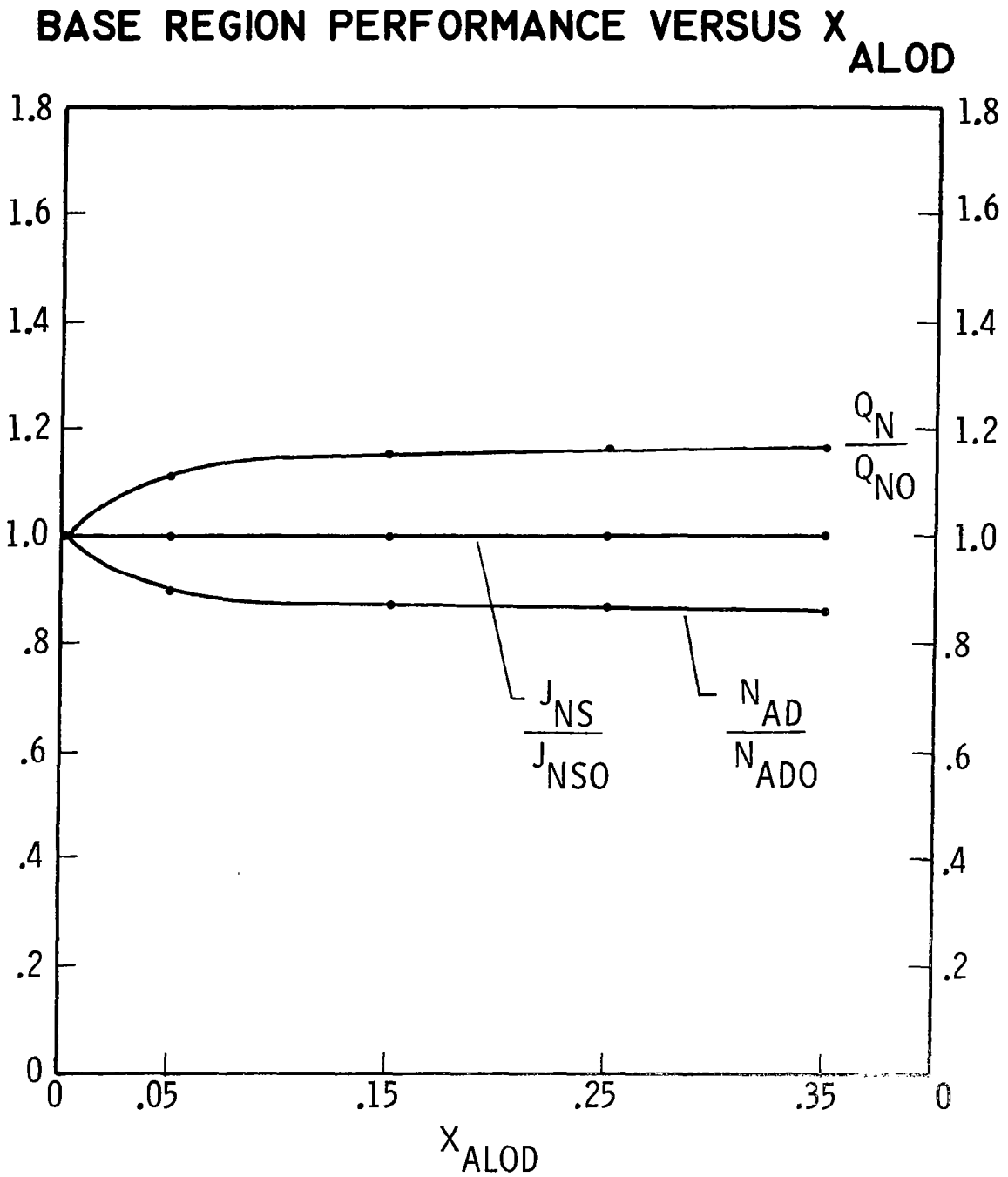

Fig. 2. Normalized electron short-circuit current density (J_{NS}/J_{NSO}) versus X_{ALOD} compared to photon density absorbed in the base region (N_{AD}/N_{ADO}), and to electron collection efficiency (Q_N/Q_{No}). (Y_L = 20 μm).

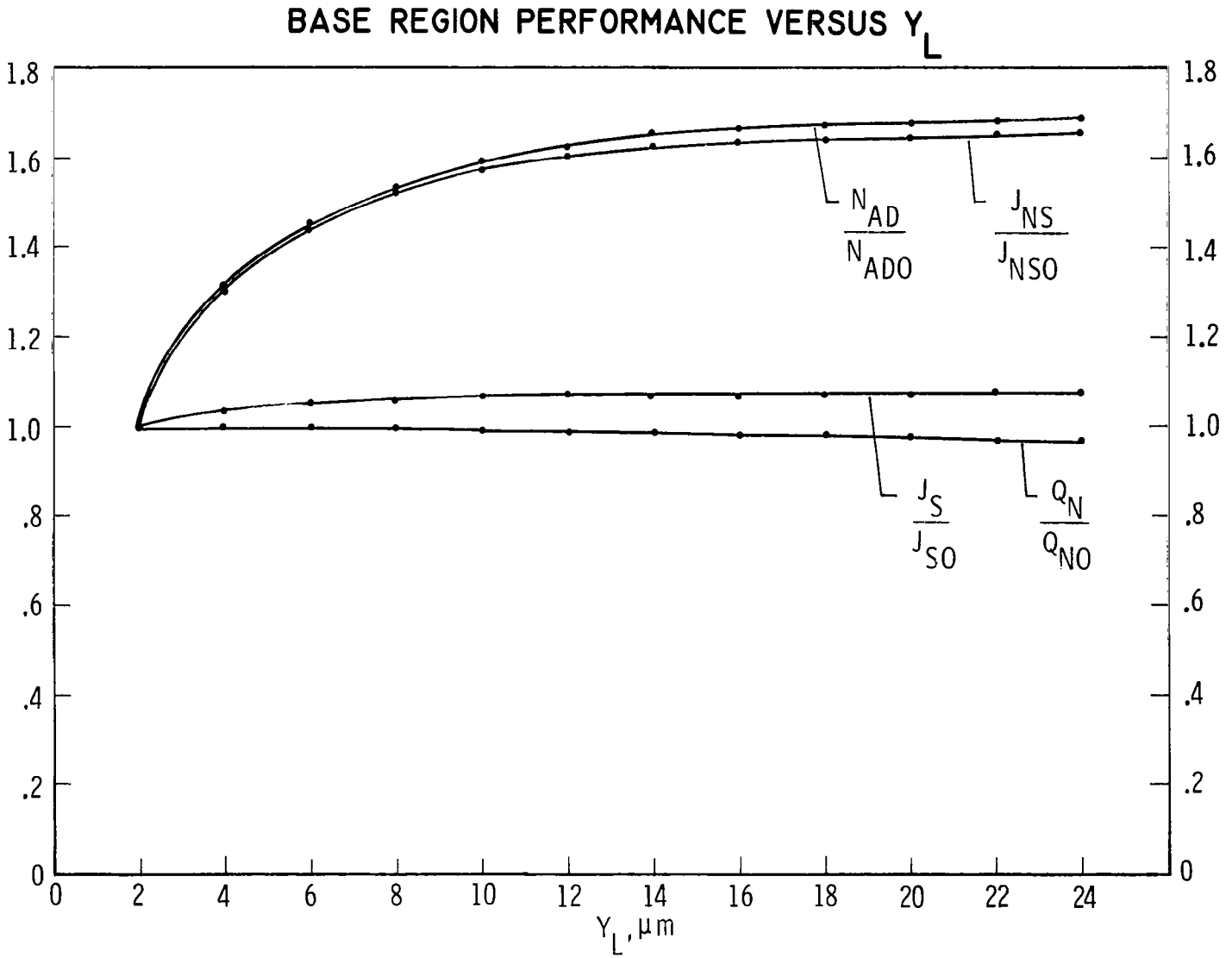

Fig. 3. Normalized electron short-circuit current density (J_{NS}/J_{NSO}) versus base-region thickness Y_L compared to photon density absorbed in the base region (N_{AD}/N_{ADO}), to electron collection efficiency (Q_N/Q_{NO}), and to total short-circuit current density (J_S/J_{SO}). (X_{ALOD} = 0.35).

17. GaAs SOLAR CELL DEVELOPMENT

R. C. Knechtli, S. Kamath, and R. Loo
Hughes Research Laboratories

The motivation for developing GaAs solar cells is based on their superior efficiency when compared to silicon cells, their lower degradation with increasing temperature, and the expectation for better resistance to space radiation damage. The AMO efficiency of GaAs solar cells has been calculated by several groups and is in substantial agreement with out own calculations shown in figure 1. It is important to note however, that our calculations are conservative and are based on design parameters well within the capability of the technology which we are developing at Hughes Research Laboratories (HRL).

A key consideration in the HRL technology is the production of GaAs cells of large area (>4 cm^2) at a reasonable cost without sacrificing efficiency. The structure of the solar cells which we are developing has been discussed in a number of papers and is reproduced in figure 2. An essential requirement for the successful fabrication of such cells is the ability to grow epitaxially a uniform layer of high quality GaAs (buffer layer) on state-of-the-art GaAs substrates, and to grow on this buffer layer the required thin layer of (AℓGa)As. The technique which we use is a modified infinite melt liquid phase epitaxy (LPE) shown in figure 3. As discussed in prior papers, one essential feature of this apparatus is the meticulous control of the purity of the H_2 atmosphere in which the "infinite" melt is kept. This purity is achieved by providing an H_2 filled entry chamber as shown in figure 3 between the melt and the laboratory atmosphere. Another important factor is the exact and uniform control of the substrate temperature over its full area. This is achieved by holding the substrate on a properly designed substrate holder for insertion and equilibration into the infinite melt. With these precautions, uniform growth is obtained over the large area substrates. A sketch of the graphite substrate holder is shown in figure 4. It should be observed that the design of the apparatus shown in figure 3 and 4 can be modified to implement LPE growth on several substrates simultaneously, an important feature for higher practical production rates and correspondingly lower fabrication costs.

We have applied this technology for making solar cells of a standard size of 2 cm x 2 cm and we foresee no serious problem in going to larger sizes. Our present state of the art is an ability to make routinely 4 cm^2 cells with an AMO efficiency in excess of 15%. Our best cell to date has an AMO efficiency of 17.5%. Its current-voltage characteristics are reproduced in figure 5. The cell has the following parameters:

Doping level:	(AℓGa)As Layer	$p = 2 \cdot 10^{18}$ cm^{-3}
	Buffer layer	$n = 3 \cdot 10^{16}$ cm^{-3}
	Substrate	$n+ = 7 \cdot 10^{17}$ cm^{-3}
(AℓGa)As layer thickness		$D = 0.5$ μm
Buffer layer thickness		$t = 25$ μm
Junction depth		$x_j = 0.7$ μm

The electrical characteristics corresponding to figure 5 are:

Short-circuit current density:	j_{sc} = 29.5 mA/cm^2
Open-circuit voltage:	V_{oc} = 0.98 volt
Fill factor	F = 0.82
AMO efficiency:	η = 17.5%

In the light of these results, and those of IBM (18.5% AMO efficiency for small cells), our forecast of 20% efficiency in figure 1 does seem conservative indeed.

The temperature dependence of the efficiency of GaAs solar cells is illustrated in figures 6 and 7. These values are calculated using the same assumptions as in figure 1. The line shown in figure 7 as a "conservative estimate" neglects the increase of short-circuit current with increasing temperature. Such an increase has, however, been experimentally observed. It results from the decreasing value of the GaAs bandgap (and possible from increasing minority carrier diffusion length and quantum efficiency) with increasing temperature. Inclusion of these effects leads to the more favorable line shown in figure 7. The measured slope of efficiency vs. temperature for our experimental cells corresponds closely to the latter.

As far as resistance of GaAs solar cells to radiation damage is concerned, qualitative arguments have been made predicting relatively favorable characteristics. The limited experimental data available to date shows however, a wide scatter on the performance of practical cells. Our experimental data emphasizes the critical importance of the junction depth to minimize radiation damage. We have determined the 1 MeV electron radiation damage constant for one set of our experimental cells whose junction depth we had measured. This is shown in figure 8. The benefits anticipated from decreasing this junction depth are illustrated by the calculations shown in figure 9. However, more systematic investigations are obviously required to gain a broader perspective on the effects of high energy particle radiation on GaAs solar cells, and to optimize the design of these cells for minimum radiation damage.

The fabrication cost of GaAs solar cells is of course, an important parameter for practical space applications. In this context, it is worth observing that the cost of the material per se is surprisingly low. For reference, the semiconductor grade Ga present in one of our 4 cm^2 (Aℓ Ga)As-GaAs solar cells costs only about $0.40!

It is clear that a number of investigations are still called for to develop GaAs solar cells to their full potential. More has to be learned about the nature of radiation damage in GaAs. The effect of particle energy has to be determined both for proton and for electron irradiation. The importance of the choice of dopant has also to be established, including a comparison of the radiation damage to n- and to p-doped GaAs. Another area where further progress is possible is that of optimizing the junction quality. Fill factors as high as 0.86 have been measured in some of our 4 cm^2 cells;

this provides an incentive for controlling our fabrication technology to reproducibly obtain such results. Finally, going to thin (AℓGa)As layer thicknesses ($D < 0.5$ μm) and shallow junction depths ($x_j \simeq 0.2$ μm) places more emphasis on reliable control of the contact fabrication technology. In the context of these tasks, as well as of the results obtained to date, our view of the prospects for higher efficiency GaAs solar cells is summed up in figure 10. Figure 11 shows the rate at which we have been able so far to approach these objectives.

We wish to thank Dr. Lee Goldhammer and Dr. Bruce Anspaugh (JPL) who made the radiation damage measurements reported in this paper. The work is being continued with partial support from AFAPL and we hope to report on more comprehensive results in the next few months. Measurements on proton radiation damage will also be performed under support from NASA Langley.

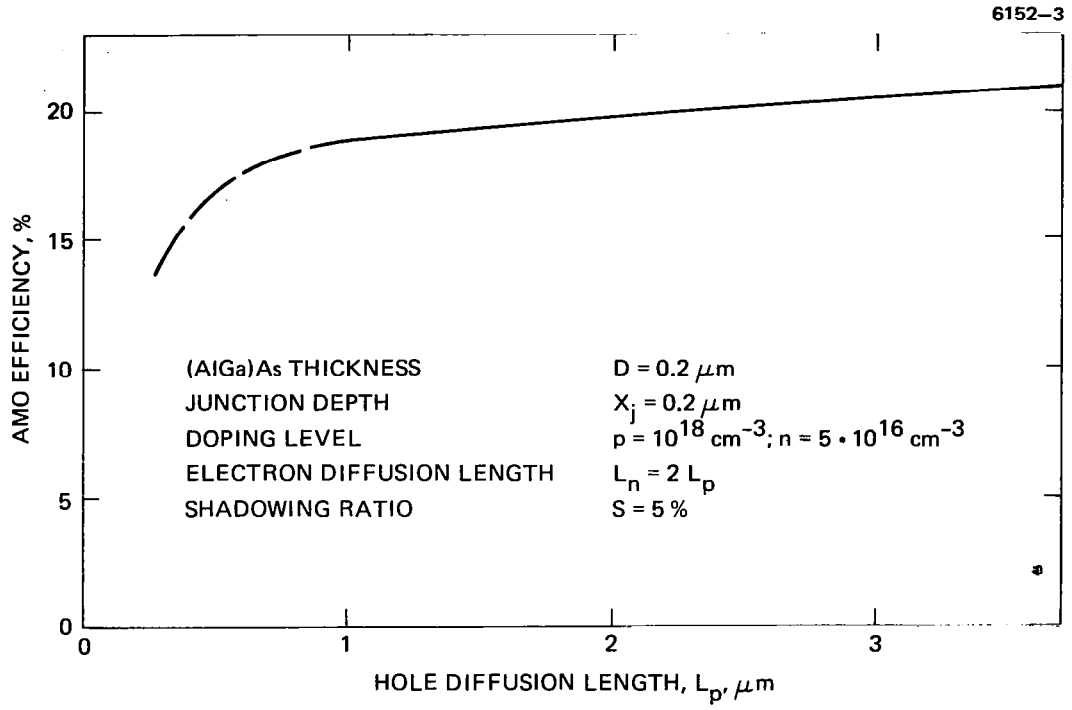

Figure 1. AMO Efficiency of (AlGa)As-GaAs Solar Cell

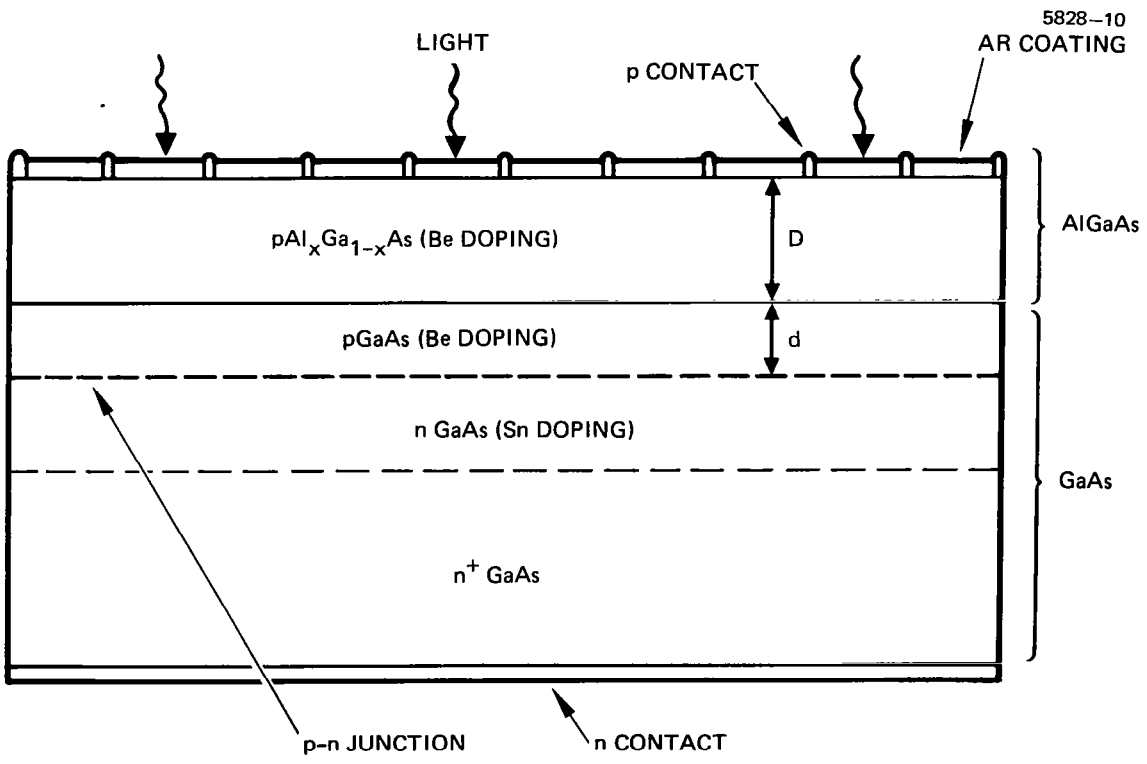

Figure 2. GaAs Solar Cell Structure

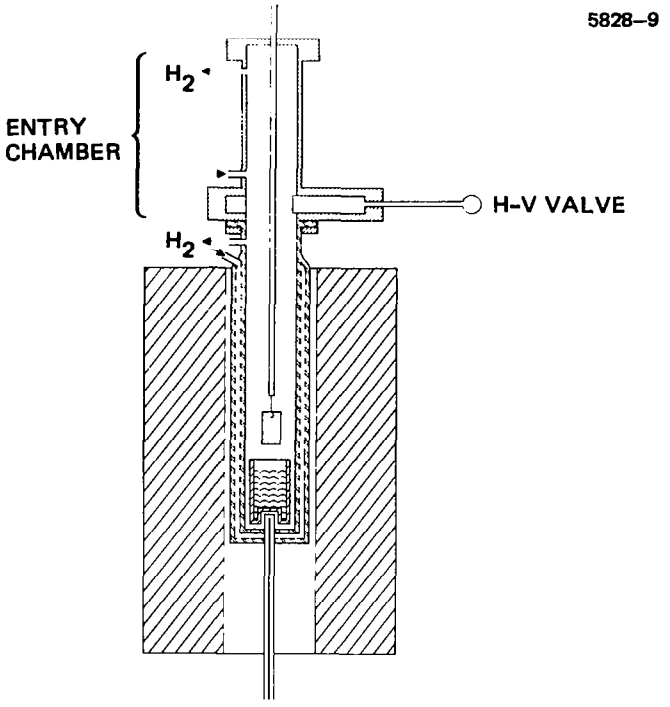

Figure 3. Hughes Liquid Phase Epitaxy Apparatus

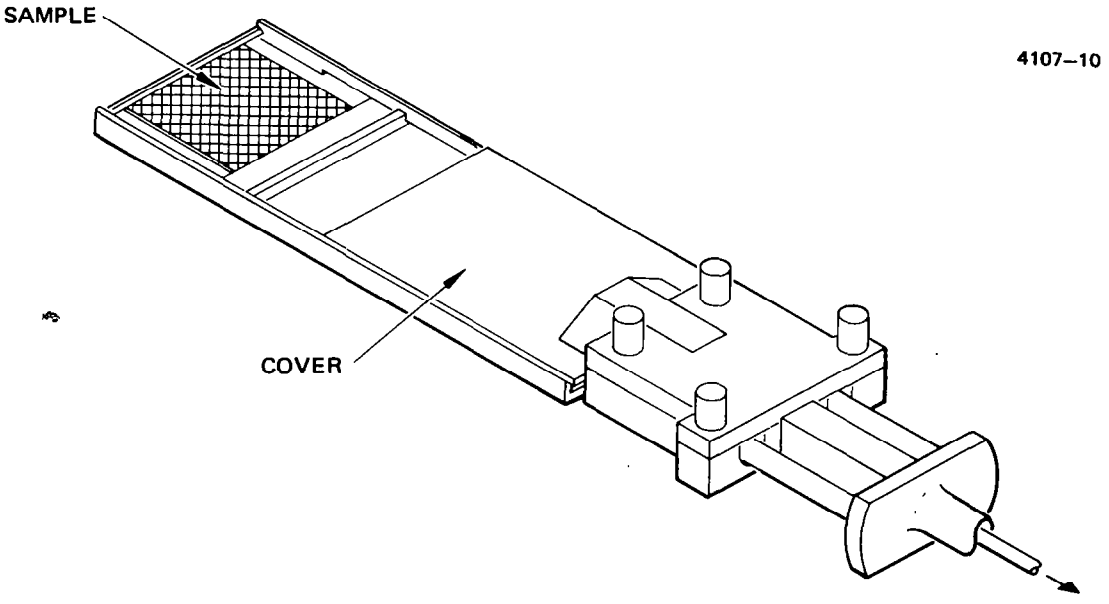

Figure 4. Graphite Substrate Holder

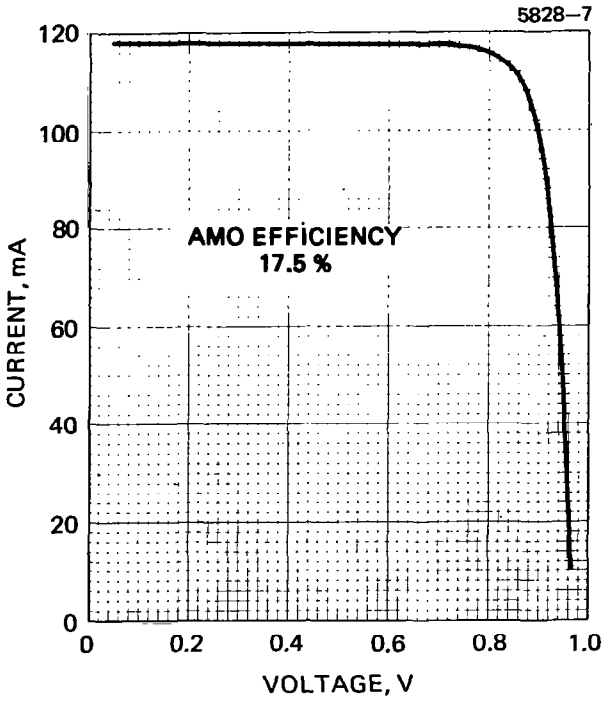

Figure 5. I-V Characteristic of 4 cm^2 Cell

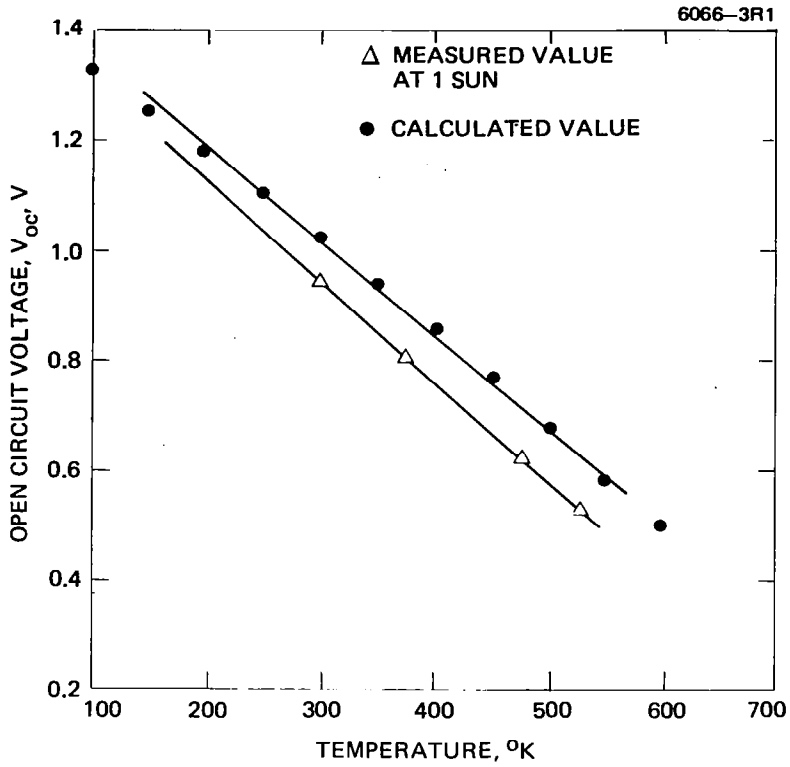

Figure 6. Open-Circuit Voltage vs Temperature

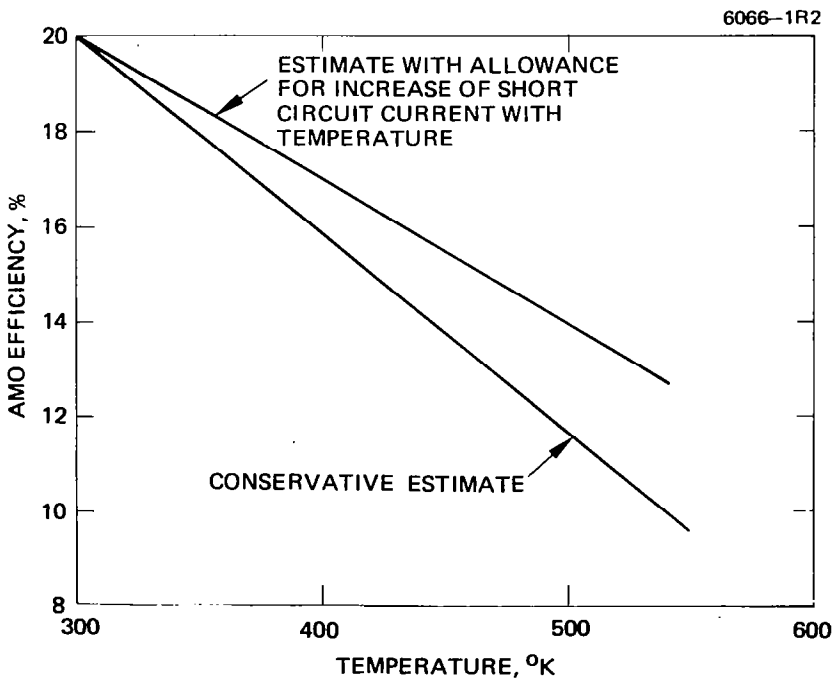

Figure 7. AMO Efficiency vs Temperature

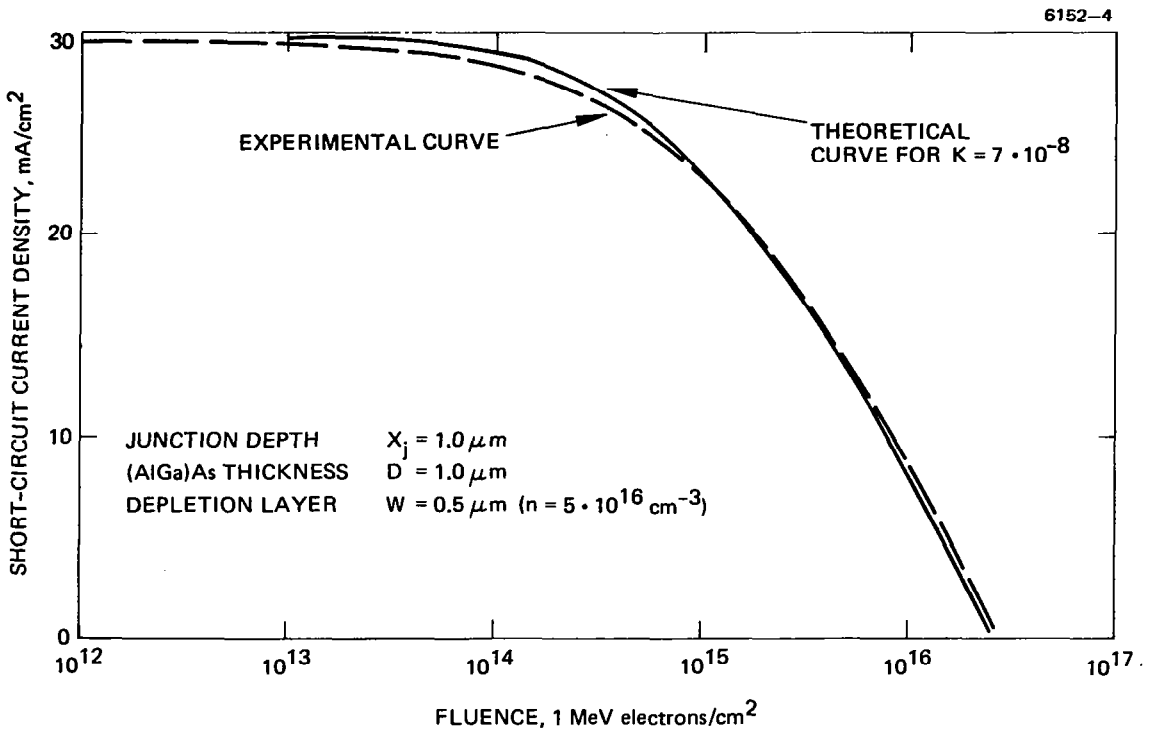

Figure 8. Evaluation of 1 MeV Electron Radiation Damage Constant K

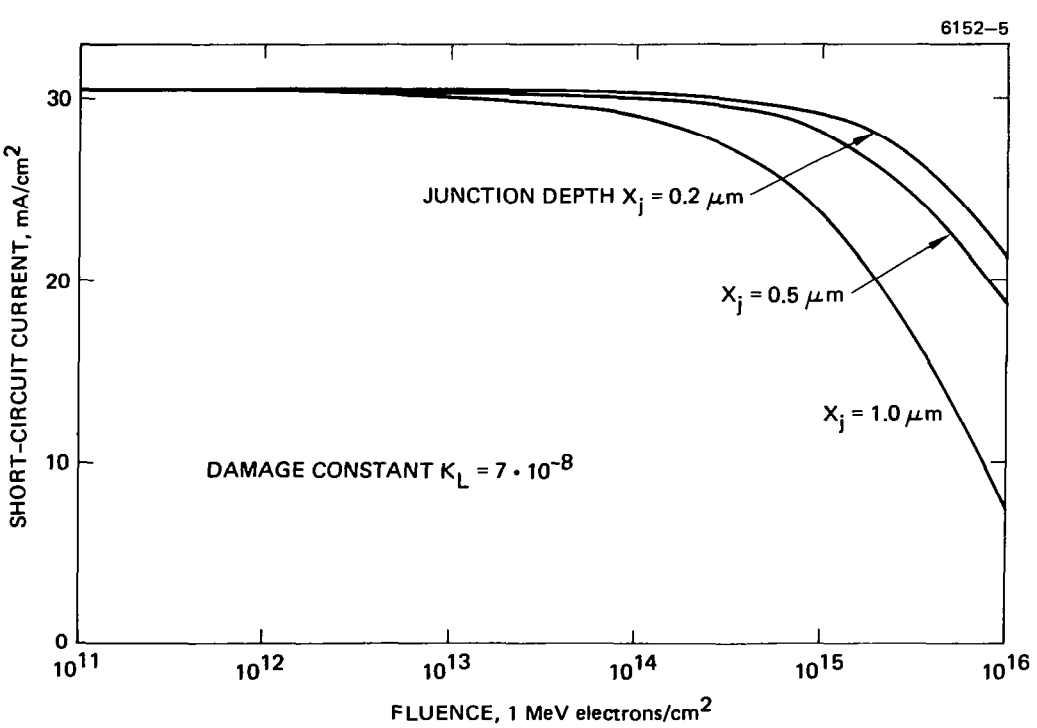

Figure 9. Electron Radiation Damage

- AMO EFFICIENCY

  $\eta > 20\ \%$

- RADIATION RESISTANCE:

  SUPERIOR RESISTANCE TO HIGH ENERGY PROTONS AND NEUTRONS

- HIGH TEMPERATURE OPERATION:

  $\eta > 12\%$ @ $T = 200\ ^{o}C$

- COST OF MATERIAL:

  0.40 $ OF Ga PER 4 cm^2 SOLAR CELL

Figure 10. Prospects for GaAs Solar Cells

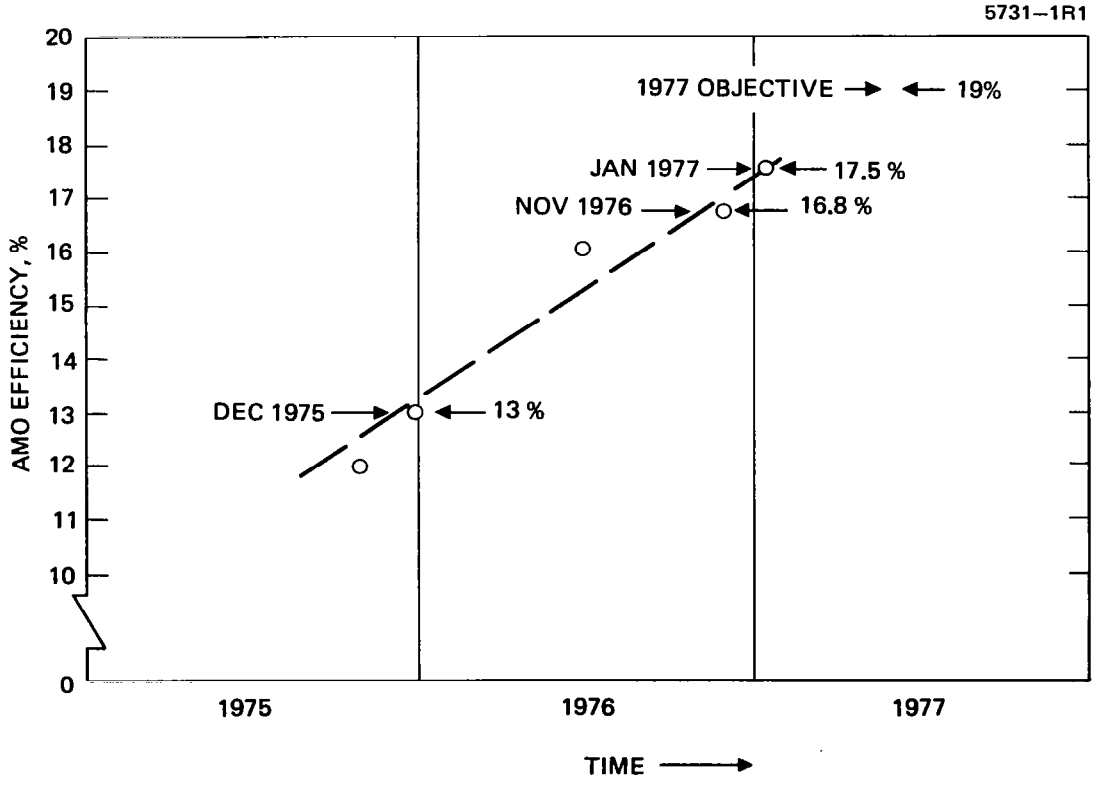

Figure 11. HRL GaAlAs/GaAs Solar Cell Efficiency

18. THE STATUS OF DEFECT STUDIES PERTINENT TO RADIATION DAMAGE IN SILICON SOLAR CELLS†

J. W. Corbett, L. J. Cheng, J. C. Corelli* and Y. H. Lee
Institute for the Study of Defects in Solids and Department of Physics
State University of New York at Albany, Albany, N.Y. 12222

SUMMARY

The status of radiation defects in silicon is briefly reviewed and discussed in relation to the problem of radiation tolerance of silicon solar cells in space.

TEXT

The approaches toward improving the radiation tolerance of silicon solar cells can be summarized in the four following questions: 1) Can you *avoid*, or reduce the amount of, *the primary damage*, e.g., interstitials and vacancies? 2) If the answer to question 1 is no, can you create a *defect recombination center*? 3) Or can you create a *defect neutralizing center*? 4) If the answer to these questions is also no, how do you minimize the amount of damage?

Question number one is not impractical. Of course the covers on solar cells do reduce the damage. Beyond that the nature of damage production at room temperature is not settled. Let me explain. In the primary damage event, the displaced atom becomes an interstitial leaving behind a vacancy. [Multiple displacements do not alter the matters being discussed and will not be treated further here.] The mobile interstitial can annihilate with its *own* vacancy, which is called *correlated* recovery and is shown as the δ-process in figure 1; the interstitial may escape its own vacancy and undergo an *uncorrelated* interaction, which is shown in figure 1 as the ε-process, where the ε-process may be annihilation at another vacancy or an interaction with an impurity as shown. If there are only isolated, mobile vacancies and interstitials in the sample and they can only annihilate, the time dependence of the recovery is shown in figure 2 with the ε-process delayed by the additional defect motion needed to get annihilation (references 1 to 12). If impurities trap a mobile defect and prevent annihilation, the probability of impurity trapping in the ε-regime is proportional to the impurity concentration, but *in the δ-regime* Schroeder

† Work supported in part by NASA Grant No. NSG 3095, the Office of Naval Research, Contract No. N00014-75-C-0919, and INTELSAT, Contract No. IS-681.
* Permanent Address: Department of Nuclear Engineering, Rensselaer Polytechnic Institute, Troy, New York 12181.

(reference 13) has shown that that probability is proportional to the *square root of the impurity concentration* (see figure 2). Thus for impurity trapping the damage retained in the sample will depend on impurity concentration as shown in figure 3. In phosphorus doped silicon the probability of [V + P] formation versus [V + O] formation is proportional to the phosphorus concentration arguing that the system is in the ε-regime with the oxygen and phosphorus competing for the vacancy. In p-type matters are not so clear, with Mooney and coworkers (reference 14) finding the probability of forming the boron-dependent defect (thought to be an interstitial-related defect) to be proportional to the square root of the boron dependence, while Kimerling's data (reference 15) favors a linear dependence; in either event it is thought that either boron or carbon (in those experiments) trap the mobile interstitial resulting in a mobile impurity interstitial. If the square root dependence proves to be true,that argues that the vacancy-interstitial capture radius is large in p-type and that *removing the trapping impurities could greatly reduce the net damage*.

The following paper (reference 16) will discuss in more detail the defect recombination center (i.e., a center which facilitates vacancy-interstitial annihilation by trapping first one and then the other) and the defect neutralizing center (e.g., a center, such as a dislocation or void, whose properties are essentially unchanged as it traps a vacancy or an interstitial). As will be seen, *not enough is known about defects in silicon* to fully assess the prospects for achieving such centers, and certainly we do not know enough to know how to minimize the damage (the fourth question mentioned above).

The fact that we have insufficient knowledge of defects in silicon may seem surprising since it is about thirty years since the transistor was introduced and there have been extensive studies since that time. In fact we believe that there is more detailed information about defects in silicon than in any other system, due in large part to the foundation of detailed information established in EPR studies on substitutional and interstitial atoms and other defects (see references 17-22). We have illustrated (reference 22) how little is known about diffusion and electrical levels of impurity atoms and about interstitial and vacancy-related defects. For example, to varying degrees of certainty the following vacancy-related defects have been identified (see reference 21 for specific references on defects): V, V_2, V_3, V_4 (planar), V_4 (nonplanar), V_5 (nonplanar); [V + O], [V_2 + O], [V_2 + O_2], [V_3 + O], [V_3 + O_2], [V_3 + O_3]; [V + P], [V + As], [V + Sb]; [V + B], [V + Aℓ], [V + Ga]; [V + C], [V + Ge], [V + Sn]; and [V + O + C]. In figure 4 we show those elements in the periodic table for which some information exists in the literature. But to answer the questions raised above we feel you need to know the following information about the main defects: configuration; electrical levels and carrier capture mechanisms and parameters; diffusion mechanisms and parameters; and defect interaction mechanisms and parameters. Such parameters do not exist for even those defects which occur in a silicon solar cell, much less for those which *might* occur.

For example, we have recently found that silicon from most sources has iron-containing precipitates and that this iron can resolve the long-standing

controversy about self-diffusion in silicon as being due to a vacancy mechanism. But what role does the iron play in the radiation-tolerance of solar cells? It is not known.

The questions posed above are tractable. It just takes a committed effort and funding!

REFERENCES

1. Fletcher, R. C.; and Brown, W. L.: Phys. Rev. 92, 585 (1953).

2. Waite, T. R.: Phys. Rev. 107, 463 (1957).

3. Waite, T. R.: Phys. Rev. 107, 471 (1957).

4. Yurkov, B. Ya.: Fiz. Tverd. Tela 3, 3563 (1961) [Sov. Phys. Solid State 3, 2591 (1962)].

5. Dettman, K.: Phys. Stat. Sol. 10, 269 (1965).

6. Corbett, J. W.: Phys. Rev. Letters 21, 817 (1968).

7. Corbett, J. W.: Rad. Effects 1, 85 (1969).

8. Simpson, H. M.; and Chaplin, R. L.: Phys. Rev. 178, 116 (1969).

9. Simpson, H. M.; and Sosin, A.: Rad. Effects 3, 1 (1970).

10. Peak, D.; and Corbett, J. W.: Phys. Rev. B 5, 1226 (1972).

11. Peak, D.; Brosious, P.; Lee, Y. H.; St. Peters, M.; Frisch, H. L.; and Corbett, J. W.: Rad. Effects 15, 61 (1972).

12. Peak, D.; and Corbett, J. W.: Rad. Effects 22, 225 (1974).

13. Schroeder, K.: Rad. Effects 5, 255 (1970).

14. Mooney, P. M.; Cheng, L. J.; Süli, M.; Gerson, J. D.; and Corbett, J. W.: Phys. Rev., in press.

15. Kimerling, L. C.: IEEE Trans. Nucl. Sci. NS-23, 1497 (1976).

16. Cheng, L. J.; Sours, P. W.; Karins, J. P.; Corelli, J. C.; and Corbett, J. W.: THIS CONFERENCE.

17. Feher, G.: Phys. Rev. 114, 1219 (1959).

18. Ludwig, G.; and Woodbury, H. H.: in "Solid State Physics" ed. F. Seitz and D. Turnbull (Academic Press, N.Y. 1962) Vol. 13, p. 223.

19. Watkins, G. D.: in "Radiation Damage in Semiconductors" ed. P. Baruch (Dunod, Paris, 1965) p. 97.

20. Corbett, J. W.: "Electron Damage in Semiconductors and Metals" (Academic Press, N.Y., 1966).

21. Corbett, J. W.; and Bourgoin, J. C.: in "Point Defects in Solids", eds. J. H. Crawford, Jr. and L. M. Slifkin (Plenum, N.Y., 1975) p. 1.

22. Corbett, J. W.; Bourgoin, J. C.; Cheng, L. J.; Corelli, J. C.; Lee, Y. H.; Mooney, P. M.; and Weigel, C.: in "Defects in Semiconductors, 1976" (Inst. of Physics, London, 1977), p. 1.

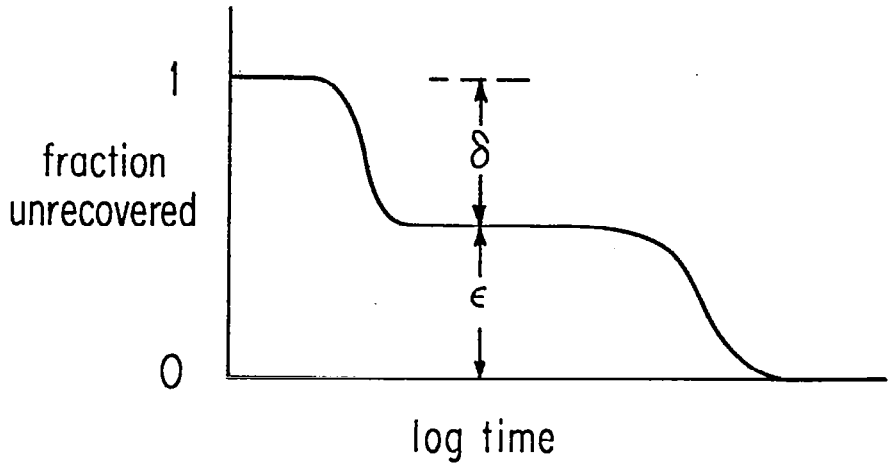

FIG. 1. TIME DEPENDENCE OF VACANCY - INTERSTITIAL ANNIHILATION SHOWING THE CORRELATED (δ) AND UNCORRELATED (ϵ) RECOVERY.

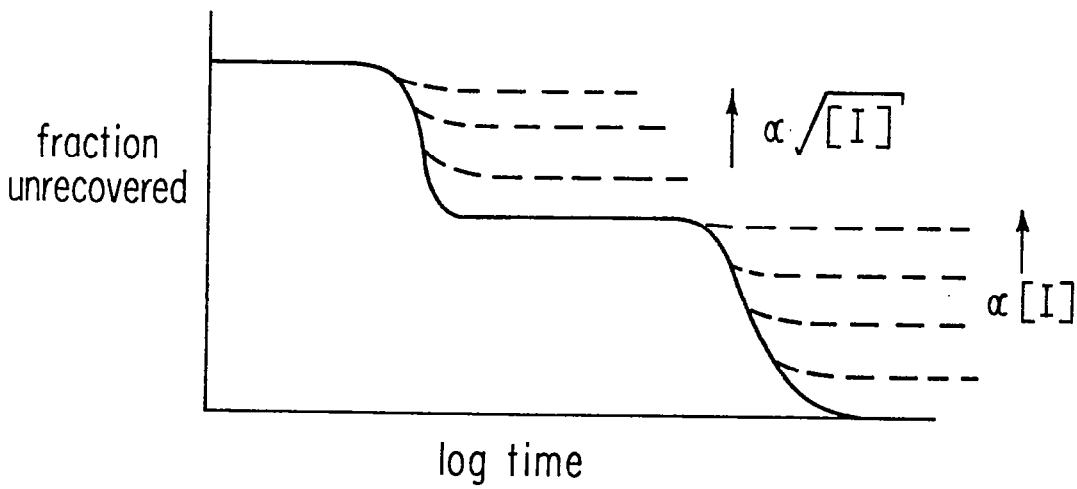

FIG. 2. TIME DEPENDENCE OF THE VACANCY- INTERSTITIAL ANNIHILATION WITH THE DASHED LINES SHOWING THE DEPENDENCE OF THE RETENTION OF DAMAGE ON THE IMPURITY CONCENTRATION, [X].

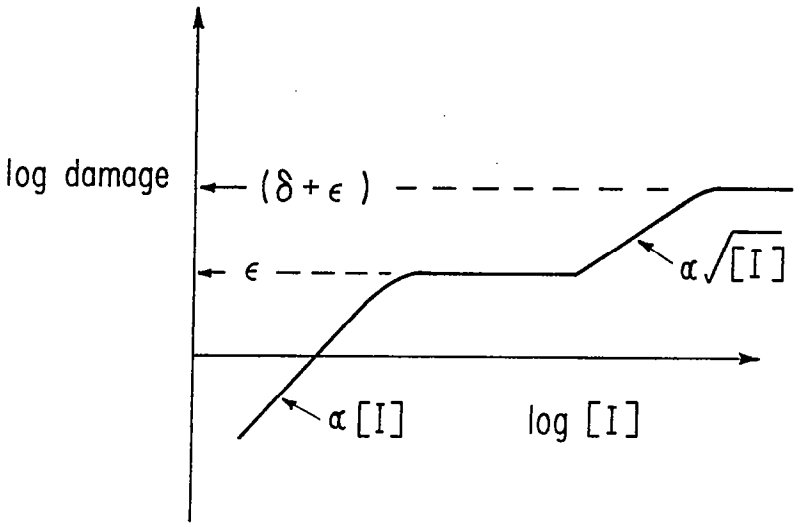

FIG. 3. THE DAMAGE WHICH ESCAPES ANNIHILATION BY IMPURITY TRAPPING VERSUS THE IMPURITY CONCENTRATION, [X].

(IMPURITY + VACANCY) PAIRS IN SILICON

I	II											III	IV	V	VI	VII	VIII
H																	He
Li	Be											B	C	N	O	F	Ne
Na	Mg											Al	Si	P	S	Cl	Ar
K	Ca	Sc	Ti	V	Cr	Mn	Fe	Co	Ni	Cu	Zn	Ga	Ge	As	Se	Br	Kr
Rb	Sr	Y	Zr	Nb	Mo	Tc	Ru	Rh	Pd	Ag	Cd	In	Sn	Sb	Te	I	Xe
Cs	Ba	*	Hf	Ta	W	Re	Os	Ir	Pt	Au	Hg	Tl	Pb	Bi	Po	At	Rn
Fr	Ra	**															
* →		La	Ce	Pr	Nd	Pm	Sm	Eu	Gd	Tb	Dy	Ho	Er	Tm	Yb	Lu	
** →		Ac	Th	Pa	U	Np	Pu	Am	Cm	Bk	Cf	Es	Fm	Md	No	Lw	

FIG. 4. THE STIPLED SQUARES IN THE PERIODIC TABLE SHOW THOSE ELEMENTS FOR WHICH SOME INFORMATION ABOUT VACANCY + IMPURITY PAIRS IN SILICON EXISTS IN THE LITERATURE.

19. EFFECTS OF DEFECT RECOMBINATION CENTERS ON RADIATION DAMAGE IN SOLAR CELLS†

L. J. Cheng, P. W. Sours, J. P. Karins, J. C. Corelli* and J. W. Corbett
Institute for the Study of Defects in Solids and Department of Physics
State University of New York at Albany, Albany, N.Y. 12222

ABSTRACT

Defect production in silicon is modeled on a computer by solving a large system of rate equations. The model includes the main, known defects that are stable at operating temperatures of solar cells in outer space; most of these defects are secondary and tertiary defects. The preliminary result shows that the presence of defect recombination centers for primary defects (i.e., vacancy and interstitial) can effectively reduce the production rates of those stable defects and, consequentially, improve the lifetime of solar cells operating in radiation environment. The characteristics of the defect recombination center required for better solar cell performance along with prospective candidates will be discussed.

INTRODUCTION

The radiation-induced defects in silicon responsible for the deterioration of solar cells are mainly impurity-associated complexes, such as the vacancy-oxygen-carbon complex (the K-center) (ref. 1). In principle, if the formation of these impurity-associated defects could be avoided, the radiation tolerance of silicon cells would be improved drastically. One trivial way is to remove all undesired impurities from silicon crystals, specially oxygen and carbon. The concentration of oxygen and carbon in very pure silicon now commercially available are in the order of 10^{16} atoms/cm^3. The availability of purer crystals in the future is still an open question. In addition, oxygen appears to be always (unintentionally) introduced into silicon during the diffusion process for junction formation. An alternative way to reduce the importance of these impurities is to introduce sinks for both vacancies and interstitials to reduce the chance of the primary defects reaching the impurities. These sinks are called defect recombination centers, because the vacancy and the interstitial atom recombine at the site, thus removing the defect.

---

† Work partially supported by NASA Grant NSG 3095, ONR Contract N00014-75-C-0919, and INTELSAT Contract No. IS-681.

* Permanent Address: Department of Nuclear Engineering, Rensselaer Polytechnic Institute, Troy, New York 12181.

In this paper, we shall discuss effects of defect recombination centers on radiation damage in silicon. The next section presents preliminary results from a computer modeling of defect production in p-type silicon. The model illustrates the effect of defect recombination centers. In the last section we shall discuss the prospect for improving solar cell radiation tolerance.

DEFECT PRODUCTION MODELING

Silicon is the most thoroughly studied semiconductor from the point of view of radiation damage. However, the kinetics of defect production is far from fully understood. Many essential data concerning the interactions between the primary defects and imperfections are not available. The model to be presented here is a simplified one described by means of a system of rate equations. We restrict ourselves to silicon with impurities of oxygen, carbon and boron only, which are the major known impurities in p-type silicon used for solar cells. In our model, free mobile single vacancies, free mobile self-interstitial atoms, and immobile divacancies are created at constant rates under irradiation. The carbon and the boron interstitial created by the Watkins replacement mechanism with self-interstitials are considered to be mobile. The interaction between any two of the defects, including impurities, is governed by a capture rate (per defect) in the form of $4\pi DR$ where D is the diffusion coefficient of the mobile species and R is the effective capture radius. We assume the following reactions:

$V + I$	$\rightarrow$	recombination		(1)
$V + O$	$\rightarrow$	A	(ref. 2)	(2)
$V + V$	$\rightarrow$	V_2		(3)
$V + A$	$\rightarrow$	VA	(ref. 3)	(4)
$I + C_s$	$\rightarrow$	C_I	(ref. 4)	(5)
$I + B_s$	$\rightarrow$	B_I	(ref. 5)	(6)
$I + I$	$\rightarrow$	I_2	(ref. 6)	(7)
$I + VA$	$\rightarrow$	A		(8)
$I + A$	$\rightarrow$	O	(refs. 7 and 8)	(9)
$I + V_2$	$\rightarrow$	V		(10)
$V + C_I$	$\rightarrow$	C_s		(11)
$V + B_I$	$\rightarrow$	B_s		(12)
$B_I + O$	$\rightarrow$	B_IO	(ref. 9)	(13)
$C_I + A$	$\rightarrow$	V-O-C + I	(refs. 9 and 10)	(14)
$I + V_T$	$\rightarrow$	V_T		(15)
$V + V_T$	$\rightarrow$	V_T		(16)

$$V + V_2 \rightarrow V_T \quad (17)$$

$$V + VA \rightarrow V_T \quad (18)$$

where V ≡ single vacancy, I ≡ self-interstitial, O ≡ interstitial oxygen, C_S ≡ substitutional carbon, B_S ≡ substitution boron, V_2 ≡ divacancy, A ≡ the vacancy-oxygen complex (the A-center), C_I ≡ the interstitial carbon, B_I ≡ the interstitial boron, VA ≡ the divacancy-oxygen complex, I_2 ≡ di-interstitial, B_IO ≡ the boron-oxygen interstitial pair, V-O-C ≡ the vacancy-oxygen-carbon complex (the k-center), and V_T ≡ the defect recombination center. Experimental evidence for some of these reactions are available in the literature (refs. 2-10). Other reactions are generally accepted. The defect recombination center is a general term for any imperfection which posses the necessary properties. We include the trivacancy, the trivacancy-oxygen complex, and higher-order complexes in our computation, as indicated in Eqns.(17) and (18). In addition, we assume that the defect recombination center will not disappear once it is introduced. With the generation rate G for the Frenkel pair and G_{V2} for divacancies and interstitials, Eqns. (1-18) yield the system of simultaneous differential equations, shown in Table I. The system can be solved numerically using a computer. Nevertheless, the problem represents a non-trivial exercise in numerical analysis. Such coupled equations are known as "stiff equations". The major problem is that there may be several widely differing eigen-values (or time constants) for the matrices, used to solve the equations and the numerical methods can become wildly inaccurate if care is not taken (refs. 11 and 12). We have successfully solved the system of equations with limited ranges of parameters. The work is still in progress. Here, we present some of our preliminary results to illustrate the importance of the defect recombination center in the radiation tolerance of solar cells.

Figures 1 and 2 show typical solutions given as log [ ] vs. log time, with the parameter values listed in Table II. The main feature worth noting is that the production rates of the defects, such as C_I,B_I,V-O,V-O-C, and B_IO, decrease substantially when the product of the defect recombination center concentration and its capture radius increases to the point where it is comparable to those of the impurities. In addition, the computation shows another feature that only V-O-C and B_IO are dominant when the irradiation time is long ($\gtrsim$ several seconds, as indicated in the figures). This is consistent with experimental observations (ref. 9), showing the validity of our modeling.

DEFECT RECOMBINATION CENTERS

That the introduction of a suitable concentration of defect recombination centers into silicon could be an effective way to improve the radiation tolerance of silicon solar cells is illustrated by the computation given in the last section. In this section, we shall discuss properties of the ideal defect recombination center and evaluate candidates.

An effective defect recombination center must posses three properties. First, its presence in the crystal should not deteriorate the material properties essential for solar cell performance. Second, its capture cross sections for vacancies and interstitials should be reasonably large. Finally, the product, after trapping a vacancy or an interstitial or a mobile interstitial impurity atom produced during radiation damage should not affect the minority carrier lifetime. Four possible types of defect recombination centers could be introduced into silicon: 1) isolated impurities; 2) impurity pairs; 3) high order vacancy or interstitial aggregates; and 4) impurity clusters (or precipitates).

Many isolated impurities in silicon are electrically inactive. Among them, oxygen and carbon are usually quoted. They have reasonably large capture cross sections for primary defects. Unfortunately, their products with primary defects, the vacancy-oxygen complex and the carbon interstitial (ref. 13) are electrically active. Therefore they cannot be our desired defect recombination centers. The properties of many other impurities in silicon have been studied. Most of them give rise to energy levels deep in the forbidden energy gap of silicon and act as carrier recombination centers (ref. 14). They are not qualified to be defect recombination centers. However, there are still many impurities whose properties in silicon have not been investigated (see Figure 3) (ref. 15). This area is clearly worth exploring.

Impurity pairs, such as phosphorus-boron and lithium-boron, exist in silicon. They are usually electrically inactive. It is known that the isolated phosphorus atom in silicon is a good trap for the vacancy and the isolated boron atom for the interstitial. Conceptually, when presented together in the lattice the (P-B) pair could become an effective defect recombination center. Lithium-associated pairs could play some role in the reduction of radiation damage in Li-doped silicon. Unfortunately, Li-pairs are not stable at room temperature. Figure 4 shows impurity pairs in silicon which we are aware of. Possibilities for other impurity pairs with better properties exist, but little work has been done in this field to date.

High order vacancy or interstitial aggregates could be good defect recombination centers. Because they consist of a large number of vacancies or interstitials, an increase or decrease of one constituent caused by trapping a primary defect should not charge the general properties of the aggregate. The recent work of Corelli, et al. (ref. 16) indicates that high order defects exist in neutron-irradiated silicon after 500°C annealing giving rise to shallow levels; the recovery of sample resistivity is nearly completed at this point. This observation implies that these high order defects may be acceptable defect recombination centers. Further studies are needed.

Finally, we discuss the fourth type of defect recombination center — uniformly distributed clusters of an impurity or a compound of two or more impurities. The clusters can be in the form of precipitates. The cluster should act as a dopant in the material, which causes the formation of a space-charge region around it. As the minority carrier reflecting (p^+) back contact

avoids carrier recombination losses at the back surface of solar cells, the barrier at the space-charge region can prevent the entry of minority carriers into the cluster. Usually, the barrier is too small to produce any significant effect on the motion of the primary defects. Therefore, a primary defect can be trapped at the cluster and form a complex with an impurity. The complex within the space-charge region should not affect the carrier recombination properties in the bulk, even though it is a carrier recombination center by nature.

In the above, we have introduced four types of possible defect recombination centers in silicon. Experimental observations favorable to the fourth type are starting to appear. In 1964, Mandelkorn, et al. (ref. 17) reported that the damage rate in solar cells made of gadolinium-doped silicon was significantly lower than that of boron-doped solar cells. No further work was noticed until Antonenko, et al. (ref. 18) reported a similar result recently. They give an explanation for the reduction of radiation effects in Gd-doped silicon, which is similar to that of the fourth type discussed above. Gadolinium forms metallic clusters in silicon, when its concentration is in the order of $10^{17}/cm^3$ or larger (ref. 19). Many problems accompany the use of GD-doped silicon for solar cells. For example, the minority carrier diffusion length in Gd-doped silicon, reported in reference 17, is in the order of 100 μ, which is considerably less than that of $\gtrsim$ 500 μ in boron-doped solar cells. Other rare earth elements as dopants may create solar cells with similar radiation tolerance, possible even better. We have found no study on silicon doped with other rare earth elements. We believe this is a highly promising area. More studies on these materials are urgently needed.

REFERENCES

1. Lee, Y. H.; Cheng, L. J.; Mooney, P. M.; and Corbett, J. W.: This meeting.

2. Watkins, G. D.; Corbett, J. W.; and Walker, R. M.: J. Appl. Phys. 30, 1198 (1959).

3. Lee, Y. H.; and Corbett, J. W.: Phys. Letters 60A, 55 (1977).

4. Watkins, G. D.; and Brower, K. L.: Phys. Rev. Lett. 36, 1329 (1976).

5. Watkins, G. D.: Phys. Rev. B 12, 5824 (1976).

6. Lee, Y. H.; Gerasimenko, N. N.; and Corbett, J. W.: Phys Rev. B 14, 4506 (1976).

7. Cheng, L. J.; and Corbett, J. W.: to be published.

8. Kholodar', G. A.; Danhovskii, Yu. V.; Konoplyanyi, V. V.; and Vinetskii, Y. L.: Sov. Phys. Semicond. 10, 1016 (1976).

9. Mooney, P. M.; Cheng, L. J.; Süli, M.; Gerson, J. D.; and Corbett, J. W.: Phys. Rev. B, April 15, (1977).

10. Lee, Y. H.; Corbett, J. W.; and Brower, K. L.: Phys. Sol. Stat. (b), in press (1977).

11. Gear, C. W.: Comm. of the ACM 14, 196 (1971); 185 (1971).

12. Enright, W. H.: SIAM J., Numer. Anal. 11, 231 (1974).

13. Lee, Y. H.; Cheng, L. J.; Mooney, P. M.; Gerson, J. D.; and Corbett, J. W.: Solid State Commun. 21, 109 (1977).

14. Sze, S. M.: Physics of Semiconductor Devices (Wiley-Interscience, New York, 1969).

15. Corbett, J. W.; Bourgoin, J. C.; Cheng, L. J.; Corelli, J. C.; Lee, Y. H.; Mooney, P. M.; and Weigel, C.: Inst. Phys. Conf. Ser. No. 31 (1977) p. 1.

16. Corelli, J. C.; Mills, D.; Gruver, R.; Cuddeback, D.; Lee, Y. H.; and Corbett, J. W.: Inst. Phys. Conf. Ser. No. 31 (1977), p. 251.

17. Mandelkorn, J.; Schwartz, L.; Broder, J.; Hautz, H.; and Ulman, R.: J. Appl. Phys. 35, 2258 (1964).

18. Antonenko, R. S.; Kornyushin, S. I.; Shakhovtsov, V. I.; Shindich, V. L.; Yaskovets, I. I.: Sov. Phys. Semicond. 10, 942 (1977).

19. Andrianov, D. G.; Bochkarev, E. P.; Grishin, V. P.; Karpov, Yu. A.; and Sovel'ev, A. F.: Sov. Phys. Semicond. 8, 320 (1974).

TABLE I. SIMULTANEOUS DIFFERENTIAL EQUATIONS FOR THE REACTIONS LISTED IN EQUATIONS (1-18)

$$\frac{d[V]}{dt} = G - 4\pi(D_V + D_I)R_{VI}[V][I] - 4\pi D_V[V](R_{VO}[O] + R_{VB_I}[B_I] + 2R_{VV}[V] + R_{VA}[A] + R_{VV_2}[V_2] + R_{VVA}[VA] + R_{VV_T}[V_T] + R_{VI_2}[I_2] + R_{VC_I}[C_I]) + 4\pi D_I R_{IV_2}[I][V_2]$$

$$\frac{d[I]}{dt} = G + 2G_{V_2} - 4\pi(D_V + D_I)R_{VI}[V][I] - 4\pi D_I[I](R_{IB_S}[B_S] + R_{IA}[A] + R_{IV_2}[V_2] + 2R_{II}[I] + R_{IV_T}[V_T] + R_{IVA}[VA] + R_{IC_S}[C_S]) + 4\pi R_{C_IA}D_C[C_I][A]$$

$$\frac{d[O]}{dt} = -4\pi D_V R_{VO}[V][O] + 4\pi D_I R_{IA}[I][A] - 4\pi D_{B_I} R_{B_IO}[B_I][O]$$

$$\frac{d[A]}{dt} = 4\pi D_V R_{VO}[V][O] - 4\pi D_I R_{IA}[I][A] - 4\pi D_V R_{VA}[V][A] + 4\pi D_I R_{IVA}[I][VA]$$

$$\frac{d[B_S]}{dt} = 4\pi D_V R_{VB_I}[V][B_I] - 4\pi D_I R_{VB_S}[I][B_S]$$

$$\frac{d[B_I]}{dt} = 4\pi D_I R_{IB_S}[I][B_S] - 4\pi D_V R_{VB_I}[V][B_I] - 4\pi D_B R_{B_IO}[B_I][O]$$

$$\frac{d[V_2]}{dt} = G_{V_2} + 8\pi R_{VV} D_V [V]^2 - 4\pi D_V R_{VV_2}[V][V_2] - 4\pi D_I R_{IV_2}[I][V_2]$$

TABLE I. (CONTINUED)

$$\frac{d[VA]}{dt} = 4\pi D_V R_{VA}[V][A] - 4\pi D_V R_{VVA}[V][VA] - 4\pi D_I R_{IVA}[I][VA]$$

$$\frac{d[V_T]}{dt} = 4\pi D_V R_{VV_2}[V][V_2] + 4\pi D_V R_{VVA}[V][VA]$$

$$\frac{d[I_2]}{dt} = 8\pi D_I R_{II}[I]^2 - 4\pi R_{VI_2}[V][I_2]$$

$$\frac{d[C_S]}{dt} = 4\pi D_I R_{IC_S}[I][C_S] - 4\pi D_V R_{VC_I}[I][C_I]$$

$$\frac{d[C_I]}{dt} = 4\pi D_I R_{IC_S}[I][C_S] - 4\pi D_V R_{VC_I}[V][C_I] - 4\pi D_{C_I} R_{C_I A}[C_I][A]$$

$$\frac{d[V\text{-}O\text{-}C]}{dt} = 4\pi D_{C_I} R_{C_I A}[C_I][A]$$

$$\frac{d[B_I O]}{dt} = 4\pi D_{B_I}[B_I][O],$$

where [X] is the concentration of species X, $D_X \equiv$ the diffusion coefficient of species X, and $R_{XY} \equiv$ the effective capture radius of species Y for species X.

TABLE II. PARAMETERS USED IN NUMERICAL COMPUTATION WHERE RESULTS ARE SHOWN IN FIGURES 1 AND 2.

Capture Radius

$$R_{IV} = R_{VO} = R_{VB_I} = R_{VV} = R_{VA} = R_{VV_2} = R_{VVA}$$
$$= R_{VI} = R_{VC_I} = R_{IV_2} = R_{IB_S} = R_{IA} = R_{IV}$$
$$= R_{IVA} = R_{IC_S} = R_{C_IA} = R_{B_IO} = R_{VB_I}$$
$$= 5\ \mathring{A}$$
$$R_{VV_T} = R_{IV_T} = 50\ \mathring{A}$$

Diffusion Coefficients

$$D_V = 4.15\text{x}10^{-7}\ cm^2/sec$$
$$D_I = 3.16\text{x}10^{-3}\ cm^2/sec$$
$$D_{B_I} = 1\text{x}10^{-6}\ cm^2/sec$$
$$D_{C_I} = 1\text{x}10^{-7}\ cm^2/sec$$

Generation Rates

$$G = 5\text{x}10^{12}/cm^2/sec$$
$$G_{V_2} = 5\text{x}10^{9}/cm^2/sec$$

Initital Conditions

$$[O] = [B_S] = [C_S] = 10^{17}/cm^3$$
$$[V] = [I] = [B_I] = [C_I] = [A] = [V_2]$$
$$= [VA] = [I_2] = [V\text{-}O\text{-}C] = [B_IO] = 0,$$

Table II. (CONTINUED)

except

$[V_T] = 0$ for Figure 1.

and $[V_T] = 10^{17}$ for Figure 2.

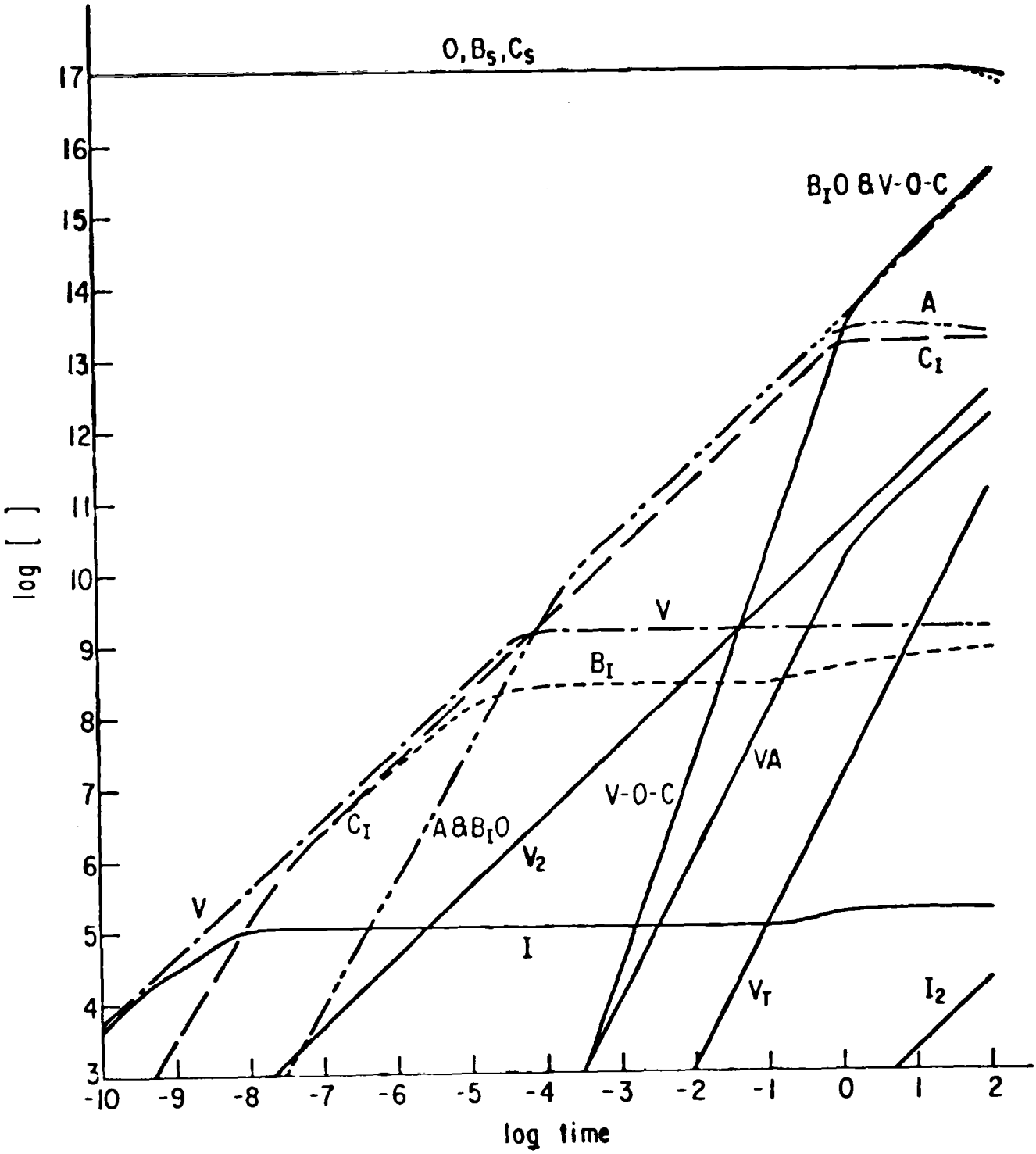

FIG. 1 COMPUTATION RESULT WITH INITIAL CONCENTRATION OF DEFECT RECOMBINATION CENTER BEING ZERO

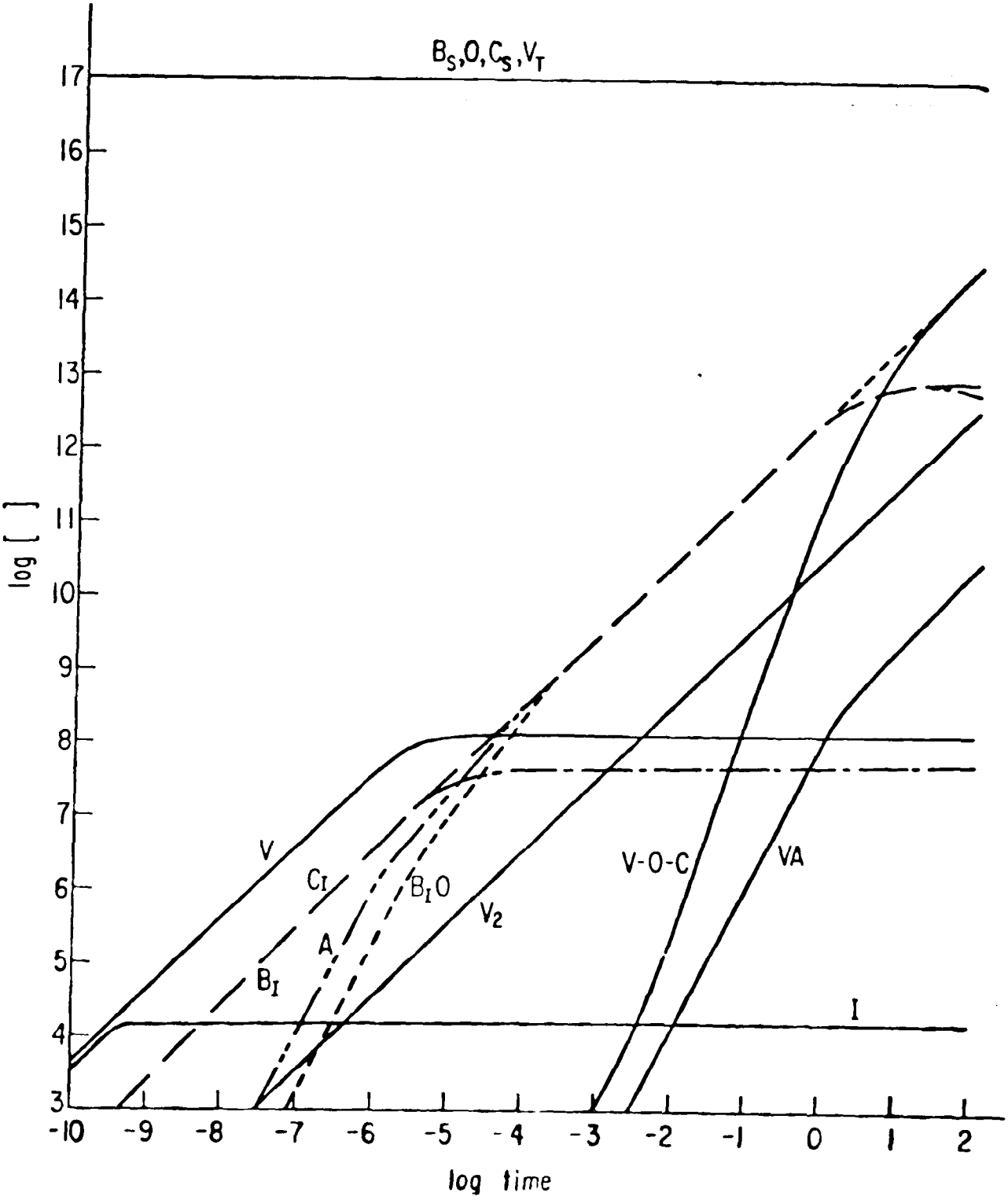

FIG. 2 COMPUTATION RESULT WITH INITIAL CONCENTRATION OF DEFECT RECOMBINATION CENTER BEING $10^{17}/cm^3$.

ELECTRICAL LEVELS IN SILICON

I	II											III	IV	V	VI	VII	VIII
H																	He
Li	Be											B	C	N	O	F	Ne
Na	Mg											Al	Si	P	S	Cl	Ar
K	Ca	Sc	Ti	V	Cr	Mn	Fe	Co	Ni	Cu	Zn	Ga	Ge	As	Se	Br	Kr
Rb	Sr	Y	Zr	Nb	Mo	Tc	Ru	Rh	Pd	Ag	Cd	In	Sn	Sb	Te	I	Xe
Cs	Ba	*	Hf	Ta	W	Re	Os	Ir	Pt	Au	Hg	Tl	Pb	Bi	Po	At	Rn
Fr	Ra	**															
* →		La	Ce	Pr	Nd	Pm	Sm	Eu	Gd	Tb	Dy	Ho	Er	Tm	Yb	Lu	
** →		Ac	Th	Pa	U	Np	Pu	Am	Cm	Bk	Cf	Es	Fm	Md	No	Lw	

FIG. 3 PERIODIC TABLE SHOWING THE ELEMENTS FOR WHICH MEASUREMENTS OF ELECTRICAL LEVELS IN SILICON HAVE BEEN MADE

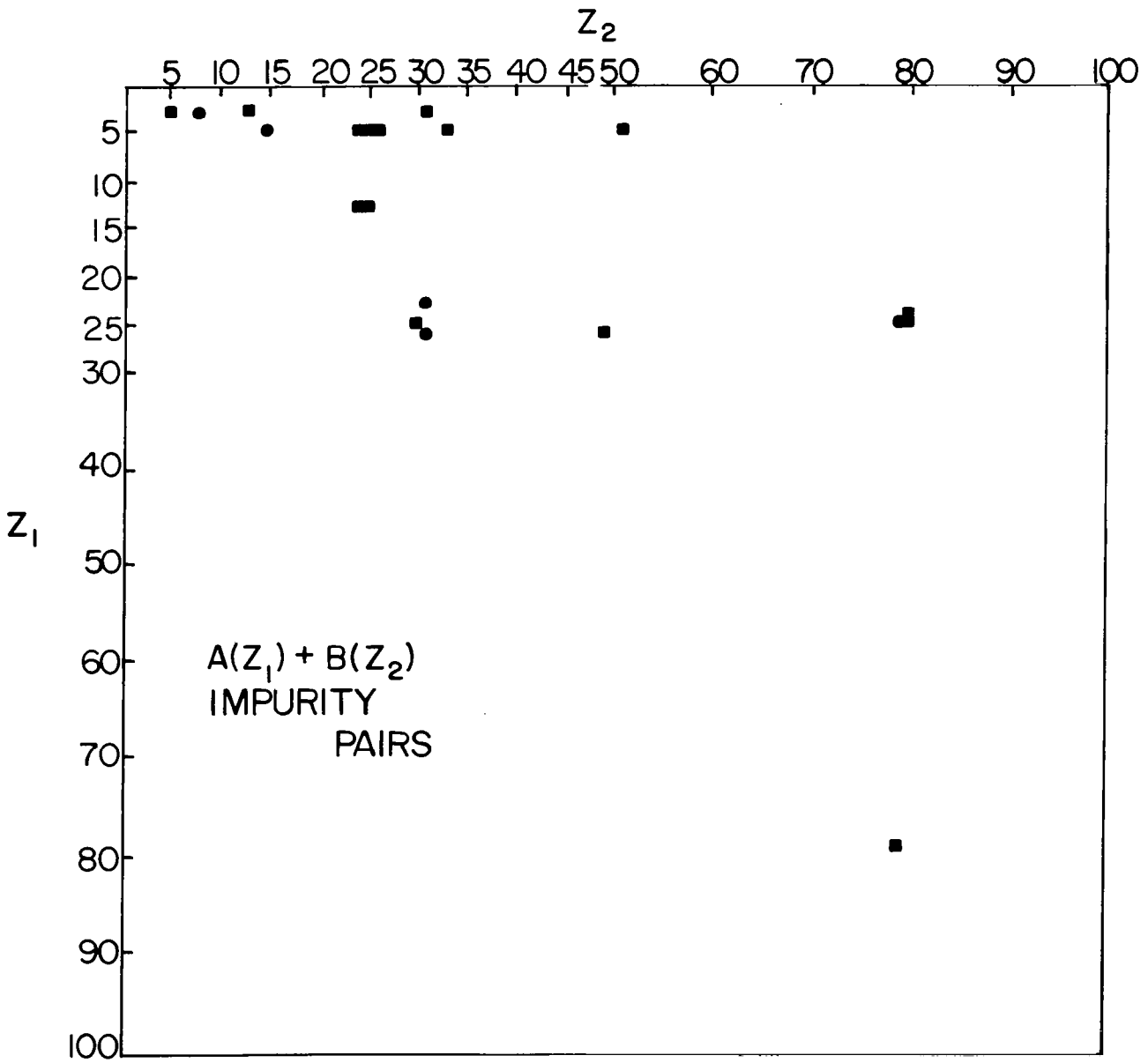

FIG. 4 IMPURITY PAIRS IN SILICON

20. EPR AND TRANSIENT CAPACITANCE STUDIES ON ELECTRON-IRRADIATED SILICON SOLAR CELLS†

Y. H. Lee, L. J. Cheng, P. M. Mooney* and J. W. Corbett
Institute for the Study of Defects in Solids and Department of Physics
State University of New York at Albany, Albany, N.Y. 12222

ABSTRACT

One and two ohm-cm solar cells irradiated with 1 MeV electrons at 30°C were studied using both EPR and transient capacitance techniques. In 2 Ω-cm cells, we observed Si-G6 and Si-G15 EPR spectra and majority carrier trapping levels at (E_V + 0.23) eV and (E_V + 0.38) eV, each of which corresponds to the divacancy and the [carbon-oxygen-vacancy] complex, respectively. In addition, a boron-associated defect with a minority carrier trapping level at (E_C-0.27) eV was observed. In 1 Ω-cm cells, the G15 spectrum and majority carrier trap at (E_V + 0.38) eV are absent and an isotropic EPR line appears at g = 1.9988 (±0.0003); additionally we observed a majority carrier trapping center at (E_V + 0.32) eV, which could be associated with impurity lithium. The formation mechanism of these defects are discussed according to the isochronal annealing data in electron-irradiated p-type silicon.

INTRODUCTION

Recent experimental developments in electron paramagnetic resonance (EPR) and deep-level transient spectroscopy (DLTS) have improved our understanding of the role of impurity carbon in irradiated silicon. Watkins and Brower (ref. 1) attributed the G12 EPR spectrum to a carbon interstitial [C_I^+], which is very similar in many aspects to the one identified earlier in an optical experiment (ref. 2). Direct correlation between the EPR and DLTS data (ref. 3) has shown that [C_I^+] gives rise to a donor level at (E_V + 0.30) eV with the hole capture cross section being $\sigma_p > 10^{-17} cm^2$. Above room temperature, [C_I^+] becomes unstable and interacts with other defects to yield more stable defects; if the carbon concentration is high enough (> 10^{17} cm^{-3}), the carbon-carbon pair (G11 spectrum; [C_S+C_I]) can be formed (ref. 4); in oxygen-rich samples, [V + O] traps [C_I] to yield carbon-oxygen-vacancy complex (C+O+V]; G15 spectrum) (ref. 5). In this report, we will describe a carbon-associated defect as well as other defects we observed by EPR and DLTS in n/p solar cells.

---

† Work partially supported by NASA Grant NSG 3095 and ONR Contract N00014-75-C-0919 and INTELSAT Contract No. IS-681.

* Permanent address: Department of Physics and Astronomy, Vassar College Poughkeepsie, N.Y. 12601.

EXPERIMENTAL TECHNIQUES

Two n/p silicon solar cells, whose base material is B-doped Czochralski silicon and whose resistivities are ρ = 1.0 Ω-cm and 2.0 Ω-cm, respectively, were irradiated with 1.0 MeV electrons, using the 4.2 MeV Dynamitron at SUNY/Albany. During irradiation, the cell temperature was kept below 30°C; the electron fluence was $\sim 10^{17}$e/cm^2 for EPR measurements and $\sim$ (1-8.)x10^{16}e/cm^2 for DLTS measurements. The EPR samples were sliced along the <110>, after the back contact and front glass cover was chemically removed by HF and HNO_3. Our DLTS technique is similar to the transient capacitance spectroscopy reported by Lang (ref. 6); the activation energy for carrier emission was measured with the accuracy of ±0.02 eV; also, the carrier capture cross section, σ_p (hole) and σ_n (electron), was measured to the accuracy of one significant figure. [The authors are very grateful to Dr. A. Meulenberg (COMSAT Corp.) who kindly supplied the cells.]

RESULTS AND DISCUSSION

Figure 1 shows a typical EPR spectrum observed at 77°K with the external magnetic field, $\vec{H}_o$, parallel to <100>. The well-known divacancy center ($[V_2]^+$; G6 spectrum) (ref. 7) is present in both cells, but the G15 spectrum (or K-center) (ref. 8) and an isotropic line at g = 1.9988 (±0.0003), which we tentatively called RCA2, depend strongly on the sample characteristics, i.e., G15 which arises from $[C+O+V]^+$ (ref. 5) was observed only in the 2 Ω-cm cell, while RCA2 was seen in the 1 Ω-cm cell. The DLTS spectra shown in figure 2 also indicates a clear distinction between these two cells; in the 2 Ω-cm cells we observed two majority carrier trapping centers located at (E_v + 0.23) eV and (E_v + 0.38) eV, respectively, and one minority carrier trapping center located at (E_c - 0.27) eV; in the 1 Ω-cm cells, the majority trap at (E_v + 0.38) eV is absent and three other majority traps were found at (E_v + 0.24) eV, (E_v + 0.26) eV and (E_v + 0.32) eV, respectively. The minority carrier trapping center at (E_c - 0.27) eV was consistently observed in both cells, as was the majority carrier trapping center at (E_v + 0.23) eV which has been correlated with $[V_2]^+$ (ref. 9), although it was severely perturbed by the presence of the (E_v + 0.24) eV trap in 1 Ω-cm cell. We summarize the DLTS data in table I. The minority trap at (E_c - 0.27) eV was found to be associated with oxygen and boron impurities and thought to arise from an interstitial defect of oxygen and boron (ref. 10). The (E_v + 0.38) eV level is actually a superposition of two different defects, each of which has a different capture cross-section and annealing characteristics (300°C and 400°C, respectively). The major portion of the DLTS signal arises from $[C+O+V]^+$ (ref. 3, 5 and 10), which gives rise to a defect energy level at (E_v + 0.30) eV (ref. 5 and 8); the difference in energy position between EPR and DLTS is presumably owing to the superposition of two defects in the DLTS signal.

Three majority carrier traps at (E_v + 0.24) eV, (E_v + 0.26) eV and (E_v + 0.32) eV in the 1 Ω-cm cells appear neither in 2 Ω-cm cells nor in other

p-type silicon samples. This is very similar to the behavior of the isotropic EPR signal at g = 1.9988. We note that Goldstein (ref. 11) and later Passenheim, et al., (ref. 12) observed an EPR spectrum at g = 1.9985 in Li-doped Czochralski silicon and attributed it to the donor state of [Li + O]. Also, Urli (ref. 13) argued that [Li + O + V] results in a trap at (E_V + 0.32) eV, which is in agreement with the one observed by DLTS. Since Li was not deliberately incorporated in the 1 Ω-cm cells (ref. 14), it is not clear whether impurity lithium was precipitated in as-grown silicon or during device fabrication. The center we observed might be associated with another unknown impurity, but this impurity should suppress the formation of [C + O + V], as the lithium impurity does (ref. 15). Thus, EPR, photo-luminescence and electrical measurements all seem to support our identification of the isotropic line as RCA2 which is associated with lithium and oxygen impurities.

Figure 3 shows the energy dependence of the [C + O + V] production rate, measured by EPR (ref. 8), along with that of other major defects in electron-irradiated silicon (ref. 16). It clearly indicates that [C + O + V] is one of the dominant defects in irradiated oxygen-rich silicon. We estimated from the DLTS data of (E_V + 0.38) eV that [C + O + V] would have a minority carrier capture cross section of $\sigma_n \sim 10^{-12} - 10^{-15}$ cm^2. This supports the view that [C + O + V] is a dominant recombination center in silicon solar cells (ref.17). One way to account for the large production rate of [C + O + V] is to say that the defect interaction between the [V + O] and the mobile [C_I] yields [C + O + V] and releases a self-interstitial [I] (ref. 5); i.e.,

$$[O + V] + [C_I] \rightarrow [C + O + V] + [I].$$

Other formation mechanisms such as

$$[O + V_2] + [C_I] \rightarrow [C + O + V]$$

are concievable, but cannot be a dominant effect, because the production rate of [O + V_2] is comparable to that of [V_2] (ref. 18). It may be possible that the self-interstitial so produced diffuses out either to the sample surface or to dislocation, but it may as well participate in the defect annealing by recombining with a vacancy-type defect. If Li is present, the situation changes; since the migration energy of [Li_I] is 0.66 eV, lower than that (0.80 eV) of [C_I], [Li_I] may interact with [O + V] earlier than [C_I] does. Thus, we expect the interaction,

$$[O + V] + [Li_I] \rightarrow [Li_I + O + V]$$

to occur, as suggested by Vavilov (ref. 19). This provides a reasonable explanation for our EPR and DLTS results.

Finally, we summarize in figure 4 those defects that could be created by electron irradiation near room-temperature; defects are classified by their energy level and labeled by their model, if it is known; also, the sample characteristics divide them into four groups, i.e., n-type or p-type and Czochralski or float-zone silicon. The energy levels in figure 4 are all

determined by optically bleaching the corresponding EPR signal. Although a variety of oxygen-dependent centers have been identified unambiguously in oxygen-rich samples, there still remain many oxygen-dependent EPR spectra which certainly require more study to unravel their defect structure. We should point out that the defect interaction and its evolution could be more complicated than what we have described in [C + O + V], since some of those defects in figure 4 are simultaneously present in irradiated silicon.

SUMMARY AND CONCLUSION

EPR and DLTS show consistently that the [carbon-oxygen-vacancy] complex (G15 or K center) acts as a dominant recombination center in an n/p silicon solar cell and that the formation of G15 can be suppressed by introducing another impurity that is mobile at room temperature, such as lithium.

REFERENCES

1. Watkins, G. D.; and Brower, K. L.: Phys. Rev. Lett. 36, 1329 (1976).
2. Bean, A. R.; and Newman, R. C.: Solid State Commun. 8, 175 (1970).
3. Lee, Y. H.; Cheng, L. J.; Gerson, J. D.; Mooney, P. M.; and Corbett, J. W.: Solid State Commun. 21, 109 (1977).
4. Brower, K. L.: Phys. Rev. B9, 2607 (1974).
5. Lee, Y. H.; Corbett, J. W.; and Brower, K. L.: Phys. Stat. Sol. (b), in press (1977).
6. Lang, D. V.: J. Appl. Phys. 45, 3014 (1974).
7. Watkins, G. D.; and Corbett, J. W.: Phys. Rev. 138, A543 (1965).
8. Almeleh, N.; Goldstein, B.: Phys. Rev. 149, 687 (1966).
9. Kimerling, L. C.: IEEE Trans.-Nucl. Sci., NS-23, 1497 (1976).
10. Mooney, P. M.; Cheng, L. J.; Süli, M.; Gerson, J. D.; and Corbett, J. W.: Phys. Rev. B15, April 15, 1977.
11. Goldstein, B.: Phys. Rev. Lett. 17, 428 (1966).
12. Passenheim, B. C.; Naber, J. A.; and Berger, R. A.: Conf. Record of the Eighth IEEE Photovoltaic Specialists Conf., p. 260 (1970).
13. Urli, N. B.: Rad. Effects 9, 93 (1971).

14. Meulenberg, Jr., A.: private communication.

15. Johnson, E. S.; Compton, W. D.; Noonan, J. R.; and Streetman, B. G.: J. Appl. Phys. 44, 5411 (1973).

16. Corbett, J. W.; and Watkins, G. D.: Phys. Rev. 138, A555 (1965).

17. Gorodetskii, S. M.; Grigor'eva, G. M.; Kreinin, L. B.; Lazovskii, V. V.; Landsman, A. P.; and Sominskii, M. S.: Sov. Phys.-Semicond. 2, 90 (1968).

18. Lee, Y. H.; and Corbett, J. W.: Phys. Rev. B13, 2653 (1976).

19. Vavilov, V. S.: Sov. Phys.-Uspekhi 7, 797 (1965).

TABLE I - CARRIER TRAPS IN n/p SILICON SOLAR CELLS IRRADIATED WITH 1.0 MeV ELECTRONS AT 30°C

Sample	Energy Level (eV)	Production rate (cm^{-1})	Carrier Capture Cross Section (cm^{-2})	Defect Model	Ref.
1 Ω-cm cell	$E_v + 0.24$	∿ 0.03	$\sigma_p \sim 3x10^{-17}$		
	$E_v + 0.26$	∿ 0.02	$\sigma_p \sim 4x10^{-17}$		
	$E_v + 0.32$	?	?	$[Li+O+V]^+$	
	$E_c - 0.27$	0.08	$\sigma_n = 2x10^{-13}$	$[O_I+B_I]$	10
2 Ω-cm cell	$E_v + 0.23$	0.0015	$\sigma_p = 2x10^{-16}$	$[V_2]^+$	7,9
	$E_v + 0.38$	0.011	$\sigma_{p_1} = 2x10^{-16}$	$[C+O+V]^+$	3,5,10
			$\sigma_{p_2} = 2x10^{-19}$		
	$E_c - 0.27$	0.04	$\sigma_n = 2x10^{-13}$	$[O_I+B_I]$	10

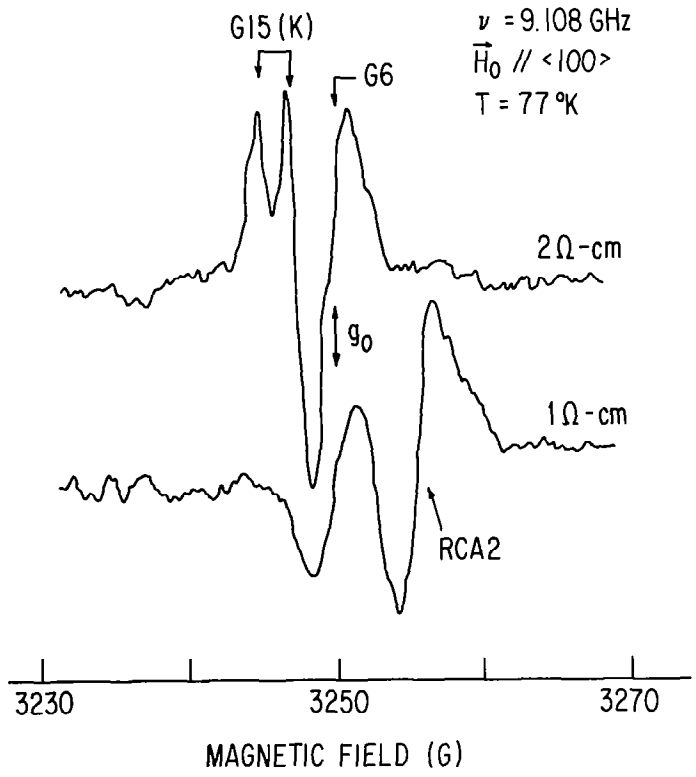

FIG. 1 EPR SPECTRA OBSERVED IN N/P SILICON SOLAR CELLS

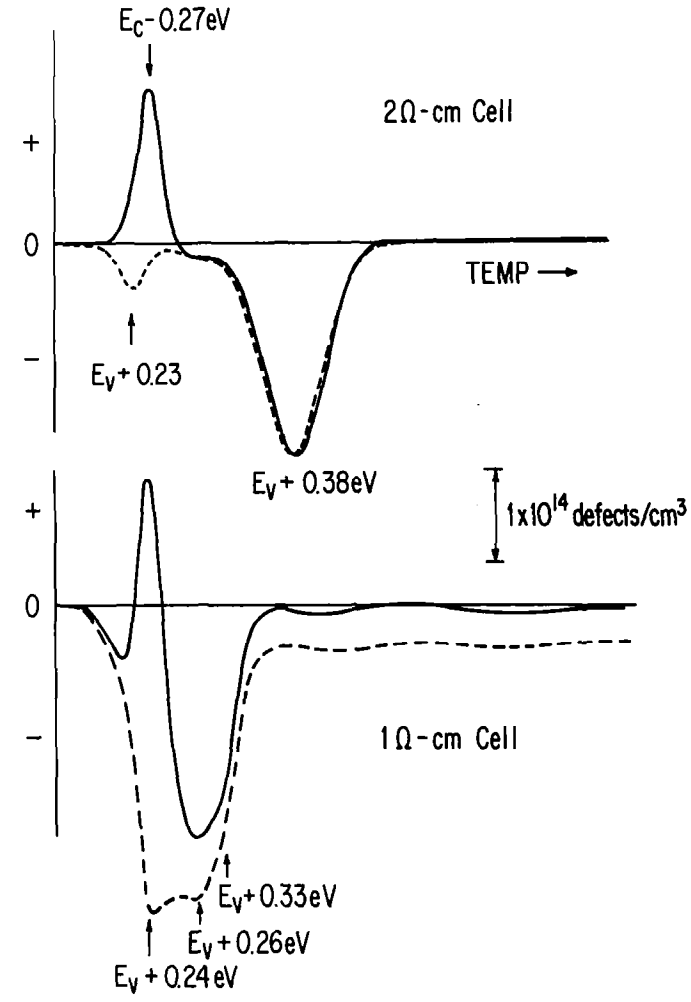

FIG. 2 TRANSIENT CAPACITANCE SPECTRA TAKEN WITH (SOLID LINE) OR WITHOUT (DOTTED LINE) MINORITY CARRIER INJECTION.

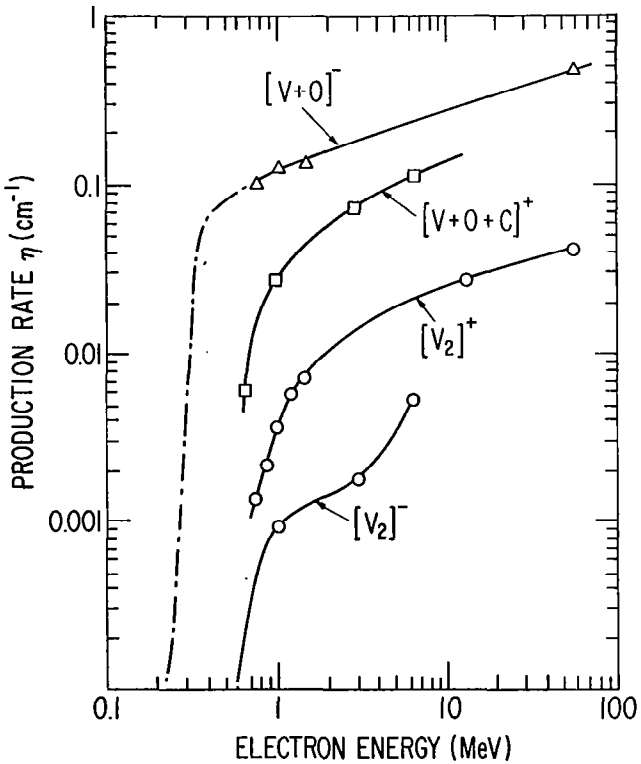

FIG. 3 DEFECT PRODUCTION RATE VERSUS INCIDENT ELECTRON ENERGY.

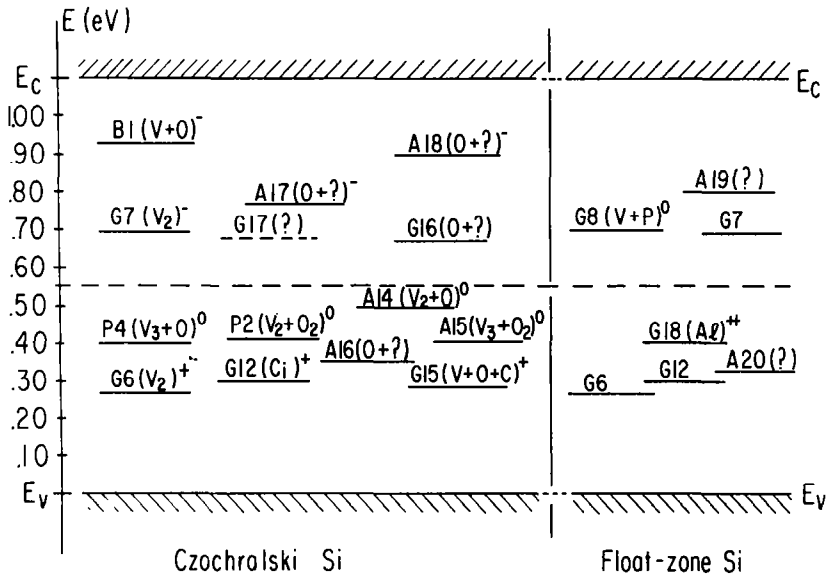

FIG. 4 DEFECT ELECTRICAL LEVELS IN ELECTRON-IRRADIATED SILICON OBSERVED BY EPR.

21. RADIATION TESTS OF SEP SOLAR CELLS*

Henry Oman
Boeing Aerospace Company

SUMMARY

OCLI-manufactured solar cells specially designed for Solar Electric Propulsion (SEP) were tested with radiation fluences up to 10^{12} protons having energies of 1.5, 1.0, and 0.5 MeV, and with fluences up to 10^{16} electrons having 1.0 MeV energy. NASA-supplied Spectrolab cells having a back-surface field were also irradiated with the same particles and fluences. Cell performances are described by curves in which normalized and absolute values of maximum power, maximum-power voltage, short-circuit current, and open-circuit voltage are plotted as a function of fluence.

INTRODUCTION

Low cost, high efficiency solar cells were previously identified as a required development in SEP system analyses performed for NASA-MSFC by Boeing. Solar panels for SEP must generate power in a solar intensity range from 10 suns** at 0.316 astronomical units (AU) to 0.0175 suns at 7.6 AU. The corresponding temperatures range from +255°C to -190°C. Neither conventional solar cells nor the new high efficiency solar cells are suitable for all SEP missions because they are designed and optimized for performance at only near-Earth conditions. In the SEP program, Boeing and OCLI designed a solar cell that will have an efficiency of at least 11.4 percent at 1.0 AU, after cover installation, and will have adequate performance for missions to Mercury (0.387 AU) or Jupiter (5.2 AU). The SEP solar cell was designed with the aid of the Boeing Solar Cell Performance Code computer program.

The detailed cell design was done by OCLI, Boeing's subcontractor, supported by the Boeing analysis. The N-on-P SEP cell is made from 2 ohm-cm silicon, 200 μm (8 mils) thick, has a 0.2 micrometer (μm) junction depth, and both of its contacts are on the cell's back surface. This SEP cell has no back-surface field. Finished cells were tested at the Boeing Space Center in Kent, Washington, where representative groups of cells were exposed to all of the mission environments, including radiation and ultraviolet, the range of expected combinations of temperature and illumination intensity, and thermal cycling and thermal shock. MSFC furnished 200 Spectrolab back-surface field cells which were also subjected to the same conditions.

---

*This work was done on NASA-MSFC Contract NAS8-31670.
**Solar intensity is given in terms of suns where 1.0 sun is the solar intensity at a heliocentric radius of 1.0 AU.

SEP SOLAR CELL RADIATION

Eighty 2 by 4 cm solar cells, 40 from Spectrolab and 40 from OCLI were irradiated. Each group of 40 was divided into 4 sets of 10 cells each, with one set from each group receiving 1.0 MeV electron bombardment and the other three sets from each group receiving 0.5 MeV, 1.0 MeV and 1.5 MeV proton bombardment. All radiation comes from a Dynamitron accelerator. The solar cells were mounted on an aluminum sample plate which in turn was mounted to a water-cooled copper heatsink. The temperature of each cell during measurements was measured by a copper-constantan thermocouple. The solar spectrum for cell performance measurements was provided by a Spectrolab X25L solar simulator calibrated at 1.0 solar constant (AMO) with a standard N/P solar cell traceable to a balloon flight standard solar cell. The illumination entered the test chamber through a G.E. 125 quartz window in the chamber door.

The particle beam, electron or proton, was scattered by an aluminum foil to spread the beam and reduce its energy. During beam dosimetry the solar cell mounting plate was rotated 180° to avoid irradiating the cells. The beam current from the accelerator was measured with a sample-plane Faraday cup.

Radiation Test Data

On the pages that follow are plotted solar cell performance, measured at 25°C with air-mass zero sunlight, after exposure to the various fluences of electrons and protons. Average values for each fluence are shown as dots and the extreme values of the tested cells are shown as bars. Two scales are provided on each vertical axis, one for absolute values and one for normalized values. The solid curves and range bars represent the measured performance of Spectrolab cells. Dashed lines show the corresponding normalized characteristics of OCLI cells. Absolute values of the characteristics of OCLI cells can be calculated by multiplying normalized values by the following initial values

Figure	Irradiation	Plotted Spectrolab Characteristic	Initial Value for OCLI Characteristic
1	1.5 MeV protons	Maximum power	124 mW
2		Voltage at maximum power	0.497 V
3		Short-circuit current	279 mA
4		Open-circuit voltage	0.598 V
5	1.0 MeV protons	Maximum power	121 mW
6		Voltage at maximum power	0.485 V
7		Short-circuit current	282 mA
8		Open-circuit voltage	0.600 V
9	0.5 MeV protons	Maximum power	120 mW
10		Voltage at maximum power	0.488 V
11		Short-circuit current	274 mA
12		Open-circuit voltage	0.600 V

Figure	Irradiation	Plotted Spectrolab Characteristic	Initial Value for OCLI Characteristic
13	1.0 MeV electrons	Maximum power	123 mW
14		Voltage at maximum power	0.490 V
15		Short-circuit current	0.282 mA
16		Open-circuit voltage	0.600 V

Noteworthy is the effectiveness of 0.5 MeV protons in degrading solar cells. The cells had no covers during irradiation, and the 0.5 MeV protons apparently came to rest in a critical region in the solar cell. Also, as predicted, the 1 MeV electrons disabled the P^+ back-surface field, causing the Spectrolab cells to degrade more severely than the OCLI cells, which did not have the back-surface field, from a normalized power output standpoint. However, after irradiation by 10^{16} one-MeV electrons, the Spectrolab and OCLI cells had essentially the same absolute output, whereas the initial output of the Spectrolab cells was considerably higher.

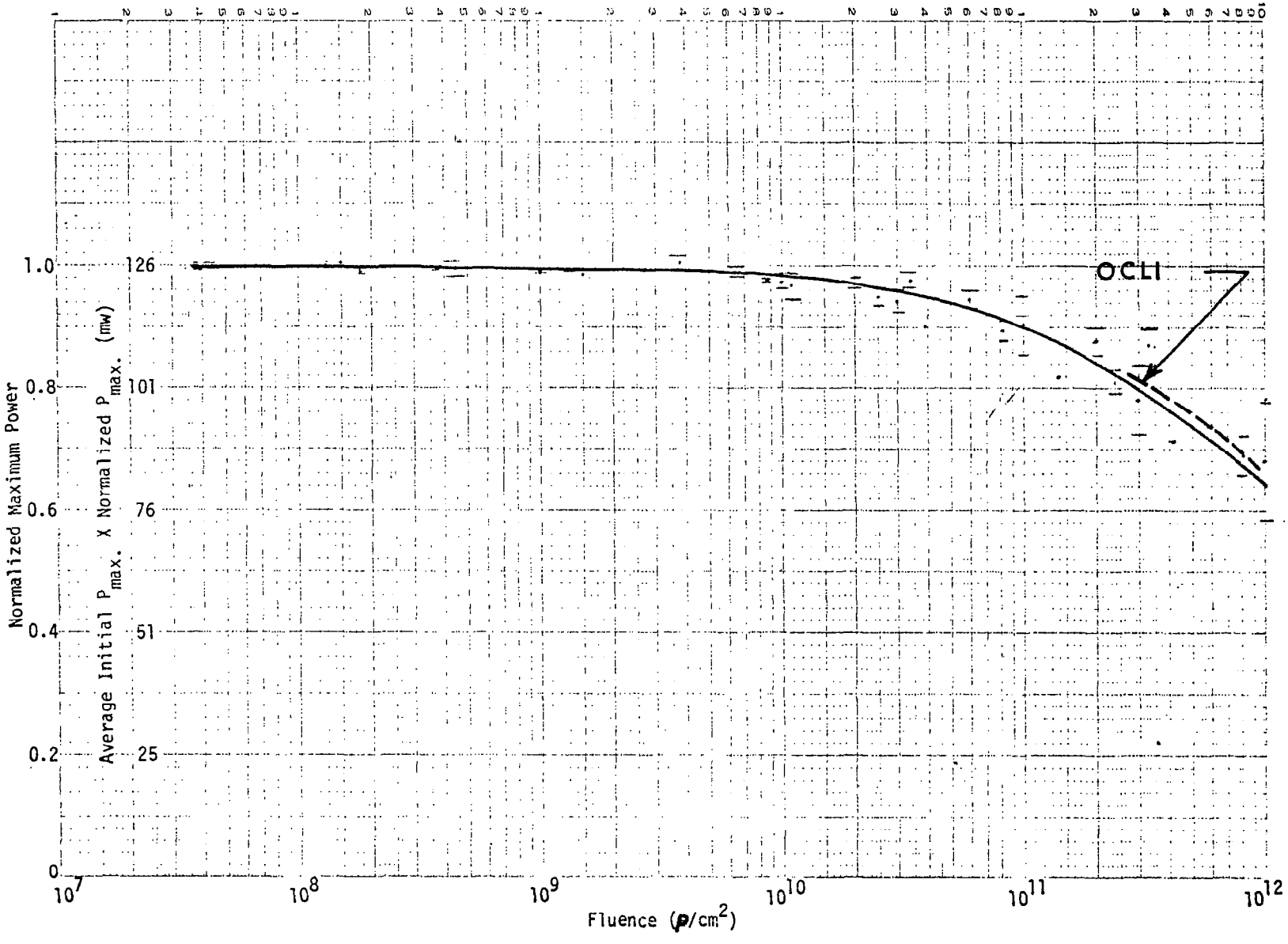

Figure 1. 1.5 MeV protons on Spectrolab Cells

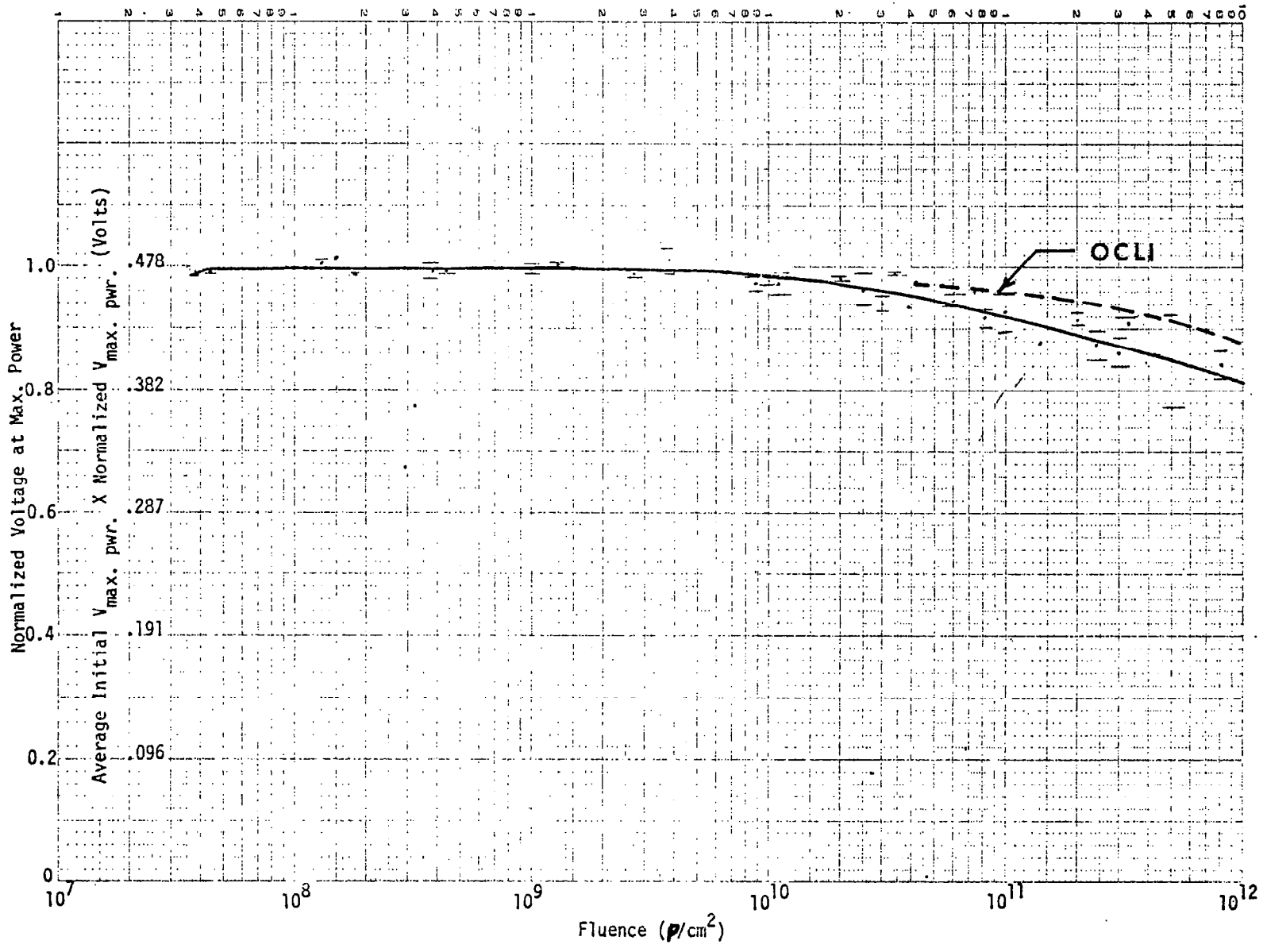

Figure 2. 1.5 MeV protons on Spectrolab Cells

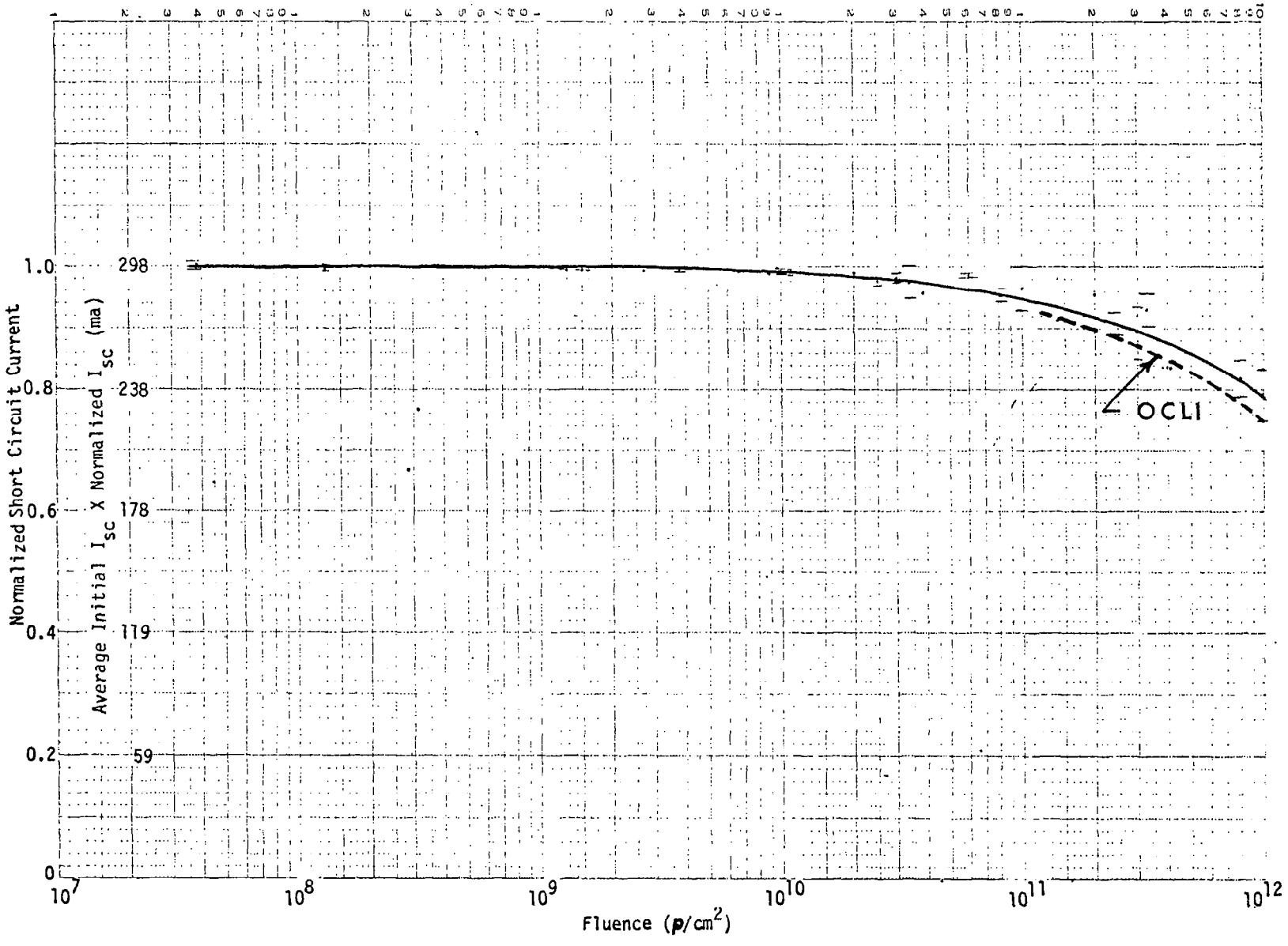

Figure 3. 1.5 MeV protons on Spectrolab Cells

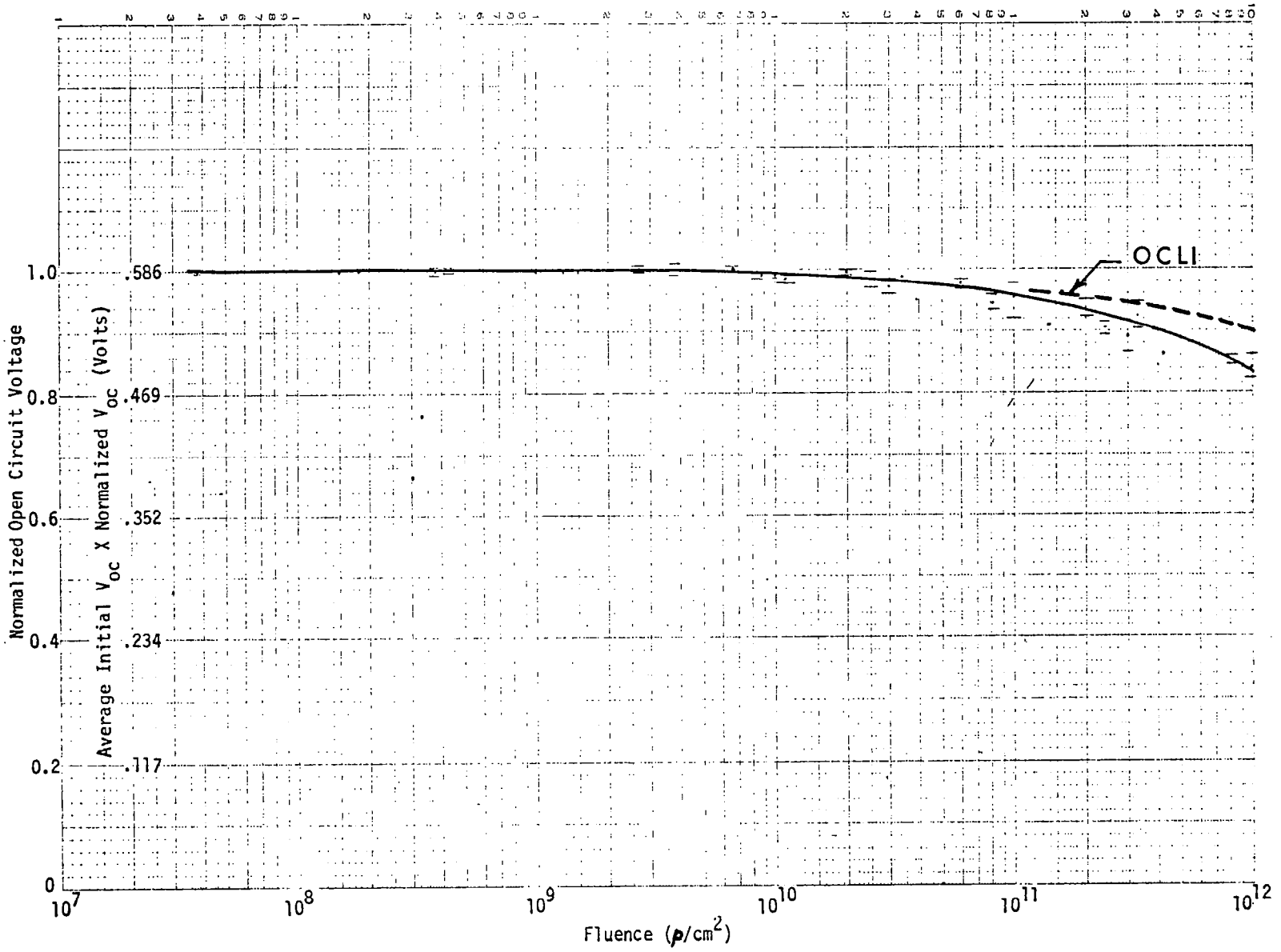

Figure 4. 1.5 MeV protons on Spectrolab Cells

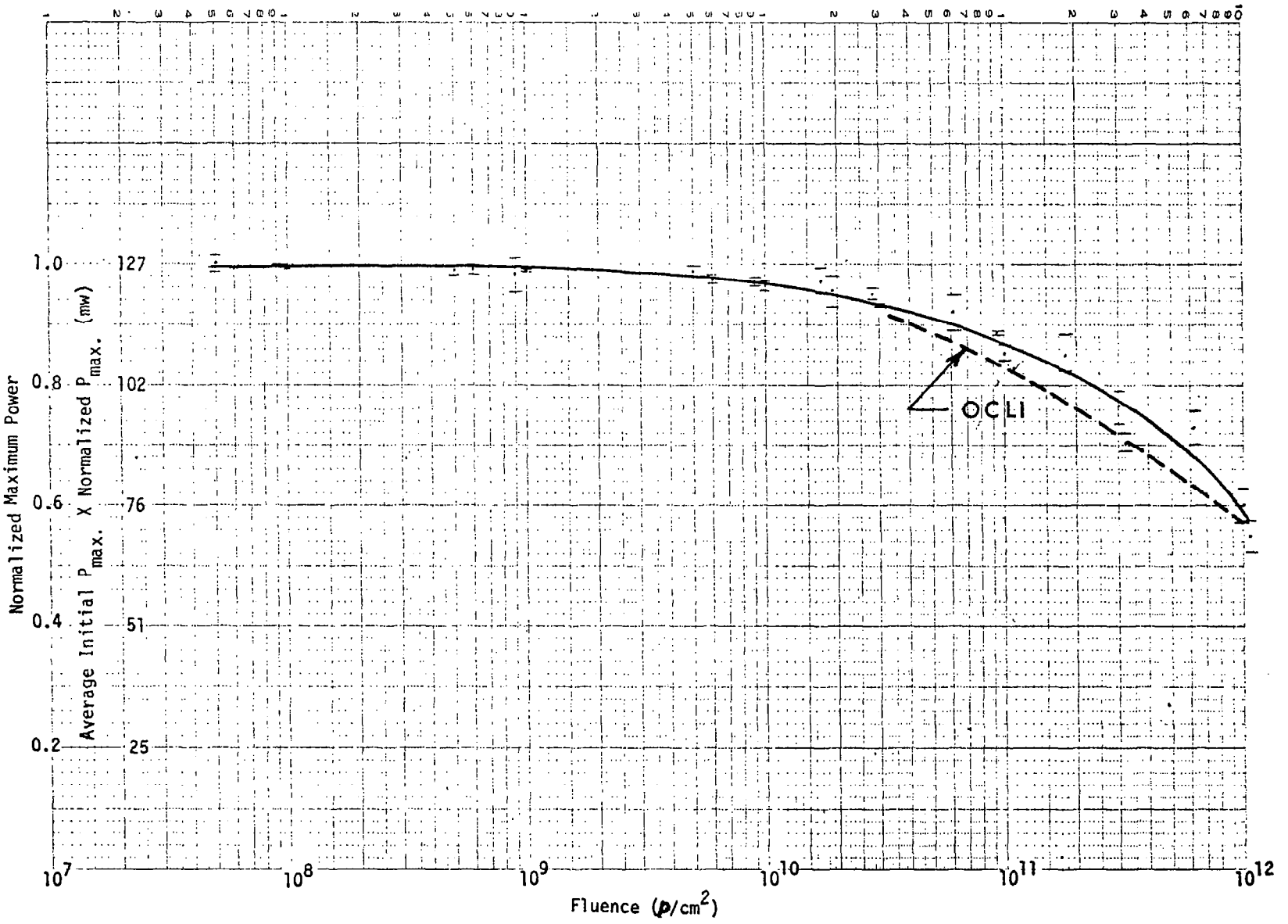

Figure 5. 1.0 MeV protons on Spectrolab Cells

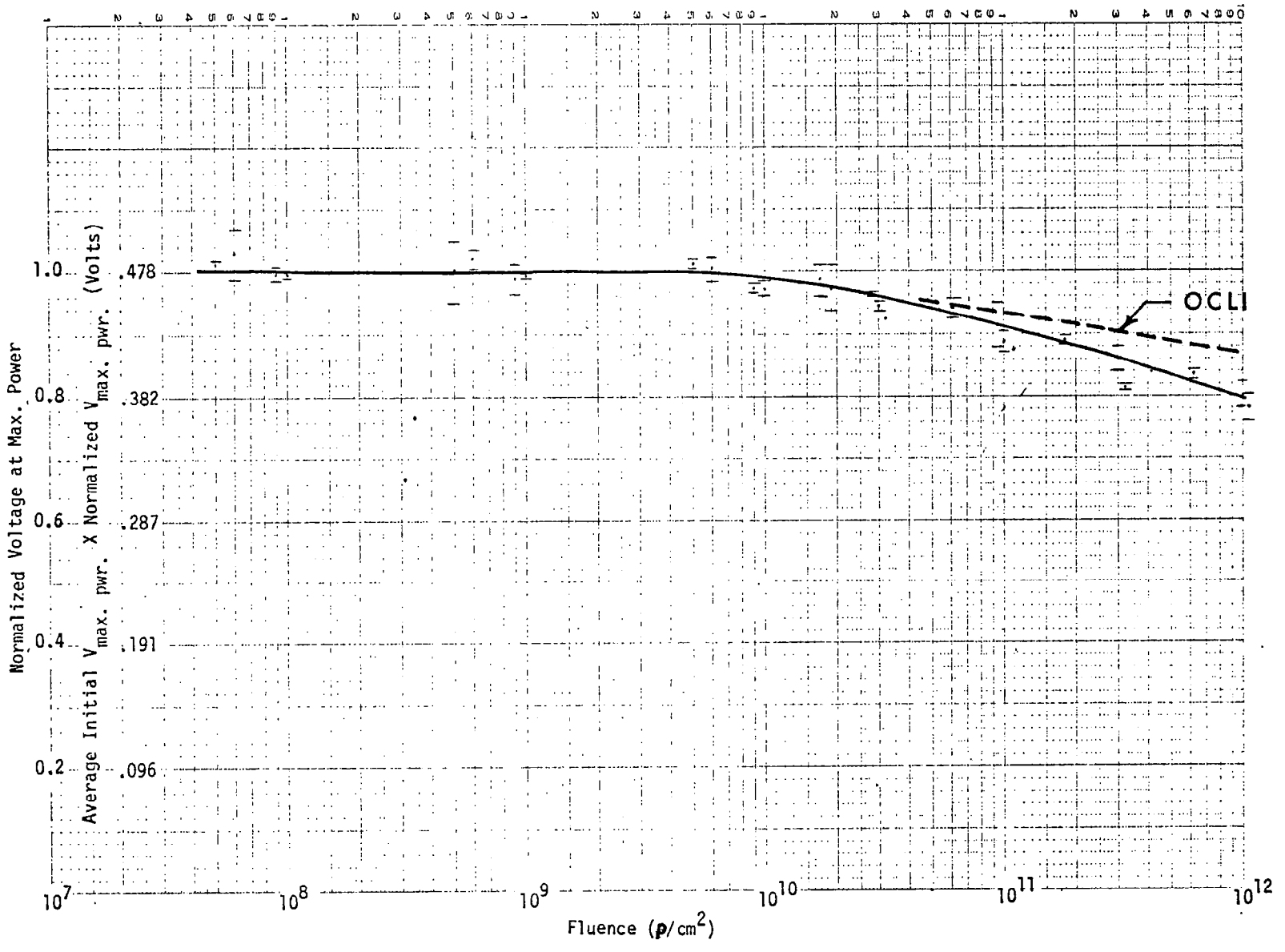

Figure 6. 1.0 MeV protons on Spectrolab Cells

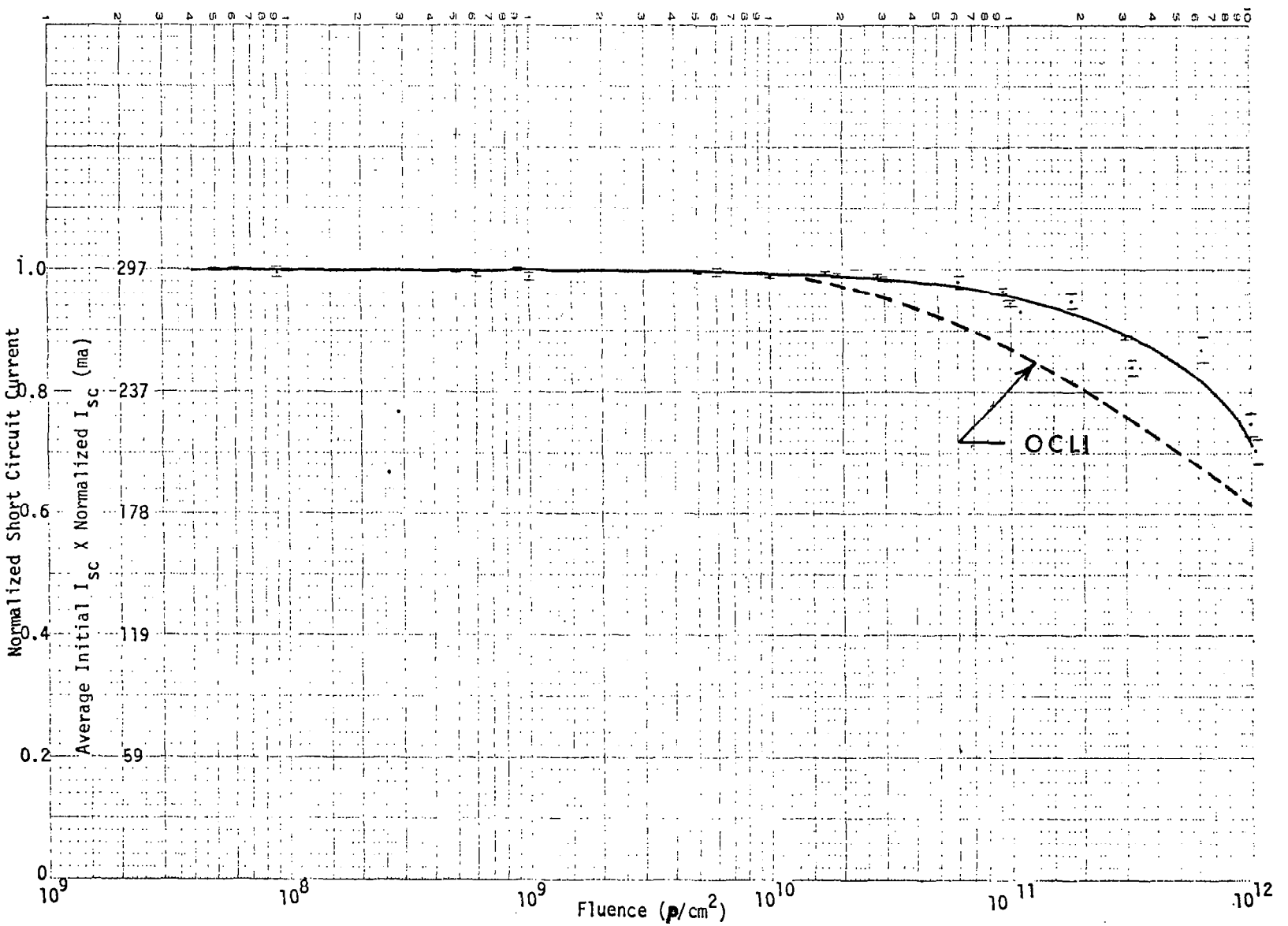

Figure 7. 1.0 MeV protons on Spectrolab Cells

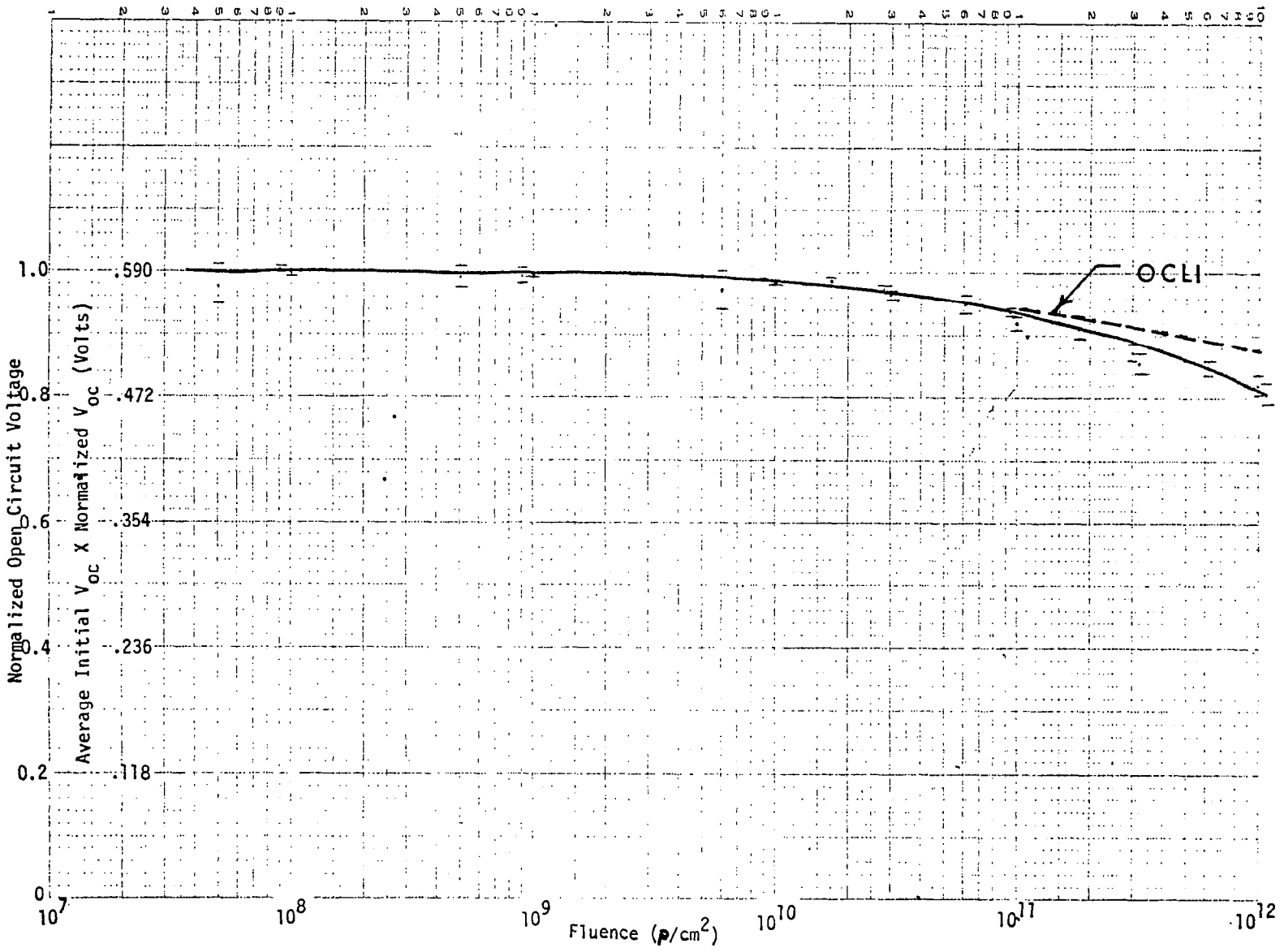

Figure 8. 1.0 MeV protons on Spectrolab Cells

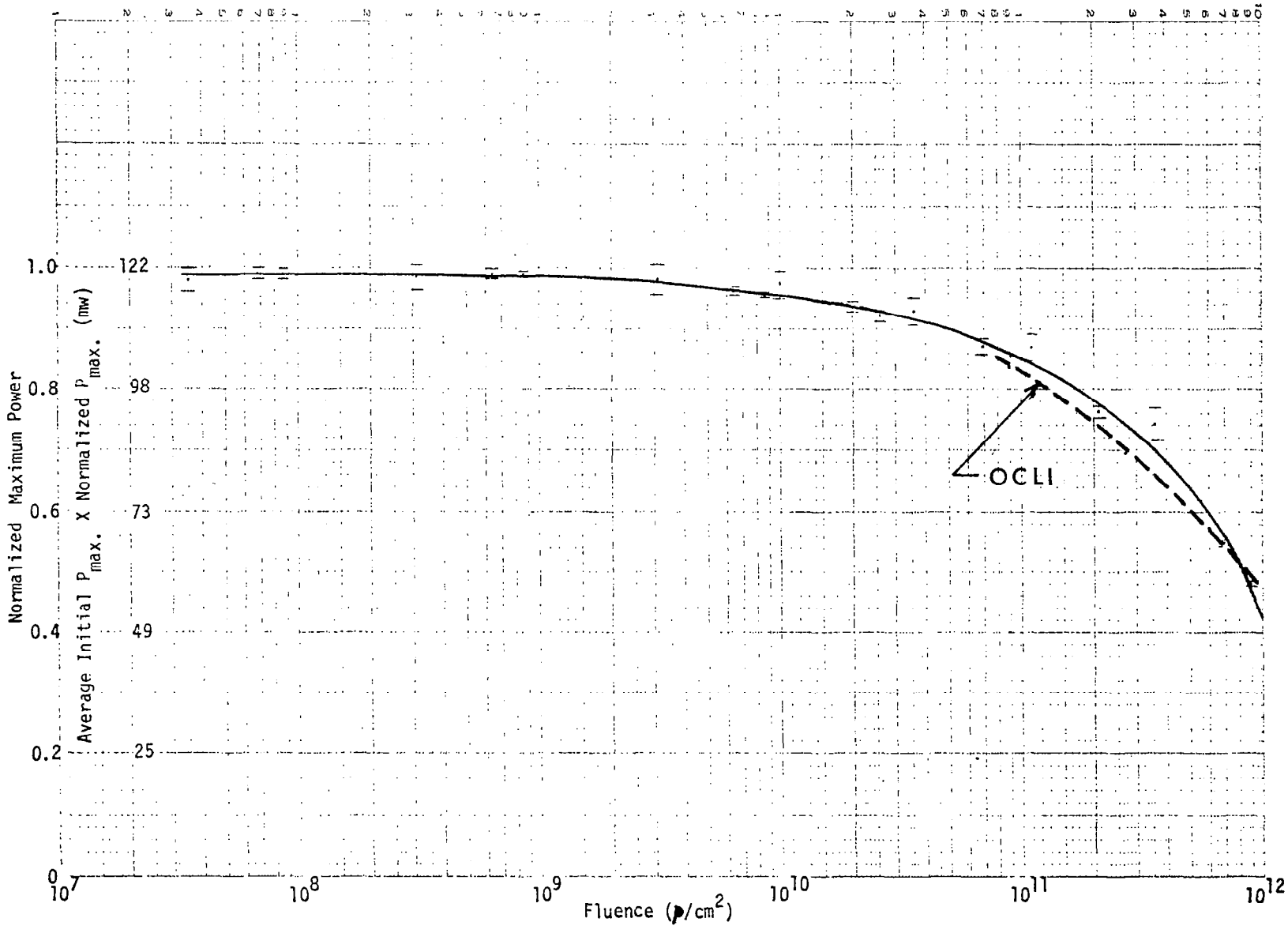

Figure 9. 0.5 MeV protons on Spectrolab Cells

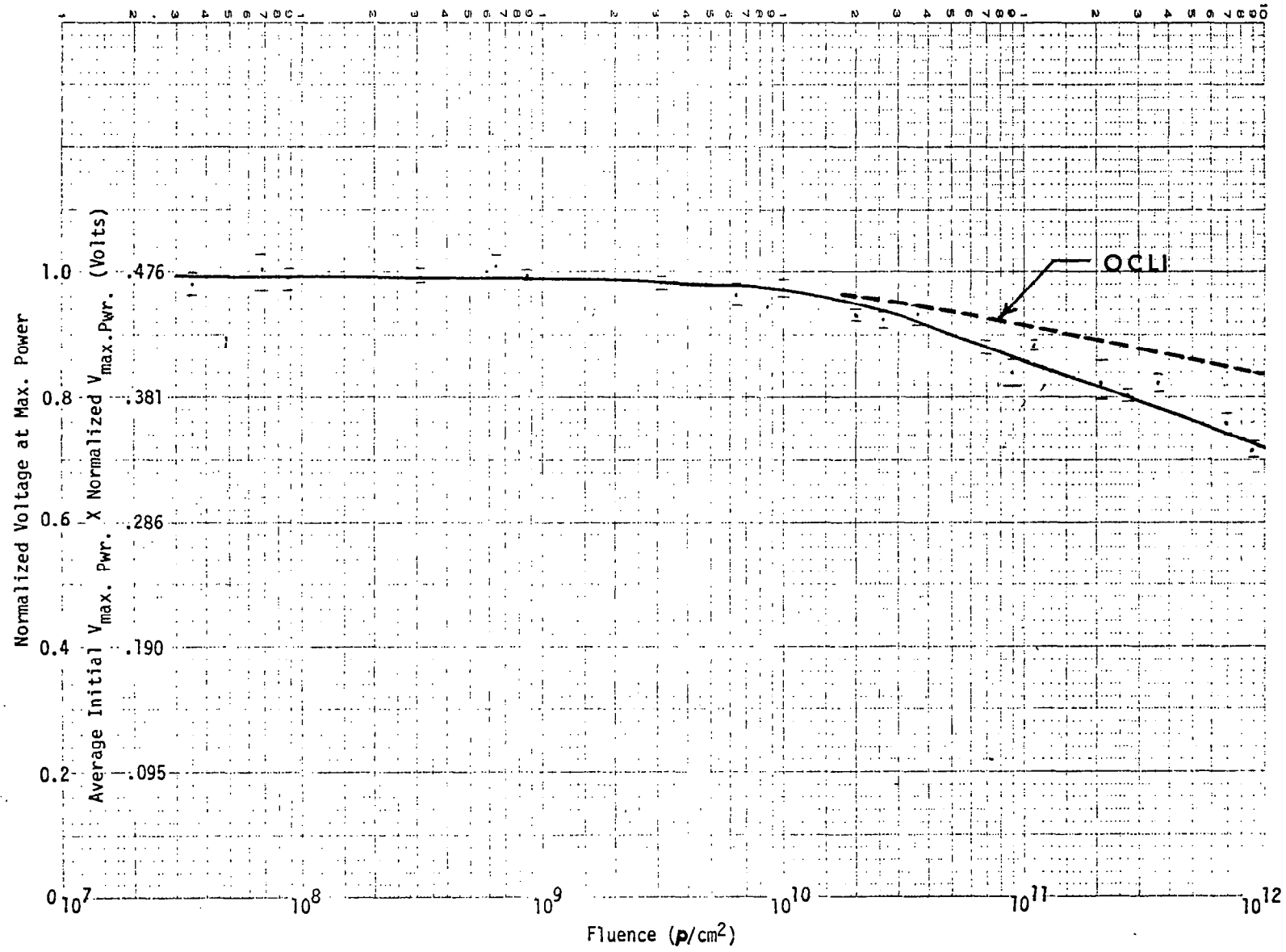

Figure 10. 0.5 MeV protons on Spectrolab Cells

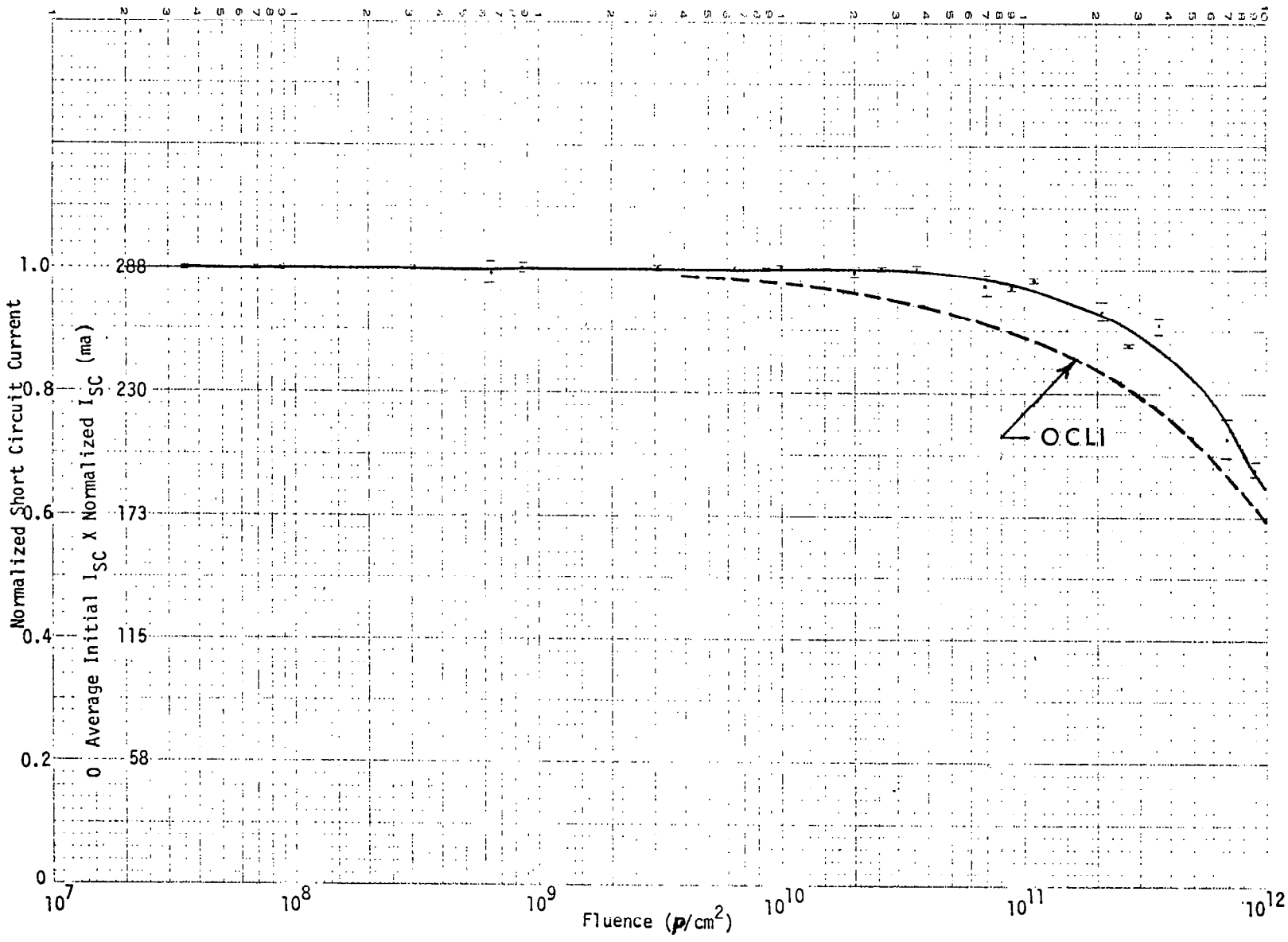

Figure 11 0.5 MeV protons on Spectrolab Cells

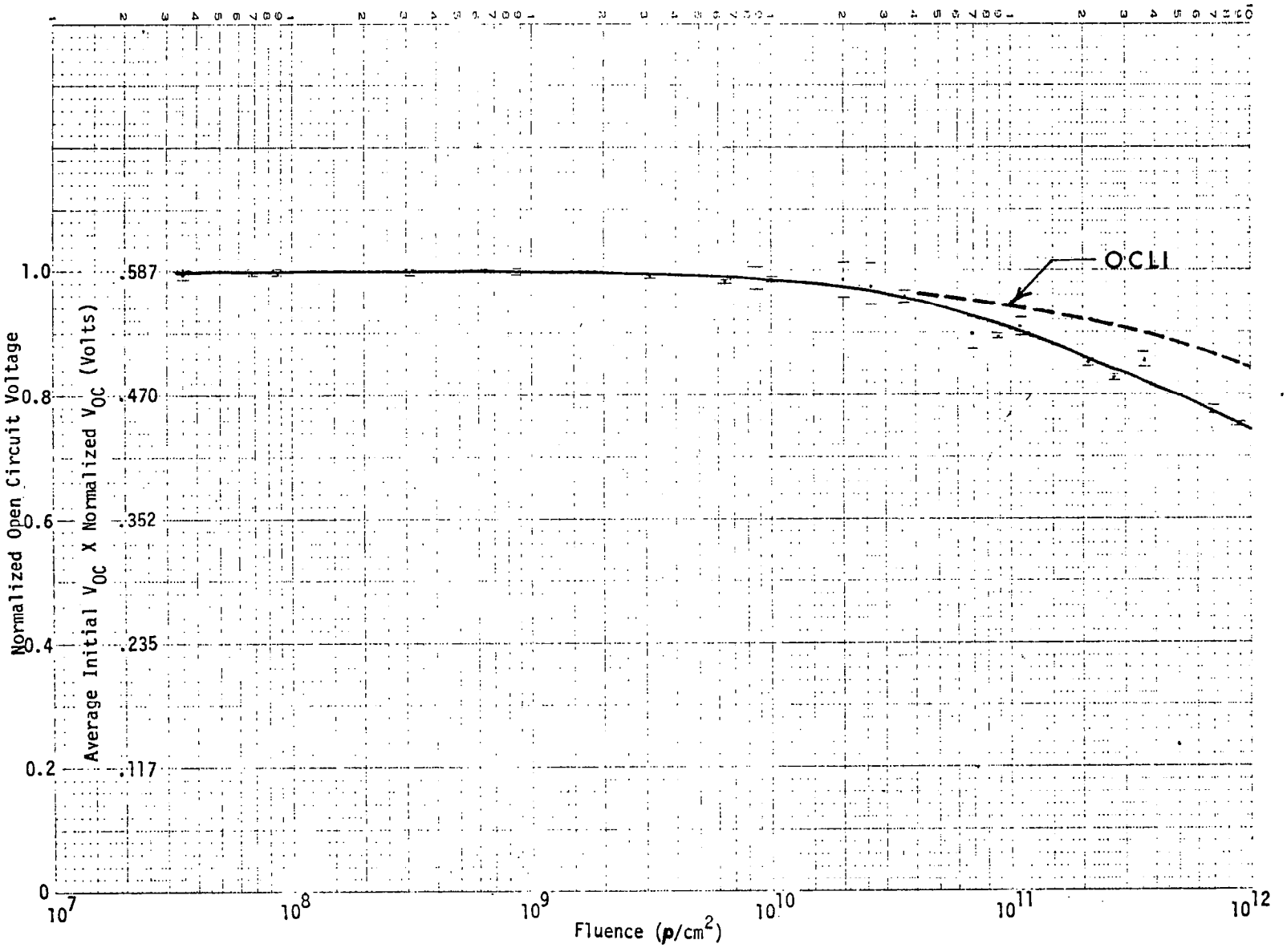

Figure 12. 0.5 MeV protons on Spectrolab Cells

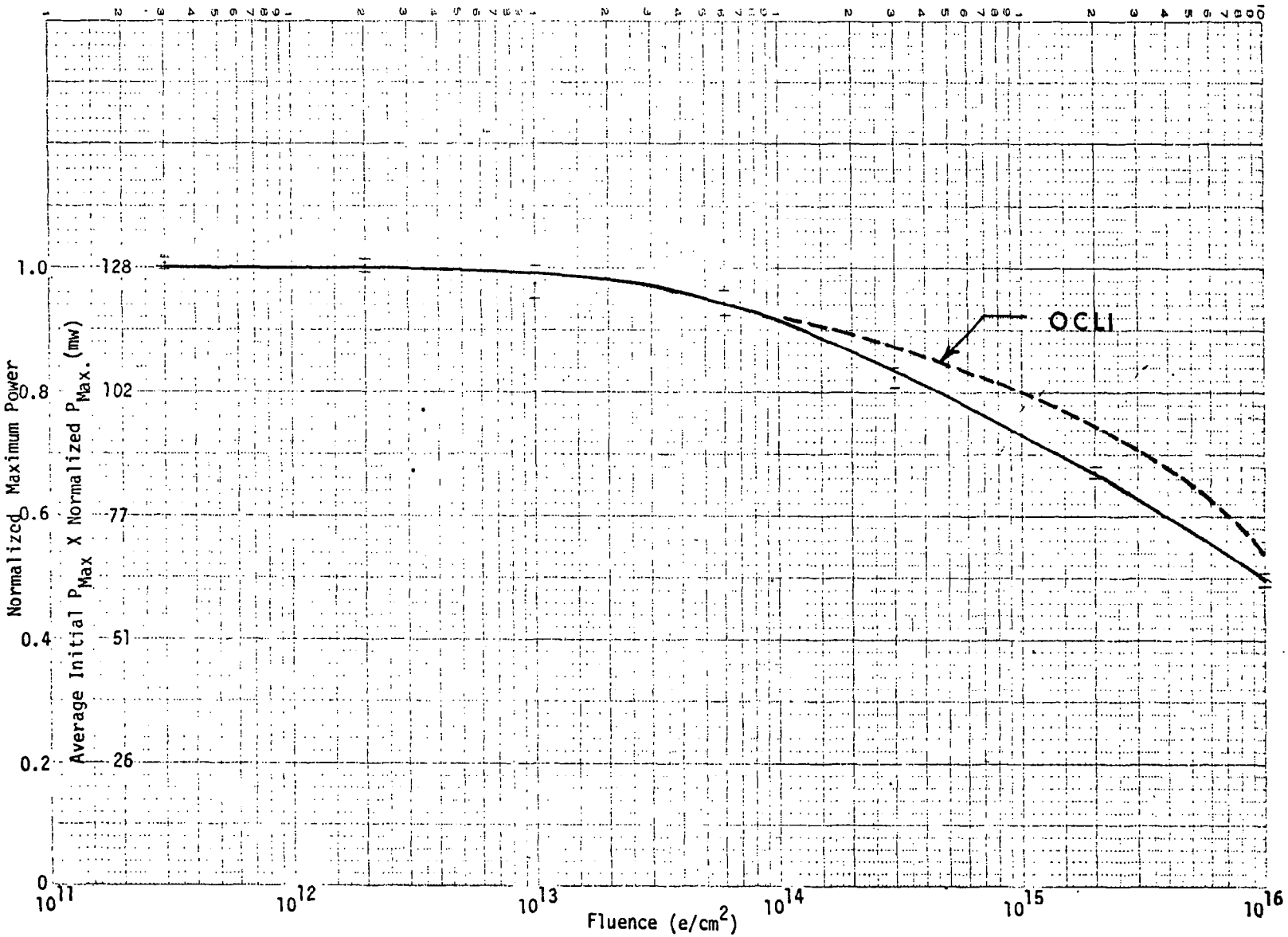

Figure 13. 1.0 MeV electrons on Spectrolab Cells

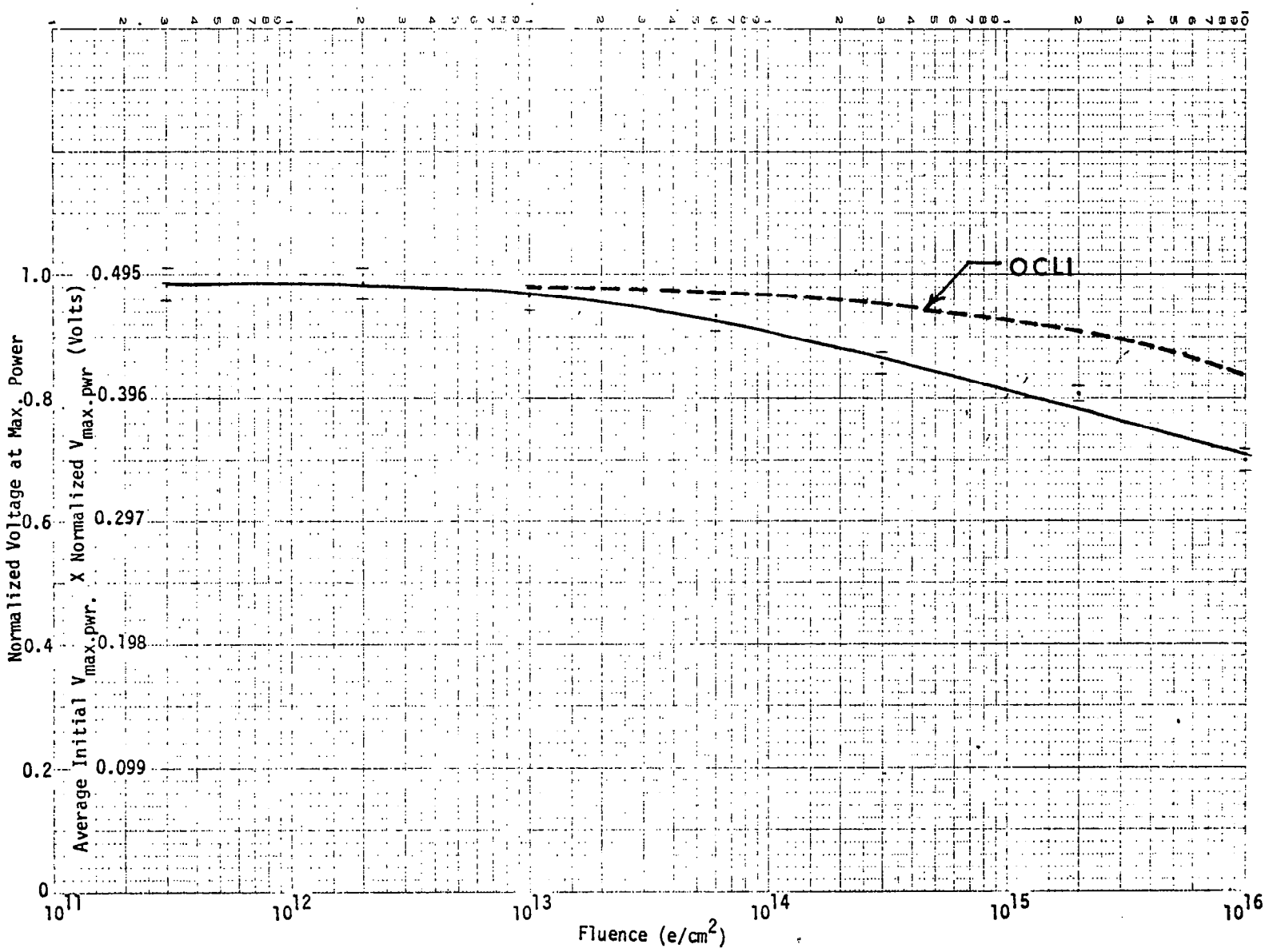

Figure 14. 1.0 MeV electrons on Spectrolab Cells

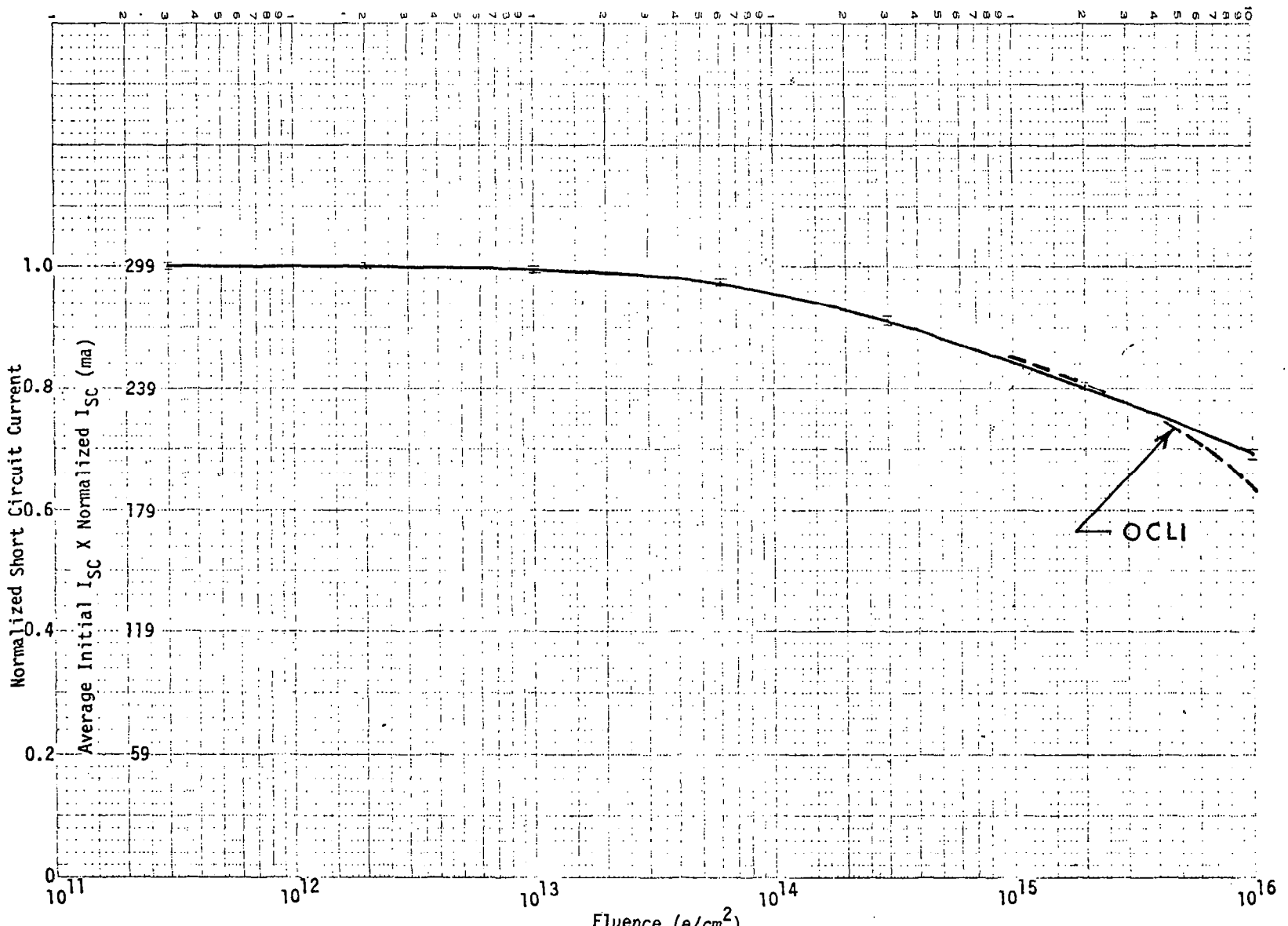

Figure 15. 1.0 MeV electrons on Spectrolab Cells

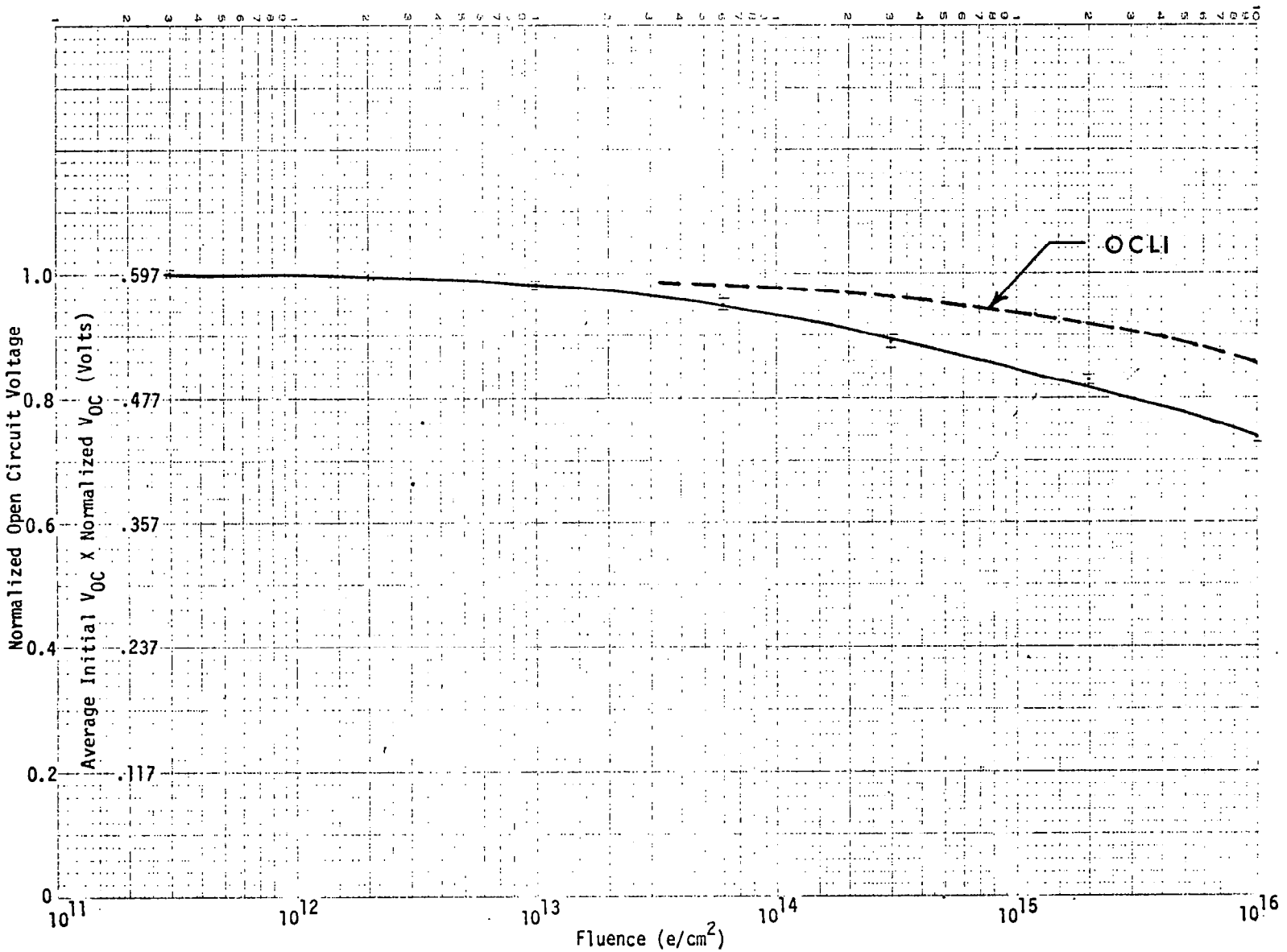

Figure 16. 1.0 MeV electrons on Spectrolab Cells

22. ELECTRON IRRADIATION OF MODERN SOLAR CELLS

Bruce E. Anspaugh
Jet Propulsion Laboratory

Tetsuo F. Miyahira
Xerox-Electro-Optical Systems

SUMMARY

A number of modern solar cell types representing 1976 technology (as well as some older types) were irradiated with 1 MeV electrons (and a limited number with 2 MeV electrons and 10 MeV protons). After irradiation, the cells were annealed, with I-V curves measured under AMO at 30°C. The purpose of the program was to provide data to be incorporated in the revision of the Solar Cell Radiation Handbook. Cell resistivities ranged from 2 to 20 ohm-cm, and cell thicknesses from 0.05 to 0.46 mm. Cell types examined were conventional, shallow junction, back surface field (BSF), textured, and textured with BSF.

INTRODUCTION

The last four years have ushered in a reawakening in the solar cell world. Solar cell technology, virtually stagnant for a ten-year prior period, has advanced in almost daily quantum jumps. In this time we have seen the development of shallow junction cells, textured surface cells, BSF cells, and cells with combinations of all the above. Silicon solar cell efficiencies of over 15% (AMO) are no longer uncommon. Concurrently, we have seen the revival of the GaAs solar cell with its hope for higher efficiency, radiation hardness, and high temperature applicability. Large area GaAs cells of over 16% (AMO) are now available. All this activity has taken place since the previous edition of the Solar Cell Radiation Handbook went to press in 1973. We find that the commonly used space quality cells described therein would probably go into the reject bins of today's cell production lines.

The radiation work reported here is the result of our attempt to update the cell degradation data in the handbook so that it would reflect early 1976 technology.

EXPERIMENTAL METHOD

The matrix of cells selected for this effort is shown in table 1. All are 2 x 2 cm in size, with thicknesses (in mm) entered in the table. The conventional cells had junction depths of 0.3 to 0.4 μm and antireflection

This paper presents the results of one phase of research carried out at the Jet Propulsion Laboratory, California Institute of Technology, under Contract No. 7-100, sponsored by the National Aeronautics and Space Administration.

coatings of SiO_x, features common to cells manufactured in the late 1960's and early 1970's. All other cells had junction depths of 0.1 to 0.2 μm and anti-reflection coatings of Ta_2O_5. The conventional cells had rather thick grid lines, while the cells with shallow junctions had patterns of many closely spaced, thin grid lines. The cells in the matrix represent products from three solar cell manufacturers.

Cells were obtained for this experiment from manufacturers who furnished 10 to 15 cells of each appropriate category with the stipulation that the electrical properties of the cells conform to the average expected on a production line. Thus, we expected that our electrical parameter data would represent reasonable estimates of average cell behavior, but standard deviations derived from the data would be speculative because of non-random population sampling.

Seven cells of each type were selected at random from those furnished. The sample selection comments above do not apply to the 0.05 and 0.46 mm 2 ohm-cm cells. Here we were able to select from a population of several dozen, but the selection is probably not truly random due to prior grading by the manufacturers.

The cells selected for radiation testing were attached to copper plates, 14 to a plate, with each plate therefore accommodating two of the entries in table 1. RTV-560 was used to attach the cells to the plates. Contact was made to the cells by soldering silver ribbons (0.1 x 0.4 mm in cross-section) to each cell, the ribbons in turn connected to standoffs fixed in the copper plate. Two contacts were made to the front of each cell and two to the base, allowing connection in the external measurement circuit in a four terminal configuration.

The plate of cells is mounted in our vacuum radiation chamber on a temperature controllable target plane (fig. 1). The target plane is rotated into normal incidence with the electron beam during irradiation, and into normal incidence with the simulator beam during electrical characterization. The copper plate is maintained at 28°C during irradiation and electrical measurements. This resulted in a cell temperature of 30°C, as monitored by a fine copper-constantin thermocouple soldered to a cell contact.

The solar simulator used was an Aerospace Controls Corp. Model 302, using on Osram 2.5 kW xenon arc lamp. The beam is filtered for a close match to the solar spectrum. The beam intensity for these measurements was set using a primary balloon flight standard cell mounted on the external, temperature controlled BFS station. The intensity is set at the external station slightly higher than AMO to compensate for the losses in the fused silica window and to achieve an accurate AMO at the target plane. Intercomparisons of the working standard with freshly flown balloon flight standard cells are made frequently to ensure that no degradation occurs in the calibration of the working standard. The ACC simulator has proved to be a remarkably consistent solar spectral source, since all balloon flight cells measured in its beam correlate to within ± 1% of their readings in near-space. Light losses in the fused silica window are carefully checked before and after each series

of radiation runs on a plate and the entire run rejected and repeated if the "inside/outside" calibration has changed by more than 1%.

The source of electrons is the 3 MeV JPL Dynamitron. As the electrons enter the experimental vacuum chamber, they traverse a 0.013 cm aluminum scattering foil. The electrons, striking the foil with 1.05 MeV energy, undergo multiple scattering collisions to emerge with an energy of 1.00 MeV and illuminate the target plane 86 cm distant with a beam uniformity of $\pm 5\%$. Beam intensity is measured at the center of the 13 cm square target plate with a Faraday cup. The sample irradation sequence of fluences (in e/cm^2) is as follows: 5+12, 1+13, 2+13, anneal, 5+13, 1+14, anneal, 2+14, anneal, 5+14, anneal, 1+15, anneal, 3+15, anneal, 1+16, anneal (where the nomenclature z+yy has the usual meaning of $z \times 10^{yy}$). "Anneal" means that the samples were annealed approximately 16 hours at 60°C, which has been previously shown to complete nearly all achievable annealing at this temperature. I-V curves are taken before and after each step in the above sequence. At the beginning of the 5+14 irradiation, water is circulated through the water-cooled plate in the chamber for prevention of excessive outgassing and loss of vacuum caused by electron-beam heating. In addition, the LN_2 cold shroud is cooled to -10°C and held there for the remainder of the irradiations to act as a sink for possible outgas products. A run is completed with a light calibration check and by statistical analysis of the data.

RESULTS

General Remarks

Results are presented in the form of curves, depicting cell J_{sc}, V_{oc}, and P_{max} plotted against the log of electron fluence in figures 2 through 16. Total cell area has been used to calculate the power and current densities (4.00 cm^2 for all cells used in this study). The 2 ohm-cm cells were specified to be in the range 1 to 3 ohm-cm, the 10 ohm-cm cells to be between 7 and 14 ohm-cm, and the 20 ohm-cm cells to be between 14 and 45 ohm-cm. Thickness tolerances were unspecified. Neither cell thickness nor resistivity were measured independently in our laboratory and it should be recognized that uncertainties in these values require us to temper our conclusions regarding relative cell performance. Several curves are marked with a star. The starred curves represent cells which did not achieve as high an electrical output as expected, or which would fit observed trends in other cell groups. Data for the 20 ohm-cm cells with BSF are plotted as dashed lines. It was expected at one time that the BSF might impart this high resistivity cell with a high V_{oc} typical of lower resistivity cells, yet retain the radiation hardness of high resistivity cells. The present data shows that the hoped for radiation hardness did not materialize.

V_{oc} Data

The V_{oc} plots show the clear advantage of the BSF for increasing the voltage. However, in 10 ohm-cm cells, the voltage advantage disappears for

fluences greater than 10^{14} e/cm^2. Figure 15 shows that the BSF cells may exhibit a V_{oc} advantage over the entire fluence range when they are very thin and made of 2 ohm-cm silicon; but since these cells are not pure BSF cells, this conclusion needs further verification. The 0.05 mm BSF cells are marked with a (?) because the P+ alloying was performed without first removing the diffused n layer on the rear surface which was residual from the junction diffusion; consequently, the field produced may not compare with that of the other cells in this test. The 0.125 mm cell marked BSF is a violet cell and may not be directly comparable either. Whatever the reason, these thin BSF cells exhibit a higher V_{oc} after 10^{15} e/cm^2 than their thicker counterparts made of either 10 or 20 ohm-cm silicon. In fact, the presence of a BSF on thick cells after 10^{14} e/cm^2 appears to be a distinct disadvantage. The textured, conventional, and shallow junction cells of like thickness and resistivity exhibited roughly the same V_{oc} throughout the radiation test. The textured cells seemed generally to have slightly lower V_{oc} than their conventional counterparts, possibly due to a slightly higher temperature at the junction than measured by our thermocouple on the contact strip.

J_{sc} Data

Figures (2+3n) depict J_{sc} behavior under irradiation. As one progresses from conventional to shallow junction to textured cells, one expects an increasingly high current output and that the relative advantage remain after radiation. This is because the shallow junction cells obtain more of their current from electron-hole pairs produced very near the junction by photons in the blue portion of the solar spectrum, a response not affected by radiation.

The textured cell, which also has a shallow junction, refracts the light as it enters the surface and causes all electron-hole pairs to be produced nearer the junction. They, therefore, require somewhat lower values of diffusion length to assure diffusion to the junction. Wherever a direct comparison is possible, the J_{sc} increase in going from conventional to shallow structure is seen to be about equal to the increase going from shallow junction to textured structure. BSF cells have higher current outputs than shallow junction cells out to fluences of 10^{14} or 10^{15} e/cm^2. Here the field appears to be no longer effective, and the cells apparently revert to behavior as though they were simply shallow junction cells. Textured cells appear to have higher initial J_{sc} than BSF cells, but this advantage diminishes as cell thickness decreases. If the trend were to continue as shown here (compare figures 2 and 5 for 0.3 and 0.2 mm, 10 ohm-cm cells), the BSF process may be more important than texturing for cells thinner than 0.1 mm if one had to choose one or the other. Although we have only two examples of cells which are both textured and made with a BSF, it seems reasonable to conclude that such cells are superior to all others of comparable resistivity and thickness, and remain so after radiation.

P_{max} Data

The P_{max} curves (actually maximum power density is plotted), reveal that for a given thickness, the progression to higher power is in the order:

conventional, shallow junction, textured, BSF, textured with BSF. On the thicker cells (0.3 mm), the advantage of BSF over texturing disappears after about 10^{13} e/cm^2. After 10^{15} e/cm^2, the BSF cells lose their power advantage over textured cells, and for 10 ohm-cm cells they also lose their advantage over shallow junction cells. Here again, the field is seen to not simply disappear; it causes the cells to have poorer performance after radiation, than they would have without it. The cells with both texturing and BSF retain their power output supremacy after radiation as they did in J_{sc} and V_{oc}; so this cell design proves to be the hardest of those tested here.

Figures 14, 15, and 16 are plots of electrical parameters for a mixed bag of 2 ohm-cm cells after radiation. The 0.05 mm thick cells were irradiated with 1 and 2 MeV electrons and 10 MeV protons, with the results plotted in these figures. The purpose was to check the energy dependence of the electron damage coefficient in these cells for comparison with the energy dependence commonly used for thicker cells. Reference 1 (fig. 4.1) shows the damage coefficient of 2 MeV electrons to be three times greater than the damage coefficient for 1 MeV electrons. Figure 14 gives direct confirmation of this dependence. Three times as many 1 MeV electrons as 2 MeV electrons are required to produce a given short-circuit current degradation. Figures 15 and 16 show that the same relationship is also true for P_{max} and approximately so for V_{oc}. Reference 1 addresses the relative effectiveness of electrons and protons in producing degradation in solar cells by the relationship:

$$1 \text{ 10 MeV proton} = 3000 \text{ 1 MeV electrons} \qquad (1)$$

This was tested by irradiating some of the 0.05 mm cells with 10 MeV protons at the U.C. Davis cyclotron. For comparison with the 1 MeV electron data, the proton data was normalized in such a manner as to agree exactly with the pre-irradiation electron data. The circles are plots of the normalized solar cell parameters after proton irradiation, but the actual proton fluences used were multiplied by 3000 for direct comparison with the electron data. Equation (1) is seen to be quite well vindicated by the P_{max} and J_{sc} data, but a factor of approximately 2000 would fit the V_{oc} degradation data more satisfactorily.

It is interesting to note in figures 14 and 16 that the thinnest new cells (0.05 mm, which is thinner than newsprint) produced more in terms of raw power and short-circuit current after irradiation than cells which were in common use on spacecraft five years ago, but are nine times as thick.

DISCUSSION

A wide range of solar cell types, including both old and new designs, was irradiated with electrons, and a few with protons. The light I-V characteristics of the cells were monitored before and after each of the 10 irradiation steps. The important cell parameters are reported in this paper and found to behave in an expected manner. Limited electron energy dependent damage checks were made on the thinnest cells and confirmed commonly used energy dependencies

for thicker cells. The effect of protons relative to electrons in damaging the thin cells was checked and found also to conform to known relationships for thicker cells.

REFERENCE

1. Carter, J. R. and Tada, H. Y.: The Solar Cell Radiation Handbook. TRW No. 21945-6001-RU-00, JPL Contract No. 953362, 28 June 1973.

TABLE 1. SOLAR CELL RADIATION MATRIX

CELL TYPE	RESISTIVITY, OHM-CM 2	10	20
CONVENTIONAL	.15, .20, .30, .46	.15, .20, .30	
SHALLOW JUNCTION	.20, .30	.20, .30	
BSF	.05, .125, .25	.20, .30	.20, .30
TEXTURED	.20, .30	.20, .30	
TEXTURED & BSF	.25	.20	

TABULATED VALUES ARE CELL THICKNESSES IN mm.

SAMPLE SIZE = 7 FOR EACH ENTRY.

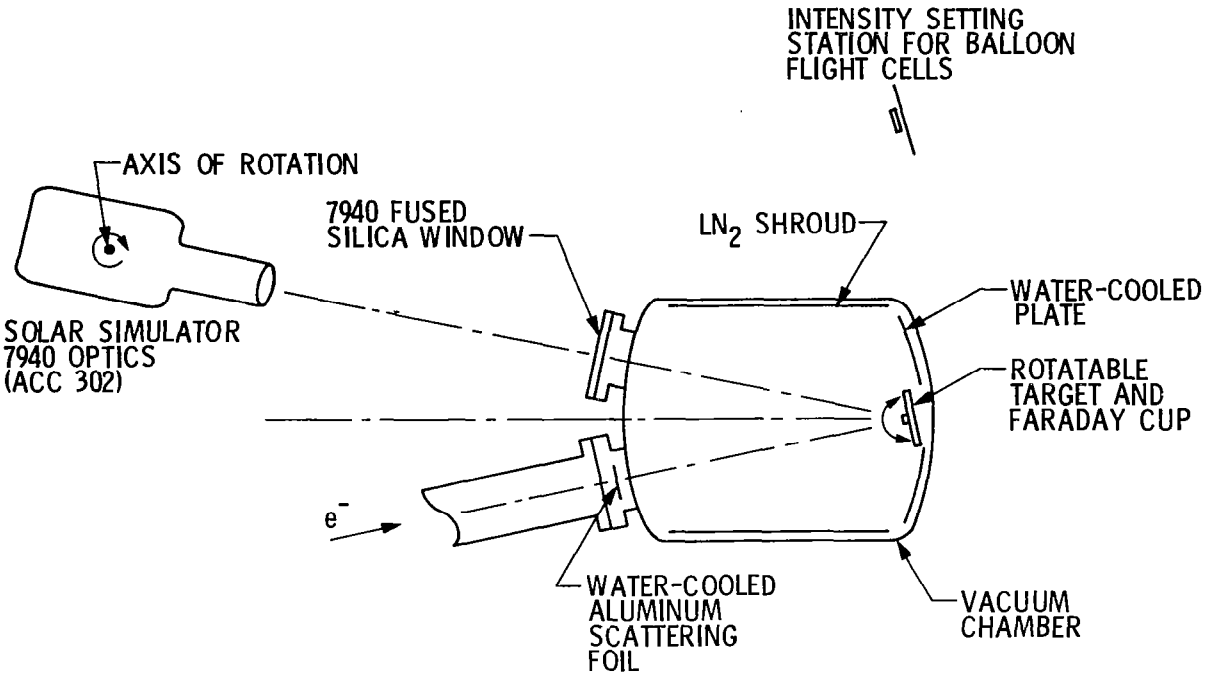

Figure 1. Schematic of Solar Cell Radiation Geometry

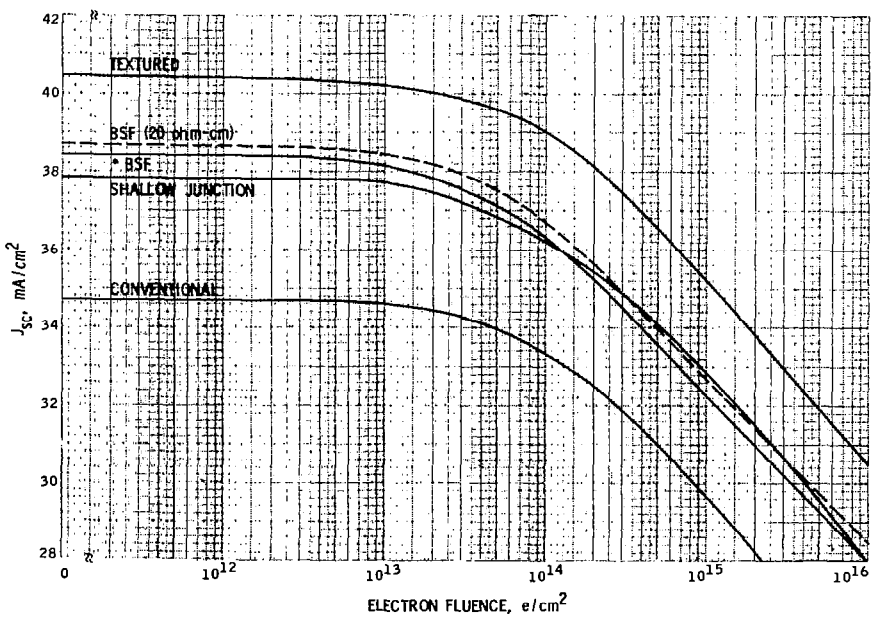

Figure 2. J_{sc} vs 1 MeV Electron Fluence 10 and 20 ohm-cm, 0.300 mm Cells, AMO, 30°C

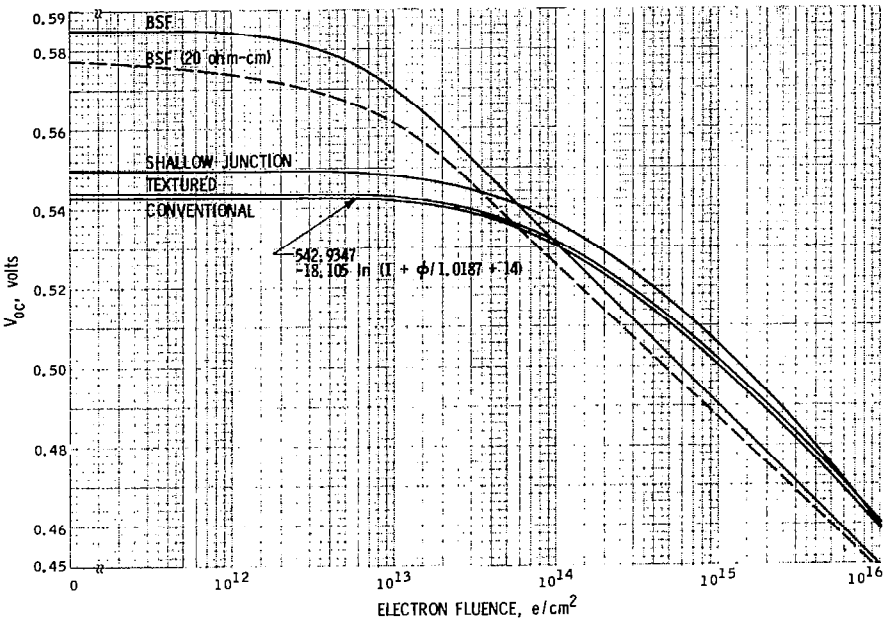

Figure 3. V_{oc} vs 1 MeV Electron Fluence 10 and 20 ohm-cm, 0.300 mm Cells, AMO, 30°C

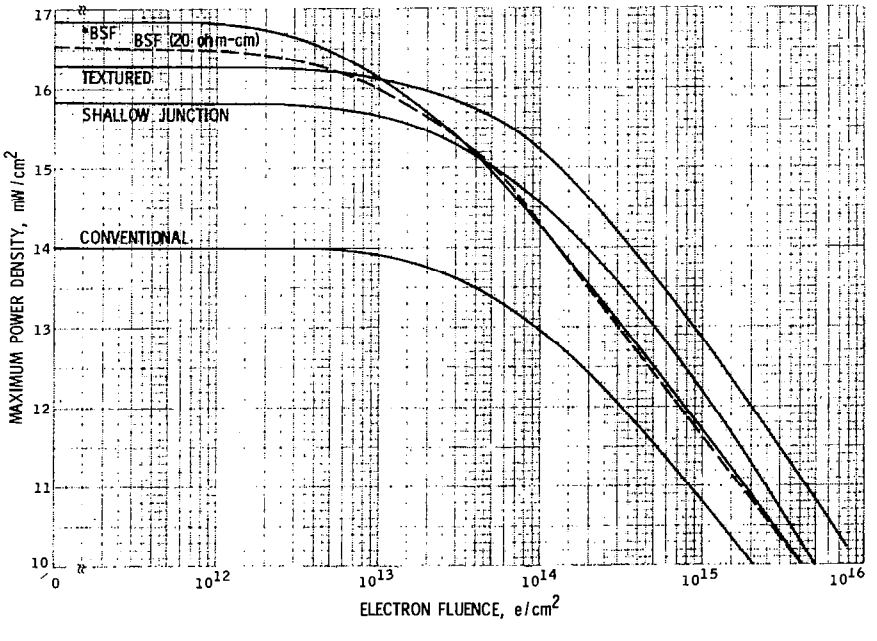

Figure 4. P_{max} vs 1 MeV Electron Fluence 10 and 20 ohm-cm, 0.300 mm Cells, AMO, 30°C

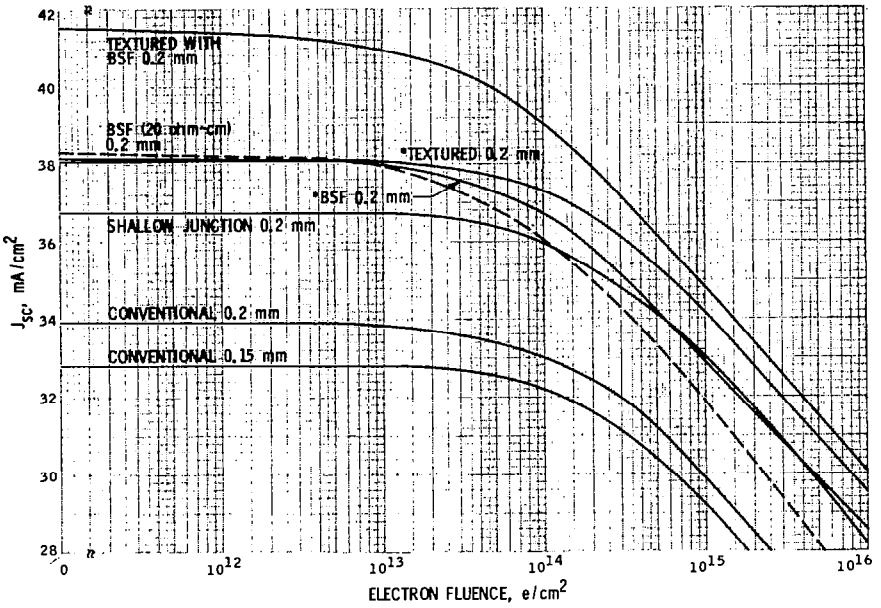

Figure 5. J_{sc} vs 1 MeV Electron Fluence 10 and 20 ohm-cm, 0.200 and 0.150 mm Cells, AMO, 30°C

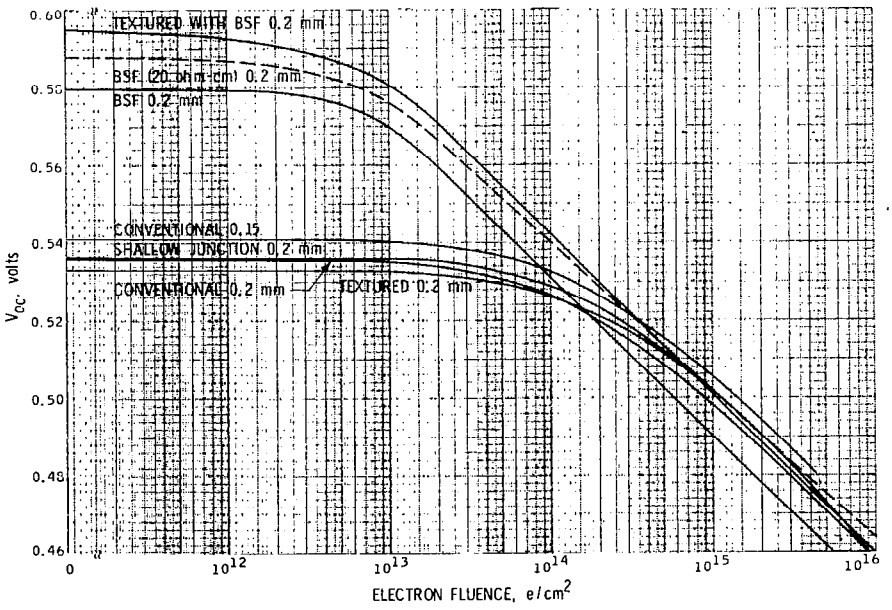

Figure 6. V_{oc} vs 1 MeV Electron Fluence 10 ohm-cm, 0.200 mm and 0.150 mm Cells, AMO, 30°C

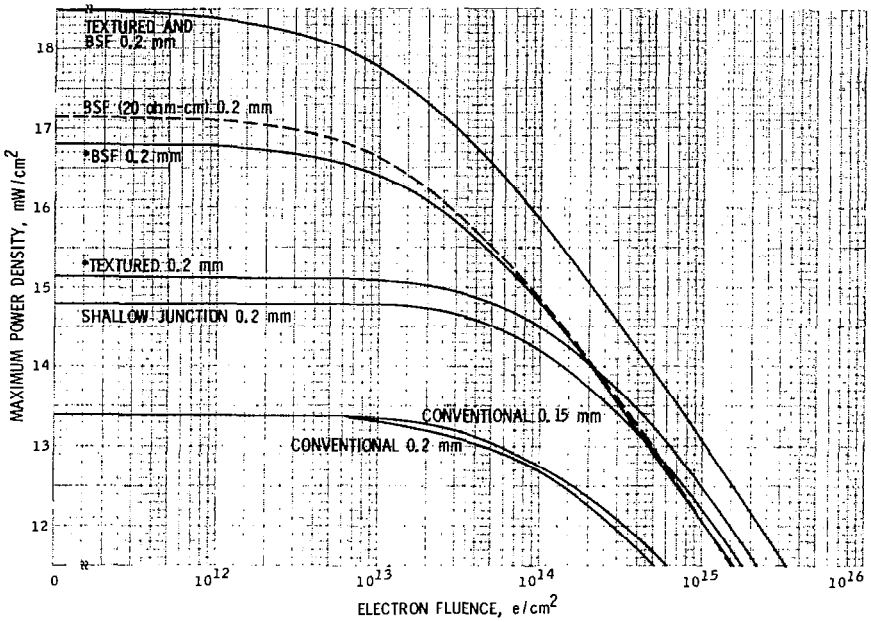

Figure 7. P_{max} vs 1 MeV Electron Fluence 10 and 20 ohm-cm, 0.200 and 0.150 mm Cells, AMO, 30°C

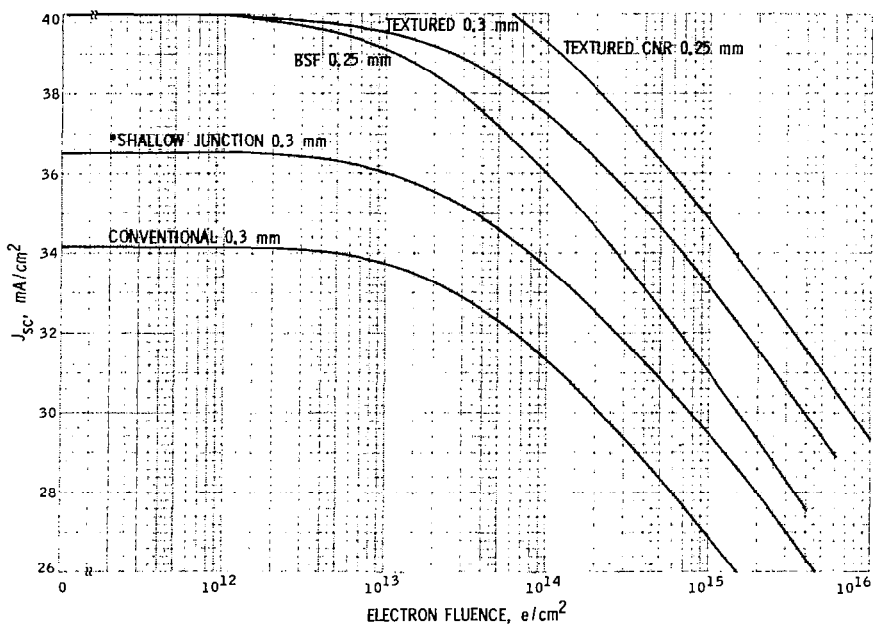

Figure 8. J_{sc} vs 1 MeV Electron Fluence 2 ohm-cm, 0.30 and 0.25 mm Cells, AMO, 30°C

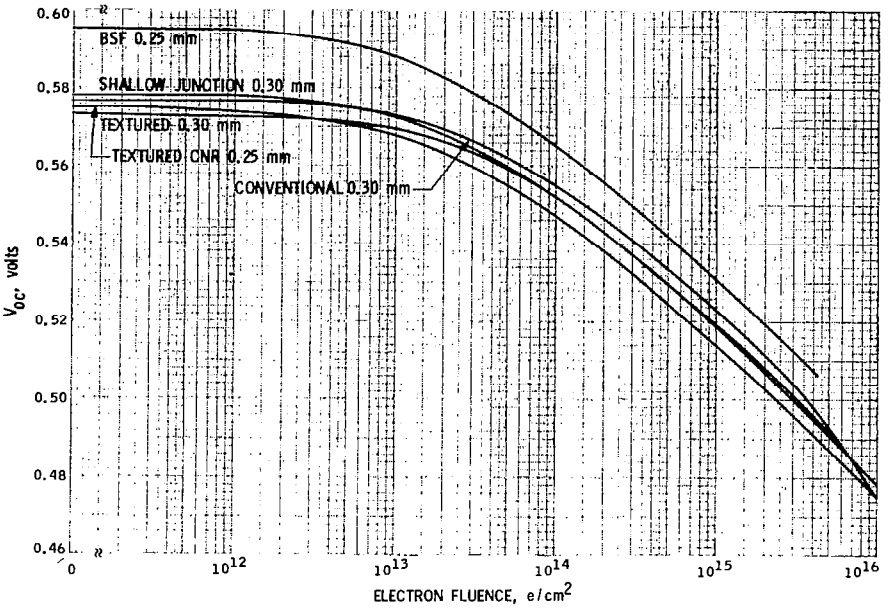

Figure 9. V_{oc} vs 1 MeV Electron Fluence 2 ohm-cm, 0.30 and 0.25 mm Cells, AMO, 30°C

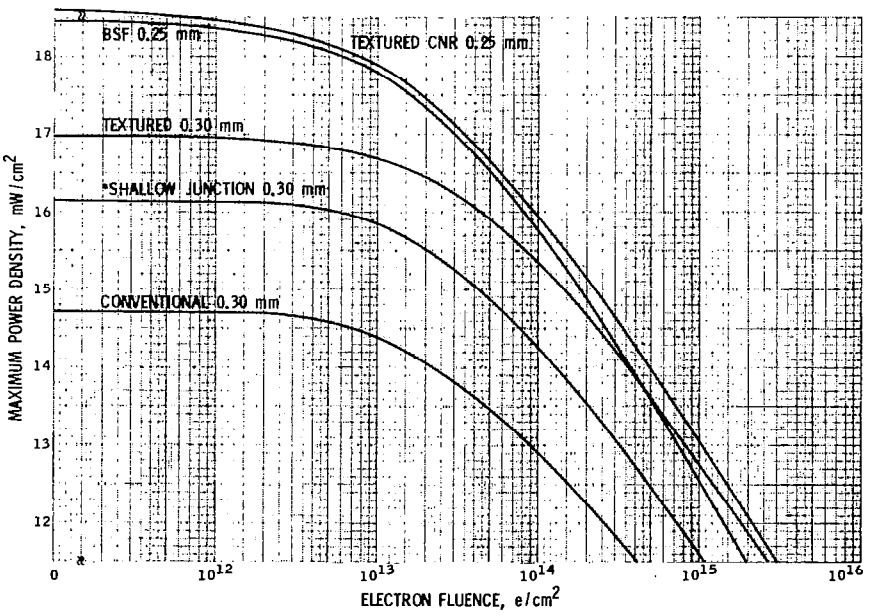

Figure 10. P_{max} vs 1 MeV Electron Fluence 20 ohm-cm, 0.30 and 0.25 mm Cells, AMO, 30°C

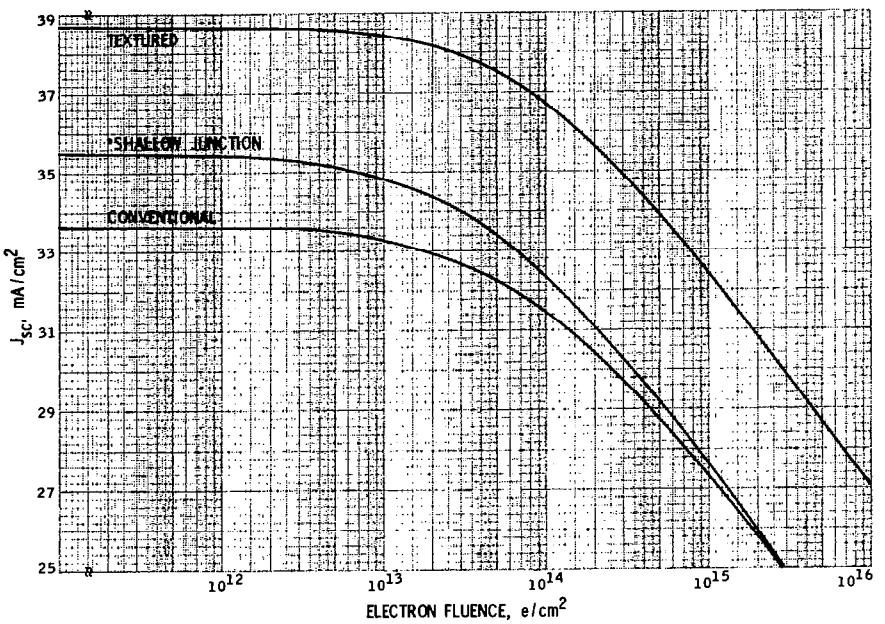

Figure 11. J_{sc} vs 1 MeV Electron Fluence 2 ohm-cm, 0.20 mm Cells, AMO, 30°C

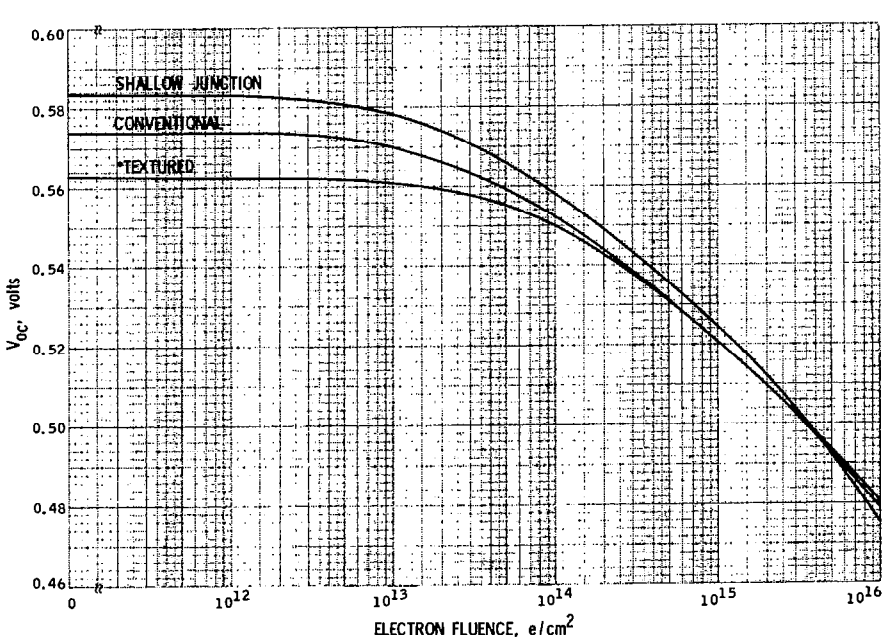

Figure 12. V_{oc} vs 1 MeV Electron Fluence 2 ohm-cm, 0.20 mm Cells, AMO, 30°C

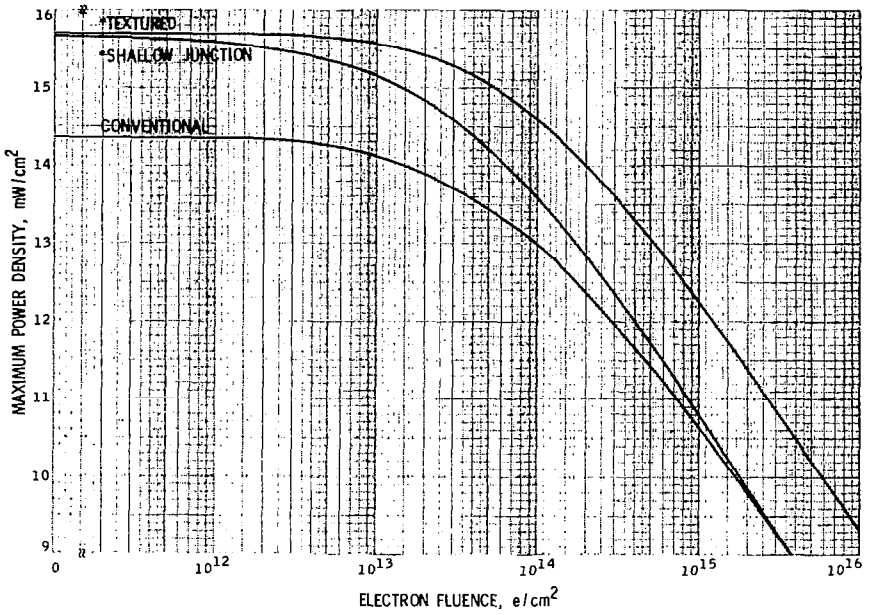

Figure 13. P_{max} vs 1 MeV Electron Fluence 2 ohm-cm, 0.20 mm Cells, AMO, 30°C

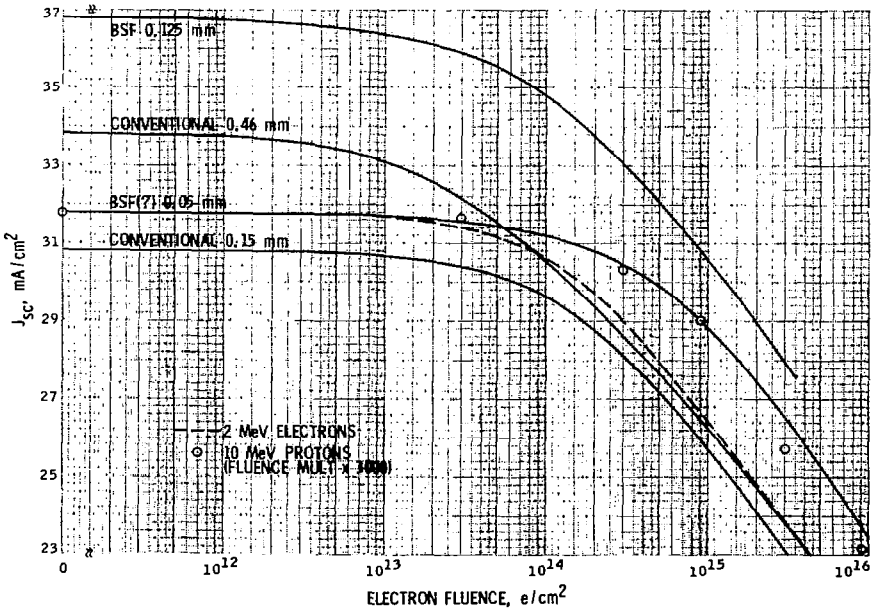

Figure 14. J_{sc} vs Electron Fluence and 3000 x Proton Fluence Misc 2 ohm-cm Cells, AMO, 30°C

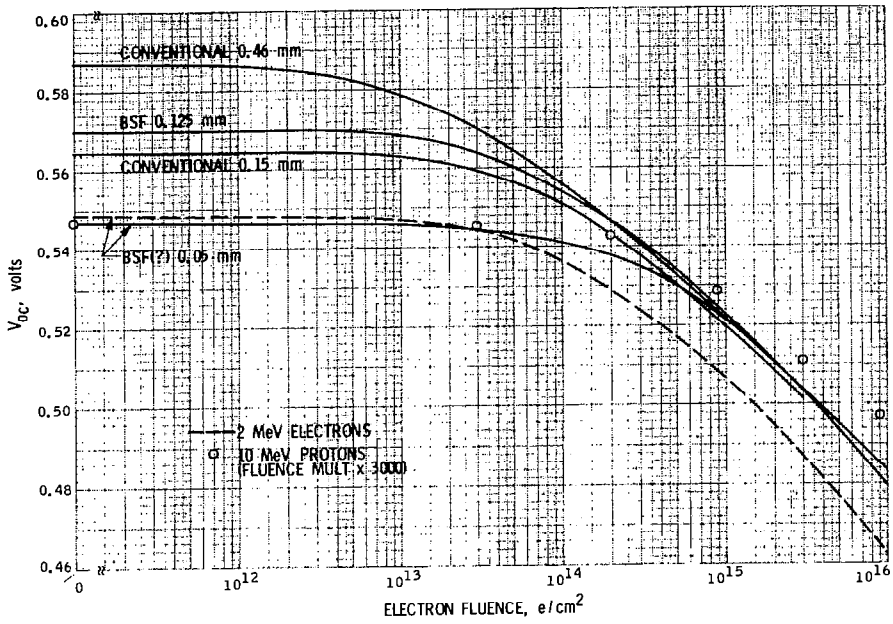

Figure 15. V_{oc} vs Electron Fluence and 3000 x Proton Fluence
Misc 2 ohm-cm Cells, AMO, 30°C

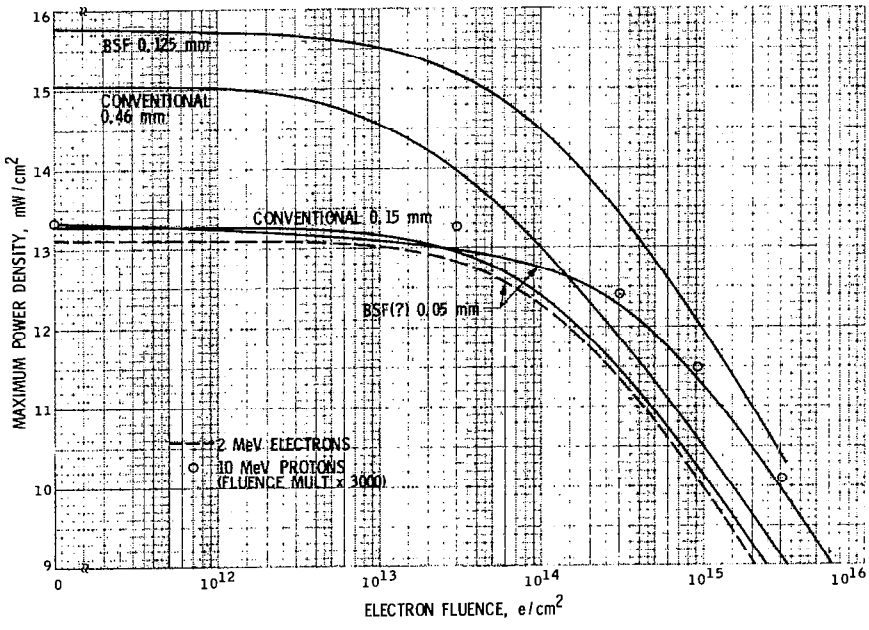

Figure 16. P_{max} vs Electron Fluence and 3000 x Proton Fluence
Misc 2 ohm-cm Cells, AMO, 30°C

23. IONIZATION INDUCED DAMAGE IN CRYSTALLINE SILICON*

A. Meulenberg, Jr.
Communications Satellite Corporation

SUMMARY

The conventional description (ref. 1) of proton damage in silicon cannot predict the plateau beginning at about 10 MeV in the damage versus proton energy curve (ref. 2) (fig. 1). The expected curve shows a steady drop with increasing incident proton energy since fewer knock-on ions are generated per unit length at higher energies. An extreme description (ref. 3), assuming that all proton and knock-on silicon energy is converted into displacements, approaches the experimental curve but still does not give a reasonable fit. It is apparent that something is missing in the theoretical description, either in the nature of the defects formed and/or in the manner of their formation. Close examination of the interaction of the energetic knock-on atoms with the local lattice environment reveals a damage mechanism (ref. 4) which does satisfy the experimental data.

Figure 2 is a sketch indicating a proton-atom interaction with high energy transfer. The proton path is delineated by a trail of ionization, and the silicon ion path is characterized by much heavier ionization terminating in a dense displacement cluster. At collision, many of the silicon electrons are stripped off, and the resulting energetic ion subsequently loses energy rapidly by Coulomb interaction with bound electrons. The rate of energy loss depends on the charge state and velocity of the knock-on ion. For ion energies in excess of 1 MeV, the intensity of ionization is sufficient to permit lattice atoms, stripped of their binding electrons, to reorient randomly before having an opportunity to recombine with electrons and re-establish the lattice. The path of a knock-on ion thus becomes a thin cylinder of amorphous material within the crystal.

Amorphous silicon has a Fermi level closer to mid-band than does single crystal silicon, and a strong field would therefore result around this damaged region (ref. 5). The field would produce a large depletion region, representing a very large capture cross section for minority carriers.

With increasing energy, the ions deposit more energy per unit path length up to about 5 MeV; beyond this energy, dE/dx levels off. Only in a region

*This paper is based upon work performed in COMSAT Laboratories under the sponsorship of the International Telecommunications Satellite Organization (INTELSAT). Views expressed in this paper are not necessarily those of INTELSAT.

where the damage per knock-on increases rapidly enough with energy to compensate for the fewer knock-on ions generated can a plateau result in the damage-energy curve. When the knock-on damage increases too slowly and levels off, the total damage per proton curve returns to its downward slope. Figure 1 shows the experimentally observed damage versus proton energy relationship (solid curve), including the plateau between proton energies of ~10 and 35 MeV. The dashed line represents the theoretical relation without inclusion of ionization-induced damage. The region beyond the dashed line results from the proposed new mechanism which dominates at high energies. This mechanism should also apply to damage from fast neutrons and from cosmic rays.

REFERENCES

1. G. J. Dienes and G. H. Vineyard, Radiation Effects in Solids, Volume II, New York: Interscience Publishers, Inc., 1957.

2. A. Meulenberg, Jr. and F. C. Treble, "Damage in Silicon Solar Cells from 2- to 155-MeV Protons," Conference Record of the 10th IEEE Photovoltaic Specialists Conference, Palo Alto, California, November 13-15, 1973, pp. 359-365.

3. J. A. Barker, H. Flocker, and J. Films, "Proton Induced Lattice Displacements in Silicon," Applied Physics Letters, Vol. 2, No. 5, 1963, pp. 104-106.

4. A. Meulenberg, Jr., "Proton Damage to Silicon from Laboratory and Space Sources," 12th IEEE Photovoltaic Specialists Conference, Baton Rouge, LA, November 15-18, 1976, pp. 224-228.

5. R. R. Holmes, "Carrier Removal in Neutron Irradiated Silicon," IEEE Transactions on Nuclear Science, Vol. NS-17, No. 6, December 1970, pp. 137-143.

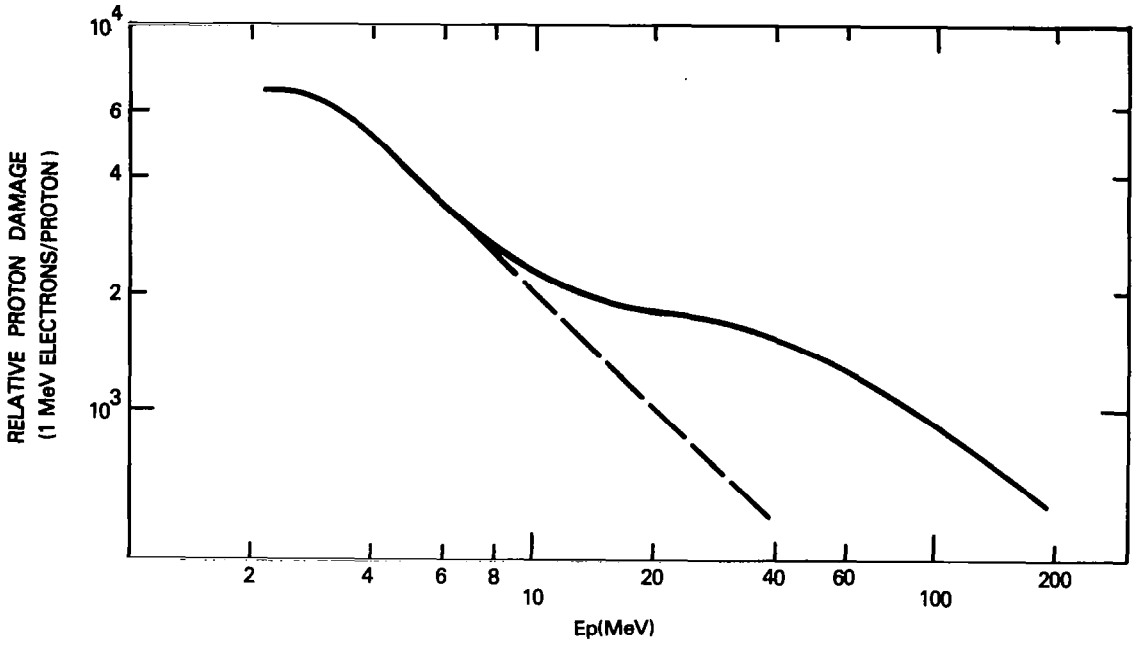

Figure 1. Relative Damage vs Energy for Normally Incident Protons. Dashed Line is the Theoretical Value Without Considering Ionization the Induced Damage Mechanism

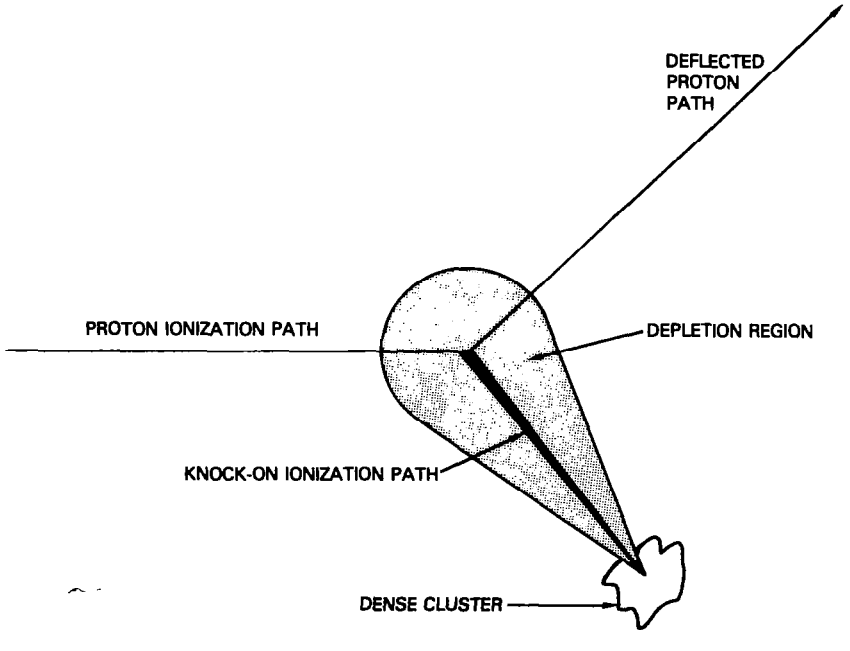

Figure 2. Energetic Knock-on Ion Damage

24. RADIATION DAMAGE PROFILE STUDIES IN ION IMPLANTED SILICON*

J.P. Sadowski and E.B. Hale, Physics Department,
University of Missouri, Rolla, Missouri 65401

Polished silicon targets held at a temperature of $80^{o}K$ are bombarded with energetic ions to create amorphous silicon. Integral depth profiles of amorphous silicon are shown for selected ion masses (Li^{+} thru Xe^{+}), energies (20 to 200 keV), and doses (10^{12} to 10^{17} ions/cm^{2}). Depth profiling is accomplished in the following manner: The amount of amorphous silicon present in the bombarded target is measured on an electron spin resonance spectrometer. Silicon is then stripped from the surface of the target by an anodic-oxidation, HF stripping technique. The depth of the strip is checked by use of a multi-beam interferometer, and the amorphous ESR signal is again measured. The process is continued until the total integral depth distribution of amorphous silicon is obtained. A thin, saturated, buried amorphous layer is seen to form at the critical dose. For larger doses, this saturation spreads over an extended depth. At the critical dose a close match exists between the experimental integral depth profiles of amorphous silicon and theoretical integral depth distributions of energy deposited into atomic processes [1,2]. Finally the experimental results are used to verify the Critical Energy Density Theory for the formation of amorphous silicon by ion bombardment[3,4].

REFERENCES

1. D.K. Brice, Ion Implantation Range and Energy Deposition Distributions (Plenum, New York, 1975).
2. K.B. Winterbon, Ion Implantation Range and Energy Deposition Distributions (Plenum, New York, 1975).
3. F.L. Vook, Radiation Damage and Defects in Semiconductors, ed. by J.E. Whitehouse (Inst. of Phys., London, 1972), p. 60.
4. J.R. Dennis and E.B. Hale, Appl. Phys. Lett. 29, 523 (1976).

*Work supported by Army Research Office-Research Triangle, N.C.

25. ULTRAVIOLET DAMAGE IN SOLAR CELL ASSEMBLIES WITH VARIOUS UV FILTERS*

A. Meulenberg, Jr.
Communications Satellite Corporation

SUMMARY

A series of experiments was undertaken to obtain information on the extent and nature of ultraviolet damage to the new violet and non-reflective type solar cell assemblies. An additional purpose was to determine the potential advantages of using coverslides with no filters or filters with cut-off wavelengths below 0.35 μm.

The experiments consisted of three types of tests on fused silica coverslides with 0.35- and 0.30-μm cut-off filters and no cut-off filters, as well as on ceria-doped microsheet coverslides. The tests measured short circuit current (I_{SC}) of and reflectance (ρ) from covered cells and reflectance plus transmission ($\rho + T$) of coverslide-adhesive-fused silica "sandwiches". Ultraviolet irradiation for over 1500 hours at one sun conditions (AM0) was carried out under vacuum of about 10^{-6} torr. Periodic measurements were made without breaking vacuum.

A previous test (ref. 1) gave results for violet type cells under ultraviolet irradiation (fig. 1). The present test shows nearly identical results for non-reflective type cells with 0.35-μm cut-off filters (fig. 2) or ceria-doped coverslides (fig. 3). The unnormalized control curve (fig. 2) indicates the day-to-day variations in cell data and is used to normalize the other results. The 0.30-μm filtered cell (a non-radiation-hardened filter not optimized for maximum transmission) in fig. 2 shows greater than average degradation, which, as indicated by the other tests, is primarily in the filter and adhesive.

The unfiltered cell (fig. 3) shows an abrupt drop in the first 20 UVSH and very little subsequent degradation. The deviation from a straight line fit in the semi-log plot is marked and the data could indicate that, at high doses, filtration is not useful for cells with thin adhesive layers. No saturation effect is noted in the protected cells at 2000 UVSH so that linear extrapolation on these curves would seem reasonable. The nonlinear behavior of the non-filtered cell and the systematic deviation of the 0.30-μm filtered cell

*This paper is based upon work performed in COMSAT Laboratories under the sponsorship of the International Telecommunications Satellite Organization (INTELSAT). Views expressed in this paper are not necessarily those of INTELSAT.

are displayed in the ρ + T measurements, which give independent support to all of the above data.

Results of the tests indicated that most (~70 percent) of the damage was in the coverslide-adhesive system, and much of this in the filter itself. An important part of the loss in transmission came from an increase in refractive index resulting from an increase in absorption in both absorption and multi-layer filter assemblies. Results extrapolated to one year in space indicate a UV degradation in I_{SC} of ~2.4 percent for Ta_2O_5 coated cells and ~3 percent for T_iO_x coated cells with UV filters. The non-reflective cells without filters would degrade by about 3.5 percent.

REFERENCE

1. A. Meulenberg, D. J. Curtin and R. W. Cool, "Comparative Testing of High Efficiency Silicon Solar Cells," 12th IEEE Photovoltaic Specialists Conference, Baton Rouge, LA, November 15-18, 1976, pp. 238-246.

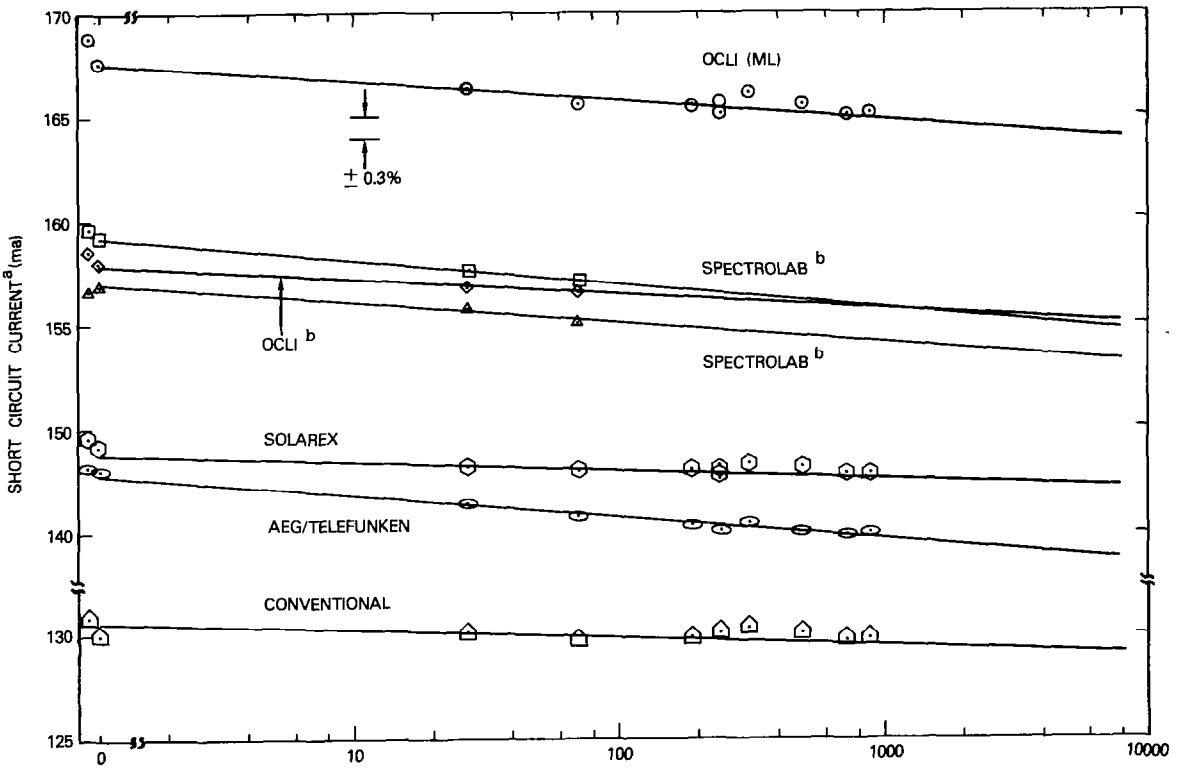

(a) I_{SC} is not corrected for reflection from system window.

(b) Data points, deleted to avoid crowding, follow pattern in OCLI (ML).

Figure 1. Degradation of Short-circuit Current with Ultraviolet Exposure for Flat Surface Solar Cells

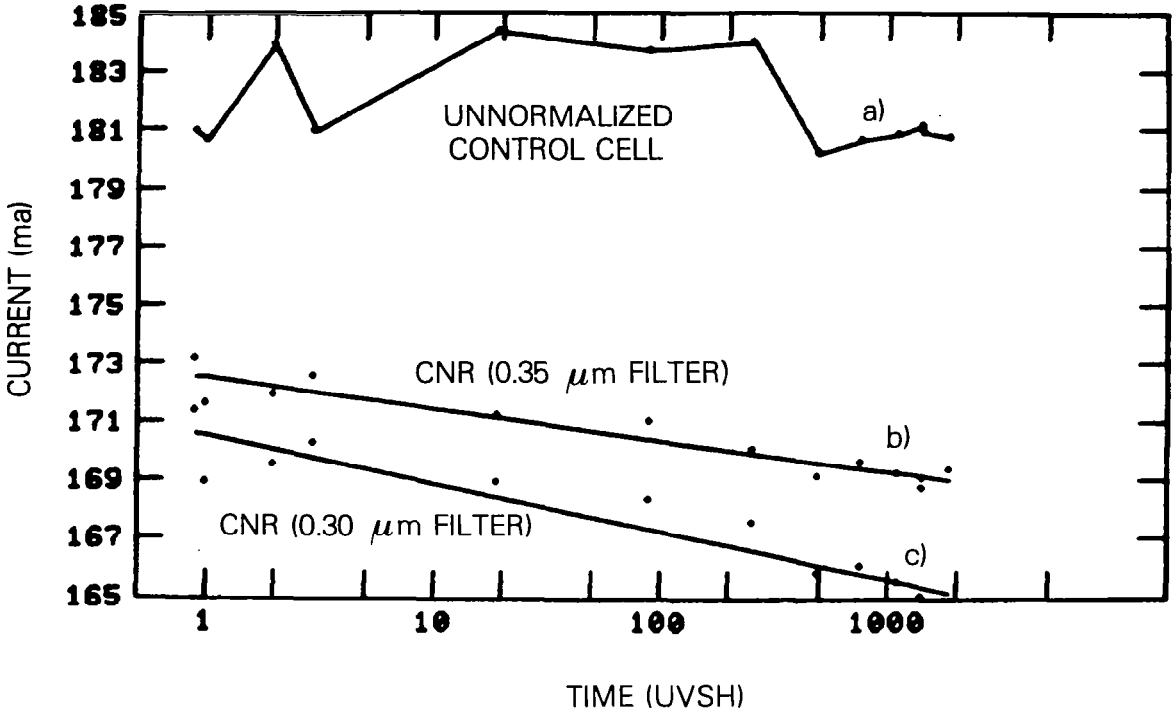

Figure 2. UV Degradation in Short-circuit Current for Solar Cells Having Fused Silica Coverslides with Cut-off Filters

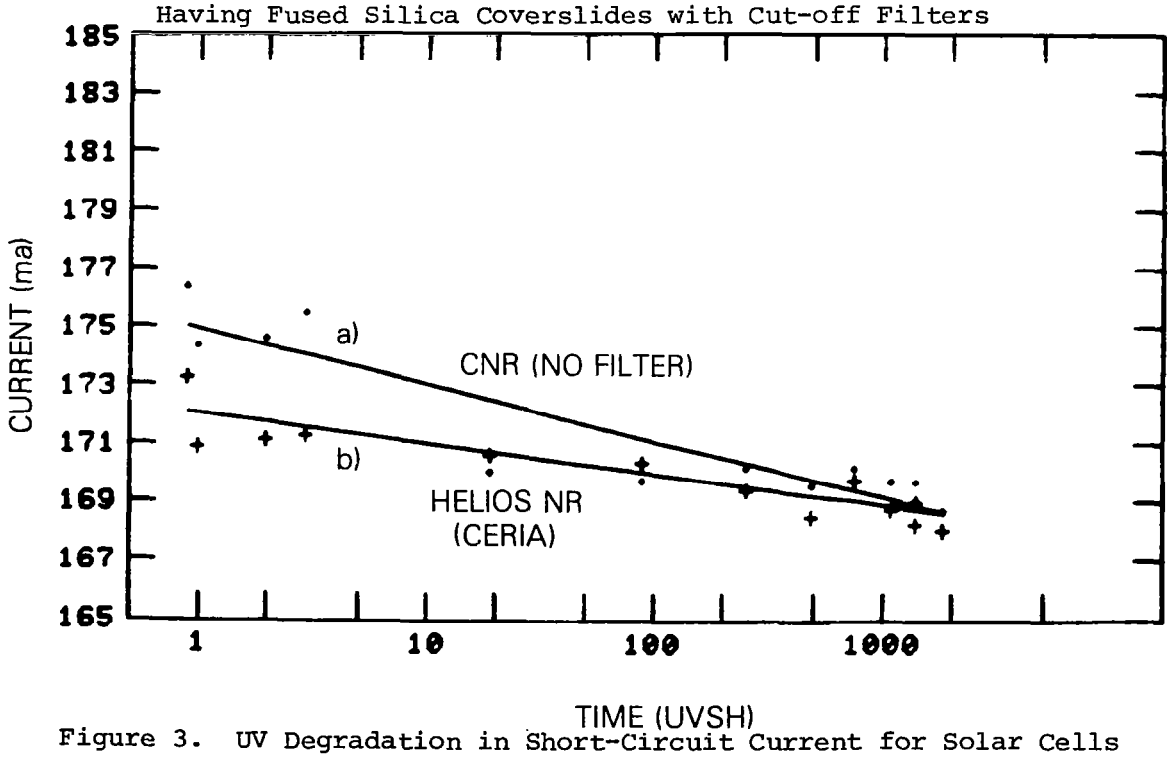

Figure 3. UV Degradation in Short-Circuit Current for Solar Cells with Fused Silica and Ceria-Doped Microsheet Coverslides But No UV Filters

26. ELECTRON, PROTON AND FISSION SPECTRUM NEUTRON RADIATION DAMAGE IN ADVANCED SILICON AND GALLIUM ARSENIDE SOLAR CELLS

W. Patrick Rahilly
Air Force Aero Propulsion Laboratory
Wright-Patterson Air Force Base, Ohio

Bruce Anspaugh
Jet Propulsion Laboratory
Pasedena, California

SUMMARY

High energy electron, proton and fission spectrum neutrons were used to irradiate advanced silicon and gallium arsenide solar cells currently under development. The specific cells of interest were the non-reflecting vertical junction silicon cells in development at Solarex Corporation, and the gallium (aluminum) arsenide - gallium arsenide cells under investigation by Hughes Research Laboratories, Varian Associates and by Rockwell International. Results of the experiments reveal a superior radiation resistance of the gallium arsenide cells over the silicon cells for the neutron environments. However, the gallium arsenide cell data indicated poor resistance to the electrons and they were suggestive of poor performance in proton environments with energies below 5 Mev (without covers).

INTRODUCTION

Since Air Force and NASA missions in space encounter the earth's Van Allen belt, a continual particle damage assessment of newly evolving solar cell technology is needed in order to provide a useful information feedback into these developments. Very encouraging efficiencies (greater than 17% AMO) have been demonstrated for gallium arsenide solar cells. However, the effect of the various nuclear particles on these cells is sketchy to say the least. The most recent vertical junction structures are also encouraging in that they are showing much higher efficiencies before irradiation than in the past with the attendant resistance to particle damage as expected.

In this paper, results of silicon and gallium arsenide solar cells irradiated with nuclear particles are presented. As a means of comparison, COMSAT non-reflecting cells and Solarex Chevron cells were exposed to the same environments. The data reported are for a limited number of cells because of availability. However, definite trends have been established with specific developmental steps indicated for improved performance.

DESCRIPTION OF EXPERIMENTS AND TEST CELLS

Proton Irradiations

The 10 Mev proton irradiations were carried out at the University of Calif.-Davis facility. The fluences levels used were $1X10^{10}$ p's/cm^2, $1X10^{11}$ p's/cm^2 and $1X10^{12}$ p's/cm^2. The samples were pre-irradiation characterized at AFAPL and at JPL with post irradiation measurements made at both laboratories; very little difference in the measurements was observed for the AFAPL and JPL data. The cells were divided into two sets for comparison of front and backside irradiation effects. All data was accumulated at 25°C and AMO conditions.

Neutron Irradiations

The neutron exposures were conducted at the White Sands Fast Burst Reactor Facility, White Sands Missle Range, New Mexico. The samples were pre-tested at AFAPL, packaged in envelopes, exposed and returned to AFAPL for post irradiation evaluation. Each of the selected fluence levels was dosimetered for neutron and gamma fluence levels. The neutron fluence levels were $1.2X10^{10}$ n's/cm^2, $1.2X10^{11}$ n's/cm^2 and $1.2X10^{12}$ n's/cm^2 (with energies greater than 3 Mev). These fluences correlate to $1X10^{11}$, $1X10^{12}$ and $1X10^{13}$ n's/cm^2 1 Mev equivalent in silicon. All current-voltage data were obtained under simulated AMO and 25°C conditions.

Electron Irradiations

The 1 Mev electron irradiations were performed in vacuum using the JPL Dynamitron. The irradiations were performed in the following manner: The samples were affixed to a test plate, placed in the vacuum chamber and pre-irradiation characterized. The cells were then exposed to $1X10^{13}$ e's/cm^2 and characterized again while in vacuo. Upon reaching $1X10^{14}$ e's/cm^2 and subsequent to each irradiation to higher fluences, the samples were annealed at 60°C for more than eighteen hours. After a fluence of $1X10^{16}$ e's/cm^2 was reached, the samples were annealed at 60°C for greater than eighteen hours, tested, annealed at 125°C for more than four hours and tested again. The latter anneal was performed to determine the amount of recovery in the gallium arsenide cells as suggested previously (1). All measurements were taken 25°C and simulated AMO conditions.

It is necessary to point out that the gallium arsenide cells tested under electron bombardment were the same cells that were exposed to the neutrons. This was done because of limited availability and to note any significant effects associated with neutron damage followed by electron damage. The electron test included three vertical junction cells that were not previously irradiated and one vertical junction cell that had been exposed to the $1X10^{11}$ n's/cm^2 (1 Mev equivalent in silicon) fluence. The results of these experiments are discussed in subsequent paragraphs and include non-neutron irradiated but electron irradiated gallium arsenide cell data gathered by Hughes (2).

Solar Cell Samples

Table I provides a brief description of the silicon and gallium arsenide cells used in the particle irradiation experiments. The Chevron cells were purchased in January 1976, the CNR cells were procured in August 1976 and the vertical junction cells were developmental cells delivered to AFAPL for test purposes in September 1976 and March 1977. The Varian cells were purchased in May 1976, the Hughes cells were delivered under contract to AFAPL in August 1976 and the Rockwell cells were delivered to AFAPL under purchase order in January 1977. These dates are provided in order to give the reader an indication of cell technology status. None of the gallium arsenide cells were specifically designed for high radiation resistance. Also, the vertical junction cells do not represent the optimum design from the standpoints of conversion efficiency and radiation resistance.

Maximum power density data was used to establish a commonality for all cells tested. This commonality cannot be construed to permit an upward size scaling for the smaller cells (smaller than 2cmX2cm). Thickness values for the gallium arsenide cells were not provided since essentially all photovoltaic activity occurs within the top 10 micrometers and the cells were known to be thicker than 250 micrometers. The dimensions of the detailed vertical junction geometry were approximately 8 micrometer wide walls with 7 micrometer wide and 150 micrometer deep channels. Further details are provided in the proceedings of this meeting and elsewhere (3,4).

It is necessary to point out that the Varian and Rockwell cells were specially mounted. The Varian cells were soldered onto a molybdenum block to ensure ease in handling. The Rockwell cells were mounted in IC pots for the same reason.

RESULTS AND DISCUSSION

Proton Damage

Table II gives pre and post proton irradiation power densities. The Chevron and Rockwell cells were not included in the proton tests. Because of the variation in initial power densities of the cells, comparison of their relative changes versus proton fluence were made. Both backside and front side exposures were accomplished in this test and cell results of the proton tests are shown in Figure 1. The following discussions refer to Figure 1 and are separated into silicon and gallium arsenide cell types.

Silicon Cells

The vertical junction cells performed quite well in comparison with the CNR cells for both the front and rear proton exposures. The differences observed can be accounted for the the vertical junction geometry. It is interesting to note that even though the NRVJ-B cells were covered with 12 mils of quartz they demonstrated considerable resistance over the CNR cells for

front side exposure. The differences observed for front and backside irradiations of the NRVJ-B cells is due to the thickness of these cells (14 microns). The protons entering from the backside created more damage in the walls which reduced the carrier collection efficiency more seriously than for the front side irradiations. It is expected that thinner NRVJ cells would show less separation between front and back exposure results. The CNR cells showed very little difference in relative changes for both front and rear irradiations. This was expected since the cells had only 6 mils of quartz on top and were only ten to twelve mils thick.

Gallium Arsenide Cells

The HGAAS cells showed drastic changes which are accounted for by the presence of 12 mil quartz covers on the cell fronts and the thickness of the GaAs substrate. The front side protons were deposited in the vicinity of the PN junction thus causing considerable end of range damage there. The back side protons induced even more drastic results which are also explained by the protons creating high damage in the photovoltaically active region of the cells. To the contrary the VGAAS displayed small changes since these cells did not have coverslides applied. It would be expected that these cells would perform nearly identical to the HGAAS cells if covers were present. In any case, the results for the HGAAS cells clearly indicated their sensitivity to lower energy protons (less than 5 Mev) and further that the gallium arsenide cells used in earth orbit space must be adequately covered or shielded from the proton component of the Van Allen Belt.

Neutron Damage

Table III provides pre and post neutron irradiation power densities. The HGAAS cells were not available for these tests. As for the proton data, variation in initial cell performance suggested that comparisons be made in terms of relative changes versus neutron fluence. Results for all cells are shown in Figure 2. The CNR cells for the higher neutron fluence were broken during test as indicated by the dashed line. The results of the test are discussed in relation to the information of Figure 2 and are separated by semiconductor material type.

Silicon

The relative changes clearly show the NRVJ-A cells have superior radiation resistance over the CNR and Chevron cells. This is a direct result of the vertical junction geometry. Since the neutrons create recombination centers uniformily in silicon it is expected that NRVJ cell geometry optimization will further improve their ability to survive neutrons. The CNR and Cheveron cells degrade in a manner typical for 2 ohm centimeter silicon material.

Gallium Arsenide Cells

Both the VGAAS and RGAAS cells out performed all silicon cells. This is not unexpected however, since the neutrons transfer more energy per collision to the silicon atoms (Ga and As are heavier). The observed difference between

the VGAAS and RGAAS results for the highest fluence, although not considerable, may be associated with the thickness of the P type GaAs layer. These results are consistent with results obtained with the electron irradiations.

Electron Damage

The vertical junction cells exposed to the 1 Mev electron irradiations were not representative of the conversion efficiencies that Solarex has achieved previously (3,4). However, these cells were tested because of availability. The gallium arsenide cells tested were those cells that had been exposed to the fission spectrum neutrons. These particular cells are those identified in Table III with an asterisk and were used because of limited quantities on hand. The discussions that follow are based on information revealed in Figure 3,4,5, and 6. Figure 3 summarizes electron damage results for the silicon cells including results obtained previously by JPL for the CNR cells. Figure 4 illustrates the behavior of the gallium arsenide cells made by Varian and Rockwell, and includes previous data generated for gallium arsenide cells from Hughes Research Laboratories (2). Figures 5 and 6 show relative changes of maximum power for the Rockwell and Varian cells respectively again with the Hughes data included.

Silicon Cells

The results shown in Figure 3 were somewhat interesting in that the degradation per decade of fluence for the vertical junction cells is about one half that for the other cells. This is due to the wall and channel geometry of these cells. Also, it was noted that the Chevron cells degraded at a slightly higher rate than the CNR cells. Attempts were made to specifically identify the silicon material used in the fabrication of these Chevron cells. The required information was not available but counter doping is suspected. The silicon was obtained from Wacker and such material is known to be counterdoped in some cases with phosphorus (5). The presence of the N dopant can increase the density of recombination centers form during irradiation.

Gallium Arsenide Cells

The electron damage data shown in Figure 4 is somewhat difficult to explain since details of the cell fabrication are not known to the authors. However, some information on the Hughes Cells (used for comparison) is known and comparison suggests an explanation. The comparisons are best made using Figures 5 and 6. Figure 5 shows the normalized powers for the Rockwell cells and the Hughes cell data taken from Reference (2). The most important parameter is the location of the PN junction. Figure 5 suggests that the Rockwell cells possessed deep junctions (greater than one micrometer). Figure 6 suggests that the Varian cells possessed junction depths less than one micrometer. It can be shown mathematically that the light generated current is very sensitive to junction placement in relation to electron damage. Thus if this analysis is correct, then it is very important to make the P layer very thin (<.5 micrometer) in order that more carrier generation occurs in the N layer.

Data has been reported that shows an anneal of electron damage in gallium arsenide solar cells at temperatures as low as 125°C. The results of the 125°C/four hour anneal show that no significant change occurred.

CONCLUDING REMARKS

The data reported in this paper can only suggest trends for use in the vertical junction silicon cell and the gallium arsenide development programs. When more cells become available further evaluation will be required to provide a stronger statistical base. In view of the experimental results obtained the following conclusions are made.

(a) The vertical junction solar cells offer the most promise for combined high efficiency and radiation resistance compared to other advanced silicon cell developments. By further refining the geometry to obtain narrower channels, both red response and radiation resistance will improve.

(b) The CNR cells continue to have the highest end of life output. Unfortunately this technology has not been demonstrated by anyone other than COMSAT.

(c) The electron degradation of the Chevron cells was higher than expected and the tentative conclusion is that the silicon material used was compensated with either phosphorous or arsenic.

(d) The gallium arsenide cells show excellent resistance to fission neutron damage. Since the neutrons will not transfer much energy to either gallium or arsenic (except for nuclear absorption resonances) these cells will always show higher resistance to neutron damage.

(e) The gallium arsenide cells have a limited tolerance to low energy protons. This is evidenced by the drastic changes observed for the cells with a 12 mil cover glass. Gallium arsenide solar cells will require coverslides for space application.

(f) The 125°C-four hour anneal did not induce recovery for the gallium arsenide cells exposed to $1X10^{16}$ e's/cm^2. It is concluded that a much higher temperature is required.

(g) Generally, once the gallium arsenide cell fabrication technology becomes highly reproducible with high efficiencies obtained, it will be necessary to "map out" their behaviour in electron and proton environments of various energies.

REFERENCES

1. R. Miller and J. Harris, "Gallium Arsenide Concentrator System", AIAA Conference on the Future of Aerospace Power Systems, March 1977.

2. L.J. Goldhammer, "(AlGa)As/GaAs Solar Cells for Space", Final Report F33615-76-C-2137, February 1977.

3. J. Lindmayer, C. Wrigley, "New Developments in Vertical Junction Solar Cells", Late News Item, 12th IEEE Photovoltaic Specialists Conference, November 1976.

4. J. Lindmayer, C. Wrigley and J. Wohlgemuth, "Developments in Vertical Junction Solar Cells", this proceedings.

5. J. Bernard, R.O.L. Crabb, "Photon Degradation of Electron-Proton Irradiated Silicon Solar Cells', Conference Record, 12th IEEE Photovoltaic Specialists Converence", Nov 1976.

TABLE I DESCRIPTION/IDENTIFICATION OF CELL SAMPLES

MANUFACTURER	IDENTIFICATION	AREAL SIZE	CELL THICKNESS	RESISTIVITY	COVER
SOLAREX	NRVJ-A	2CM x 2CM	14 MILS	1.5 Ω-CM	NO
SOLAREX	NRVJ-B	2CM x 2CM	14 MILS	2 Ω-CM	12 MILS
SOLAREX	CHEVRON	2 CM x 2CM	14 MILS	2 Ω-CM	NO
COMSAT	CNR	2CM x 2CM	10-12 MILS	2 Ω-CM	6 MILS
HUGHES	HGAAS	2CM x 2CM	> 10 MILS		12 MILS
ROCKWELL	RGAAS	1CM x 1CM	> 10 MILS		NO
VARIAN	VGAAS	1.27CM x 1.27CM	> 10 MILS		NO

TABLE II PRE/POST PROTON DAMAGE DATA (MW/CM²)

	1×10^{10}		1×10^{11}		3×10^{11}		1×10^{12}	
	PRE	POST	PRE	POST	PRE	POST	PRE	POST
NRVJ-B(F)[a]	–	–	14.63	13.01	–	–	14.01	10.04
NRVJ-B (B)	–	–	16.73	14.13	–	–	15.93	10.80
CNR (F)	–	–	19.63	BROKEN	–	–	19.95	12.59
CNR (B)	–	–	19.56	16.10	–	–	19.60	12.62
HGAAS (F)	–	–	21.37	19.70	–	–	20.87	12.43
HGAAS (B)	–	–	22.13	17.75	–	–	22.04	6.24
VGAAS (F)	17.98	17.97	15.70	14.84	20.73	18.20	18.35	14.38

a (F) = FRONT (B) = BACK

TABLE III PRE/POST NEUTRON DAMAGE DATA (MW/CM²)

	1.2×10^{10}		1.2×10^{11}		1.2×10^{12}	
	PRE	POST	PRE	POST	PRE	POST
NRVJ-A	17.69	16.22	17.76	14.41	17.40	11.17
CHEVRON	16.83	15.35	16.80	12.62	17.04	9.37
CNR	19.23	17.27	19.40	14.91	19.67	BROKEN
ROCKWELL	15.63	15.62*	19.89	19.81*	17.00	14.37*
VARIAN	14.50	14.48*	16.52	15.85*	16.71	14.81*

* THESE CELLS WERE USED FOR ELECTRON IRRADIATIONS ALSO

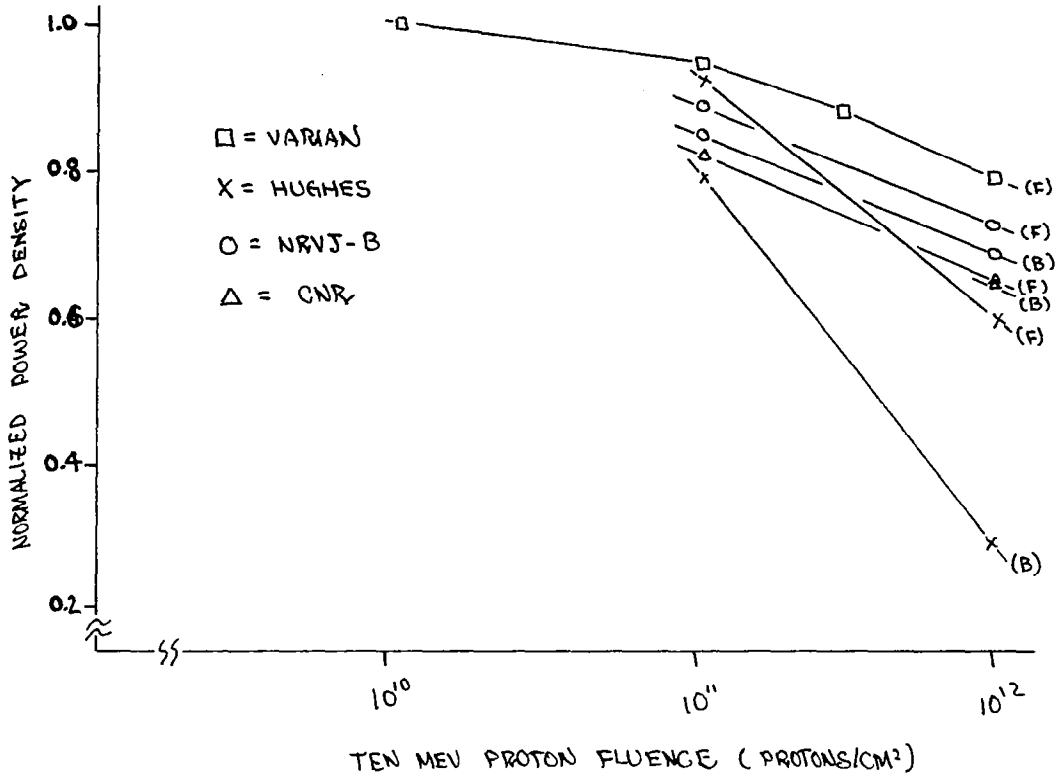

FIGURE 1 EFFECT OF HIGH ENERGY PROTONS

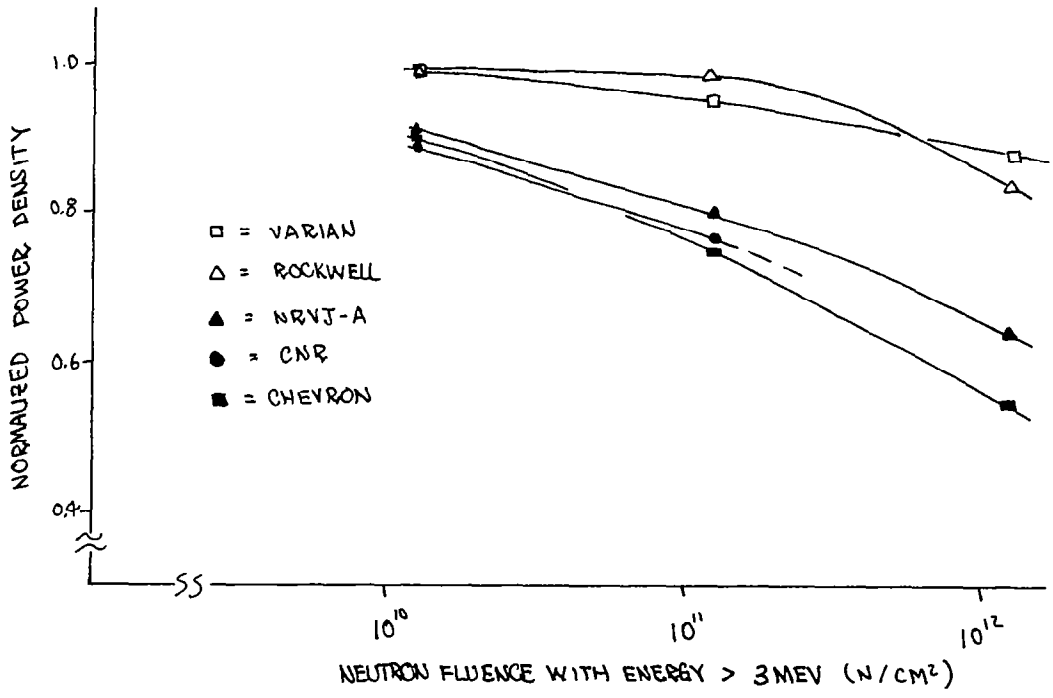

FIGURE 2 EFFECT OF FISSION NEUTRONS

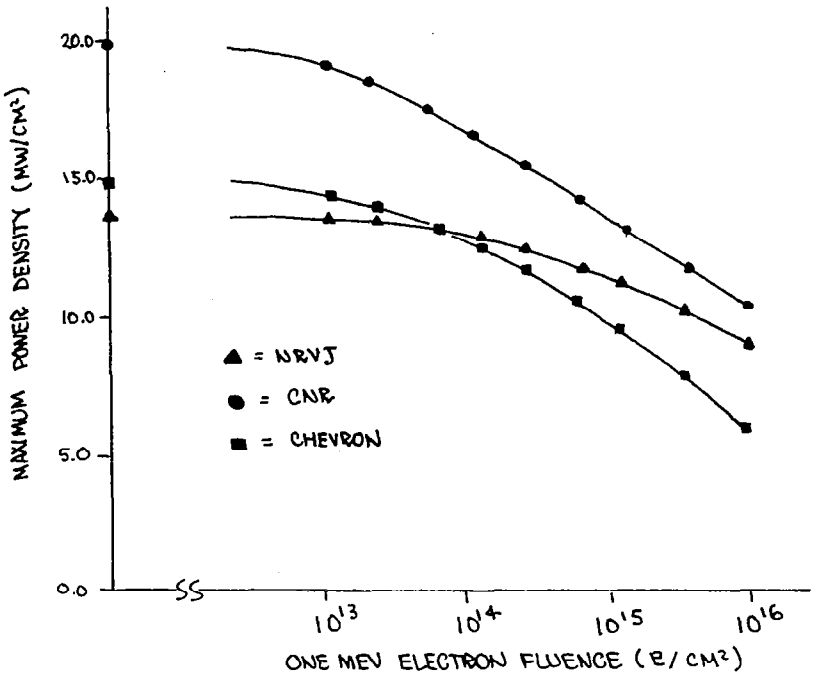

FIGURE 3 EFFECT OF HIGH ENERGY ELECTRONS

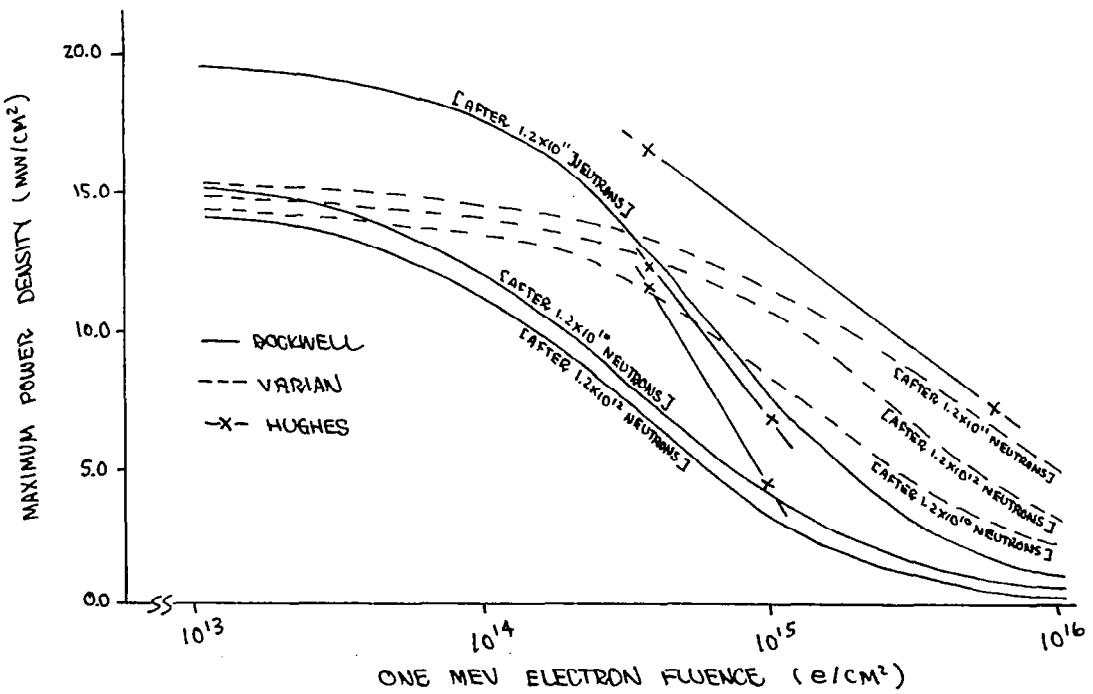

FIGURE 4 MAXIMUM POWER DENSITY VERSUS ELECTRON FLUENCE

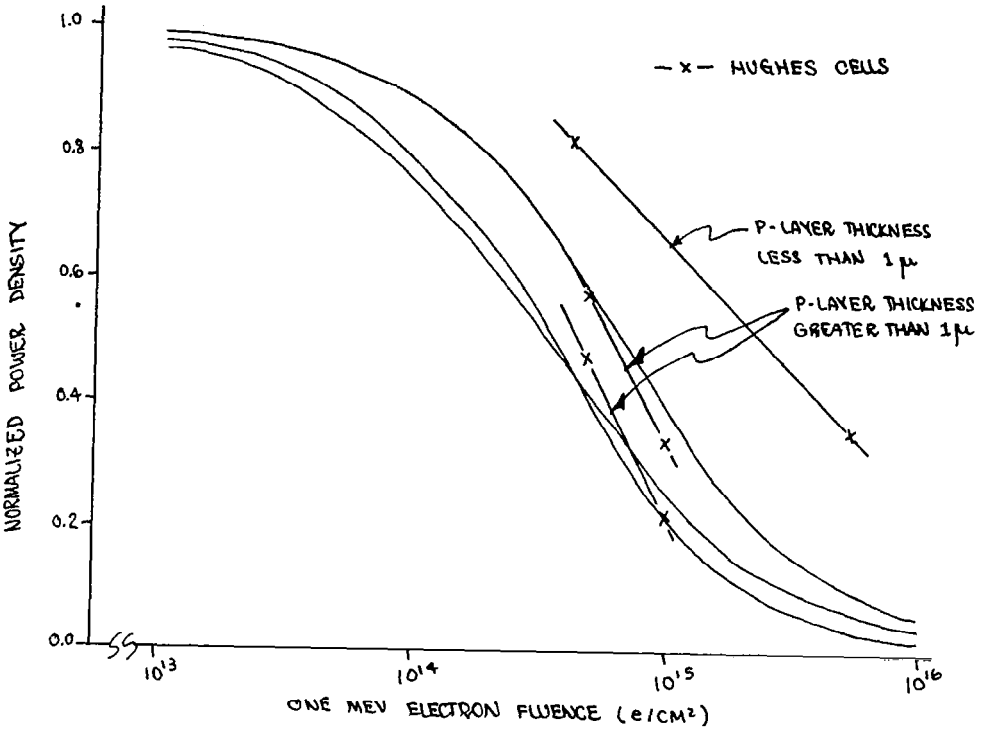

FIGURE 5 RADIATION DAMAGE FOR ROCKWELL CELLS IN RELATION TO JUNCTION DEPTH

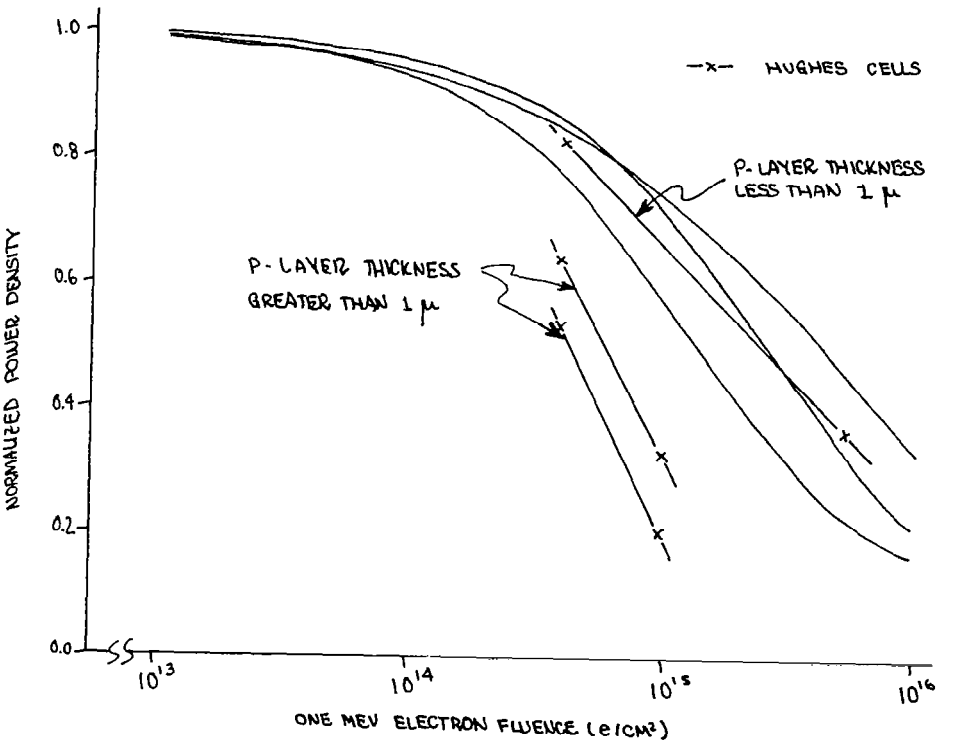

FIGURE 6 RADIATION DAMAGE FOR VARIAN CELLS IN RELATION TO JUNCTION DEPTH

ATTENDEES

Bruce Anspaugh
Jet Propulsion Laboratory
4800 Oak Grove Drive
Pasadena, CA 91103

Cosmo R. Baraona
NASA Lewis Research Center
21000 Brookpark Road
Cleveland, OH 44135

Jerry E. Beam
AFAPL
Wright Patterson AFB, OH 45433

Dan Bernatowicz
NASA Lewis Research Center
21000 Brookpark Road
Cleveland, OH 44135

Henry W. Brandhorst
NASA Lewis Research Center
21000 Brookpark Road
Cleveland, OH 44135

J. Broder
NASA Lewis Research Center
21000 Brookpark Road
Cleveland, OH 44135

L. C. Brown
Ohio State University
Columbus, OH 43210

Li-Jen Cheng
State University of New York
at Albany
1400 Washington Avenue
Albany, NY 12222

Edward N. Clarke
Worcester Polytechnic Institute
Worcester, MA 01609

Michael G. Coleman
Motorola, Inc.
P. O. Box 2953
Phoenix, AZ 85062

James W. Corbett
State University of New York
at Albany
Albany, NY 12222

John C. Corelli
Rensselaer Polytechnic Institute
Troy, NY 12181

Robert V. D'Aiello
RCA Laboratories
Princeton, NJ 08540

Harry C. Gatos
Massachusetts Institute of
Technology
Cambridge, MA 02139

Michael P. Godlewski
NASA Lewis Research Center
21000 Brookpark Road
Cleveland, OH 44135

Leland J. Goldhammer
Hughes Aircraft
19316 Entradero Avenue
Torrance, CA 90503

Chandra Goradia
Cleveland State University
Cleveland, OH 44115

Manju Goradia
Cleveland State University
Cleveland, OH 44115

Edward B. Hale
University of Missouri-Rolla
Rolla, MO 65401

Russell E. Hart, Jr.
NASA Lewis Research Center
21000 Brookpark Road
Cleveland, OH 44135

John R. Hauser
North Carolina State University
Electrical Engineering Department
Raleigh, NC 27607

Harold Hovel
IBM Corporation
P.O. Box 218
Yorktown Heights, NY 10598

James A. Hutchby
NASA Langley Research Center

Hampton, VA 23665

P. A. Iles
OCLI
Photoelectronics Division
15251 Don Julian Road
Industry, CA 91746

G. S. Kamath
Hughes Research Laboratory
3011 Malibu Canyon Road
Malibu, CA 90265

Allen R. Kirkpatrick
Simulation Physics, Inc.
Patriots Park
Bedford, MA 01730

R. Knechtti
Hughes Research Laboratory
3011 Malibu Canyon Road
Malibu, CA 90265

Young H. Lee
State University of New York
at Albany
1400 Washington Avenue
Albany, NY 12222

Fred Lindholm
University of Florida
Electrical Engineering Dept.
Gainesville, FL 32611

Bernard Lubarsky
NASA Lewis Research Center
21000 Brookpark Road
Cleveland, OH 44135

Leonard M. Magid
ERDA
Washington, DC 20545

Walter Matzen
Texas Instruments
P.O. Box 5012
13500 N. Central Expressway
Dallas, TX 75222

Andrew Meulenberg
COMSAT
Clarksburg, MD 20734

John Minnucci
Simulation Physics, Inc.
Patriots Park
Bedford, MA 01730

James A. Naber
IRT Corporation
P.O. Box 80817
San Diego, CA 92037

Henry Oman
Boeing Aerospace Co.
P. O. Box 3999
Seattle, WA 98124

Fred H. Pollak
Yeshiva University
c/o Belfer Graduate School of
Science
2495 Amsterdam Avenue
New York, NY 10033

Jack Posner
JARAH Consultants, Inc.
1727 Ladd Street
Silver Spring, MD 20902

Robert A. Pryor
Motorola, Inc.
P.O. Box 2953
Phoenix, AZ 85062

W. Patrick Rahilly
USAF Aero Propulsion Laboratory
POE-2
WPAFB, OH 45433

Bernd Ross
AF Consultant
2154 Blackmore Court
San Diego, CA 92109

Bernie Sater
NASA Lewis Research Center
21000 Brookpark Road
Cleveland, OH 44135

Luther W. Slifer, Jr.
NASA Goddard Space Flight Center
Greenbelt Road
Greenbelt, MD 20771

Joseph R. Srour
Northrop Research and
Technology Center
3401 West Broadway
Hawthorne, CA 90250

Richard J. Stirn
Jet Propulsion Laboratory
4800 Oak Grove Drive
Pasadena, CA 91103

Clifford K. Swartz
NASA Lewis Research Center
21000 Brookpark Road
Cleveland, OH 44135

Gilbert H. Walker
NASA Langley Research Center
Hampton, VA 23665

I. Weinberg
NASA Lewis Research Center
21000 Brookpark Road
Cleveland, OH 44135

R. D. Westbrook
Oak Ridge National Laboratory
P.O. Box X
Oak Ridge, TN 37830

John H. Wohlgemuth
Solarex Corporation
1335 Piccard Drive
Rockville, MD 20850

Richard F. Wood
Oak Ridge National Laboratory
P.O. Box X
Oak Ridge, TN 37830

1. Report No.	2. Government Accession No.	3. Recipient's Catalog No.
NASA CP-2020		

4. Title and Subtitle	5. Report Date
SOLAR CELL HIGH EFFICIENCY AND RADIATION DAMAGE	October 1977
	6. Performing Organization Code
7. Author(s)	8. Performing Organization Report No. E-9334
9. Performing Organization Name and Address	10. Work Unit No.
	11. Contract or Grant No.
12. Sponsoring Agency Name and Address National Aeronautics and Space Administration Washington, D.C. 20546	13. Type of Report and Period Covered Conference Publication
	14. Sponsoring Agency Code

15. Supplementary Notes

16. Abstract

A conference on Solar Cell High Efficiency and Radiation Damage was held at the Lewis Research Center on April 28-29, 1977, in which representatives of government, industry, and universities participated. Sessions were held on silicon solar cell analysis and fundamental measurements, silicon cell technology, gallium arsenide research and technology, and radiation effects on silicon and gallium arsenide cells. This proceedings is composed of brief papers or summaries covering the formal presentations. Included also is the Chairman's summary of the meeting, which contains the major topics raised in the numerous discussion periods.

17. Key Words (Suggested by Author(s))	18. Distribution Statement
Solar cell; Solar cells; Radiation damage; High efficiency; Silicon; Gallium arsenide	Unclassified - unlimited STAR Category 44

19. Security Classif. (of this report)	20. Security Classif. (of this page)	21. No. of Pages	22. Price*
Unclassified	Unclassified	253	A12

* For sale by the National Technical Information Service, Springfield, Virginia 22161

NASA-Langley, 1977